

Multicompartmental Carriers for Medical Applications

by

Asish C Misra

A dissertation submitted in partial fulfillment
of the requirements for the degree of
Doctor of Philosophy
(Biomedical Engineering)
in the University of Michigan
2014

Doctoral Committee:

Professor Joerg Lahann, Chair
Professor Nicholas A. Kotov
Professor Gary D. Luker
Professor Michael J. Solomon
Professor Shuichi Takayama

To my family & friends

Acknowledgements

I would like to convey my deepest gratitude and thanks to my PhD advisor, Professor Joerg Lahann. His exceptional guidance and thoughtful insight allowed me to develop critical scientific skills and pursue novel research interests with encouragement. He has helped me acquire a great amount of new knowledge and skills in areas that I initially was far from familiar with. I am honored to be his student and to have the opportunity to work in his lab, which has been an immensely rewarding experience. I would also like to thank my committee members, Professor Nicholas A. Kotov, Professor Gary D. Luker, Professor Michael J. Solomon, and Professor Shuichi Takayama, for their support during my years here, for guiding me through the defense process.

I would also like to express my thanks to the many people I have been fortunate to have worked with, including all of my colleagues in the Lahann group, and collaborators at Michigan and elsewhere. Much of this work would not have been possible without their tremendous efforts. I would like to thank Dr. Srijanani Bhaskar for helping me get started on the PEI based endosome-sensing carriers. I would like to thank Dr. Tae-Hong Park for developing and synthesizing the virus-mimicking particles (VMPs), and working closely with me on the design of the corresponding *in vitro* experiments. I would like to thank Dr. Sampa Saha and Dr. Hakan Durmaz for synthesizing the library of functionalized polylactides. Dr. Hakan Durmaz and Artak Shahnas synthesized the MIBG conjugates, and I am grateful very grateful to them. I would like to thank Randy P. Carney, Maria Ricci, and the Stellacci group for their helpful discussions and collaborations on the VMP work, and providing us with striped gold nanoparticles. I am also very thankful to Dr. Marek Grzelczak, Dr. Ana Sanchez Iglesias, and the Liz-Marzán group for their great insight and discussions, in addition to providing us with plasmonic nanoparticles of exceptional quality. I would also like to thank Amanda Stacer and the Luker group for their invaluable help and work on

targeting triple negative breast cancer, especially with the *in vivo* studies. I would also like to thank the Yanik group for collaborating with us on the targeting neuroblastomas.

It has been an honor and pleasure to work with each member of the Lahann group, both alum and current, and I would like to express my deepest thanks and gratitude to the alum members, Dr. Tae-Hong Park, Dr. Kyungjin Lee, Dr. Sampa Saha, Dr. Sangyeul Hwang, Dr. Himabindu Nandivada, Dr. Srijanani Bhaskar, Dr. Aftin Ross, Dr. Jaewon Yoon, Dr. Thomas Eyster, Dr. Hakan Durmaz, Dr. Amit Sitt, and Dr. Jana Soukupova, and the current members, Dr. Xiaopei Deng, Dr. Bradley Plummer, Dr. Luis Solorio, Dr. Kathleen McEnnis, Dr. Ping Li, Sahar Rahmani, Kenneth Cheng, Jake Jordahl, Ramya Kumar, Stacy Ramcharan, Nathan Jones, Hyesun Jun, Fan Xie, and Yu Liang. I would also like to thank the members of the Lahann group at the Karlsruhe Institute of Technology, Germany, for all their advice and suggestions. I would also like to express my gratitude to the staff at core facilities and NCRC for making training, measurements, scheduling, among other tasks, easy and efficient.

So many people have touched my life during this time, and I have been fortunate to meet each one. Labmates, friends, and family members have all helped me through these years as a PhD student, and I would like to thank them all. I would especially like to thank Huanan Zhang, Jaewon Yoon, and Sahar Rahmani for their friendship; this journey would not have been possible without their support – I am forever indebted to them and profoundly grateful. I would also like to thank my parents and my brother for their unconditional love.

Table of Contents

Dedication	ii
Acknowledgements	iii
List of Figures	viii
List of Appendices	xiv
Abstract	xv
Chapter	
1. Introduction	1
1.1 Current Therapeutic Modalities in Medicine	1
1.2 Carrier-based Targeted Therapies	2
1.2.1 Manufacturing Processes	2
1.2.2 Inorganic Carriers	4
1.2.3 Macromolecular Carriers	4
1.2.4 Carriers with Additional Functionalities	5
1.3 Barriers to Effective Carrier-based Therapy	6
1.4 Fabrication of Multicompartmental Carriers	8
1.5 Electrohydrodynamic Co-Jetting	9
1.6 Aims of this Study	12
1.7 References	13
2. Carriers with Therapeutic Functionalities	21
2.1 Cytosolic Delivery with Endosome-sensing Carriers	21
2.1.1 Background and Motivation	21
2.1.2 Methods	23
2.1.3 Results and Discussion	26
2.1.4 Summary	34
2.2 Towards Developing Novel Endosome-sensing Carriers	35

2.2.1 Background and Motivation	35
2.2.2 Methods	38
2.2.3 Results and Discussion	40
2.2.4 Summary	47
2.3 Additional Therapeutic Functionalities	47
2.3.1 Background and Motivation	47
2.3.2 Methods	48
2.3.3 Results and Discussion	50
2.2.4 Summary	55
2.4 References	56
3. Carriers with Targeting Capabilities	63
3.1 Targeting Cell Membranes with Virus-mimicking Particles	63
3.1.1 Background and Motivation	63
3.1.2 Methods	65
3.1.3 Results and Discussion	67
3.1.4 Summary	75
3.2 Targeting Triple Negative Breast Cancer via CXCR4	76
3.2.1 Background and Motivation	76
3.2.2 Methods	77
3.2.3 Results and Discussion	78
3.2.4 Summary	82
3.3 Targeting Neuroblastomaa via Norepinephrine Transporters	82
3.3.1 Background and Motivation	82
3.3.2 Methods	83
3.3.3 Results and Discussion	85
3.3.4 Summary	87
3.4 References	88
4. Carriers with Long Circulation Half-Lives	93
4.1 Background and Motivation	93
4.2 Methods	95
4.3 Results and Discussion	96
4.4 Summary	99
4.5 References	101

5. Towards Multifunctional Carriers	103
5.1 Background and Motivation	103
5.2 Methods	104
5.3 Results and Discussion	105
5.4 Summary	110
5.5 References	112
6. Conclusions and Future Directions	114
6.1 Impact of Multicompartmental Carriers in Targeted Therapy	114
6.2 Towards Mass Production of Multicompartmental Carriers	114
6.2.1 Uniformity and Reproducibility	114
6.2.2 High Yield Production	117
6.3 Further Development of Current Systems	119
6.3.1 Tailoring Environment-sensing Materials	119
6.3.2 Applications of Virus-mimicking Particles	120
6.3.3 Applications of Virus-mimicking Particles	122
6.4 Future Outlook	123
6.5 References	125
Appendices	126

List of Figures

- Figure 1-1.* Representation of the physiological barriers in carrier-based targeted therapies..... 6
- Figure 1-2.* Schematic of a typical EHD co-jetting setup. Photo shows a jet emitted from a Taylor cone during EHD co-jetting, adapted from ref..... 10
- Figure 1-3.* Some of the particulate carriers fabricated using EHD co-jetting. (a) Confocal and scanning electron microscopy (SEM) images of particles with compartmentalized materials of differing glass temperatures, subjected to a shape-shifting process. (b) Confocals of disks, rods, and spheres made by varying process parameters. (c), (d) Confocal images demonstrating selective surface modification. (e) Confocal image of microcylinders that have a hydrogel brush selectively grown on one side. (f) Raman confocal image of a particulate carrier with three different compartmentalized polymers. Images adapted from refs..... 11
- Figure 2-1.* (a) Bicompartamental particle design showing dissimilar compartments with complementary functions – imaging and siRNA delivery (and endosomal escape). (b), (c) Representative fluorescent CLSM and DLS data of siRNA-loaded bicompartamental particles (scale bar is 1 μm)..... 24
- Figure 2-2.* Swelling studies performed via DIC microscopy. (a) Particles incorporating higher molecular weight PEI exhibit a higher degree of swelling after four hours in PBS. (b) Particles incorporating uncrosslinked PEI are observed to have different swelling kinetics than that of crosslinked PEI, as well as eventually having dissolution of the PEI. (c) Particles with crosslinked PEI show different degrees of swelling at different pH levels after 6 hours of incubation in the appropriate buffered solutions. All scale bars are 10 μm 27
- Figure 2-3.* FTIR measurements of bicompartamental particles with PEI and DSP (crosslinker) incorporated on one side. Particles were jetted onto gold coated silicon wafers and kept at ambient conditions for 0, 24, 48, and 72 hours after jetting. At each time point, a wafer was used to perform FTIR in reflectance mode..... 28
- Figure 2-4.* (a) Swelling kinetics of bicompartamental particles with crosslinked high M_w PEI via DIC microscopy. (b) Fluorescent CLSM image of bicompartamental particles, with blue fluorescent PLGA imaging compartment, and a composite PLGA/crosslinked PEI compartment loaded with rhodamine-labeled siRNA. (c) Release kinetics of particles from (b) in PBS. All scale bars are 10 μm 29
- Figure 2-5.* (a) SEM image of bicompartamental PLGA/PLGA-PEI nanoparticles. Scale bar is 1 μm . (b) Size distribution of particles from (a) using ImageJ. (c) DLS data showing large

increase in hydrodynamic size in pH 4 compared to in pH 7.4. (d) Nanoparticles (blue) are readily uptaken by GFP-expressing breast cancer cells (MDA-MB-231/GFP). Scale bar is 20 μm 30

Figure 2-6. *In vitro* particle incubation experiments with MDA-MB-231/GFP breast cancer cells. (a) Cells with no particles or siRNA treatment. (b) Results from incubating particles and free siRNA (not loaded in the particles). (c) Results from incubation with siRNA-loaded particles. All scale bars are 50 μm . Concentrations for the particle incubation shown here were 100 $\mu\text{g/ml}$ 31

Figure 2-7. Quantification of GFP expression by image analysis. Control represents that have not been incubated with particles nor siRNA. PEI-siRNA represents a control where cells were incubated with PEI-siRNA polyplexes (1 mg/mL PEI, 1 $\mu\text{g/mL}$ siRNA). PLGA/PEI+siRNA represents cells incubated with bicompartmental particles and soluble siRNA (100 $\mu\text{g/mL}$ PLGA/PEI, 1 $\mu\text{g/mL}$ siRNA) PLGA/PEI-siRNA represents cells incubated with siRNA-loaded bicompartmental particles at a concentration of 100 $\mu\text{g/mL}$ 33

Figure 2-8. XTT assay performed on MDA-MB-231/GFP cells, incubating with various concentrations of PLGA/PEI bicompartmental particles. Cells were incubated with particles for approximately 12 hours, after which media was changed, and XTT assay was performed after another 12 hours (24 hours after start of incubation)..... 34

Figure 2-9. (a) Facile synthesis of TBA-alginate. (b) FTIR of synthesized TBA-alginate. (c) DLS data of PLGA/PLGA-PEI-DSP nanoparticles stabilized by tween 20 only (red), and tween 20 and TBA-alginate (green)..... 40

Figure 2-10. XTT assay performed on MDA-MB-231/GFP cells with PLGA/PLGA-PEI-DSP nanoparticles stabilized by tween 20 only (red), and tween 20 and TBA-alginate (blue). ... 41

Figure 2-11. (a) SEM image of PLGA/glycol chitosan (PLGA/GC) nanoparticles. Scale bar is 1 μm . (b) Corresponding DLS data for (a). (c) Luciferase based toxicity assay of PLGA/GC particles on luciferase and GFP expressing MDA-MB-231 cells. (d) Fluorescent images comparing PLGA/GC particle (control ESCs) incubation to PLGA/GC-siRNA (siRNA-loaded ESCs). (e) Quantification of GFP expression from (d). *In vitro* data obtained by Luker group..... 42

Figure 2-12. (a) SEM image of AHM_wD based carriers. (b) Zoomed in SEM image showing cup-like morphology. (c), (d) Bright field confocal images of AHM_wD based carriers incubated in pH 7.4 and 5, respectively. (e), (f) SEM images of washed AHM_wD carriers after 6 hour incubations in pH 7.4 and 5, respectively. Scale bars are (a, e, f) 10 μm , (b) 1 μm , and (c, d) 50 μm 44

Figure 2-13. (a) Synthesis scheme of vitamin C based monomer and PPVC by ADMET polymerization of the monomer. (b) ¹H NMR of monomer. (c) ¹H NMR of PPVC. All synthesis and characterization were done by Dr. Hakan Durmaz..... 46

Figure 2-14. PLGA/PPVC carriers (a) immediately after purification (t = 0⁺), (b) after 24 hour incubation in pH 7.4, and (c) after 24 hours incubation in pH 5. Scale bars are 5 μm 47

Figure 2-15. (a) DIC image of Au NR loaded PLGA carriers. (b) SEM of carriers showing porosity only on one side. (c) DIC image of carriers during NIR irradiation (no changing of focus). (d) DIC images of a carrier before (left) and after (right) NIR irradiation with focusing maintained manually throughout. Scale bars are (a, c) 50 μm (insets are 25 μm) and (b) 10 μm 51

Figure 2-16. (a) UV-Vis spectra of PLGA, Au NS, and PLGA + Au NS solutions. (b), (c) TEM images of Au NS loaded carriers. (d) UV-Vis spectra of PLGA, Au NDB, and PLGA + Au NDB solutions. (e), (f) TEM images of Au NDB loaded carriers. Scale bars are (b, e) 500 nm and (c, f) 100 nm..... 53

Figure 2-17. Raman confocal microscopy of Au NDB loaded PLGA carriers. (a) Bright field image. (b) Color map of Au NDB contribution to Raman spectra. (c) Color map of PLGA contribution. (d) Overlay of Au NDB and PLGA contributions. (e) Estimated pure Raman spectra of PLGA (blue) and Au NDBs (red) used in analysis. All scale bars are 2 μm 54

Figure 2-18. Raman confocal microscopy of Ag NC loaded PLGA carriers. (a) Bright field image. (b) Color map of Ag NC contribution to Raman spectra. (c) Color map of PLGA contribution. (d) Overlay of Ag NC and PLGA contributions. (e) Estimated pure Raman spectra of PLGA (blue) and Ag NCs (red) used in analysis (top right is zoom in of PLGA spectra). All scale bars are 5 μm 55

Figure 3-1. Schematic showing the EHD co-jetting process and fabrication of the particles..... 64

Figure 3-2. (a) Design and synthesis scheme of control particles (1-3) and virus-mimicking particles, VMPs (4). (b) Fluorescent CLSM overlay image of VMPs demonstrating their bicompartamental architecture. Scale bar is 20 μm . (c) TEM image of a VMP (with a magnified image of it on the right), showing selective surface modification with striped gold nanoparticles on one side of the particle surface. Scale bars are 500 nm for the left TEM image, and 200 nm for the right TEM image..... 68

Figure 3-3. Fluorescent CLSM overlay images of MDA-MB-231/GFP cells incubated with particles 1 (a), 2 (b), 3 (c), and 4 (d) for 6 hours at concentrations of 10 (left), 50 (middle), and 100 (right) $\mu\text{g}/\text{ml}$. Scale bars are 50 μm 69

Figure 3-4. Quantification of average number of bound and/or internalized particles per cell for 6-hour incubation experiments (Figure 3-3). Significance levels are: * $p < 0.01$, ** $p < 0.001$. *** $p < 0.0001$ 70

Figure 3-5. (a) Fluorescent CLSM images from endosomal staining studies with 10 $\mu\text{g}/\text{ml}$ of particles 1 – 4 (red & green) were incubated with MDA-MB-231/GFP cells (green) for 6 hours, followed by incubation with an endosomal stain (blue). Scale bars are 10 μm . (b) SEM images of MDA-MB-231/GFP cells after incubation with 10 $\mu\text{g}/\text{ml}$ of particles 1-4. Scale bars are 20 μm 71

Figure 3-6. 3d reconstructions of zstacks corresponding to 6-hour incubation experiments shown in Figures 3-3 and 3-4..... 72

Figure 3-7. Representative fluorescent CLSM overlay images from long-term incubation studies with particles 1 (a), 2, (b), 3 (c), and 4 (d) at a fixed concentration of 100 µg/ml, with incubation times of 6 (leftmost), 24 (second left), 48 (third left), and 72 (rightmost) hours. Scale bars are 25 µm..... 73

Figure 3-8. K-means clustering analysis of particles 1-4 at different incubation times, showing (a) average number of particles per cluster and (b) average cluster radius. Errors bars are standard error..... 74

Figure 3-9. (a) Reaction scheme for selective immobilization of AMD3100 and fluorescently labeled DNA. (b), (c) Confocal images of a microcylinder (blue on one side) after AMD3100 immobilization and labeling with fluorescent DNA (red). (d) Overlay of (b) and (c). Scale bars are 20 µm..... 79

Figure 3-10. (a) SEM image of co-jetted carriers containing PLGA and PLA-acryl on one side, and PLGA, PEI, and DSP on the other side. Scale bar is 1 µm. (b) DLS of the carriers in 0.01 v/v% Tween20/PBS..... 80

Figure 3-11. Confocal images of CXCR4-expressing cells (green) incubated with either AMD3100-immobilized (a) or unmodified control (b) carriers (blue) and their overlays. Scale bars are 20 µm..... 80

Figure 3-12. Measurement of β-arrestin levels after incubation with CXCL12 and various carriers. Control represents cells that were not incubated with CXCL12, AMD3100 or carriers. The ‘-’ sample represents cells incubated only with CXCL12. AMD particles represents cells incubated with 1 µg/ml AMD-immobilized carriers. Control particles represents cells incubated with 1 µg/ml unmodified carriers. Free AMD represents cells incubated with 1 µM free AMD3100. Study was done by the Luker group..... 81

Figure 3-13. (a) Synthesis of MIBG-PEG-FITC conjugate by Sonagashira coupling, and (b) corresponding 1H NMR of the product. Synthesis and characterization were performed by Dr. Hakan Durmaz and Artak Shahnas..... 84

Figure 3-14. Confocal images of SK-N-BE(2) cells after incubation with 100 µM (a) alkyne-PEG-FITC and (b) MIBG-PEG-FITC. Scale bars are 200 µm. (c) Quantification of the fluorescence intensity from images using ImageJ..... 85

Figure 3-15. Flow cytometry results after incubation of SK-N-BE(2) cells with (a) 100 µM MIBG-PEG-FITC and (c) 50 µM desipramine followed by 100 µM MIBG-PEG-FITC..... 86

Figure 3-16. Flow cytometry results after incubation of BE(2)-C cells with (a) 100 µM MIBG-PEG-FITC and (b) 500 µM desipramine followed by 100 µM MIBG-PEG-FITC..... 86

Figure 4-1. (a) Reaction scheme for selective immobilization of alginate. (b), (c) Confocal images of microcylinders (blue and green) after alginate immobilization and EDC coupling to rhodamine labeled PEG (red). (d) Overlay of (b) & (c). Scale bars are 20 µm..... 97

Figure 4-2. CLSM images of Raw264.7 cells (red & green) after incubation with (a) control, (b) PEG immobilized, and (c) CD47 immobilized carriers (blue). Scale bars are 10 µm..... 98

Figure 4-3. Flow cytometry data for Raw264.7 cells after incubation with (a) control, (b) PEG immobilized, and (c) CD47 immobilized carriers. (d) – (f) Corresponding histogram representations of flow data with gating at two orders of magnitude above baseline..... 99

Figure 5-1. (a) Design of multifunctional GC based carrier, showing key functional materials used in each compartment. (b) SEM and (c) TEM image of the EHD co-jetted GC based carriers. (d) IVIS image, with NIR fluorescence overlaid, of a blank eppendorf (left) and an eppendorf containing the GC based carriers. Scale bars are (b) 1 μm and (c) 200 nm..... 106

Figure 5-2. IVIS imaging, with NIR fluorescence overlaid, of mouse injected directly into the tumors with GC based carriers. (a) 1 hour and (b) 24 hours after injection. (c) Image of excised tumors, showing localization of carriers..... 107

Figure 5-3. IVIS imaging, with GFP fluorescence overlay, of mouse (Figure 5-2) implanted with bilateral GFP expressing MDA-MB-231 tumors. The centers of the tumors are necrotic..... 108

Figure 5-4. IVIS imaging, with NIR fluorescence overlaid, of mouse injected with GC based carriers through tail vein. (a) 1 hour and (b) 24 hours after injection. Image of excised (c) liver and (d) lungs, showing localization of carriers..... 109

Figure 5-5. GFP fluorescence intensities of cells measured by plate reader 48 hours after one hour incubation with AMD3100-immobilized and untargeted (no AMD3100) carriers..... 110

Figure 6-1. SEM images showing the bimodal distribution of various carriers fabricated EHD co-jetting with different parameters. (a) PLGA particles from a pure DMF solution. (b) PLGA particles from a 1:1 v/v THF:DMF. (c) Particles made from the same solution as (b), but at a five times higher flow rate. (d) PLGA particles from a low concentration solution. (e) Low molecular weight polystyrene particles. (f) High molecular weight polystyrene particles. Scale bars are (a, b, c, e) 10 μm and (d, f) 2 μm 115

Figure 6-2. DLS of PEI based nanocarriers described in Chapter 2, (a) before centrifugation, and (b) the supernatant after centrifugation..... 116

Figure 6-3. PLGA particles jetted from (a) pure DMF, (b) 1:1 v/v EtOH:DMF, (c) 1:1 v/v acetone:DMF, and (d) 1:1:2 v/v/v acetone:EtOH:DMF. Scale bars are 2 μm 117

Figure 6-4. (a) Photo of EHD co-jetting into a water bath. (b) SEM image of PLGA particles made using the setup in (a). (c) Photo of EHD co-jetting into a liquid nitrogen bath. (d) SEM of PLGA structures made using the setup in (d). All scale bars are 10 μm 118

Figure 6-5. 3D reconstruction of a confocal zstack showing virus-mimicking particles (blue and red) bound to the membranes of breast cancer cells (green). Scale bar is 10 μm 120

Figure 6-6. (a) Diagram showing how plasmonic nanoparticles may be incorporated into VMPs to investigate cell membranes using SERS. (b) Confocal brightfield image of VMPs bound to the surface of a cell. (c) Color map generated from the integration of C-H Raman peak. (d) Representative Raman spectra from a point on the cell, and from a point with both cellular material and a VMP. Scale bars are 10 μm 121

Figure 6-7. (a) Schematic showing how LbL based capsules were fabricated from EHD co-jetted microcylinders. SEM images of (b) microcylinders, (c) microcylinders after LbL, and (d) remaining microstructures after PLGA dissolution. Scale bars are 100 μm (top images) and 10 μm (bottom images)..... 123

Figure A-1. (a) PEI added to Au NRs in water. (b) Au NR PEI complexes dispersed in CHCl_3 . (c) Au NR PLA-PEG-PLA complexes dispersed in CHCl_3 . TEM images of CHCl_3 dispersions of (d) Au NR PEI complexes and (e) Au NR PLA-PEG-PLA Complexes dried on TEM grids..... 128

Figure A-2. UV-Vis spectra of Au NRs in H_2O and Au NR PEI complexes in H_2O and CHCl_3 . 129

Figure A-3. UV-Vis spectra of CHCl_3 dispersions of Au NR PEI complexes prepared by varying weight-by-weight ratios of Au NRs to PEI. Control represents UV-Vis spectra of pure Au NRs in H_2O 130

Figure B-1. Raman confocal color maps generated by peak integration from a scan of EHD co-jetted PLGA/PLGA-PS bicompartamental carriers on a silicon substrate. Color map of integration of (a) carboxyl peak ($1720\text{-}1815\text{ cm}^{-1}$) for PLGA, (b) $1575\text{-}1615\text{ cm}^{-1}$ for PS, and (c) overlay..... 133

Figure B-2. Flow diagram showing how to estimate pure spectra from a color map obtained by peak integration (top), and the resulting color map (bottom) from basis analysis..... 135

List of Appendices

Appendix A. Dispersion of Gold Nanorods in Organic Solvents	126
A-1. Background and Motivation	126
A-2. Methods	127
A-3. Results and Discussion	127
A-4. Summary	130
A-5. References	132
Appendix B. Data Analysis for Raman Confocal Microscopy	133
B-1. Background and Motivation	133
B-2. Methods	133
B-3. References	136

Abstract

Targeted particulate carrier based therapies have the potential to vastly improve current treatment modalities in medicine by concentrating a therapeutic at its desired target, and lowering its distribution in other locations, effectively increasing its therapeutic index. However, particulate carriers have yet to realize this potential, in part due to barriers resulting from their interactions with physiological processes. In this dissertation, multicompartamental carriers comprised of multiple materials, allowing for multiple functionalities within a single carrier, are manufactured by electrohydrodynamic (EHD) co-jetting. A number of carriers systems fabricated by EHD co-jetting are developed, and their potential therapeutic applications are demonstrated. In particular, endosome-sensing carriers are developed for cytosolic delivery, using existing commercially available pH-sensitive polymers, polyethyleneimine (PEI) and glycol chitosan (GC), as well as novel polymers, based on dextran and ascorbic acid. Gene silencing is achieved by delivery of siRNA to GFP expressing MDA-MB-231 cells using both PEI and GC based carriers. Additionally, we show that the PEI based carriers can be surface immobilized with AMD3100 by incorporation of a functionalized polylactide. Such carriers demonstrate binding affinity to triple negative breast cancers *in vitro*, and we demonstrate increased silencing efficacy from AMD3100 immobilized, siRNA-loaded carriers. In addition to carriers with targeting to specific cancers, virus-mimicking particles are fabricated that can selectively bind to cell membranes. It is also shown how EHD co-jetted carriers may be selectively surface modified with poly(ethylene glycol) (PEG) and CD47 to avoid uptake by Raw264.7 cells. Finally, GC based carriers capable of both siRNA delivery and live imaging are developed and their behaviors *in vivo* are explored.

Chapter 1

Introduction

Part of the material in this chapter has been adapted with modifications from the following articles:

- (1) A. C. Misra, S. Bhaskar, N. Clay, J. Lahann. "Multicompartmental Particles for Combined Imaging and siRNA Delivery." *Advanced Materials* 2012, 24, 3850-3856.
- (2) A. C. Misra, T.-H. Park, R. P. Carney, F. Stellacci, J. Lahann. "Virus-Mimicking Particles with Compositionally Anisotropic Surfaces." *In Preparation*.

1.1 Current Therapeutic Modalities in Medicine

Starting perhaps with the widespread use of antibiotics in the 1940s, scientific progress in medicine has revolutionized the standard of care. With a greater understanding of human physiology and disease pathology, an immense number of therapies have been introduced in the last 70 years, many of them based on molecular therapeutics. Several infections, cancers, and chronic diseases once considered incurable and inevitably fatal are now treatable with chemotherapeutics. For instance, vaccines have led to almost complete eradication of polio.¹ HIV is no longer a necessarily fatal disease but rather a manageable condition thanks to highly active antiretroviral therapy.^{2,3} Specific cancers have become virtually curable, such as Philadelphia chromosome-positive chronic myelogenous leukemia with the use of imatinib.^{4,5}

The biotech sector is now roughly a \$100 billion industry, with a major component being the development of pharmaceuticals.⁶ However, as major biological pathways are exhausted and certain diseases become increasingly resistant to molecular drugs, new and effective discoveries are becoming rare.^{7,8} Rather, the challenging diseases of this era may be instead addressed using combinations of chemotherapeutics and biologics.

Many of these diseases remain extremely difficult to treat despite advancements in combination therapy. Current therapies may have efficacy, but the doses administered are often limited by side effects, commonly the result of therapeutics interacting with sites other than the diseased tissue or organ affected. For example, current combination therapies for multiple myeloma show some promise, with marginally increased median survival times, but the disease remains essentially fatal.^{9,10}

The ability to home in to the particular tissue of interest, resulting in a drug biodistribution such that the target has several orders of magnitude more drug than the rest of the body, could, therefore, have significant impact in the treatment of such diseases.¹¹ Effectively, targeting allows for a drug to be more potent and less toxic systemically, allowing clinically for higher tolerable doses. Such targeting capabilities could be especially impactful in the treatment of aggressive or resistant cancers.

1.2 Carrier-based Targeted Therapies

Micro- and nano- scale carriers loaded with therapeutics targeting sites of interest have great potential to address the challenges in the treatment of refractory diseases, especially cancers with currently poor prognoses.¹¹⁻¹³ In attempting to address large-scale, reproducible fabrication of carriers with superior efficacy or potency, many different carriers have been manufactured from a variety of materials. Inorganic carriers, including gold, silver, and silica particles, have been developed with great control over size and morphology. Organic carriers, such as micelles, dendrimers, liposomes, and polymeric particles, though generally more polydisperse, can be biodegradable and have high drug loading capacity.

1.2.1 Manufacturing Processes

A wealth of synthetic strategies has been developed to produce carriers of various compositions, morphologies, and sizes. They can be broadly classified as either bottom-up or top-down strategies. Bottom-up strategies use molecular feeds to synthesize particles and are often chemical methods, while top-down strategies form particles from the processing of macromolecules.

Inorganic particles are generally fabricated via bottom-up approaches. Metallic precursors are mixed with reactive species such as reducing agents, resulting in metal precipitates, which serve as nucleation sites for further growth; a stabilizing agent, such as a surfactant, is also typically included to prevent aggregation of particles.¹⁴⁻¹⁶ For example, gold nanoparticles may be synthesized by the reaction of auric (III) chloride with citric acid, serving as both a reducing species and stabilizer.¹⁷

Silica and metal oxide particles can be synthesized via sol-gel methods, sometimes referred to as the Stöber process specifically for silica particles, in which tetraethyl orthosilicate (TEOS) is hydrolyzed to silanol, which subsequently forms silica by condensation reactions.^{14,18,19} Another major inorganic particle manufacturing process is the solvothermal method, which can be used to synthesize metal oxide nanoparticles, including magnetite. Here, metallic precursors are charged into a reaction vessel with a solvent, degassed and subsequently heated for a period of time.^{14,20}

Organic particles can be fabricated by both bottom-up and top-down processes. Emulsion polymerization is a common bottom-up method in which monomers dissolved in a solvent are emulsified in another immiscible solvent, and polymerization can occur within the confined droplets of the emulsion.²¹ It is used to produce particles composed of a variety of polymers, including polystyrene,²¹⁻²³ acrylates,²⁴ and hydrogels.²⁵ Dendrimers are also synthesized in a bottom-up manner via sequential chemical reactions.²⁶

A wide variety of top-down strategies exist for the production of polymeric particles. Micellar and liposomal structures are often formed via self-assembly using the amphiphilic character of the macromolecules involved.²⁷⁻³¹ Oil-in-water and nanoprecipitation techniques comprise another major class of top-down strategies for polymeric carrier manufacturing, involving dissolution of polymer into an organic phase, and the formation of particles by emulsifying or precipitation in surfactant-containing water.³²⁻³⁸

There are many extrusion-based techniques, involving the extrusion of polymer solution through microfluidic orifices. These methods may be pure mechanical processes, such as spray drying.³⁹⁻⁴² To produce unique architectures or have tighter control over size and shape, some other extrusion-based strategies may employ the use of additional fluid

phases⁴³⁻⁴⁵ or introduce an additional stimulus, such as temperature⁴⁶ or, in the case of electrospraying, voltage.⁴⁷⁻⁵⁰

Lithographic-based techniques comprise a unique set of processes that are able to produce highly monodisperse two-dimensional particles by employing microfabrication technologies. DeSimeone and coworkers have made reproducible, uniform masks through photolithography that are used to mold polymeric micro- and nano- particles, in a process they developed known as Particle Replication in Non-wetting Templates (PRINT).⁵¹ Doyle and coworkers also developed a set of techniques using photolithography, called (continuous and stop) flow lithography, combining flow lithography with a confocal microscope and ultraviolet (UV) laser; their methods allow for the UV crosslinking of polymer solutions in a spatially controlled manner, producing crosslinked polymeric particles.⁵²

1.2.2 Inorganic Carriers

Inorganic particles were some of the first carriers used in medical therapies; in fact, colloidal gold was used centuries ago to attempt to treat a variety of diseases, from dysentery to cancer.¹⁷ Gold nanoparticles have been used in a number of drug delivery applications by conjugating small molecule drugs to their surfaces.⁵³⁻⁵⁵ Mesoporous silica-based carriers have been shown to have especially high drug-loading efficiencies due to their high surface area, allowing for large amount of drug to be incorporated via physical adsorption.⁵⁶⁻⁶⁰ In some cases, the pores are closed off with stimuli-responsive molecules or particles, allowing for triggered release of the encapsulated drug.^{56,61}

1.2.3 Macromolecular Carriers

Macromolecule based carriers are one of the most diverse classes of carrier systems given the broad range of materials to choose from. Lipid-based carriers are one of the oldest classes of drug delivery vehicles, and, given their composition, have fairly good biocompatibility.⁶²⁻⁶⁴ Lipofectamine, one of the most successful commercial liposomal formulations, is now a common method for *in vitro* gene transfection.⁶⁵⁻⁶⁷ Several liposomal formulations have been approved for clinical use, although they generally are not targeted therapies, employing passive targeting strategies such as using the enhance permeation and

retention effect.^{63,64} Nonetheless, there has been much research into immobilizing ligands on the surface of liposomes for targeting.⁶⁴

Several carriers based on biodegradable polymers, such as poly(lactide-co-glycolic acid) (PLGA), have been developed. Polyesters like PLGA can be hydrolyzed under physiologic conditions, resulting in byproducts that can be metabolized.^{68,69} Many different drugs have been successfully loaded and delivered via biodegradable polymer-based carriers, which are now in preclinical or clinical trials.^{12,70} Some carriers, such as Abraxane, an albumin-based nanoparticle loaded with paclitaxel, are even approved for clinical use.^{12,68,70}

A wide range of stimuli-responsive and functional polymers can be used to provide additional functionalities.⁷¹ Cationic, pH-responsive polymers, including polyethyleneimine (PEI) and chitosan, are commonly used for transfection.⁷²⁻⁷⁴ Temperature-sensitive polymers, such as poly(N-isopropylacrylamide) (PNIPAAm), allow for controlled delivery based on changes in local temperatures.⁷¹ Polymers can also be designed to respond to different physiologic signals; for example, glucose-responsive polymeric materials have been developed, releasing insulin in response to increased glucose levels.^{75,76}

1.2.4 Carriers with Additional Functionalities

Carriers have been used for medical therapies via functionalities other than delivery of drugs. Employing the physical properties of certain carriers has resulted in novel therapies that may have significant potential clinically. Gold nanorods and superparamagnetic particles have served both as sensitizers to photothermal and magnetothermal ablation, respectively, as well as imaging contrast agents.⁷⁷⁻⁸² Gold nanorods exhibit surface plasmon resonance when irradiated with near-infrared light, resulting in the generation of thermal energy; this thermal energy results in local changes in temperature large enough to thermally ablate cells.⁷⁷⁻⁷⁹ In particular, Bhatia and coworkers have studied photodynamic therapy with gold nanorods, demonstrating efficacy *in vivo*.^{79,83,84} Iron oxide particles are also able to cause thermal ablation by generating heat in response to an alternating magnetic field.^{80,81} Additionally, studies have shown that quantum dots may be used for photodynamic therapy as well; instead of photothermal ablation, quantum dots activated by light generate reactive singlet oxygen species, known to be exceptionally cytotoxic.⁸⁵

1.3 Barriers to Effective Carrier-based Therapy

Despite advances in the fabrication and engineering of intricate particulate carriers, they have not realized their full potential in a clinical setting. Many of the barriers to effective targeted therapy may be attributed to complex interactions between carriers and various physiological, and pathophysiological, processes. Such barriers, as depicted in Figure 1-1, can be roughly classified into the following categories (which are neither exhaustive nor mutually exclusive): administration, circulation, targeting, therapeutic effects, and clearance.

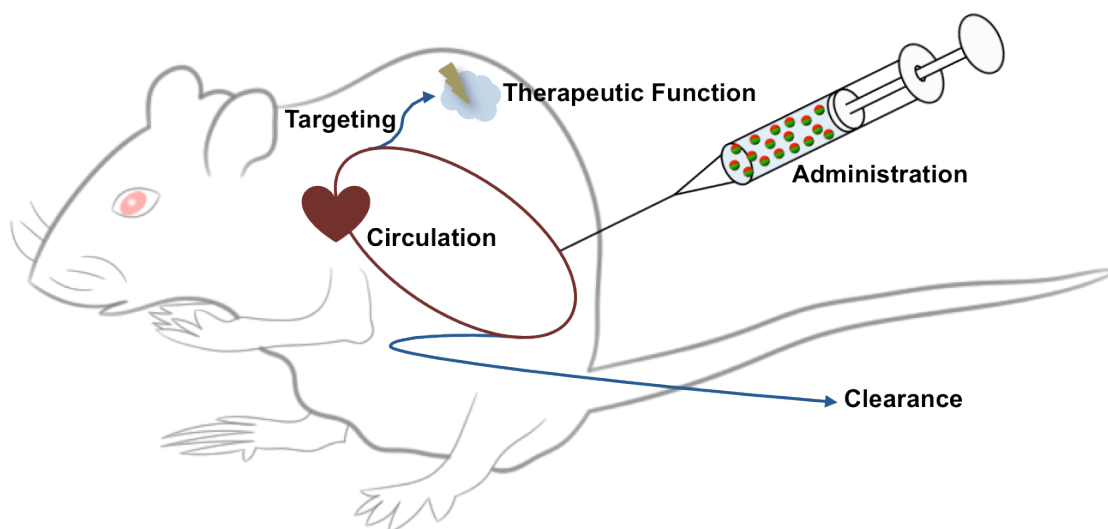


Figure 1-1. Representation of the physiological barriers in carrier-based targeted therapies.

Challenges with the administration of a carrier are generally similar to those for most other therapies. The typical mode of administration is parenteral, typically intravenous, as this allows for higher bioavailability.⁸⁶ Enteral routes afford very low bioavailabilities for particulate carriers – in the case of oral administration, only one study to date has demonstrated substantial amounts of nanoparticles reaching systemic circulation through the gastrointestinal tract.^{86,87} Therefore, intravenous injection is currently the route of choice for most applications.

Particulate carriers have unique barriers to long half-lives due primarily to the immune system's effectiveness in removing them from circulation.^{11,13} With respect to size range (nanometers to micrometers), particles are similar to foreign organisms such as viruses or bacteria. The innate immune system, in particular the reticuloendothelial system, is adept at

nonspecifically phagocytosing foreign particulate material.^{11,13} Typically, surface modification of carriers with a hydrophilic polymer like poly(ethylene glycol) (PEG) somewhat prolongs circulation by reducing protein adsorption.^{12,13,70} However, many other carrier properties can affect clearance by the immune system; certain sizes, shapes, mechanical properties, and immobilization of cell surface markers have all been shown to help prolong circulation times.⁸⁸⁻⁹⁰

While some advances have been made, effective targeting to a desired tissue remains somewhat elusive. Current biodistribution studies have shown, at best, one to two orders of magnitude higher concentrations of drug at the desired site compared to untargeted carriers or free drug; however, this improvement generally amounts to around only 1-2% of the total drug administered reaching the desired target.^{91,92} Hence, there is substantial room for improving localization of carriers to the target site.

In an *in vitro* setting, a relatively high concentration of particles may be used to achieve a therapeutic effect, merely due to the increased probability of particles interacting with cells and reaching the desired site. However, in an *in vivo* or clinical setting, only a small amount of particles may be exposed to the cells of interest at any given time. Some functionalities may not require entry into a cell; for instance, in the case of thermal ablation, proximity to target cells may suffice. In other instances, entry into the cell is critical, as in the case of delivery of certain therapeutics and all nucleic acids and peptide and/or proteins.¹³ Entry into the cell is typically via endocytosis, confining carriers to the harsh environment of an endosome or lysosome – it is necessary to escape this environment and reach the cytosol to deliver a functional payload.^{13,93}

Clearance is an issue that is arguably overlooked in particulate carrier design, but is nonetheless important. The immune system again plays an important role as it can effectively clear particulate material from circulation.^{11-13,93} However, depending on the biodegradability of the material, such particles may persist in various tissues and organs for potentially long durations.¹² Choice of material, such as fast hydrolyzing polyesters, can be employed to limit the footprint particulate carriers leave *in vivo*, but they do not necessarily have the optimal properties for every therapeutic intervention.

While certain carriers may be effective in addressing one barrier, none have addressed all barriers. Inorganic nanoparticles are arguably the most well defined carrier systems, usually having exceptional monodispersity with respect to size and shape.¹² They therefore can have some of the most reproducible *in vivo* results, and the ability to produce extremely small nanoparticles (less than around 5-6 nm) allows for renal clearance.⁹⁴ They also allow for unique functional abilities other than drug delivery, such as enhanced imaging and alternative therapeutic interventions, such as sensitization to photothermal ablation or other forms of photodynamic therapy.^{78,79,81,85} However, larger inorganic particles, which are not clearable renally, are not biodegradable, and can therefore accumulate in various tissues.¹² Although some studies show that there may be little acute toxicity, the long-term effects of inorganic nanoparticles are unknown.^{12,95,96} Liposomes have excellent biocompatibility, but can be rather ineffective and may have issues with circulation and targeting, as well as issues with lack of stability.^{12,64} Polymeric particles have the potential for highly selective targeting, but have short circulation times and, depending on the polymer, can be highly biocompatible or quite cytotoxic.^{12,69,97} On the other hand, the diverse range of polymers available affords polymeric particles a high degree of functionality.⁷¹

1.4 Fabrication of Multicompartmental Carriers

Incorporating multiple materials with different functionalities into a multicompartmental carrier may better address the barriers to effective targeted therapy. Multicompartmental carriers may be considered a class of anisotropic particles, the fabrication and study of which have become of great interest for numerous applications as well as a fundamental science. A number of methods have been developed for producing such anisotropic particles that may be applicable to targeted therapy. For instance, the Weitz group employs their microfluidic extrusion technique with multiple immiscible phases to fabricate multicompartmental polymersomes and emulsions, by forming multiple polymersomes (droplets) within a larger polymersome (droplet).⁹⁸⁻¹⁰⁰ They have been able to show compartmentalized encapsulation of multiple small molecules, and have the ability to control the number of compartments within a given droplet.^{99,100} Using these carriers, they have shown sequential release of small molecules, demonstrating control over multiple release kinetics profiles.¹⁰⁰ However, the material choices are somewhat constrained, as the

polymers used are generally amphiphilic, and the particles are quite large, ranging from around 50 to 500 μm , which may not be suitable for many therapeutic applications.

The Doyle group has also been able to synthesize multicompartmental particles via their continuous and stop flow lithography methods – by using multiple parallel, laminar flows (containing photocrosslinkable polymers), they are able to generate multicompartmental particles by UV crosslinking in a spatially controlled manner, using masks, as the flows pass through the confocal microscopy setup.^{101,102} The particles tend to be two-dimensional, although this group has been developing some novel methods to fabricate truly three-dimensional particles.^{103,104} While this set of techniques can potentially allow for rapid fabrication of particles, the material choices are constrained to photocrosslinkable polymers, and the produced carriers are fairly large (at least 10 μm). Hence, multicompartmental carriers fabricated via flow lithography may not be well suited for therapeutic applications either.

The DeSimone group has begun to fabricate multicompartmental particles via the PRINT process – by sequential partial filling and curing in the mold, several materials can be molded into a single carrier.¹⁰⁵ While this method produces extremely monodisperse multicompartmental carriers, the process is limited to curable polymers. Additionally, the process is arguably time-intensive with potentially multiple filling and curing steps – the fabrication time would scale with the number of compartments desired.

Electrohydrodynamic (EHD) co-jetting is another process, developed by our group, that allows for relatively fast fabrication of particulate carriers with spatially and temporally controllable composition and function, and versatile control over size, shape, and anisotropy.^{50,106-132} EHD co-jetting may serve as a viable method for rapid production of multicompartmental particles. With the appropriate size, shape, and diversity of composition, EHD co-jetted particles have the potential to address the barriers in particulate carrier-based therapy.

1.5 Electrohydrodynamic Co-Jetting

Based on the more commonly known technique of electrospraying (or electrospinning, depending on whether particles or fibers are produced), EHD co-jetting involves two or

more solutions, generally polymeric, that are extruded through a nozzle under a laminar flow regime, as shown in Figure 1-2. Upon application of a DC voltage, the droplet at the end of the needle becomes distorted and forms a Taylor cone,¹³³ from which a high-speed jet is emitted; in accordance with Rayleigh instability,¹³⁴ the jet breaks into droplets or forms a continuous fiber. Because of high surface area to volume ratios, the solvent evaporates virtually instantaneously, leading to ultrafast precipitation and solid particulate or fibrous matter. Due to the laminar flow of the jetting solutions, the interface between solutions is conserved throughout the process leading to multicompartmental particles or fibers. Therefore, the architecture and composition designed by the selection of materials and geometry of the jetting orifice, through which the solutions are extruded, is maintained in the resulting solid particles or fibers.

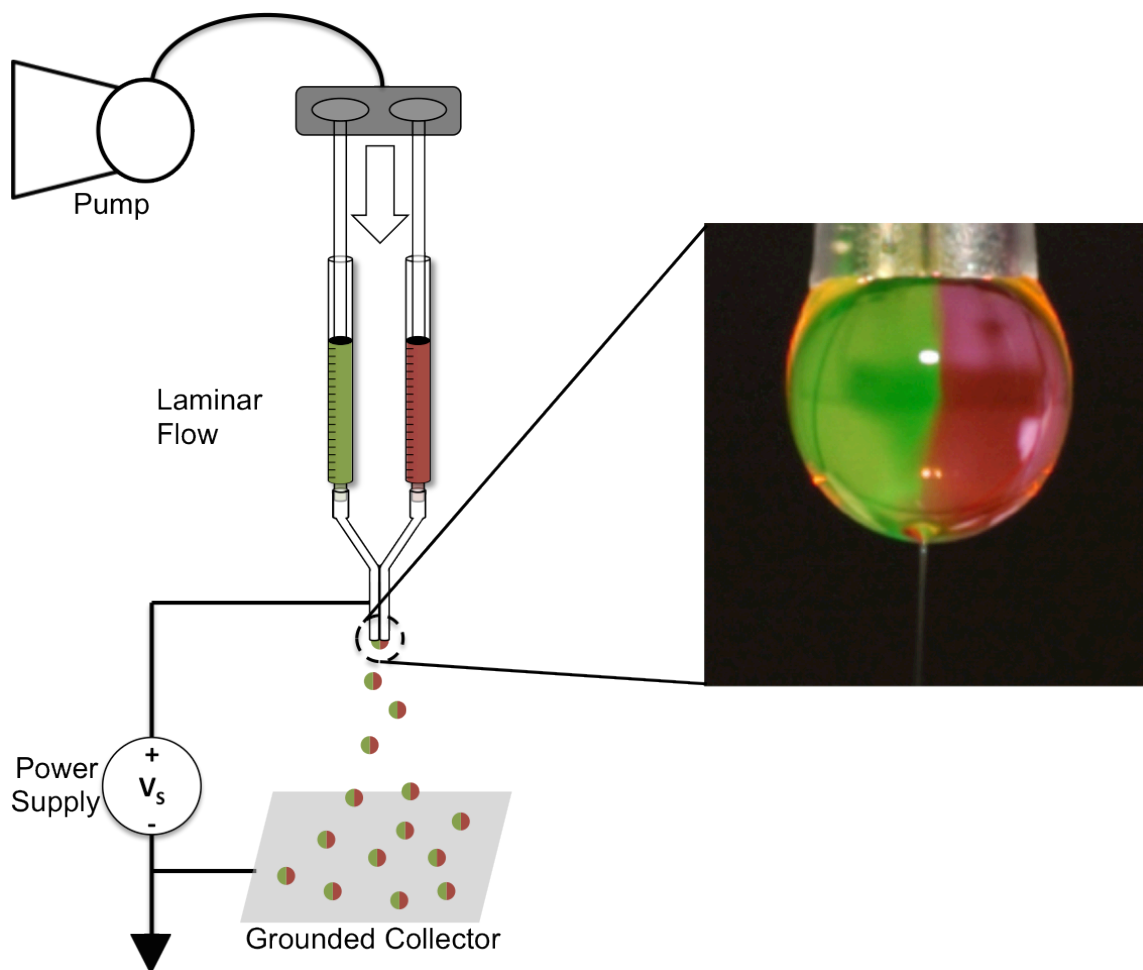


Figure 1-2. Schematic of a typical EHD co-jetting setup. Photo shows a jet emitted from a Taylor cone during EHD co-jetting, adapted from ref.⁵⁰

Variation of solution parameters, such as solvent, concentration, polymer choice, molecular weight, and process parameters, including flow rate, needle configuration, and voltage, as well as post-processing (chemical or physical modifications), allows for a wide and diverse range of particulate carriers with respect to size, shape, composition, and anisotropy, a subset of which is seen in Figure 1-3.^{106,109,112,115,116,120-122,124,125,129-132} Additionally, the use of additives in the respective jetting solutions, such as polymers, dyes, small molecule drugs, or even nanocrystals, leads to selective loading of certain compartments within a particle.^{106-108,112,117-125,127-132} For instance, by incorporating inorganic nanoparticles into jetting solutions, the jetted carriers may exhibit properties and functions of both inorganic and organic carriers.^{117,118,123} Moreover, incorporation of chemically functional polymers into jetting solutions allows for selective surface modification of the jetted particles.^{110,114,119,121,128,131,132} Hence, via choice of additive materials, we can incorporate different functionalities of other carrier systems into a single EHD co-jetted carrier system.^{109,118,122,124,125,129}

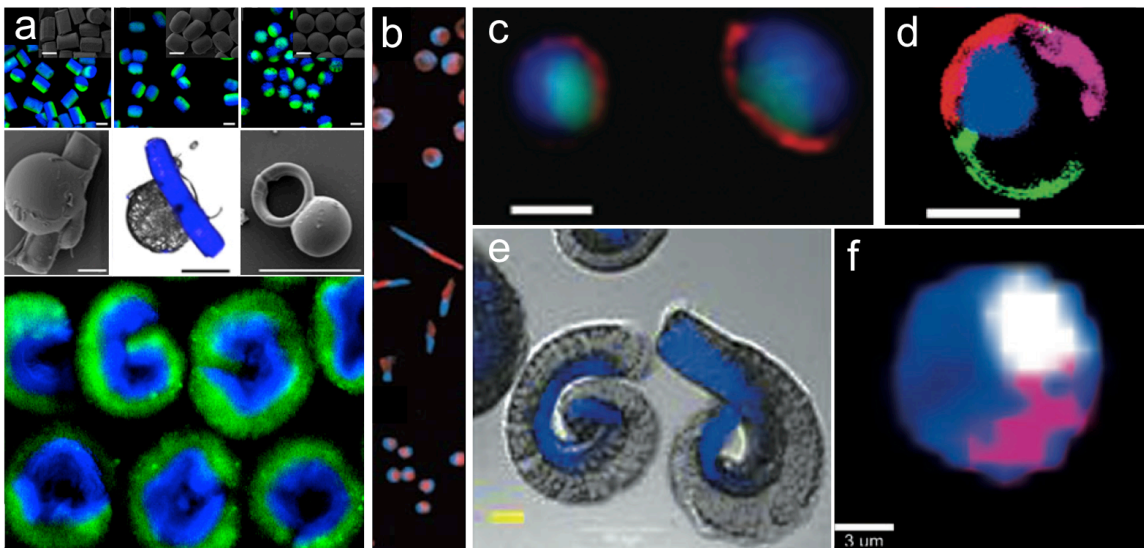


Figure 1-3. Some of the particulate carriers fabricated using EHD co-jetting. (a) Confocal and scanning electron microscopy (SEM) images of particles with compartmentalized materials of differing glass temperatures, subjected to a shape-shifting process. (b) Confocals of disks, rods, and spheres made by varying process parameters. (c), (d) Confocal images demonstrating selective surface modification. (e) Confocal image of microcylinders that have a hydrogel brush selectively grown on one side. (f) Raman confocal image of a particulate carrier with three different compartmentalized polymers. Images adapted from refs.^{121,124,128,131,135}

1.6 Aims of this Study

This dissertation attempts to show how EHD co-jetting may be used to produce carriers capable of addressing at least some of the physiological barriers to targeted therapy. Specifically, the following aims outline the work presented.

Aim 1 – To develop carriers with therapeutic functionalities. Here we focus on cytosolic delivery by carriers with endosome sensing and escaping functionalities. RNA interference by delivery of siRNA is demonstrated, highlighting the effectiveness of these carriers. Additionally, we incorporate a number of different inorganic nanomaterials into particles for alternative functionalities.

Aim 2 – To develop carriers with targeting capabilities. Given the ability to fabricate particles with anisotropic surfaces, an unconventional targeting modality is developed, resulting in particles capable of binding with high affinity to cellular membranes. We also show more conventional targeting can be achieved with particles fabricated by EHD co-jetting.

Aim 3 – To develop carriers with long circulation half-lives. Bulk and surface properties are important for prolonging the circulation of carriers. Here we demonstrate versatile surface modification of EHD co-jetted carriers to achieve reduced nonspecific uptake by phagocytic cells.

Aim 4 – Towards multifunctional carriers. Given the independent validation of several particle systems as described above, here we demonstrate the integration of multiple functionalities into a single carrier, with both therapeutic effects and targeting capabilities, showing the ability of EHD co-jetted carriers to address multiple physiological barriers.

1.7 References

- 1 Modlin, J. F. Focus on Research: The Bumpy Road to Polio Eradication. *New Engl J Med* **362**, 2346-2349, doi:Doi 10.1056/Nejmp1005405 (2010).
- 2 Porter, K. *et al.* Determinants of survival following HIV-1 seroconversion after the introduction of HAART. *Lancet* **362**, 1267-1274 (2003).
- 3 Kitahata, M. M. *et al.* Effect of Early versus Deferred Antiretroviral Therapy for HIV on Survival. *New Engl J Med* **360**, 1815-1826, doi:Doi 10.1056/Nejmoa0807252 (2009).
- 4 Kantarjian, H. *et al.* Hematologic and cytogenetic responses to imatinib mesylate in chronic myelogenous leukemia. *New Engl J Med* **346**, 645-652, doi:Doi 10.1056/Nejmoa011573 (2002).
- 5 Talpaz, M. *et al.* Imatinib induces durable hematologic and cytogenetic responses in patients with accelerated phase chronic myeloid leukemia: results of a phase 2 study. *Blood* **99**, 1928-1937, doi:Doi 10.1182/Blood.V99.6.1928 (2002).
- 6 Grimaldi, A. The outlook for biotech exits. *Nat Biotechnol* **32**, 227-228, doi:Doi 10.1038/Nbt.2852 (2014).
- 7 Kola, I. & Landis, J. Can the pharmaceutical industry reduce attrition rates? *Nat Rev Drug Discov* **3**, 711-715, doi:Doi 10.1038/Nrd1470 (2004).
- 8 Kessel, M. The problems with today's pharmaceutical business-an outsider's view. *Nat Biotechnol* **29**, 27-33, doi:Doi 10.1038/Nbt.1748 (2011).
- 9 Kumar, S. K. *et al.* Improved survival in multiple myeloma and the impact of novel therapies. *Blood* **111**, 2516-2520, doi:Doi 10.1182/Blood-2007-10-116129 (2008).
- 10 Richardson, P. G. *et al.* Lenalidomide, bortezomib, and dexamethasone combination therapy in patients with newly diagnosed multiple myeloma. *Blood* **116**, 679-686, doi:Doi 10.1182/Blood-2010-02-268862 (2010).
- 11 Brannon-Peppas, L. & Blanchette, J. O. Nanoparticle and targeted systems for cancer therapy. *Advanced drug delivery reviews* **64**, 206-212, doi:Doi 10.1016/J.Addr.2012.09.033 (2012).
- 12 Peer, D. *et al.* Nanocarriers as an emerging platform for cancer therapy. *Nat Nanotechnol* **2**, 751-760, doi:Doi 10.1038/Nnano.2007.387 (2007).
- 13 Petros, R. A. & DeSimone, J. M. Strategies in the design of nanoparticles for therapeutic applications. *Nat Rev Drug Discov* **9**, 615-627, doi:Doi 10.1038/Nrd2591 (2010).
- 14 Cushing, B. L., Kolesnichenko, V. L. & O'Connor, C. J. Recent advances in the liquid-phase syntheses of inorganic nanoparticles. *Chem Rev* **104**, 3893-3946, doi:Doi 10.1021/Cr030027b (2004).
- 15 Brust, M., Walker, M., Bethell, D., Schiffrin, D. J. & Whyman, R. Synthesis of Thiol-Derivatized Gold Nanoparticles in a 2-Phase Liquid-Liquid System. *J Chem Soc Chem Comm*, 801-802, doi:Doi 10.1039/C39940000801 (1994).
- 16 Jana, N. R., Gearheart, L. & Murphy, C. J. Wet chemical synthesis of high aspect ratio cylindrical gold nanorods. *J Phys Chem B* **105**, 4065-4067, doi:Doi 10.1021/Jp0107964 (2001).
- 17 Daniel, M. C. & Astruc, D. Gold nanoparticles: Assembly, supramolecular chemistry, quantum-size-related properties, and applications toward biology, catalysis, and nanotechnology. *Chem Rev* **104**, 293-346, doi:Doi 10.1021/Cr030698+ (2004).
- 18 Stober, W., Fink, A. & Bohn, E. Controlled Growth of Monodisperse Silica Spheres in Micron Size Range. *J Colloid Interf Sci* **26**, 62-&, doi:Doi 10.1016/0021-9797(68)90272-5 (1968).

- 19 Bogush, G. H., Tracy, M. A. & Zukoski, C. F. Preparation of Monodisperse Silica Particles - Control of Size and Mass Fraction. *J Non-Cryst Solids* **104**, 95-106, doi:Doi 10.1016/0022-3093(88)90187-1 (1988).
- 20 Laurent, S. *et al.* Magnetic iron oxide nanoparticles: Synthesis, stabilization, vectorization, physicochemical characterizations, and biological applications. *Chem Rev* **108**, 2064-2110, doi:Doi 10.1021/Cr068445e (2008).
- 21 Ugelstad, J., Elaasser, M. S. & Vanderhojw. Emulsion Polymerization - Initiation of Polymerization in Monomer Droplets. *J Polym Sci Pol Lett* **11**, 503-513, doi:Doi 10.1002/Pol.1973.130110803 (1973).
- 22 Okubo, M. Control of Particle Morphology in Emulsion Polymerization. *Makromol Chem-M Symp* **35-6**, 307-325, doi:Doi 10.1002/Masy.19900350119 (1990).
- 23 Im, S. H., Jeong, U. Y. & Xia, Y. N. Polymer hollow particles with controllable holes in their surfaces. *Nature materials* **4**, 671-675, doi:Doi 10.1038/Nmat1448 (2005).
- 24 Colver, P. J., Colard, C. A. L. & Bon, S. A. F. Multilayered Nanocomposite Polymer Colloids Using Emulsion Polymerization Stabilized by Solid Particles. *J Am Chem Soc* **130**, 16850-+, doi:Doi 10.1021/Ja807242k (2008).
- 25 Dupin, D., Fujii, S., Armes, S. P., Reeve, P. & Baxter, S. M. Efficient synthesis of sterically stabilized pH-responsive microgels of controllable particle diameter by emulsion polymerization. *Langmuir* **22**, 3381-3387, doi:Doi 10.1021/La0523258h (2006).
- 26 Fischer, M. & Vogtle, F. Dendrimers: From design to application - A progress report. *Angew Chem Int Edit* **38**, 885-905 (1999).
- 27 Yokoyama, M. *et al.* Polymer Micelles as Novel Drug Carrier - Adriamycin-Conjugated Poly(Ethylene Glycol) Poly(Aspartic Acid) Block Copolymer. *J Control Release* **11**, 269-278 (1990).
- 28 Yasugi, K., Nagasaki, Y., Kato, M. & Kataoka, K. Preparation and characterization of polymer micelles from poly(ethylene glycol)-poly(D,L-lactide) block copolymers as potential drug carrier. *J Control Release* **62**, 89-100, doi:Doi 10.1016/S0168-3659(99)00028-0 (1999).
- 29 Nasongkla, N. *et al.* cRGD-functionalized polymer micelles for targeted doxorubicin delivery. *Angew Chem Int Edit* **43**, 6323-6327, doi:Doi 10.1002/Anie.200460800 (2004).
- 30 Antonietti, M. & Forster, S. Vesicles and liposomes: A self-assembly principle beyond lipids. *Advanced Materials* **15**, 1323-1333, doi:Doi 10.1002/Adma.200300010 (2003).
- 31 Szoka, F. & Papahadjopoulos, D. Procedure for Preparation of Liposomes with Large Internal Aqueous Space and High Capture by Reverse-Phase Evaporation. *P Natl Acad Sci USA* **75**, 4194-4198, doi:Doi 10.1073/Pnas.75.9.4194 (1978).
- 32 Gref, R. *et al.* Biodegradable Long-Circulating Polymeric Nanospheres. *Science* **263**, 1600-1603, doi:Doi 10.1126/Science.8128245 (1994).
- 33 Li, Y. P. *et al.* PEGylated PLGA nanoparticles as protein carriers: synthesis, preparation and biodistribution in rats. *J Control Release* **71**, 203-211, doi:Doi 10.1016/S0168-3659(01)00218-8 (2001).
- 34 Perez, C. *et al.* Poly(lactic acid)-poly(ethylene glycol) nanoparticles as new carriers for the delivery of plasmid DNA. *J Control Release* **75**, 211-224, doi:Doi 10.1016/S0168-3659(01)00397-2 (2001).
- 35 Govender, T., Stolnik, S., Garnett, M. C., Illum, L. & Davis, S. S. PLGA nanoparticles prepared by nanoprecipitation: drug loading and release studies of a water soluble drug. *J Control Release* **57**, 171-185, doi:Doi 10.1016/S0168-3659(98)00116-3 (1999).

- 36 Fonseca, C., Simoes, S. & Gaspar, R. Paclitaxel-loaded PLGA nanoparticles: preparation, physicochemical characterization and in vitro anti-tumoral activity. *J Control Release* **83**, 273-286, doi:Pii S0168-3659(02)00212-2
Doi 10.1016/S0168-3659(02)00212-2 (2002).
- 37 Farokhzad, O. C. *et al.* Targeted nanoparticle-aptamer bioconjugates for cancer chemotherapy in vivo. *P Natl Acad Sci USA* **103**, 6315-6320, doi:Doi 10.1073/Pnas.0601755103 (2006).
- 38 Dhar, S., Gu, F. X., Langer, R., Farokhzad, O. C. & Lippard, S. J. Targeted delivery of cisplatin to prostate cancer cells by aptamer functionalized Pt(IV) prodrug-PLGA-PEG nanoparticles. *P Natl Acad Sci USA* **105**, 17356-17361, doi:Doi 10.1073/Pnas.0809154105 (2008).
- 39 Pohlmann, A. R., Weiss, V., Mertins, O., da Silveira, N. P. & Guterres, S. S. Spray-dried indomethacin-loaded polyester nanocapsules and nanospheres: development, stability evaluation and nanostructure models. *Eur J Pharm Sci* **16**, 305-312 (2002).
- 40 Raula, J., Eerikainen, H. & Kauppinen, E. I. Influence of the solvent composition on the aerosol synthesis of pharmaceutical polymer nanoparticles. *Int J Pharm* **284**, 13-21, doi:Doi 10.1016/J.ijpharm.2004.07.003 (2004).
- 41 Li, X. A., Anton, N., Arpagaus, C., Belleteix, F. & Vandanune, T. F. Nanoparticles by spray drying using innovative new technology: The Buchi Nano Spray Dryer B-90. *J Control Release* **147**, 304-310, doi:Doi 10.1016/J.jconrel.2010.07.113 (2010).
- 42 Vehring, R. Pharmaceutical particle engineering via spray drying. *Pharm Res* **25**, 999-1022, doi:Doi 10.1007/S11095-007-9475-1 (2008).
- 43 Shum, H. C., Kim, J. W. & Weitz, D. A. Microfluidic fabrication of monodisperse biocompatible and biodegradable polymersomes with controlled permeability. *J Am Chem Soc* **130**, 9543-9549, doi:Doi 10.1021/Ja802157y (2008).
- 44 Amstad, E., Kim, S. H. & Weitz, D. A. Photo- and Thermoresponsive Polymersomes for Triggered Release. *Angew Chem Int Edit* **51**, 12499-12503, doi:Doi 10.1002/Anie.201206531 (2012).
- 45 Duncanson, W. J. *et al.* Microfluidic synthesis of monodisperse porous microspheres with size-tunable pores. *Soft Matter* **8**, 10636-10640, doi:Doi 10.1039/C2sm25694k (2012).
- 46 Kaufman, J. J. *et al.* Structured spheres generated by an in-fibre fluid instability. *Nature* **487**, 463-467, doi:Doi 10.1038/Nature11215 (2012).
- 47 Yao, J., Lim, L. K., Xie, J. W., Hua, J. S. & Wang, C. H. Characterization of electrospraying process for polymeric particle fabrication. *J Aerosol Sci* **39**, 987-1002, doi:Doi 10.1016/J.jaerosci.2008.07.003 (2008).
- 48 Park, C. H. & Lee, J. Electrosprayed Polymer Particles: Effect of the Solvent Properties. *J Appl Polym Sci* **114**, 430-437, doi:Doi 10.1002/App.30498 (2009).
- 49 Almeria, B., Fahmy, T. M. & Gomez, A. A multiplexed electrospray process for single-step synthesis of stabilized polymer particles for drug delivery. *J Control Release* **154**, 203-210, doi:Doi 10.1016/J.jconrel.2011.05.018 (2011).
- 50 Roh, K. H., Martin, D. C. & Lahann, J. Biphasic Janus particles with nanoscale anisotropy. *Nature materials* **4**, 759-763, doi:Doi 10.1038/Nmat1486 (2005).
- 51 Rolland, J. P. *et al.* Direct fabrication and harvesting of monodisperse, shape-specific nanobiomaterials. *J Am Chem Soc* **127**, 10096-10100, doi:Doi 10.1021/Ja051977c (2005).
- 52 Dendukuri, D., Pregibon, D. C., Collins, J., Hatton, T. A. & Doyle, P. S. Continuous-flow lithography for high-throughput microparticle synthesis. *Nature materials* **5**, 365-369, doi:Doi 10.1038/Nmat1617 (2006).

- 53 Ghosh, P., Han, G., De, M., Kim, C. K. & Rotello, V. M. Gold nanoparticles in delivery applications. *Advanced drug delivery reviews* **60**, 1307-1315, doi:Doi 10.1016/J.Addr.2008.03.016 (2008).
- 54 Paciotti, G. F., Kingston, D. G. I. & Tamarkin, L. Colloidal gold nanoparticles: A novel nanoparticle platform for developing multifunctional tumor-targeted drug delivery vectors. *Drug Develop Res* **67**, 47-54, doi:Doi 10.1002/Ddr.20066 (2006).
- 55 Brown, S. D. *et al.* Gold Nanoparticles for the Improved Anticancer Drug Delivery of the Active Component of Oxaliplatin. *J Am Chem Soc* **132**, 4678-4684, doi:Doi 10.1021/Ja908117a (2010).
- 56 Slowing, I. I., Vivero-Escoto, J. L., Wu, C. W. & Lin, V. S. Y. Mesoporous silica nanoparticles as controlled release drug delivery and gene transfection carriers. *Advanced drug delivery reviews* **60**, 1278-1288, doi:Doi 10.1016/J.Addr.2008.03.012 (2008).
- 57 Liong, M. *et al.* Multifunctional inorganic nanoparticles for imaging, targeting, and drug delivery. *ACS nano* **2**, 889-896, doi:Doi 10.1021/Nn800072t (2008).
- 58 Lu, J., Liong, M., Zink, J. I. & Tamanoi, F. Mesoporous silica nanoparticles as a delivery system for hydrophobic anticancer drugs. *Small* **3**, 1341-1346, doi:Doi 10.1002/Sml.200700005 (2007).
- 59 Chen, J. F., Ding, H. M., Wang, J. X. & Shao, L. Preparation and characterization of porous hollow silica nanoparticles for drug delivery application. *Biomaterials* **25**, 723-727, doi:Doi 10.1016/S0142-9612(03)00566-0 (2004).
- 60 Kim, J. *et al.* Multifunctional Uniform Nanoparticles Composed of a Magnetite Nanocrystal Core and a Mesoporous Silica Shell for Magnetic Resonance and Fluorescence Imaging and for Drug Delivery. *Angew Chem Int Edit* **47**, 8438-8441, doi:Doi 10.1002/Anie.200802469 (2008).
- 61 Zhao, Y. N., Trewyn, B. G., Slowing, I. I. & Lin, V. S. Y. Mesoporous Silica Nanoparticle-Based Double Drug Delivery System for Glucose-Responsive Controlled Release of Insulin and Cyclic AMP. *J Am Chem Soc* **131**, 8398-+, doi:Doi 10.1021/Ja901831u (2009).
- 62 Allen, T. M. Liposomal drug delivery. *Curr Opin Colloid In* **1**, 645-651 (1996).
- 63 Lian, T. & Ho, R. J. Y. Trends and developments in liposome drug delivery systems. *J Pharm Sci-US* **90**, 667-680, doi:Doi 10.1002/jps.1023 (2001).
- 64 Torchilin, V. P. Recent advances with liposomes as pharmaceutical carriers. *Nat Rev Drug Discov* **4**, 145-160, doi:Doi 10.1038/Nrd1632 (2005).
- 65 Kohama, T. *et al.* Molecular cloning and functional characterization of murine sphingosine kinase. *J Biol Chem* **273**, 23722-23728, doi:Doi 10.1074/Jbc.273.37.23722 (1998).
- 66 Dalby, B. *et al.* Advanced transfection with Lipofectamine 2000 reagent: primary neurons, siRNA, and high-throughput applications. *Methods* **33**, 95-103, doi:Doi 10.1016/J.Ymeth.2003.11.023 (2004).
- 67 Zhao, M. *et al.* Lipofectamine RNAiMAX: An efficient siRNA transfection reagent in human embryonic stem cells. *Mol Biotechnol* **40**, 19-26, doi:Doi 10.1007/S12033-008-9043-X (2008).
- 68 Malam, Y., Loizidou, M. & Seifalian, A. M. Liposomes and nanoparticles: nanosized vehicles for drug delivery in cancer. *Trends Pharmacol Sci* **30**, 592-599, doi:Doi 10.1016/J.Tips.2009.08.004 (2009).
- 69 Kumari, A., Yadav, S. K. & Yadav, S. C. Biodegradable polymeric nanoparticles based drug delivery systems. *Colloid Surface B* **75**, 1-18, doi:Doi 10.1016/J.Colsurfb.2009.09.001 (2010).

- 70 Zhang, L. *et al.* Nanoparticles in medicine: Therapeutic applications and developments. *Clin Pharmacol Ther* **83**, 761-769, doi:Doi 10.1038/Sj.Clpt.6100400 (2008).
- 71 Ganta, S., Devalapally, H., Shahiwala, A. & Amiji, M. A review of stimuli-responsive nanocarriers for drug and gene delivery. *J Control Release* **126**, 187-204, doi:Doi 10.1016/J.Jconrel.2007.12.017 (2008).
- 72 Whitehead, K. A., Langer, R. & Anderson, D. G. Knocking down barriers: advances in siRNA delivery. *Nat Rev Drug Discov* **8**, 129-138, doi:Doi 10.1038/Nrd2742 (2009).
- 73 Huang, M., Fong, C. W., Khor, E. & Lim, L. Y. Transfection efficiency of chitosan vectors: Effect of polymer molecular weight and degree of deacetylation. *J Control Release* **106**, 391-406, doi:Doi 10.1016/J.Cornel.2005.05.004 (2005).
- 74 Akinc, A., Thomas, M., Klibanov, A. M. & Langer, R. Exploring polyethylenimine-mediated DNA transfection and the proton sponge hypothesis. *J Gene Med* **7**, 657-663, doi:Doi 10.1002/Jgm.696 (2005).
- 75 Kost, J. & Langer, R. Responsive polymeric delivery systems. *Advanced drug delivery reviews* **64**, 327-341, doi:Doi 10.1016/J.Addr.2012.09.014 (2012).
- 76 Gu, Z. *et al.* Injectable Nano-Network for Glucose-Mediated Insulin Delivery. *ACS nano* **7**, 4194-4201, doi:Doi 10.1021/Nn400630x (2013).
- 77 Huang, X. H., El-Sayed, I. H., Qian, W. & El-Sayed, M. A. Cancer cell imaging and photothermal therapy in the near-infrared region by using gold nanorods. *J Am Chem Soc* **128**, 2115-2120, doi:Doi 10.1021/Ja057254a (2006).
- 78 Kuo, W. S. *et al.* Gold Nanorods in Photodynamic Therapy, as Hyperthermia Agents, and in Near-Infrared Optical Imaging. *Angew Chem Int Edit* **49**, 2711-2715, doi:Doi 10.1002/Anie.200906927 (2010).
- 79 von Maltzahn, G. *et al.* Computationally Guided Photothermal Tumor Therapy Using Long-Circulating Gold Nanorod Antennas. *Cancer Res* **69**, 3892-3900, doi:Doi 10.1158/0008-5472.Can-08-4242 (2009).
- 80 Hergt, R., Dutz, S., Muller, R. & Zeisberger, M. Magnetic particle hyperthermia: nanoparticle magnetism and materials development for cancer therapy. *J Phys-Condens Mat* **18**, S2919-S2934, doi:Doi 10.1088/0953-8984/18/38/S26 (2006).
- 81 Mornet, S., Vasseur, S., Grasset, F. & Duguet, E. Magnetic nanoparticle design for medical diagnosis and therapy. *J Mater Chem* **14**, 2161-2175, doi:Doi 10.1039/B402025a (2004).
- 82 McCarthy, J. R. & Weissleder, R. Multifunctional magnetic nanoparticles for targeted imaging and therapy. *Advanced drug delivery reviews* **60**, 1241-1251, doi:Doi 10.1016/J.Addr.2008.03.014 (2008).
- 83 von Maltzahn, G. *et al.* SERS-Coded Gold Nanorods as a Multifunctional Platform for Densely Multiplexed Near-infrared Imaging and Photothermal Heating. *Advanced Materials* **21**, 3175-+, doi:Doi 10.1002/Adma.200803464 (2009).
- 84 Park, J. H. *et al.* Cooperative Nanoparticles for Tumor Detection and Photothermally Triggered Drug Delivery. *Advanced Materials* **22**, 880-+, doi:Doi 10.1002/Adma.200902895 (2010).
- 85 Juzenas, P. *et al.* Quantum dots and nanoparticles for photodynamic and radiation therapies of cancer. *Advanced drug delivery reviews* **60**, 1600-1614, doi:Doi 10.1016/J.Addr.2008.08.004 (2008).
- 86 Pridgen, E. M. *et al.* Transepithelial Transport of Fc-Targeted Nanoparticles by the Neonatal Fc Receptor for Oral Delivery. *Sci Transl Med* **5**, doi:ARTN 213ra167 DOI 10.1126/scitranslmed.3007049 (2013).
- 87 Goldberg, M. & Gomez-Orellana, I. Challenges for the oral delivery of macromolecules. *Nat Rev Drug Discov* **2**, 289-295, doi:Doi 10.1038/Nrd1067 (2003).

- 88 Geng, Y. *et al.* Shape effects of filaments versus spherical particles in flow and drug delivery. *Nat Nanotechnol* **2**, 249-255, doi:Doi 10.1038/Nnano.2007.70 (2007).
- 89 Merkel, T. J. *et al.* Using mechanobiological mimicry of red blood cells to extend circulation times of hydrogel microparticles. *P Natl Acad Sci USA* **108**, 586-591, doi:Doi 10.1073/Pnas.1010013108 (2011).
- 90 Rodriguez, P. L. *et al.* Minimal "Self" Peptides That Inhibit Phagocytic Clearance and Enhance Delivery of Nanoparticles. *Science* **339**, 971-975, doi:Doi 10.1126/Science.1229568 (2013).
- 91 Alexis, F., Pridgen, E., Molnar, L. K. & Farokhzad, O. C. Factors affecting the clearance and biodistribution of polymeric nanoparticles. *Mol Pharmaceut* **5**, 505-515, doi:Doi 10.1021/Mp800051m (2008).
- 92 Bartlett, D. W., Su, H., Hildebrandt, I. J., Weber, W. A. & Davis, M. E. Impact of tumor-specific targeting on the biodistribution and efficacy of siRNA nanoparticles measured by multimodality in vivo imaging. *P Natl Acad Sci USA* **104**, 15549-15554, doi:Doi 10.1073/Pnas.0707461104 (2007).
- 93 Davis, M. E., Chen, Z. & Shin, D. M. Nanoparticle therapeutics: an emerging treatment modality for cancer. *Nat Rev Drug Discov* **7**, 771-782, doi:Doi 10.1038/Nrd2614 (2008).
- 94 Choi, H. S. *et al.* Renal clearance of quantum dots. *Nat Biotechnol* **25**, 1165-1170, doi:Doi 10.1038/Nbt1340 (2007).
- 95 Fadeel, B. & Garcia-Bennett, A. E. Better safe than sorry: Understanding the toxicological properties of inorganic nanoparticles manufactured for biomedical applications. *Advanced drug delivery reviews* **62**, 362-374, doi:Doi 10.1016/J.Addr.2009.11.008 (2010).
- 96 Xu, Z. P., Zeng, Q. H., Lu, G. Q. & Yu, A. B. Inorganic nanoparticles as carriers for efficient cellular delivery. *Chem Eng Sci* **61**, 1027-1040, doi:Doi 10.1016/J.Ces.2005.06.019 (2006).
- 97 Lv, H. T., Zhang, S. B., Wang, B., Cui, S. H. & Yan, J. Toxicity of cationic lipids and cationic polymers in gene delivery. *J Control Release* **114**, 100-109, doi:Doi 10.1016/J.Jconrel.2006.04.014 (2006).
- 98 Shum, H. C., Zhao, Y. J., Kim, S. H. & Weitz, D. A. Multicompartment Polymersomes from Double Emulsions. *Angew Chem Int Edit* **50**, 1648-1651, doi:Doi 10.1002/Anie.201006023 (2011).
- 99 Wang, W. *et al.* Controllable microfluidic production of multicomponent multiple emulsions. *Lab Chip* **11**, 1587-1592, doi:Doi 10.1039/C1lc20065h (2011).
- 100 Kim, S. H., Shum, H. C., Kim, J. W., Cho, J. C. & Weitz, D. A. Multiple Polymersomes for Programmed Release of Multiple Components. *J Am Chem Soc* **133**, 15165-15171, doi:Doi 10.1021/Ja205687k (2011).
- 101 Pregibon, D. C., Toner, M. & Doyle, P. S. Multifunctional encoded particles for high-throughput biomolecule analysis. *Science* **315**, 1393-1396, doi:Doi 10.1126/Science.1134929 (2007).
- 102 Lee, J. *et al.* Universal process-inert encoding architecture for polymer microparticles. *Nature materials* **13**, 524-529, doi:10.1038/nmat3938 (2014).
- 103 Jang, J. H., Dendukuri, D., Hatton, T. A., Thomas, E. L. & Doyle, P. S. A route to three-dimensional structures in a microfluidic device: Stop-flow interference lithography. *Angew Chem Int Edit* **46**, 9027-9031, doi:Doi 10.1002/Anie.200703525 (2007).
- 104 Bong, K. W., Pregibon, D. C. & Doyle, P. S. Lock release lithography for 3D and composite microparticles. *Lab Chip* **9**, 863-866, doi:Doi 10.1039/B821930c (2009).
- 105 Zhang, H. *et al.* Fabrication of multiphasic and regio-specifically functionalized PRINT (R) particles of controlled size and shape. *New J Phys* **11**, doi:Artn 075018

- Doi 10.1088/1367-2630/11/7/075018 (2009).
- 106 Roh, K. H., Martin, D. C. & Lahann, J. Triphasic nanocolloids. *J Am Chem Soc* **128**, 6796-6797, doi:Doi 10.1021/Ja060836n (2006).
- 107 Roh, K. H., Yoshida, M. & Lahann, J. Water-stable biphasic nanocolloids with potential use as anisotropic imaging probes. *Langmuir* **23**, 5683-5688, doi:Doi 10.1021/La062274r (2007).
- 108 Yoshida, M., Roh, K. H. & Lahann, J. Short-term biocompatibility of biphasic nanocolloids with potential use as anisotropic imaging probes. *Biomaterials* **28**, 2446-2456, doi:Doi 10.1016/J.Biomaterials.2007.01.048 (2007).
- 109 Kazemi, A. & Lahann, J. Environmentally Responsive Core/Shell Particles via Electrohydrodynamic Co-jetting of Fully Miscible Polymer Solutions. *Small* **4**, 1756-1762, doi:Doi 10.1002/Sml.200800565 (2008).
- 110 Bhaskar, S., Roh, K. H., Jiang, X. W., Baker, G. L. & Lahann, J. Spatioselective Modification of Bicompartmental Polymer Particles and Fibers via Huisgen 1,3-Dipolar Cycloaddition. *Macromolecular rapid communications* **29**, 1655-1660, doi:Doi 10.1002/Marc.200800459 (2008).
- 111 Bhaskar, S. & Lahann, J. Microstructured Materials Based on Multicompartmental Fibers. *J Am Chem Soc* **131**, 6650-+, doi:Doi 10.1021/Ja900354b (2009).
- 112 Bhaskar, S., Hitt, J., Chang, S. W. L. & Lahann, J. Multicompartmental Microcylinders. *Angew Chem Int Edit* **48**, 4589-4593, doi:Doi 10.1002/Anie.200806241 (2009).
- 113 Mandal, S., Bhaskar, S. & Lahann, J. Micropatterned Fiber Scaffolds for Spatially Controlled Cell Adhesion. *Macromolecular rapid communications* **30**, 1638-1644, doi:Doi 10.1002/Marc.200900340 (2009).
- 114 Yoshida, M. *et al.* Structurally Controlled Bio-hybrid Materials Based on Unidirectional Association of Anisotropic Microparticles with Human Endothelial Cells. *Advanced Materials* **21**, 4920-+, doi:Doi 10.1002/Adma.200901971 (2009).
- 115 Doshi, N., Zahr, A. S., Bhaskar, S., Lahann, J. & Mitragotri, S. Red blood cell-mimicking synthetic biomaterial particles. *P Natl Acad Sci USA* **106**, 21495-21499, doi:Doi 10.1073/Pnas.0907127106 (2009).
- 116 Bhaskar, S., Pollock, K. M., Yoshida, M. & Lahann, J. Towards Designer Microparticles: Simultaneous Control of Anisotropy, Shape, and Size. *Small* **6**, 404-411, doi:Doi 10.1002/Sml.200901306 (2010).
- 117 Lim, D. W., Hwang, S., Uzun, O., Stellacci, F. & Lahann, J. Compartmentalization of Gold Nanocrystals in Polymer Microparticles using Electrohydrodynamic Co-Jetting. *Macromolecular rapid communications* **31**, 176-182, doi:Doi 10.1002/Marc.200900597 (2010).
- 118 Hwang, S. *et al.* Anisotropic hybrid particles based on electrohydrodynamic co-jetting of nanoparticle suspensions. *Physical Chemistry Chemical Physics* **12**, 11894-11899, doi:Doi 10.1039/C0cp00264j (2010).
- 119 Bhaskar, S. *et al.* Engineering, Characterization and Directional Self-Assembly of Anisotropically Modified Nanocolloids. *Small* **7**, 812-819, doi:Doi 10.1002/Sml.201001695 (2011).
- 120 Lee, K. J. *et al.* Compartmentalized Photoreactions within Compositionally Anisotropic Janus Microstructures. *Macromolecular rapid communications* **32**, 431-437, doi:Doi 10.1002/Marc.201000558 (2011).
- 121 Saha, S. *et al.* Chemically Controlled Bending of Compositionally Anisotropic Microcylinders. *Angew Chem Int Edit* **51**, 660-665, doi:Doi 10.1002/Anie.201105387 (2012).

- 122 Hwang, S. & Lahann, J. Differentially Degradable Janus Particles for Controlled Release Applications. *Macromolecular rapid communications* **33**, 1178-1183, doi:Doi 10.1002/Marc.201200054 (2012).
- 123 Lv, W. P. *et al.* Anisotropic Janus Catalysts for Spatially Controlled Chemical Reactions. *Small* **8**, 3116-3122, doi:Doi 10.1002/Sml.201200192 (2012).
- 124 Lee, K. J. *et al.* Spontaneous shape reconfigurations in multicompartmental microcylinders. *P Natl Acad Sci USA* **109**, 16057-16062, doi:Doi 10.1073/Pnas.1213669109 (2012).
- 125 Park, T. H. *et al.* Photoswitchable Particles for On-Demand Degradation and Triggered Release. *Small* **9**, 3051-3057, doi:Doi 10.1002/Sml.201201921 (2013).
- 126 Lee, K. J., Park, T. H., Hwang, S., Yoon, J. & Lahann, J. Janus-Core and Shell Microfibers. *Langmuir* **29**, 6181-6186, doi:Doi 10.1021/La4009416 (2013).
- 127 Lv, W. P. *et al.* A Facile Route Towards Inorganic Particles with Two Distinct Compartments Based on Electro-Hydrodynamic Co-Jetting. *Part Part Syst Char* **30**, 936-939, doi:Doi 10.1002/Ppsc.201300123 (2013).
- 128 Sokolovskaya, E., Yoon, J., Misra, A. C., Brase, S. & Lahann, J. Controlled Microstructuring of Janus Particles Based on a Multifunctional Poly(ethylene glycol). *Macromolecular rapid communications* **34**, 1554-1559, doi:Doi 10.1002/Marc.201300427 (2013).
- 129 Rahmani, S., Park, T. H., Dishman, A. F. & Lahann, J. Multimodal delivery of irinotecan from microparticles with two distinct compartments. *J Control Release* **172**, 239-245, doi:Doi 10.1016/J.jconrel.2013.08.017 (2013).
- 130 Yoon, J., Kota, A., Bhaskar, S., Tuteja, A. & Lahann, J. Amphiphilic Colloidal Surfactants Based on Electrohydrodynamic Cojetting. *Acs Appl Mater Inter* **5**, 11281-11287, doi:Doi 10.1021/Am403516h (2013).
- 131 Rahmani, S. *et al.* Chemically Orthogonal Three-Patch Microparticles. *Angew Chem Int Edit* **53**, 2332-2338, doi:Doi 10.1002/Anie.201310727 (2014).
- 132 Park, T. H. *et al.* Spatioselective growth of metal-organic framework nanocrystals on compositionally anisotropic polymer particles. *Adv Mater* **26**, 2883-2888, doi:10.1002/adma.201305461 (2014).
- 133 Ganan-Calvo, A. M. Cone-jet analytical extension of Taylor's electrostatic solution and the asymptotic universal scaling laws in electrospraying. *Phys Rev Lett* **79**, 217-220, doi:Doi 10.1103/Physrevlett.79.217 (1997).
- 134 Luedtke, W. D. *et al.* Nanojets, electrospray, and ion field evaporation: Molecular dynamics simulations and laboratory experiments. *J Phys Chem A* **112**, 9628-9649, doi:Doi 10.1021/Jp804585y (2008).
- 135 Yoon, J., Lee, K. J. & Lahann, J. Multifunctional polymer particles with distinct compartments. *J Mater Chem* **21**, 8502-8510, doi:Doi 10.1039/C1jm10673b (2011).

Chapter 2

Carriers with Therapeutic Functionalities

Part of the material in this chapter has been adapted with modifications from the following article:

A. C. Misra, S. Bhaskar, N. Clay, J. Lahann. "Multicompartmental Particles for Combined Imaging and siRNA Delivery." *Advanced Materials* 2012, 24, 3850-3856.

2.1 Cytosolic Delivery with Endosome-sensing Carriers

2.1.1 Background and Motivation

The controlled delivery of genetic material, such as genes, plasmids, or siRNA, holds great promise for the therapy of a number of debilitating diseases.¹⁻³ While the fundamental concept of permanent or temporary genetic manipulation has been widely embraced by the scientific community, severe concerns remain about the safe and efficient transfer of the genetic material into human cells, where it needs to be released in order to interact with the cell nucleus.^{1,2,4} In addition it is desirable, in many cases, to combine gene delivery with a secondary function, such as release of a chemotherapeutic agent or an imaging modality. The main barriers to delivery fall broadly into two categories: first, the cell membrane represents an effective barrier against the influx of foreign genetic material resulting in notoriously low transfection rates. Second, a host of nucleases exist in the human body, which cause rapid breakdown of any unprotected genetic material. A number of approaches have been developed to address these challenges including electroporation,⁵ viral vectors,^{6,7} cationic liposomal formulations,¹ and nanoparticles.^{1,2}

While some of these methods have shown moderate to high levels of transfection rates, they are all associated with certain limitations. Electroporation is efficient, but cumbersome and practically limited to *in vitro* applications.⁵ The use of viruses can have high efficacy due to evolutionary optimization and is applicable *in vitro* as well as *in vivo*, but comes with

substantial safety concerns.^{1,2,4,7} If methods other than electroporation or viral vectors are used, macromolecules or particles are generally required for extracellular protection and transport into the cytosol. However, cellular uptake of polymer vehicles involves defined cellular mechanisms, such as receptor-mediated endocytosis.⁸ Almost always, the genetic material will then be localized in an endosomal compartment, where it can be deactivated due to abundant nuclease levels and the acidic pH environment.^{3,9} Therefore, nanoparticle-based strategies have targeted endosomal escape to overcome liposomal degradation and facilitate release of payload into the cytosol.¹ Positively charged polymers, such as poly(ethylene imine) (PEI),¹ polylysine,^{1,2} or cationic acrylate polymers,^{10,11} can effectively complex oppositely charged DNA or RNA and are thus well suited for gene delivery. In addition, cationic polymers with large numbers of secondary and tertiary amines can act as superabsorbents that expand under the acidic conditions of the endosome and ultimately rupture the endosomal compartment physically or osmotically via the “proton sponge” effect.^{2,12} This delivery approach has been pursued for nucleic acids^{13,14} as well as small molecule drugs.^{15,16}

It would however be desirable to combine multiple functions, such as dual release of genetic material and cytostatic drugs, or release and simultaneous imaging of the particles to monitor intracellular particle fate.¹⁷⁻¹⁹ While the highly charged nature of cationic polymers has been successfully utilized to complex oppositely charged DNA or RNA fragments, incorporation of additional functional moieties with different chemical properties is more difficult generally requiring fairly sophisticated chemical conjugation techniques.²⁰⁻²³ In principle, this could be achieved by using a combination of two different types of nanoparticles: one made of a cationic polymer to enable endosomal escape and intracellular delivery of the genetic material, and a second one to provide an additional imaging functionality. However, if a mixture of two independent particles is used, the fate of the particles is not necessarily coupled, and prevalence of one type of particle over the other is likely, at least for specific body sites. Moreover, instead of the desirable synergistic effects, separate particles may actually compete for cellular uptake due to the finite endocytic uptake capacity of the target cells.²⁴⁻²⁶ The herein proposed approach employs multifaceted polymer nanoparticles that enable DNA loading and inclusion of imaging modalities on the same particle, although in two distinct compartments.

We now propose to use electrohydrodynamic co-jetting²⁷⁻³⁰ to prepare orthogonal particles with two substantially different compartments for combined imaging and release, i.e., (i) a hydrogel-based release compartment (hydrophilic) and (ii) an imaging compartment (hydrophobic). The hydrophobic compartment consists of poly(DL-lactide-co-glycolic acid) [PLGA], which is suitable for loading of fluorescent dyes or nanoparticles, such as iron oxide nanocrystals.^{31,32} This additional functionality can enable monitoring of particle fate during delivery *in vitro* and *in vivo*. PLGA may also be used to load complementary therapeutics, such as doxorubicin.³³⁻³⁵ In contrast, the hydrogel compartment consists of polyethyleneimine (PEI) (as well as a small amount of PLGA), a cationic polymer that is highly water adsorbent.³⁶ At lower pH values, the primary amines of the PEI are protonated and undergo electrostatic repulsion. Macroscopically, this causes the hydrogel to swell.³⁷ Because the endosomes of mammalian cells are generally at lower pH levels than the physiological blood pH level of around 7.4, the PEI hydrogel compartment can be used to “detect” the acidic pH of the endosome, once it enters via endocytosis. It then swells, thereby either mechanically breaking the endosome, or inducing osmotic bursting. Additionally, due to PEI’s cationic nature, it is suitable for complexation of nucleic acids (due to their anionic character). As shown in Figure 2-1, we designed and prepared multicompartmental nanoparticles employing the PLGA compartment as an imaging modality, and the PEI compartment as an endosome sensing and escape compartment that also serves as a siRNA release compartment. The imaging compartment is labeled with a blue fluorescent polymer dye that remains in the compartment throughout the release study. In contrast, the hydrogel compartment contains the siRNA-payload along with a transient red fluorescent dye (Figure 2-1b). The nanoparticles are displayed in Figure 2-1c and feature uniform sizes and shapes.

2.1.2 Methods

Materials. Poly(DL-lactide-co-glycolic acid) [50-75 kg/mol], polyethyleneimine (60 kg/mol), blue fluorescent poly[*(m*-phenylenevinylene)-alt-(2,5-dihexyloxy-*p*-phenylenevinylene)] (PMPDHPV), and all solvents were purchased from Sigma. Dithiobis(succinimidyl propionate) [DSP] and paraformaldehyde were obtained from Thermo Scientific. Red fluorescent polythiophene polymer ADS306PT was purchased from American Dye Source, Inc. Small interfering RNAs against GFP (both tagged with rhodamine and untagged) were purchased from Qiagen. MDA-MB-231/GFP cells were purchased from Cell Biolabs. All cell

culture materials, including Dulbecco's Modified Eagle Medium (DMEM), fetal bovine serum (FBS), non-essential amino acids, and penicillin-streptomycin, were obtained from Gibco. XTT reagents were purchased from Invitrogen.

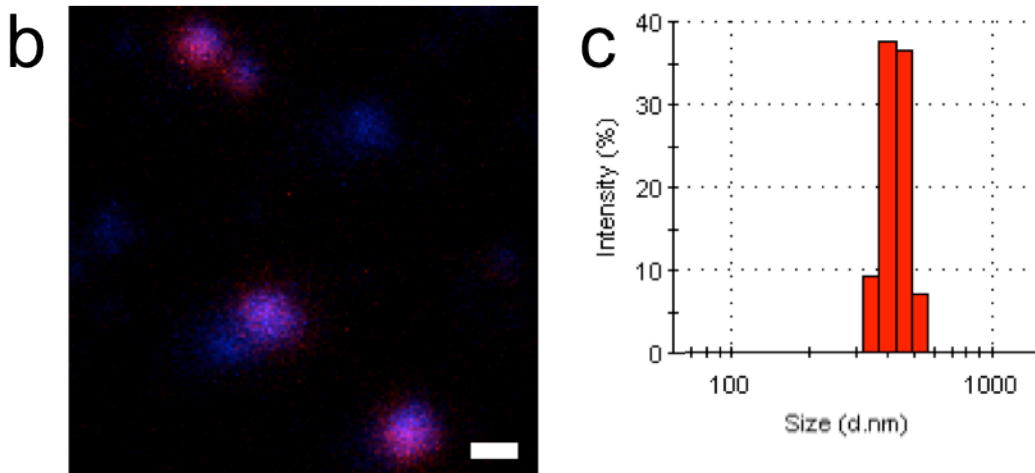
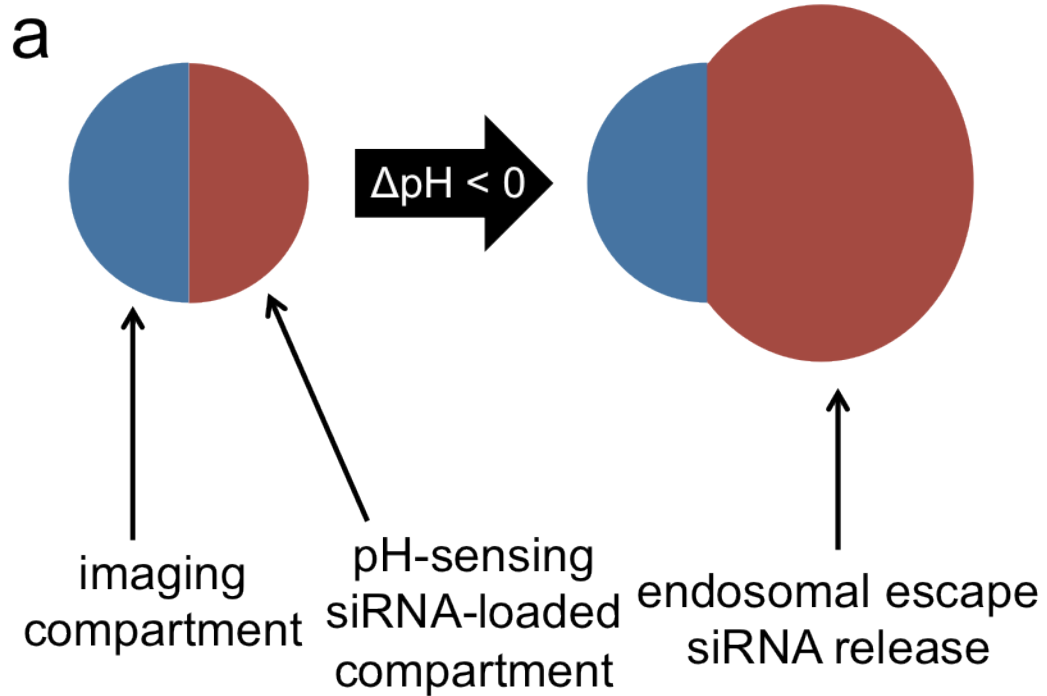


Figure 2-1. (a) Bicompartmental particle design showing dissimilar compartments with complementary functions – imaging and siRNA delivery (and endosomal escape). (b), (c) Representative fluorescent CLSM and DLS data of siRNA-loaded bicompartmental particles (scale bar is 1 μm).

Fabrication of multicompartamental particles. PLGA/PEI and PLGA/PEI-siRNA particles were produced via electrohydrodynamic co-jetting [34]. When dyes (PMPDHPV and ADS306PT) were incorporated into the jetting solutions, they were used at concentrations less than or equal to .01 w/v%. Generally, 5 w/v% polymer solutions were used for both sides, with the PLGA/PEI side having either 50:50 w/w PLGA:PEI (for characterization), or 4:1 w/w PLGA:PEI (for *in vitro* testing). A mixture of chloroform (CHCl₃) and N,N-dimethylformamide (DMF) was used as the solvent – 97:3 v/v CHCl₃:DMF was used for particles fabricated for characterization, while for the particles used in *in vitro* studies, 50:50 v/v CHCl₃:DMF was used. When DSP was used as a crosslinking agent, it was incorporated into the PEI jetting solution in the amount of 5 wt% with respect to the amount of PEI. To incorporate siRNA, it was first complexed with PEI in water, lyophilized, and then dissolved in the jetting solvent, along with PLGA (and DSP). 80 ng of siRNA were incorporated into the solution for every 1 mg of polymeric material, resulting in an siRNA loading of 80 ng siRNA/mg particle.

Particle characterization. To confirm the bicompartamental character, polymeric dyes were used, as well as rhodamine labeled siRNA, and fluorescence imaging was done using an Olympus FluoView 500 Laser Scanning Confocal Microscope (CLSM). Differential interference contrast microscopy (DIC) for swelling studies was performed using the same CLSM microscope. Scanning electron micrographs were obtained using an AMRAY 1910 Field Emission Scanning Electron Microscope (FEG-SEM). Particle size was determined by analysis of SEM images via ImageJ.

Cell culture. MDA-MB-231/GFP cells were cultured in DMEM with high glucose and glutamine, supplemented with 10% FBS, 1X non-essential amino acids, and 1X penicillin-streptomycin. Passaging was performed by washing the cells once with Dulbecco's phosphate buffered saline (D-PBS), incubating with .25% trypsin for 5-10 minutes, subsequently diluting with media, centrifuging the cells, and seeding in flasks or well plates.

GFP silencing experiments. Cells were seeded at 25000 cells/well in a 12-well plate with circular glass slides. After one day, particles and siRNA were incubated overnight (~12 hours). Media was changed every day, and cells were fixed 1, 2, 3, and 4 days after particle incubation. Cell fixing was performed by washing the cells with D-PBS and incubating with

paraformaldehyde for 30 minutes. Cells were washed once more with D-PBS, and the glass slides were then removed and mounted using ProLong Gold with DAPI. Slides were imaged using fluorescence microscopy using the same laser power settings for each channel and each sample. GFP expression was quantified using ImageJ to analyze the GFP channel from the images. Statistical significance was set at $p < 0.05$.

XTT assay. Cytotoxicity of particles was assessed by incubating varying concentrations of particles with cells seeded on a 96-well plate at a concentration of 5000 cells/well. Particles were incubated with cells for 24 hours, and XTT assay was performed as per protocol provided by Invitrogen with the XTT assay kit.

2.1.3 Results and Discussion

To characterize the compartmentalization of these particles, the size of the particles had to be increased in order to visualize the particles by confocal microscopy. Crosslinking of the PEI compartment was achieved via incorporation of dithiobis(succinimidyl propionate) (DSP), a small molecule consisting of two N-hydroxysuccinimide esters, which are reactive to amines. The swelling behavior of the PLGA/PEI particles in various buffered aqueous solutions was controlled by modifying critical jetting parameters including molecular weight or incorporation of crosslinker into the PEI jetting solution. The use of a higher molecular weight PEI resulted in a higher degree of swelling of the particles after electrohydrodynamic co-jetting (Figure 2-2a). Because equimolar amounts of crosslinker were used for both polymers, the relative crosslinking density of the lower molecular weight PEI was increased relative to the high-molecular weight PEI. Hence, the high molecular weight PEI was associated with a higher swelling capacity, as shown in Figure 2-2a. Because of this higher swelling capacity, all further experiments were conducted with the high molecular weight PEI.

Moreover, in the absence of crosslinker, swelling was faster and complete dissolution of the compartment in water eventually was observed. In contrast, crosslinked particles swelled less and remained stable in their swollen state (Figure 2-2b). This observation implies that for an uncrosslinked PEI compartment, the particle can enter a cell's endosome without much release of small molecule drugs, as minimal swelling is observed initially; after 8 hours, a swollen PEI compartment is observed clearly intact (Figure 2-2b, uncrosslinked),

implying that endosomal escape is possible. Given the timeframe of particle uptake being four to six hours,^[46] the particles should have enough time to enter cells and escape endosomes. Subsequently siRNA can then be released completely into the cytosol after 48 hours due to complete dissolution of PEI by that time (Figure 2-2b, uncrosslinked).

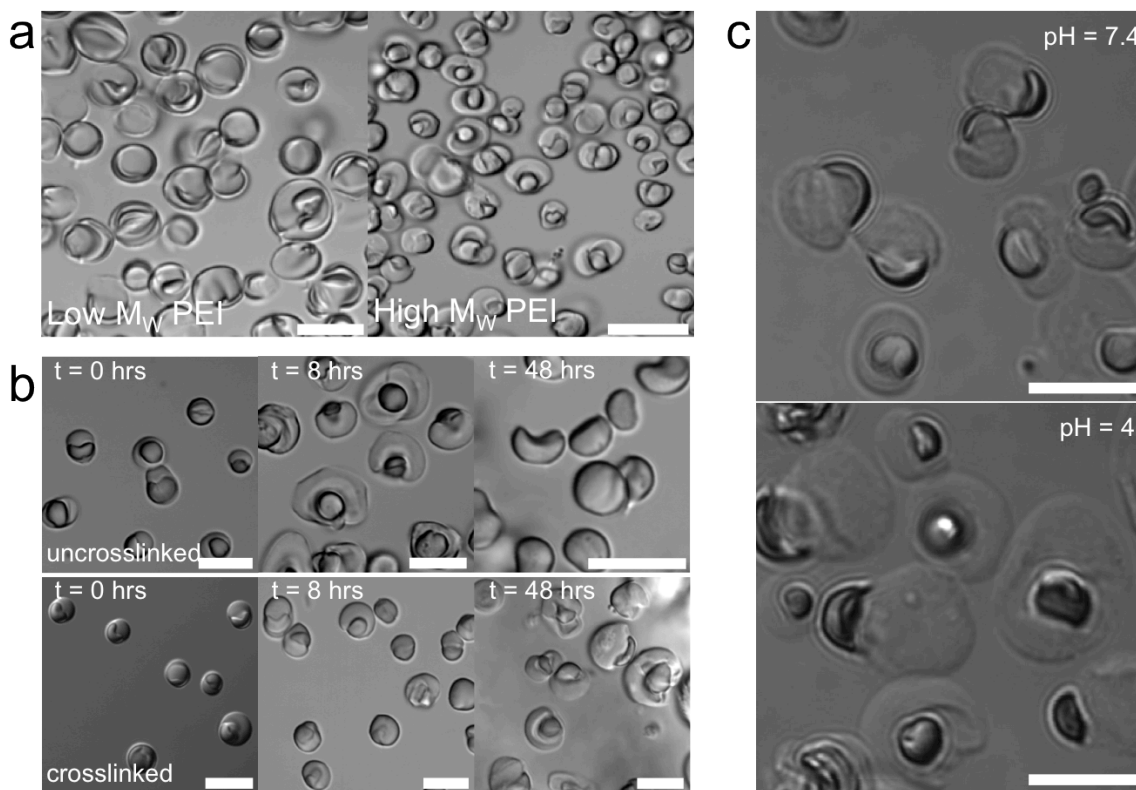


Figure 2-2. Swelling studies performed via DIC microscopy. (a) Particles incorporating higher molecular weight PEI exhibit a higher degree of swelling after four hours in PBS. (b) Particles incorporating uncrosslinked PEI are observed to have different swelling kinetics than that of crosslinked PEI, as well as eventually having dissolution of the PEI. (c) Particles with crosslinked PEI show different degrees of swelling at different pH levels after 6 hours of incubation in the appropriate buffered solutions. All scale bars are 10 μ m.

After the particles have been prepared, the crosslinking reactions between the NHS ester groups in the crosslinker and amines in the PEI can continue for a certain period in the solid state. Because we ultimately intend to use these particles for *in vitro* delivery of siRNA, it is critical that the particles were prepared as stable formulations with predictable mechanical and chemical properties. One prerequisite was therefore that the crosslinking was completed before cells were allowed to be in contact with the particles. We thus conducted a detailed Fourier transform IR (FTIR) spectroscopic analysis. To facilitate IR spectroscopy,

the particles were deposited as a thin film onto a gold-coated silicon substrate. By monitoring the loss of the peak at 1760 cm^{-1} (ester groups) and the growing peak at 1660 cm^{-1} (formation of new amide bonds), we determined that the crosslinking reaction indeed proceeds in the bulk for more than a day and then ceased after 48 hours, as shown in Figure 2-3. Based on this finding, the particles were routinely dried in air or under vacuum desiccation for at least 48 hours prior to conducting further experiments.

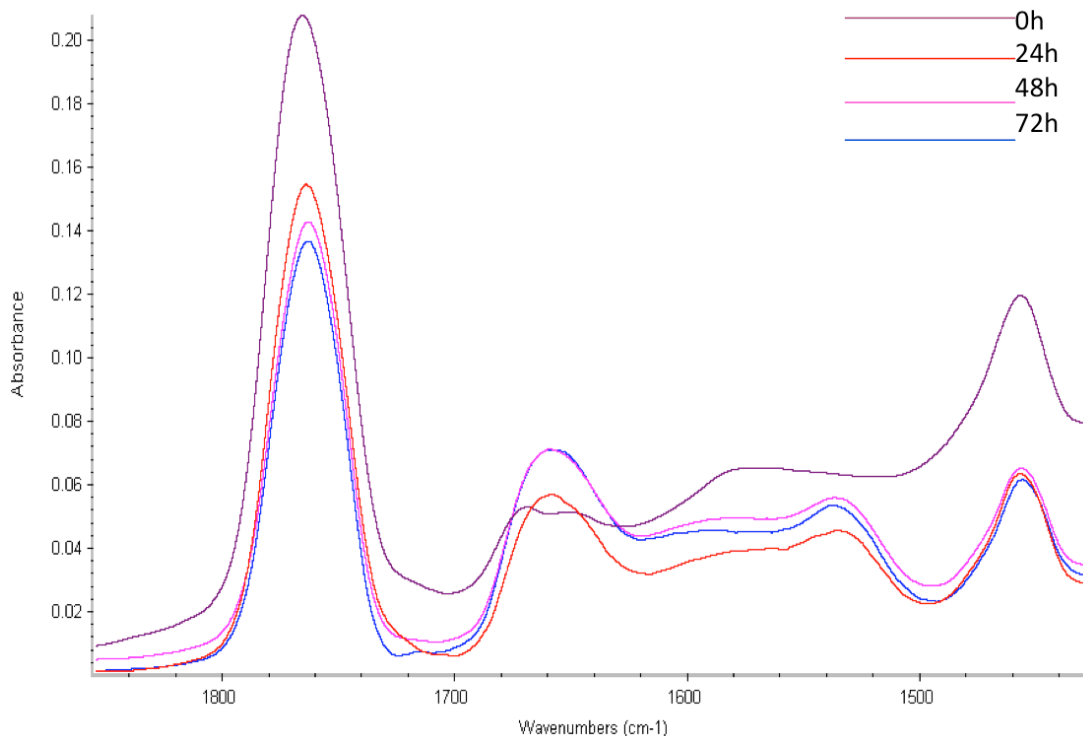


Figure 2-3. FTIR measurements of bicompartamental particles with PEI and DSP (crosslinker) incorporated on one side. Particles were jetted onto gold coated silicon wafers and kept at ambient conditions for 0, 24, 48, and 72 hours after jetting. At each time point, a wafer was used to perform FTIR in reflectance mode.

With these fully crosslinked particles, we then conducted a set of swelling experiments in phosphate buffered saline (pH = 7.4) and an aqueous acetic acid and sodium acetate buffered solution (pH = 4). As shown in Figure 2-2c, the PEI compartment was substantially more swollen at pH = 4 than at pH = 7.4. In either buffer, we observed that the bicompartamental nature of the particles was maintained as the hydrophobic PLGA compartment was clearly delineated from the hydrogel PEI hemisphere. The PLGA side did not change in either buffer, unlike the PEI compartment, which had become substantially larger. These results are shown for a PLGA/PEI compartment with 1:1 w/w PLGA:PEI, using

60 kDa (high molecular weight) PEI with 5 wt% DSP with respect to the amount of PEI. We note that the swelling rate and size of the swollen compartment can be controlled by varying the aforementioned parameters providing adequate control over final particle sizes.

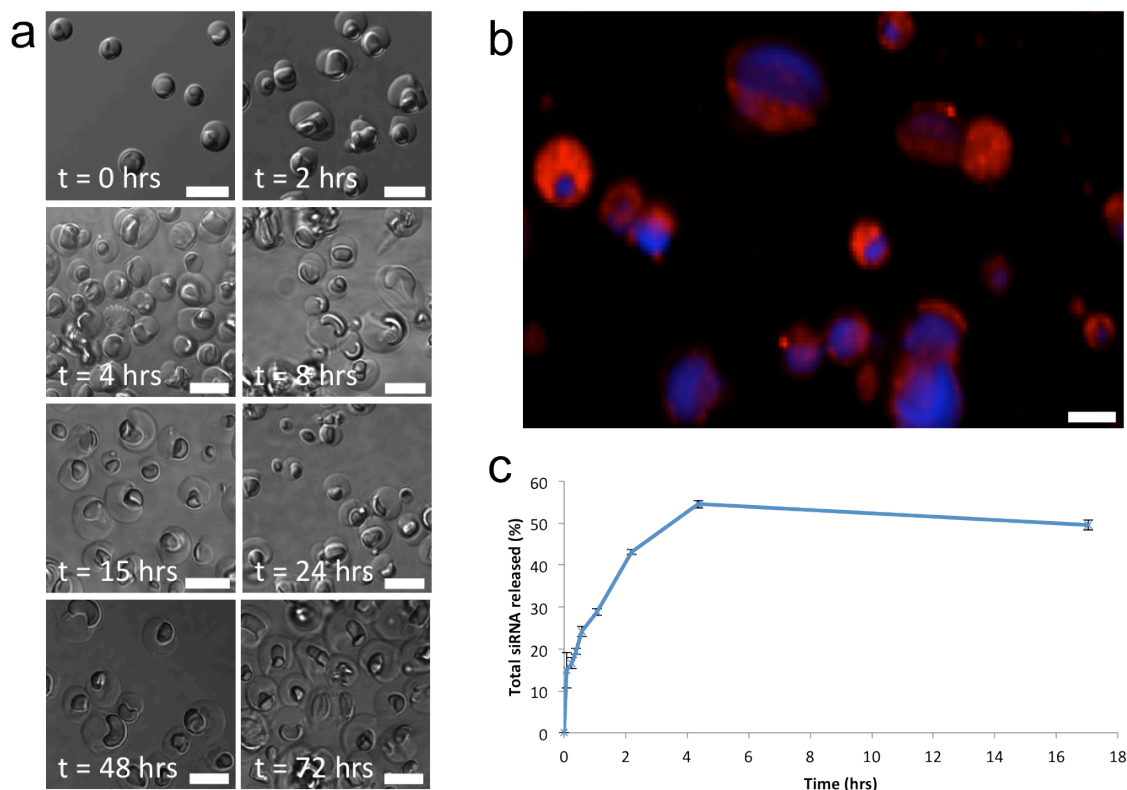


Figure 2-4. (a) Swelling kinetics of bicompartmental particles with crosslinked high M_w PEI via DIC microscopy. (b) Fluorescent CLSM image of bicompartmental particles, with blue fluorescent PLGA imaging compartment, and a composite PLGA/crosslinked PEI compartment loaded with rhodamine-labeled siRNA. (c) Release kinetics of particles from (b) in PBS. All scale bars are 10 μm .

Next, the particle swelling and release kinetics were assessed by selectively loading rhodamine-labeled siRNA into the PEI compartment. The particles reached the maximum swelling within 15 hours at pH 7.4, and maintained their dimensions thereafter (Figure 2-4a). Hence, if the particles were only placed in aqueous solution immediately before incubation with cells, as it was the case in the following experiments, minimal swelling can be expected to occur prior to endosomal uptake into the cells.³⁸ In contrast, significant swelling will occur at the lower pH after entering an endosome, ultimately breaking the endosomes either physically or by osmotic pressure.

Figures 2-4b and 2-4c demonstrate the compartmentalization and release of rhodamine-labeled siRNA at a pH of 7.4. Despite siRNA having a relatively low molecular weight, we observe that there is a clear interface between the compartment with siRNA and blue fluorescent imaging compartment. This well-defined interface, as well as the 50% release of the total siRNA loaded, may partially be attributed to the fact that the siRNA is tightly complexed with the PEI due to strong electrostatic interactions.

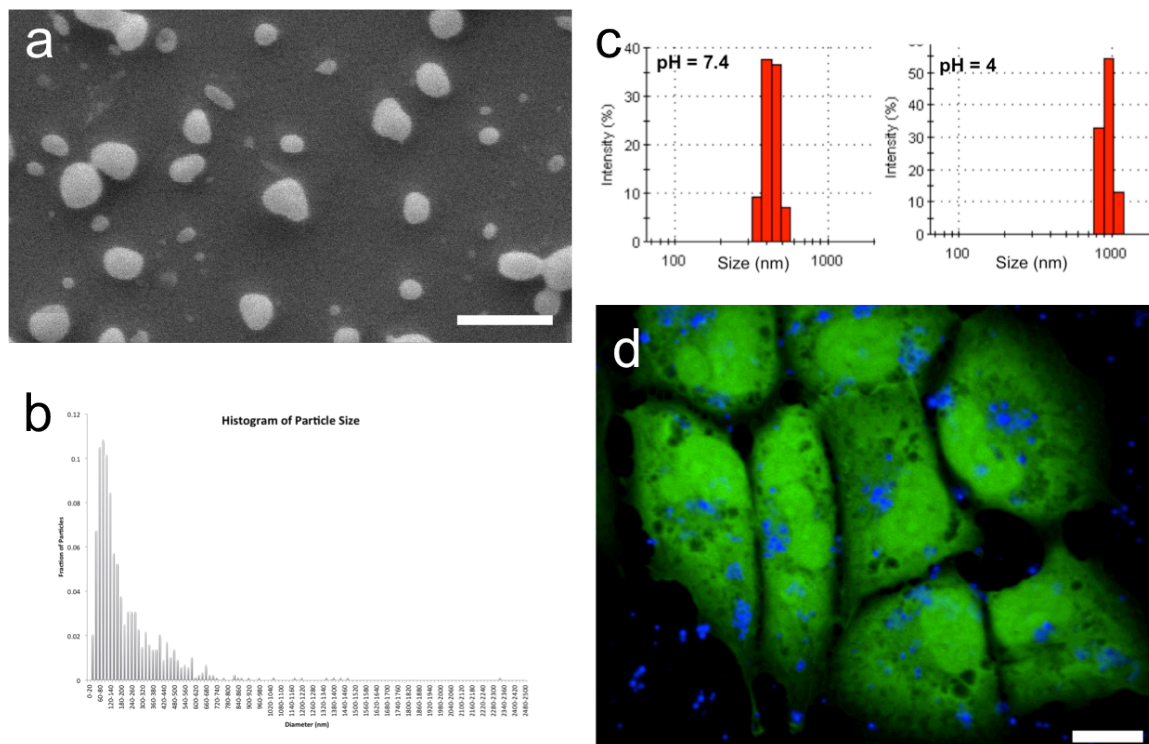


Figure 2-5. (a) SEM image of bicompartamental PLGA/PLGA-PEI nanoparticles. Scale bar is 1 μm. (b) Size distribution of particles from (a) using ImageJ. (c) DLS data showing large increase in hydrodynamic size in pH 4 compared to in pH 7.4. (d) Nanoparticles (blue) are readily uptaken by GFP-expressing breast cancer cells (MDA-MB-231/GFP). Scale bar is 20 μm.

To assess the *in vitro* uptake and efficacy of PLGA/PEI particles loaded with siRNA (PLGA/PEI-siRNA), we decreased the particle size to an average of about 216 nm, with a 95% confidence interval between 203 and 219 nm, as seen in Figure 2-5. A representative subpopulation of these particles is shown in Figures 2-1c and 2-5a – c. As shown in Figure 2-5c, we also demonstrated their pH-responsive swelling behavior by dynamic light scattering (DLS). To ensure maximum levels of delivery of siRNA, no crosslinker was used in these particles. Hence, these uncrosslinked particles should deliver their entire siRNA

payload within 48 hours, when the particles are completely dissolved (Figure 2-2b). We employed a GFP expressing epithelial breast cancer line, MDA-MB-231/GFP, and used an siRNA against GFP to assess the therapeutic efficacy of siRNA delivery using the PLGA/PEI-siRNA particles. Using the imaging modality provided by the PLGA compartment, we were able to demonstrate that the particles are uptaken readily by the MDA-MB-231/GFP cells (Figure 2-5d). Particles were incubated overnight with cells seeded on a 12-well plate; subsequent confocal imaging demonstrated a high level of blue fluorescence from the imaging compartment of the particles co-localized with green fluorescence emanating from the GFP expressing MDA-MB-231/GFP cells (Figure 2-5d), confirming particle uptake.

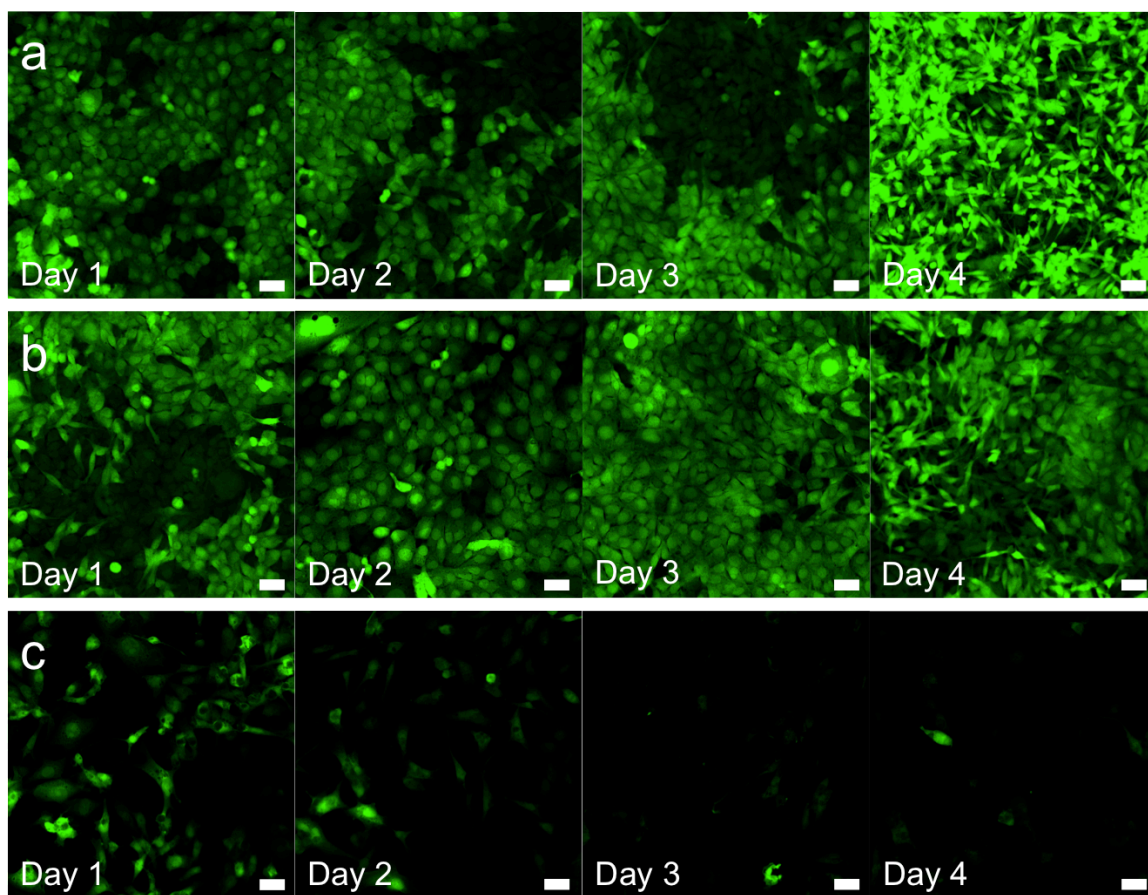


Figure 2-6. In vitro particle incubation experiments with MDA-MB-231/GFP breast cancer cells. (a) Cells with no particles or siRNA treatment. (b) Results from incubating particles and free siRNA (not loaded in the particles). (c) Results from incubation with siRNA-loaded particles. All scale bars are 50 μm . Concentrations for the particle incubation shown here were 100 $\mu\text{g}/\text{ml}$.

We further assessed the efficacy of the PLGA/PEI-siRNA nanoparticles in terms of GFP silencing in a dose-response experiment. As shown in Figures 2-6 and 2-7, the particles were able to silence GFP production within 2 days, which again coincided with the complete dissolution of the PEI compartments. When soluble siRNA was placed in the media, PLGA/PEI nanoparticles did not cause uptake of this siRNA (Figure 2-6b); only PLGA/PEI-siRNA nanoparticles (i.e., particles loaded with siRNA) resulted in silencing of GFP (Figure 2-6c). This confirms that the particles are indeed taken up and siRNA is released in the cytosol, as opposed to siRNA entering the cells from the outside environment via unspecific pathways. It might be hypothesized that PEI used at higher concentration may destabilize cell membranes and thus enhanced uptake.³⁹ Therefore, a control experiment was included, where PLGA/PEI particles without siRNA loading were prepared and then delivered to the cells together with spiked-in, free siRNA (Figure 2-6b). If there is membrane damage caused by the particles, the free siRNA should be able to enter the cytosol and silence the GFP expression. Based on our control experiment, this, however, is not the case, as no such GFP knockdown was observed, as shown in Figure 2-6b. The data shown in Figure 2-6 clearly demonstrate that siRNA is not entering via this method, but rather through endocytosis-mediated uptake of particles loaded with siRNA. Finally, the toxicity of the particles was assessed by XTT assay (Figure 2-8). The results indicated that the toxicity of the bicompartamental particles can be neglected up to concentrations of at least 100 µg/ml. Taken together, bicompartamental particles at a concentration of 100 µg/ml is not only nontoxic, but also effective at silencing GFP expression.

The GFP silencing was then quantified by image analysis. We observed GFP silencing in response to incubation with PLGA/PEI-siRNA particles, while cells incubated with PLGA/PEI particles or PLGA/PEI particles with soluble siRNA (PLGA/PEI+siRNA) did not show reduced GFP expression (Figure 2-7). We also observed a dose-dependent silencing response – incubation with a lower concentration of PLGA/PEI-siRNA particles (50 µg/ml) resulted in lower silencing of GFP – on days 2, 3, and 4, we observed GFP expression of approximately $16.94 \pm .94$, 18.69 ± 1.35 , and 24.17 ± 3.04 , respectively – these values are all consistently higher than those of GFP expression from cells incubated with PLGA/PEI-siRNA particles at a concentration of 100 µg/ml). Additional controls were performed, such as incubation of cells only with siRNA, which, as expected, was not taken up and no GFP silencing was therefore observed. The positive control of PEI complexed with siRNA was

expected to perform superior with respect to GFP silencing, as the amount of siRNA used was about two orders of magnitude higher than that used in the particles. We selected the lower siRNA levels in the Janus particles to mirror the concentrations used in other published studies.^{40,41} However, it is important to note that the control PEI-siRNA complexes only had about a third more reduction in GFP as compared to the PLGA/PEI particles, in spite of the fact that they had about two orders of magnitude less siRNA. These findings suggest that our new particles have a higher transfection efficiency than what was observed with the standard PEI transfection method.

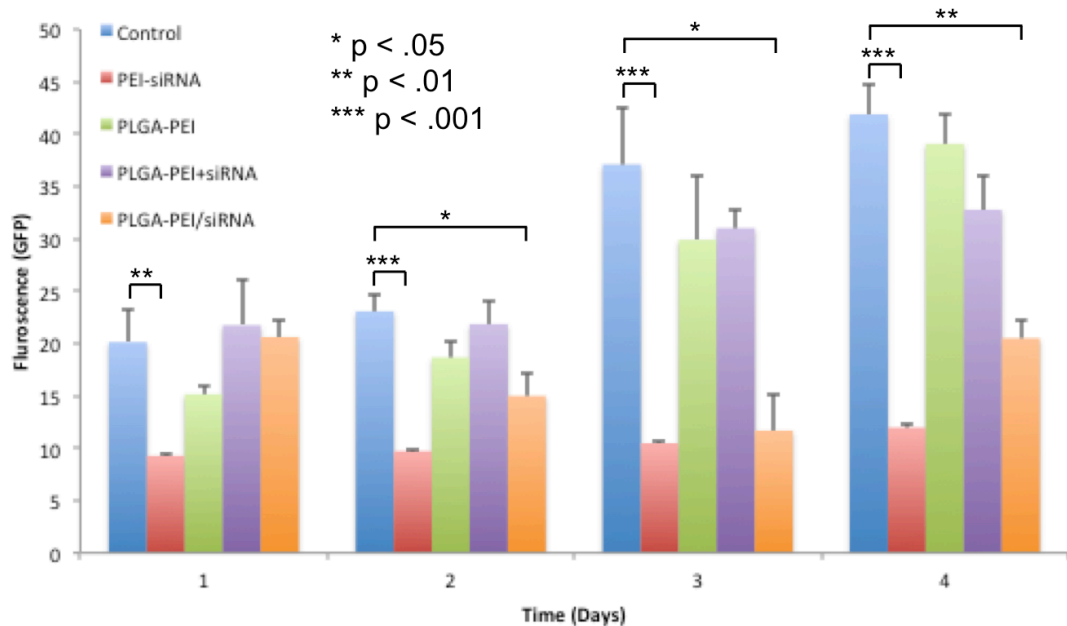


Figure 2-7. Quantification of GFP expression by image analysis. Control represents that have not been incubated with particles nor siRNA. PEI-siRNA represents a control where cells were incubated with PEI-siRNA polyplexes (1 mg/mL PEI, 1 µg/mL siRNA). PLGA/PEI+siRNA represents cells incubated with bicompartamental particles and soluble siRNA (100 µg/mL PLGA/PEI, 1 µg/mL siRNA) PLGA/PEI-siRNA represents cells incubated with siRNA-loaded bicompartamental particles at a concentration of 100 µg/mL.

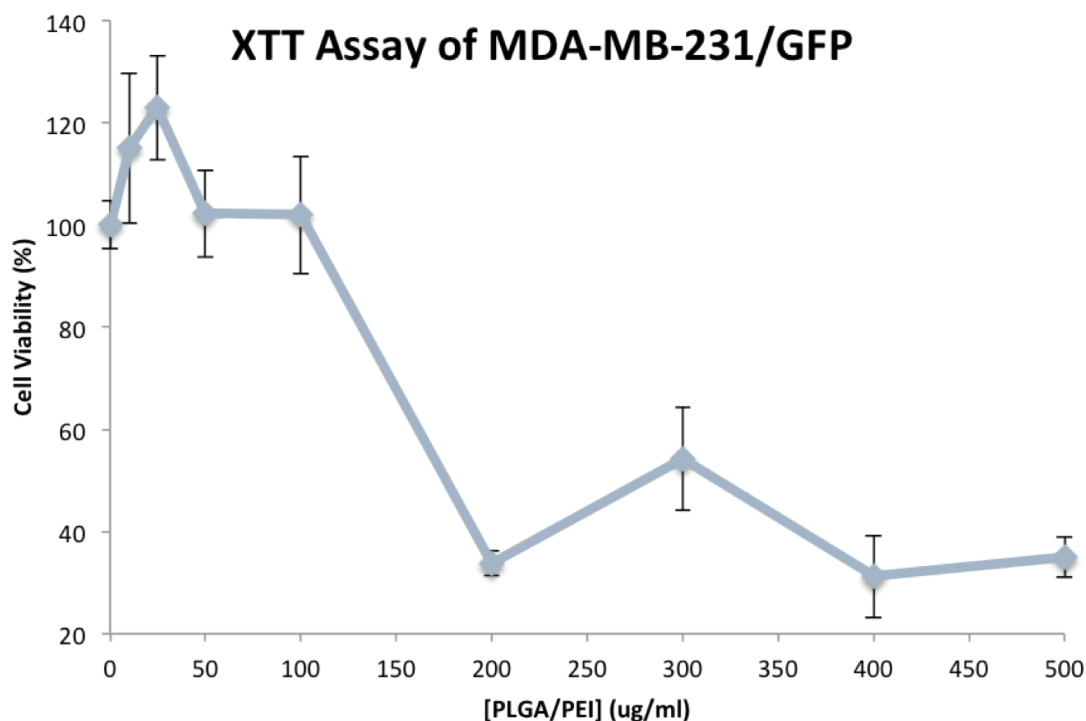


Figure 2-8. XTT assay performed on MDA-MB-231/GFP cells, incubating with various concentrations of PLGA/PEI bicompartamental particles. Cells were incubated with particles for approximately 12 hours, after which media was changed, and XTT assay was performed after another 12 hours (24 hours after start of incubation).

2.1.4 Summary

In conclusion, we have produced nanoparticles with two dissimilar compartments. These novel particles allow for incorporation of dual imaging and siRNA release functions. The electrohydrodynamic co-jetting approach used to prepare these particles allowed for independent selection of the chemical composition of two individual compartments. This was then used to control of the degree of swelling as well as the amount of siRNA released in a given period. The pH-sensitive PEI compartment allows for sensing of the endosomal environment, further swelling and bursting out of the endosome, thereby allowing the siRNA to be released in the cytosol where it would be biologically active. Finally, we assessed the *in vitro* efficacy of the particles to silence GFP expression in MDA-MB-231/GFP using an anti-GFP siRNA. The siRNA-loaded particles were able to silence GFP at a level comparable to our positive control, PEI-siRNA complexes, using two orders of magnitude lower amounts of siRNA. These nanocarriers have the potential to serve as delivery vectors for multiple drugs as well as gene delivery, allowing for synergistic effects, which are known

to be effective in combating diseases such as cancer.^{42,43} Additionally, the potential of “theranostics” maybe achieved through these particles as imaging modalities may be incorporated. Here we incorporated a fluorescent dye, but it is conceivable that a NIR dye, or even an MRI contrast agent, may be used. Manufacturing nanoparticles with multiple compartments could provide multiple functionalities that otherwise could not be incorporated into the same particle, allowing for a wide array of possible applications.

2.2 Towards Developing Novel Endosome-sensing Carriers

2.2.1 Background and Motivation

As shown by many studies, polyethyleneimine (PEI) is a pH-responsive polymer that is highly efficient in escaping endosomal compartments;^{12,44,45} however, as a cationic polymer, PEI is fairly toxic, as well as non-biodegradable.^{46,47} Carriers based on PEI are therefore dose-limited. Considerable effort has been made to mitigate the toxicity by chemically modifying PEI.^{46,48-51} PEGylation is one common method to help decrease toxicity, whether by fabricating carriers with a modified PEI with PEG chains, or by PEGylating the surface of a PEI-based carrier.⁴⁸⁻⁵¹ However, chemical modification may affect the swelling behavior of PEI, and, in the case of nucleic acid delivery, affect complexation with PEI.^{48,49} Here, we describe several approaches to possibly address this issue, and perhaps develop endosome-sensing materials even more efficient than PEI.

One explanation for the toxicity of cationic polymers like PEI is that they destabilize, at least in part by inducing pore formation, negatively charged cell membranes.³⁹ Hence, masking the positive charges by covering the surface of the carrier with another macromolecule may significantly reduce the toxicity. Alginate, an anionic polysaccharide, is biocompatible and potentially biodegradable.⁵² Progress has been made in successful chemical modification of alginate;^{53,54} in some cases, it is desirable to dissolve alginate in organic solvents to perform reactions not possible in aqueous solutions. Preparing alginate as a tetrabutylammonium (TBA) salt form that can dissolve in dimethylsulfoxide (DMSO) has allowed for chemical manipulation of alginate in organic solvents.⁵⁵⁻⁵⁸ TBA-alginate can dissolve in DMSO perhaps due to the hydrophobic character of the TBA cation. Hence, in aqueous solutions, TBA-alginate may act as a surfactant. Herein we propose using TBA-alginate to stabilize the PEI based nanoparticles fabricated by electrohydrodynamic (EHD) co-jetting.

As will be discussed later, the use of TBA-alginate only mitigates the toxicity somewhat, and so we modified our approach to use a different pH-sensitive polymer, glycol chitosan. Glycol chitosan is a modified cationic polysaccharide that has been shown to be biocompatible and also been used for transfection.⁵⁹ We suspected that although chitosan may not have as much of a proton sponge effect as PEI because there are considerably fewer amines per mole, it nonetheless would be sufficient. The results section describes more detail – in summary glycol chitosan is effective at delivering siRNA to the cytosol of cells, albeit not as efficient.

In our hands, glycol chitosan is less toxic but not more effective than PEI for cytosolic delivery, and so our other approach was to synthesize new endosome-sensing & escaping materials. As discussed before, there are two possible mechanisms that account for PEI's efficiency at escaping endosomes – large swelling under acidic conditions and generation of high osmotic pressure, via the so-called proton sponge effect.⁴⁴ Hence, materials that can swell to a large degree and generate high osmotic pressures only in endosomal environments, but remain inert otherwise, would be ideal for efficient endosome sensing and escaping. Considering these properties, hydrophilic polymers emerge as clear candidates. The osmotic pressure Π generated by a polymer in water at a concentration c can be estimated from thermodynamic considerations with a virial expansion as follows,⁶⁰ where d_1 is the polymer density relative to water and M_W is the polymer molecular weight:

$$\frac{\Pi}{RTc} = \frac{1}{M_W} + B \frac{c}{d_1^2} \left(\frac{1}{2} - \chi_{12} \right) + B \frac{c^2}{3d_1^3} + \dots$$

The coefficient B is given by $B = v_2(n_1/M_W)^2$, where v_2 is the volume of one mole of solvent (water), and n_1 is the degree of polymerization (number of monomers per polymer molecule). The ratio n_1/M_W is therefore the inverse of the molecular weight of one monomer of a polymer chain, and is independent of the molecular weight of the polymer. Hence, the second and third virial coefficients of Π are independent of the polymer molecular weight, and at higher concentrations, Π is then highly dependent on the polymer concentration and χ_{12} . In fact, it has been experimentally verified for some extremely hydrophilic polymers, the osmotic pressure, especially at higher concentrations, is

independent of the molecular weight.⁶⁰⁻⁶³ We may hence employ a higher, as opposed to lower, molecular weight polymer as it can swell to a larger degree.^{47,64-66}

The Flory-Huggins interaction parameter χ_{12} is related to the free energy change ΔG_{121} required for two polymer chains to come into contact with one another from being surrounded by water molecules: $\chi_{12} = -S_c \Delta G_{121} / kT$;⁶⁰ for a polymer to generate high osmotic pressure, the polymer molecules should more favorably interact with water molecules than themselves, resulting in a very positive ΔG_{121} , and hence a highly negative χ_{12} . ΔG_{121} is also related to the interfacial energy γ_{12} between the polymer and water, $\Delta G_{121} = -2\gamma_{12}$, and so we obtain $\chi_{12} = 2S_c \gamma_{12} / kT$.⁶⁰ This relation more clearly shows that a low χ_{12} corresponds to a low interfacial energy between polymer and water molecules. Therefore, polymers having low interfacial energies with water are desirable for generating high osmotic pressures. Such hydrophilic macromolecules include synthetic polymers like poly(ethylene glycol) (PEG) and polysaccharides such as dextran.^{60,67,68} Hence, using high molecular weight variants of these macromolecules may serve as corresponding endosome-sensing and escaping materials, which are capable of a high degree of swelling and an ability to generate high osmotic pressures.

The hydrophilic polymers described before possess the desired properties once a carrier composed of such materials reaches an endosome. However, in other environments (i.e. during circulation and outside a cell), it would be preferable for the material to not swell and exert as minimal osmotic pressure as possible. As endosomes are acidic environments, one potential strategy may be to use hydrophobic, acid-labile protecting groups to mask the hydrophilic functional groups of the polymer. For example, Fréchet and coworkers protected the hydroxyls of dextran with acetal groups, rendering the polymer relatively hydrophobic and insoluble in water; in acidic conditions, however, the hydroxyl groups become deprotected, and the dextran is soluble once again in aqueous solvents.^{69,70}

Here we demonstrate two possible endosome-sensing polymers, and formulate carriers based on them using EHD co-jetting.²⁷⁻³⁰ Both involve acid-labile acetal protecting groups that render the material with an overall hydrophobic character, which is reversed under acidic conditions such as an endosomal environment. We choose to base our polymers on biodegradable materials with low toxicity profiles, dextran and ascorbic acid, that also have

high osmotic activity.^{60,62,71-74} One is an acetal protected high molecular weight dextran, while the other is a low molecular weight polymer of an acetal protected ascorbic acid.

2.2.2 Methods

Materials. Poly(DL-lactide-co-glycolic acid) (PLGA, 85:15 lactide:glycolide, 50-75 kg/mol), polyethyleneimine (PEI, Mn = 60 kg/mol, Mw = 760 kg/mol), alginic acid (240 kg/mol), tetrabutylammonium hydroxide (TBA-OH), glycol chitosan (80 kg/mol), polyethylene glycol diglycidyl ether (PEDGE, 526 g/mol) Pluronic F127, Tween 20, dextran (1500-2800 kg/mol), 2-methoxypropene, pyridinium p-toluenesulfonate (PPTS), triethylamine (TEA), poly[(*m*-phenylenevinylene)-alt-(2,5-dihexyloxy-*p*-phenylenevinylene)] (PMPDHPV), 5,6-isopropylidene-L-ascorbic acid, 4-penteyl chloride, pyridine, Hoveyda-Grubbs catalyst 2nd generation, and all solvents were obtained from Sigma Aldrich. Dithiobis(succinimidyl propionate) (DSP) was purchased from Thermo Scientific. Dulbecco's Modified Eagle Medium (DMEM), fetal bovine serum (FBS), non-essential amino acids (NEAA), penicillin-streptomycin (pen/strep), and XTT reagents were supplied from Invitrogen. MDA-MB-231/GFP cells were obtained from Cell Biolabs.

Synthesis of TBA-alginate. TBA-alginate was synthesized based on a protocol described before.⁵⁵ Briefly, up to 5 g of alginic acid was dispersed in at least 100 ml of ultrapure water. An equal amount, by weight, of TBA-OH was added, turning the mixture from cloudy white to transparent, hazy brown. The mixture was allowed to stir for about 15 minutes at ambient conditions, and then freeze dried. TBA-alginate is the resulting dried product with a white to slightly yellow color.

Synthesis of acetalated high molecular weight dextran (AHM_{wD}). AHM_{wD} was synthesized based on a protocol by Fréchet and coworkers for the acetalation of lower molecular weight dextrans.⁶⁹ Briefly, 1 g dextran was dissolved in 50 ml of DMSO. About 25 mg PPTS was added, and then 5 ml 2-methoxypropene was added slowly. The reaction was stirred for 3 hours at room temperature, and AHM_{wD} was precipitated out by pouring the reaction mixture into 200 ml of 1 v/v% TEA/H₂O. The precipitate was purified by washing several times with water via centrifugation and resuspension, and then freeze dried.

Synthesis of poly(protected vitamin C) (PPVC). PPVC was obtained by acyclic diene metathesis (ADMET) polymerization of a monomer based on an acetalated form of vitamin C, 5,6-isopropylidene-L-ascorbic acid. The monomer, 2,3-di-O-pent-4-enoate-5,6-isopropylidene-L-ascorbic acid, was formed by room temperature esterification of 5,6-isopropylidene-L-ascorbic-acid and 4-pentenoyl chloride in dichloromethane with a catalytic amount of pyridine. ADMET polymerization was done at 60 °C for 2 days under intermittent vacuum, using Hoveyda-Grubbs second generation catalyst. The polymer was then precipitated in hexane. Monomer and PPVC synthesis courtesy of Dr. Hakan Durmaz.

Fabrication of PEI, glycol chitosan, AHM_wD, and PPVC based carriers. All carriers were fabricated by electrohydrodynamic (EHD) co-jetting as previously described.²⁷⁻³⁰ Briefly, for PEI-based carriers, a 5.25 w/v% 1:1:0.1 w/w/w PLGA:PEI:DSP in 1:1 v/v CHCl₃:DMF solution and a 5 w/v% PLGA in 1:1 v/v CHCl₃:DMF solution were co-jetted at 0.1 ml/hr, 30 cm height, and 10.2-11.4 kV; after jetting they were allowed to crosslink for 72 hours at room temperature. Glycol chitosan based carriers were made by co-jetting at 0.1 ml/hr, 30 cm, and 11.4-13.2 kV the following: 1) 1.3 w/v% 5:1:2 w/w/w glycol chitosan:Pluronic F127:PEGDE (with and without siRNA) in 1:1 v/v DMF:H₂O and 2) 1 w/v% PLGA in DMF; after crosslinking, they were allowed to crosslink for 72 hours at 37 °C. AHM_wD based carriers (monocompartmental) were made by the jetting of a 1 w/v% AHM_wD in 9:1 v/v CHCl₃:DMF solution at 0.1 ml/hr, 30 cm, and 5.7 kV. PPVC-based carriers were made by co-jetting the following at 0.2 ml/hr, 30 cm, and ~7.5 kV: 1) 5 w/v% PLGA and 2) 5 w/v% PPVC both in 95:5 v/v CHCl₃:DMF.

Characterization techniques. FTIR spectroscopy was done using a Thermo Scientific Nicolet 6700. A FluoView 500 Laser Scanning Confocal Microscope (CLSM) was used for fluorescence and differential interference contrast (DIC) imaging. Scanning electron micrographs were obtained using an AMRAY 1910 Field Emission Scanning Electron Microscope (SEM). Confocal bright field images were captured using the white light source of a WITec alpha300R. Dynamic light scattering (DLS) was performed using a Malvern Zetasizer Nano ZSP.

Cell culture. MDA-MB-231/GFP cells were cultured as per protocol provided by Cell Biolabs, using DMEM supplemented with 10% FBS, 1x NEAA, and 1x pen/strep. For XTT assays, 96-

well plates were seeded at 10000 cells/well. The following day, media was replaced with media and varying concentrations of particles (with and without TBA-alginate). After 24 hours incubation, XTT assay was performed as per Invitrogen protocol, using a Biotek Synergy 2 plate reader. For glycol chitosan carriers, the *in vitro* experiments were performed by the Luker lab using their own GFP and luciferase-expressing MDA-MB-231 cell line.

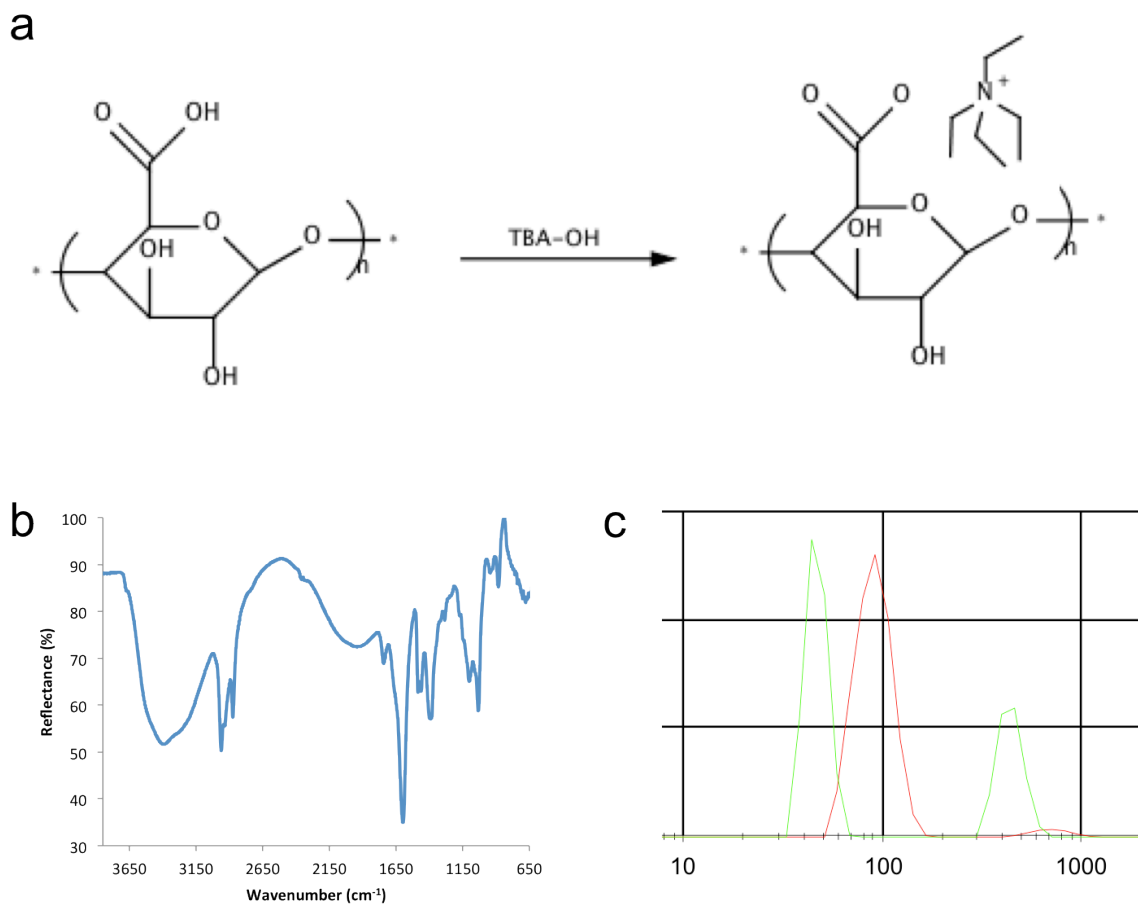


Figure 2-9. (a) Facile synthesis of TBA-alginate. (b) FTIR of synthesized TBA-alginate. (c) DLS data of PLGA/PLGA-PEI-DSP nanoparticles stabilized by tween 20 only (red), and tween 20 and TBA-alginate (green).

2.2.3 Results and Discussion

TBA-alginate is readily obtained by simply reacting alginate with TBA-OH, as shown in Figure 2-9a. We note from the FTIR spectra (Figure 2-10b) the broad hydroxyl band around 3300 cm^{-1} , the sharp carboxylate peak at around 1610 cm^{-1} , and the C-H stretches from TBA cations in the $2800\text{--}3000\text{ cm}^{-1}$ range, consistent with previously reported literature.⁵⁷ When first attempting to stabilize PLGA/PLGA-PEI-DSP carriers with TBA-alginate, we used

relatively low amounts of the surfactant. However, we observed significant visible aggregation, perhaps attributed to electrostatic interactions between PEI and alginate. By incubating the carriers in an excess of TBA-alginate so that surfactant molecules are not interacting with multiple particles, with a 10:1 w/w TBA-alginate:carrier ratio, we observed no visible aggregation. As seen from DLS (Figure 2-9c), carriers in tween 20 (red) are mostly well dispersed, with a size of around 100 nm, but there is a small peak at around 800 nm, which may be attributed to aggregates. In contrast, carriers stabilized in tween 20 and TBA-alginate (green), have reduced amount of aggregation, as the secondary is shifted to around 400 nm. It is also noted that the primary peak shifts down to around 50 nm; this shift may indicate that the 100 nm peak represents dimers of particles, but the shift may also be attributed to difficulty of resolving multiple peaks with DLS – given the relatively high amount of TBA-alginate, the shifted peak may be accounting for small aggregates, such as micelles, of surfactant.

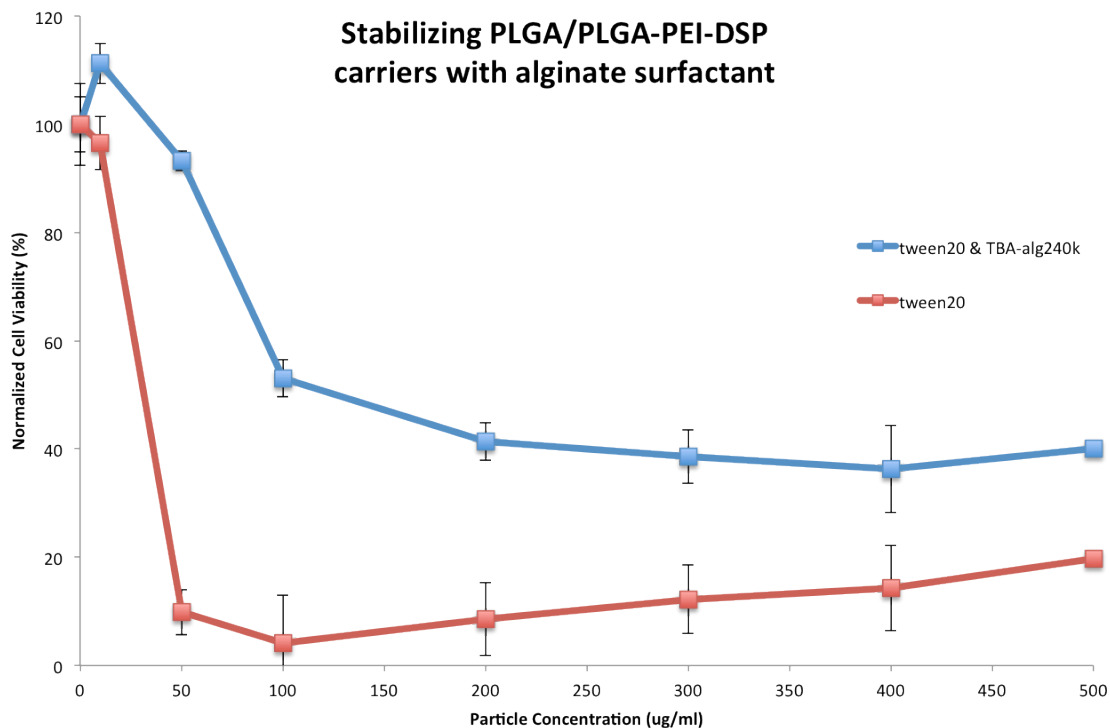


Figure 2-10. XTT assay performed on MDA-MB-231/GFP cells with PLGA/PLGA-PEI-DSP nanoparticles stabilized by tween 20 only (red), and tween 20 and TBA-alginate (blue).

We compared the toxicity of tween 20 and TBA-alginate stabilized PEI-based nanocarriers to tween 20 stabilized PEI-based nanocarriers by measuring cell viability using XTT assay

after incubating them with MDA-MB-231/GFP cells for 24 hours (Figure 2-10). At concentrations higher than 100 $\mu\text{g/ml}$, where tween 20 stabilized particles show cell viability around 10-20%, it is observed that tween 20 and TBA-alginate stabilized particles are less toxic, with cell viabilities around 40%. So while the TBA-alginate seems to help mitigate the toxicity of PEI-based carriers, it does not completely eliminate it. It is possible that in the complex media, the TBA-alginate may not effectively bind effectively to the carrier surfaces, and therefore may not mask their positive charge.

Based on the observations with TBA-alginate, it may not be possible to fully mitigate PEI's toxicity by charge screening with anionic surfactants. We therefore turn to alternative materials that are also effective at endosome-sensing and escaping. Chitosan is an attractive choice as it is somewhat similar to PEI with respect to pH-dependent swelling and proton buffering capacity. Additionally, it is more biocompatible and may be less toxic than PEI.^{75,76} For our studies, we choose to use glycol chitosan, which is very similar to chitosan structurally, as it has better solubility properties, and hence allows for more facile EHD co-jetting. As seen in Figure 2-11a, we are able to fabricate relatively uniform particles that are roughly the same size as the PEI-based carriers described in the previous section, as evidenced by the DLS data in Figure 2-11b.

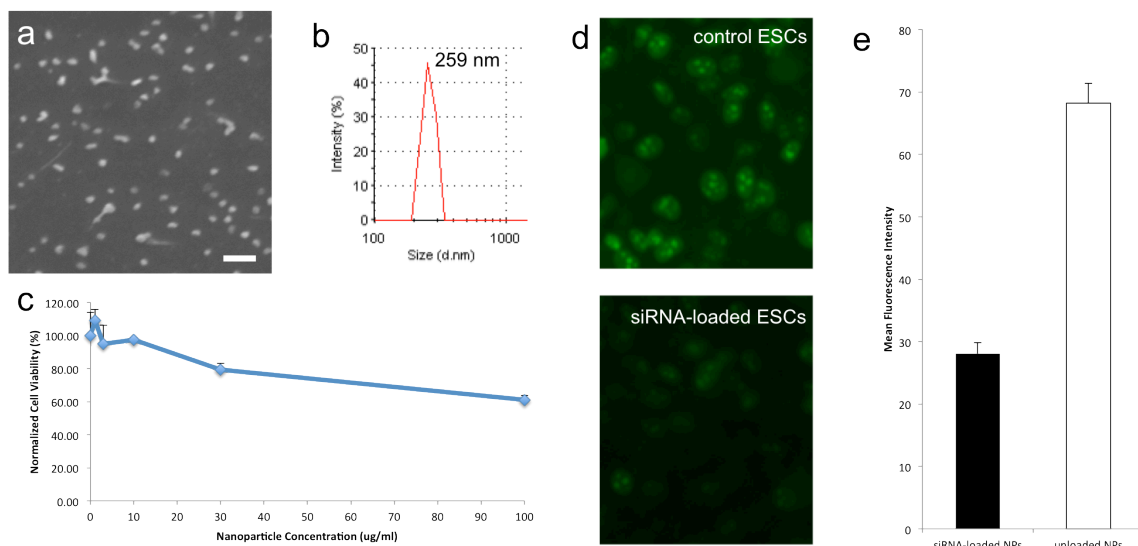


Figure 2-11. (a) SEM image of PLGA/glycol chitosan (PLGA/GC) nanoparticles. Scale bar is 1 μm . (b) Corresponding DLS data for (a). (c) Luciferase based toxicity assay of PLGA/GC particles on luciferase and GFP expressing MDA-MB-231 cells. (d) Fluorescent images comparing PLGA/GC particle (control ESCs) incubation to PLGA/GC-siRNA (siRNA-loaded ESCs). (e) Quantification of GFP expression from (d). *In vitro* data obtained by Luker group.

The toxicity of these glycol chitosan-based carriers was assessed by luciferase activity of MDA-MB-231 cells expressing both GFP and luciferase; as seen in Figure 2-11c, we find that particle concentrations up to 30 $\mu\text{g/ml}$ are relatively nontoxic. Of note, this level of toxicity is slightly lower than that of PEI-based carriers, toxic at concentrations above 10 $\mu\text{g/ml}$ (Figure 2-10). Many studies indicate chitosan's relative biocompatibility *in vivo*, and so additional studies need to be performed to further elucidate our *in vitro* findings. With toxicity evaluated, we then tested the endosome-sensing and escaping capacity of these glycol chitosan-based carriers by GFP silencing with siRNA delivery. As seen in Figure 2-11d and 2-11e, as we observe a decrease in GFP expression with a knockdown of a little over 50%, the carriers are capable of delivering functional siRNA to the cytosol. In comparison, EHD co-jetted PEI-based carriers are capable of gene silencing of almost 75%. Hence, while chitosan-based carriers may be more biocompatible, they may not be as effective.

PEI, chitosan, and other cationic, amine-containing polymers are all commonly used as endosome-sensing materials, but they all have some degree of toxicity because of their positive charge.³⁹ We hence explored developing novel endosome-sensing materials, one being an acetalated derivative of a high molecular weight dextran, AHM_{wD}. In addition to generation of osmotic pressure at acidic conditions, we expect that there would be a transient swollen gel formation as, due to the high molecular weight, the dextran would be only partially soluble until most acetal groups are completely hydrolyzed. To show these properties of our AHM_{wD}, we made carriers comprised of this polymer using EHD co-jetting, as seen in Figure 2-12a.

Other polysaccharides were also explored, but the acetalation reaction worked best with dextran, perhaps due to a number of reasons. Many polysaccharides were not as soluble in DMSO as dextran, such as chitosan and alginic acid, which has quite flexible ether linkages. Moreover, other polysaccharides' relative inflexibility may prevent successful acetalation because of steric hindrance. Additionally, chitosan and alginic acid have reactive functional groups that may affect the reaction; in particular, the carboxylic acid groups on alginic acid may prevent stable acetal protection of the hydroxyl groups. Hence, while some polysaccharides may be more suitable for endosome-sensing, dextran was chosen for its ability to be rendered inert in nonacidic conditions via acetalation.

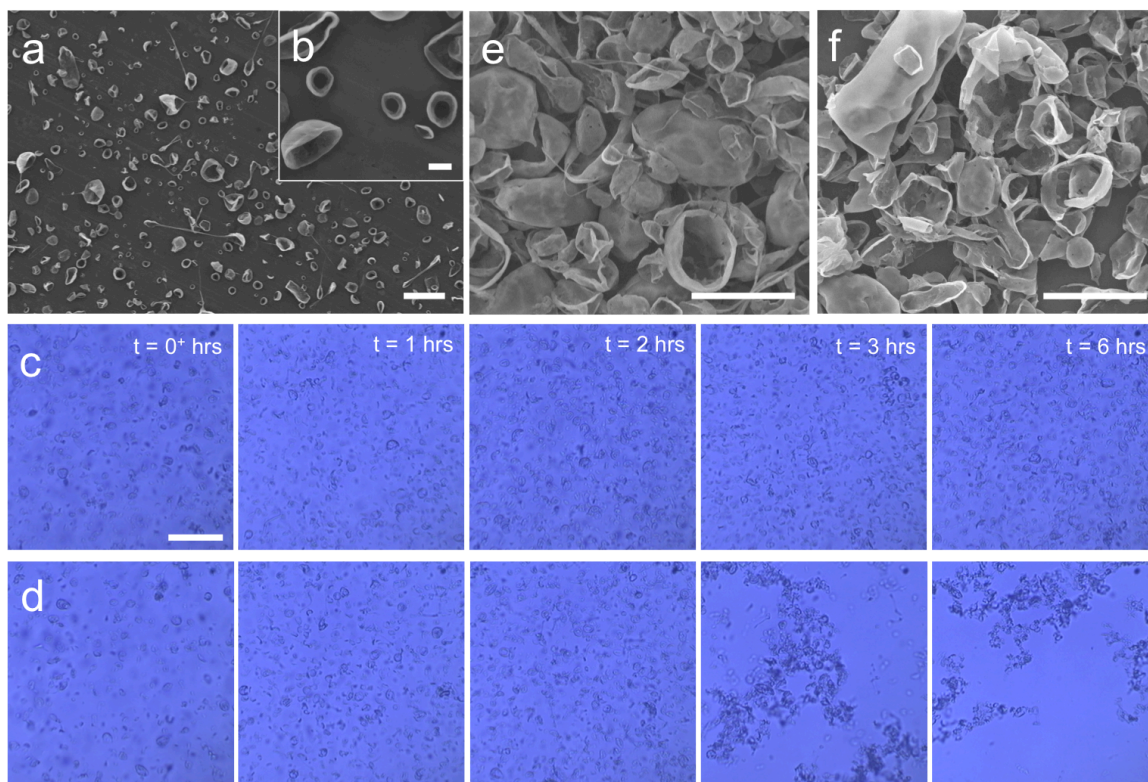


Figure 2-12. (a) SEM image of AHM_wD based carriers. (b) Zoomed in SEM image showing cup-like morphology. (c), (d) Bright field confocal images of AHM_wD based carriers incubated in pH 7.4 and 5, respectively. (e), (f) SEM images of washed AHM_wD carriers after 6 hour incubations in pH 7.4 and 5, respectively. Scale bars are (a, e, f) 10 μ m, (b) 1 μ m, and (c, d) 50 μ m.

While the AHM_wD-based carriers have a unique cup-like morphology (Figure 2-12b), they are fairly uniform, and so we performed kinetic studies at 37 °C to observe any swelling behavior at pH 7.4 and 5 (Figures 2-12c and 2-12d, respectively). As seen by the bright field and SEM images in Figures 2-12c and 2-12e, the carriers remain relatively unchanged in pH 7.4. On the other hand, after 3 hours in pH 5, aggregation and some swelling of the particles were observable (Figure 2-12d). While differences between the particle incubations at pH 7.4 and 5 are clear, the degree of swelling of the carriers in pH 5 is difficult to discern. The observed amount of swelling may not be as high for several reasons. Swollen dextran particles may not appear significantly opaque under bright field as solvated dextran is transparent, and therefore without high contrast, the swollen portion of the AHM_wD based carriers may not be seen. Moreover, the transient swelling may occur fast, and may not have been captured; i.e., more significant swelling occurred between t = 2 and 3 hours.

Additionally, when considering the mechanism of swelling, the buffered solution was assumed to penetrate completely through the AHM_wD particles, allowing for uniform deprotection; however, it may be possible that only the surface of the particles is affected – deprotection of material in the bulk will not occur until the surface is sufficiently deprotected, similar to surface erosion. After 6 hours in pH 5, there also does not appear to be much appreciable swelling from SEM (Figure 2-12f), perhaps due collapse of the particles after drying for SEM sample preparation, but some pores are found in the particles. These pores observed may be indicative of a surface erosion-like mechanism occurring. Nonetheless, we also observe that in pH 5, as the opacity from the particles decreases over time, the viscosity of the dispersion increases, perhaps due to gelling, or, at least, dissolution of sufficiently deprotected dextran.

It may be possible that the expected transient swollen state lasts for a very short period of time. To address this issue, a bifunctional small molecule, for instance, may be used to crosslink the unreacted hydroxyls, so that when the acetals are hydrolyzed, the particle structure may remain as a stable swollen hydrogel. If a process similar to surface erosion is the primary mechanism of degradation of the AHM_wD based carriers, another protected version of dextran may be explored. Two different protecting groups, one that hydrolyzes significantly faster than the other, reducing the relatively hydrophobicity, so that buffer penetration into the particle bulk is sufficient, but remains insoluble, due to the other protecting group, allowing for a transient swollen state till the second protecting group is removed.

In addition to AHM_wD, we also developed a hydrophobic, acid-labile polymer based on ascorbic acid, or vitamin C, poly(protected vitamin C) (PPVC). An acetal-protected version of vitamin C was modified via esterification to produce a compound that may undergo ADMET polymerization (Figure 2-13a). The resulting hydrophobic polymer would degrade under acidic conditions, with removal of the acetal groups in addition to hydrolysis of the esters, resulting in an osmotically active vitamin C derivative. The relatively pure monomer was characterized by NMR as shown in Figure 2-13b, with sharp peaks. After polymerization, the isolated macromolecule, a brown sticky malleable solid, has a molecular weight of around 1.5-2 kg/mol as per SEC; the NMR in Figure 2-13c shows the same peaks as the monomer but broader, indicating polymerization has occurred.

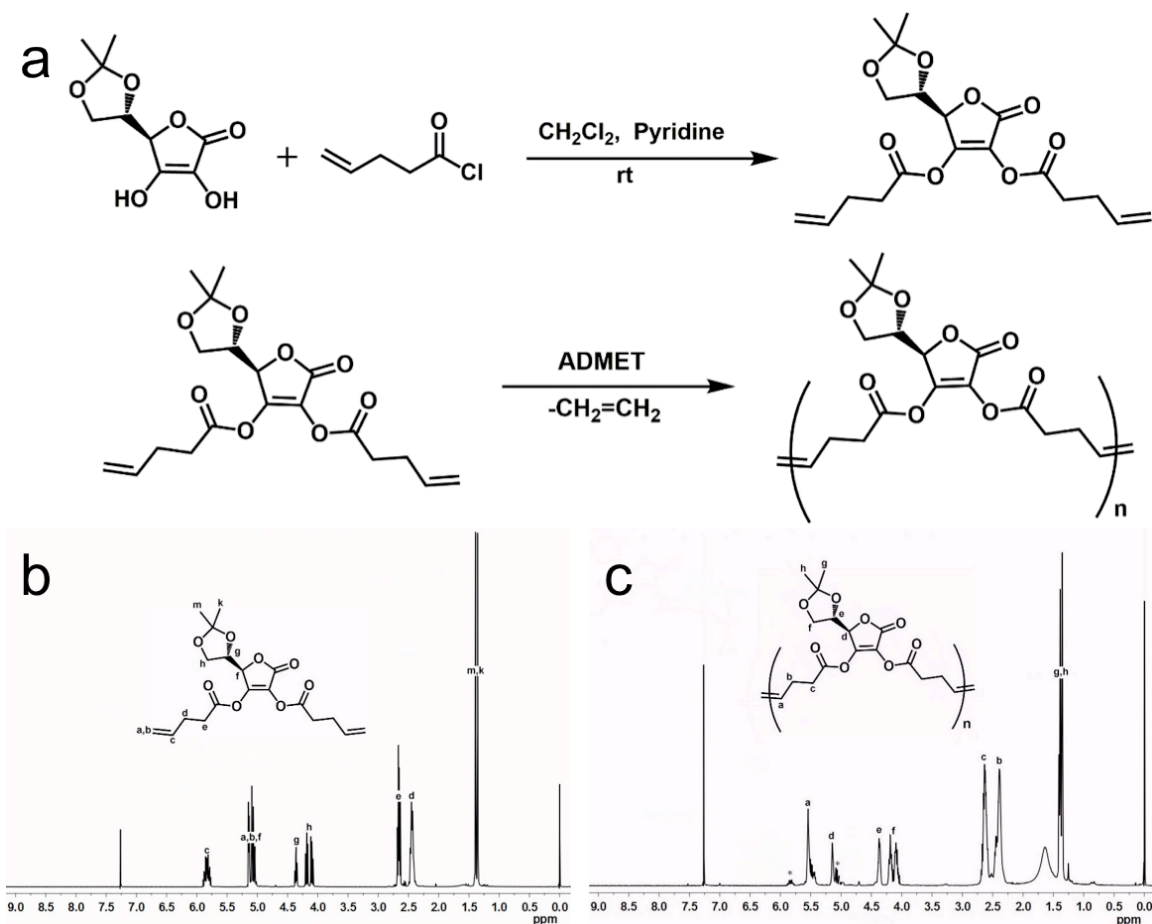


Figure 2-13. (a) Synthesis scheme of vitamin C based monomer and PPVC by ADMET polymerization of the monomer. (b) ^1H NMR of monomer. (c) ^1H NMR of PPVC. All synthesis and characterization were done by Dr. Hakan Durmaz.

Next, we fabricated carriers composed of PLGA and PPVC via EHD co-jetting, and, after purification, examined their fate after 24 hours incubation in pH 7.4 and 5 at 37 °C. As shown by the SEM image in Figure 2-14a, the particles appear smooth and fairly spherical, which does not change after incubation in pH 7.4 (Figure 2-14b). In contrast, after incubation in pH 5, as seen in Figure 2-14c, we observe both spherical particles and rough, flattened particles that appear degraded. This rough material may result from acidic degradation of PPVC, but it is unclear whether the material has leached out from the smooth particles or whether such smooth particles eventually flatten and become rough. Moreover, additional studies would be required to determine the osmotic activity of this material.

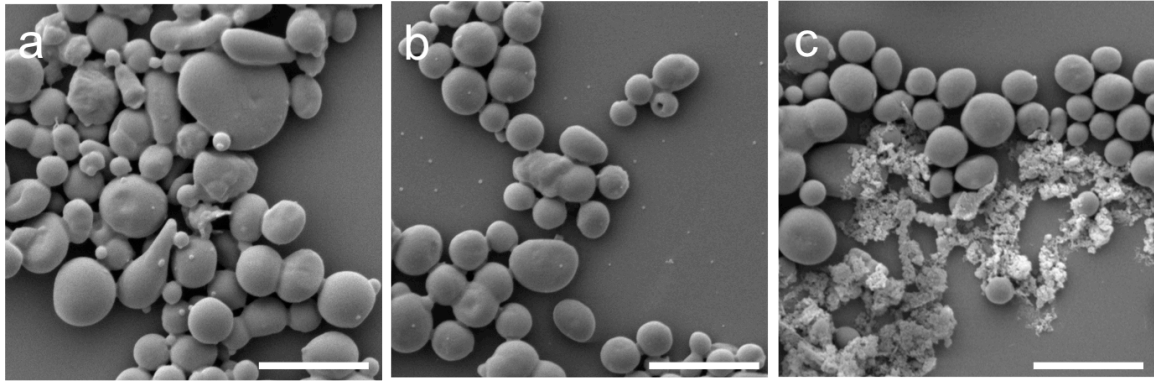


Figure 2-14. PLGA/PPVC carriers (a) immediately after purification ($t = 0^+$), (b) after 24 hour incubation in pH 7.4, and (c) after 24 hours incubation in pH 5. Scale bars are 5 μm .

2.2.4 Summary

With these studies, we have shown a few EHD co-jetted carriers that may be used in lieu of previously described PEI-based carriers for endosome-sensing and escaping. Simple use of an alginate-based surfactant is able to lower the toxicity of PEI-based carriers, albeit not completely. We find that employing other cationic amine-containing polymers, in this case glycol chitosan, may afford lower toxicity, but may also be less effective than PEI. To address these toxicity limitations, but also retain the efficient endosome-sensing and escaping functionality, we develop novel nonionic polymers, based on highly biocompatible materials, that swell and/or generate high osmotic pressures in acidic conditions, such as those found in endosomal environments. AHM_wD is capable of generation of high osmotic pressure and potentially high degrees of swelling, while PPVC is may generate osmotic pressure by degradation into its corresponding monomer. While more studies are required, our preliminary findings indicate that these two materials may be well suited for endosome-sensing and escaping.

2.3 Additional Therapeutic Functionalities

2.3.1 Background and Motivation

Plasmonic nanoparticles comprise a diverse set of materials that exhibit surface plasmon resonance (SPR) when excited by electromagnetic radiation.^{77,78} SPR involves a several order-of-magnitude enhancement in the local electric field due to oscillations of electrons at a resonant frequency.^{77,79} This enhancement has many implications – for one, some plasmonic nanoparticles, such as gold nanorods, generate thermal energy when excited by light of the appropriate wavelength.^{79,80} Other nanoparticles, such as silver nanostructures

and other gold nanoparticles, can generate higher degrees of fluorescence and Raman scattering; SPR is thought to be one of the main mechanisms accounting for surface-enhanced Raman spectroscopy (SERS).^{78,80}

These properties of plasmonic properties allow for unique biomedical applications. Because their SPR peaks are generally in the tissue-penetrable near infrared (NIR) region, gold nanorods, for example, have been employed for photodynamic therapy, using thermal ablation to eradicate tumors.^{79,81-84} Moreover, gold nanorods have also been used in photoacoustic imaging applications, *in vitro* and *in vivo*, via photothermal generation of acoustic signals.⁸⁵⁻⁸⁷ In addition, plasmonic particles have been used for a number of biosensing applications.⁸⁸⁻⁹⁰ In particular, *in vitro* and *in vivo* applications of surface enhanced Raman spectroscopy (SERS) have been especially promising.⁹¹⁻⁹⁶

While many of these functionalities are advantageous in their own individual right, there is great potential in fabricating hybrid plasmonic-macromolecular carriers that may provide capabilities like drug delivery, which are not so feasible with pure inorganic carriers, in addition to SPR-associated functions. Electrohydrodynamic (EHD) co-jetting^{27-30,47} allows for the compartmentalized loading of inorganic materials in a biocompatible macromolecular carrier; via EHD co-jetting, a number of nanocrystals, including gold and iron oxide, have been selectively localized in a compartment of a polymer carrier.^{31,32,97}

Here we present several poly(lactide-co-glycolic acid) (PLGA) based carriers containing plasmonic nanoparticles fabricated by EHD co-jetting, and demonstrate that these carriers exhibit properties associated with the corresponding SPR. First, we load gold nanorods into PLGA microcylinders, and show that such structures are able to generate local temperatures high enough to boil water. Second, we load gold nanospheres and gold nanodumbbells into PLGA microparticles, and use Raman confocal microscopy to precisely locate the inorganic nanoparticles. Third, we demonstrate a high loading of silver nanocubes in PLGA microparticles, and show that such carriers may demonstrate SERS capabilities.

2.3.2 Methods

Materials. Poly(DL-lactide-co-glycolic acid) (PLGA, 85:15 lactide:glycolide, 50-75 kg/mol), polyethyleneimine (PEI, Mn = 60 kg/mol, Mw = 760 kg/mol), tween 20, and all organic

solvents were obtained from Sigma. Gold nanorods (Au NRs) with an SPR peak around 808 nm were purchased from Nanopartz. Optimum cutting temperature (OCT) medium was obtained from Fisher Scientific. Gold nanospheres (Au NSs), gold nanodumbbells (Au NDBs), and silver nanocubes (Ag NCs) were synthesized by the Liz-Marzán group.

Fabrication of Au NR loaded carriers. Au NR-PEI complexes were prepared as described in Appendix A. Briefly, PEI and Au NRs were mixed, by vigorous vortexing, in water at specific ratios, and subsequently freeze-dried. The jetting solutions were as follows: 1) 30 w/v% PLGA in 95:5 v/v CHCl₃:DMF, 2) 30 w/v% PLGA with 15 mg/ml PEI and 300 µg/ml Au NRs in 95:5 v/v CHCl₃:DMF. Based on a previously described procedure,⁹⁸⁻¹⁰² the solutions were co-jetted, and the resulting fibers were collected on a rotating collector, embedded in OCT, sectioned with a Microme HM550 OMC cryostat microtome, and washed with .01 v/v% aqueous Tween 20 solution at least three times.

Fabrication of Au NS, Au NDB, and Ag NC loaded carriers. PLGA microparticles loaded with various metallic nanoparticles were fabricated via EHD co-jetting^{27-30,47} with the following parameters. For Au NS loaded carriers, a solution of 5 w/v% PLGA and [Au] = 0.229 mM in 1:9 v/v THF:DMF was jetted, at a flow rate of 0.2 ml/hr, distance of 30 cm, and voltage around 9.15 kV. For Au NDB loaded carriers, a 5 w/v% PLGA and [Au] = 0.935 mM in 1:1 v/v THF:DMF solution was jetted at 0.1 ml/hr and 30 cm. Finally, for Ag NC loaded carriers, a 6.51 w/v% 650:1 w/w PLGA:Ag NCs in 85:10:5 v/v/v CHCl₃:EtOH:DMF solution and 6.5 w/v% PLGA in 85:10:5 v/v CHCl₃:EtOH:DMF solution were co-jetted at 0.2 ml/hr and ~40 cm. Control pure PLGA particles were also synthesized using the same jetting solutions described except with no metallic nanoparticles.

Characterization. Scanning electron microscope (SEM) images were obtained using an AMRAY 1910 Field Emission SEM, and transmission electron microscopy (TEM) images were obtained using a Philips CM-100. Differential interference contrast (DIC) images of Au NR loaded carriers were captured with a Leica SP5X inverted confocal microscope (CM), and brightfield confocal images were captured with a WITec alpha300R.

NIR irradiation with two-photon confocal microscopy. Suspensions of the Au NR loaded carriers were purged with argon before NIR experiments. Using the Leica SP5X CM

equipped with a Mai-Tai two-photon laser, Au NR loaded carriers were irradiated with 808 nm light. For experiments in which bubbling was observed, time-lapse capturing of DIC images was performed, with a constant z maintained. To obtain high enough local temperatures for shape-shifting, focus on a single carrier was maintained by manual z-control during NIR irradiation, and DIC images were captured beforehand and afterwards.

Raman confocal microscopy. A WITec alpha300R was used for Raman microspectroscopic analysis of Au NDB and Ag NC loaded carriers as jetted on silicon wafers. A 532-nm laser was employed, using a resolution of at least 1 x 1 μm pixels; Raman signal was measured at each point for an integration time of at least 0.5 s. Estimation of pure component spectra and basis analysis were done, the details of which are described in Appendix B, to generate color maps corresponding to the relative contributions of each component (PLGA, substrate, and metallic nanoparticle).

2.3.3 Results and Discussion

After preparing complexes of gold nanorods (Au NRs) and PEI, as described in Appendix A, it became possible to disperse the Au NRs in chloroform and jet them with PLGA. After fabricating Au NR loaded PLGA microcylinders, the compartmentalization was evident from DIC images (Figure 2-15a), with one side appearing porous. The porosity was also validated from SEM images as shown in Figure 2-15b. This porosity may be attributed to the dissolution of PEI during processing of the microcylinders in aqueous solutions. The mixture of relatively high concentration PLGA with PEI in chloroform and DMF results in a cloudy but stable suspension, indicating phase separation, which may be maintained during the jetting process and hence in the resulting microcylinders – the size of the pores observed imply phase separation on the microscale.

To determine if these PLGA based microcylinders have SPR-dependent thermal energy generation capabilities, we observed them over time while a constant z plane was irradiated with 808 nm light, the SPR peak wavelength of the Au NRs used. As seen in Figure 2-15c, we noted bubble formation selectively on the porous side of microcylinders in focus. This spatially selective bubble formation is indicative of local temperature increases enough to boil the solvent. We also observed, perhaps due to the bubble formation, that the

microcylinders move rapidly and out of the plane of focus. Hence, this bubbling phenomenon may allow for applications as actuators in addition to thermal ablation.

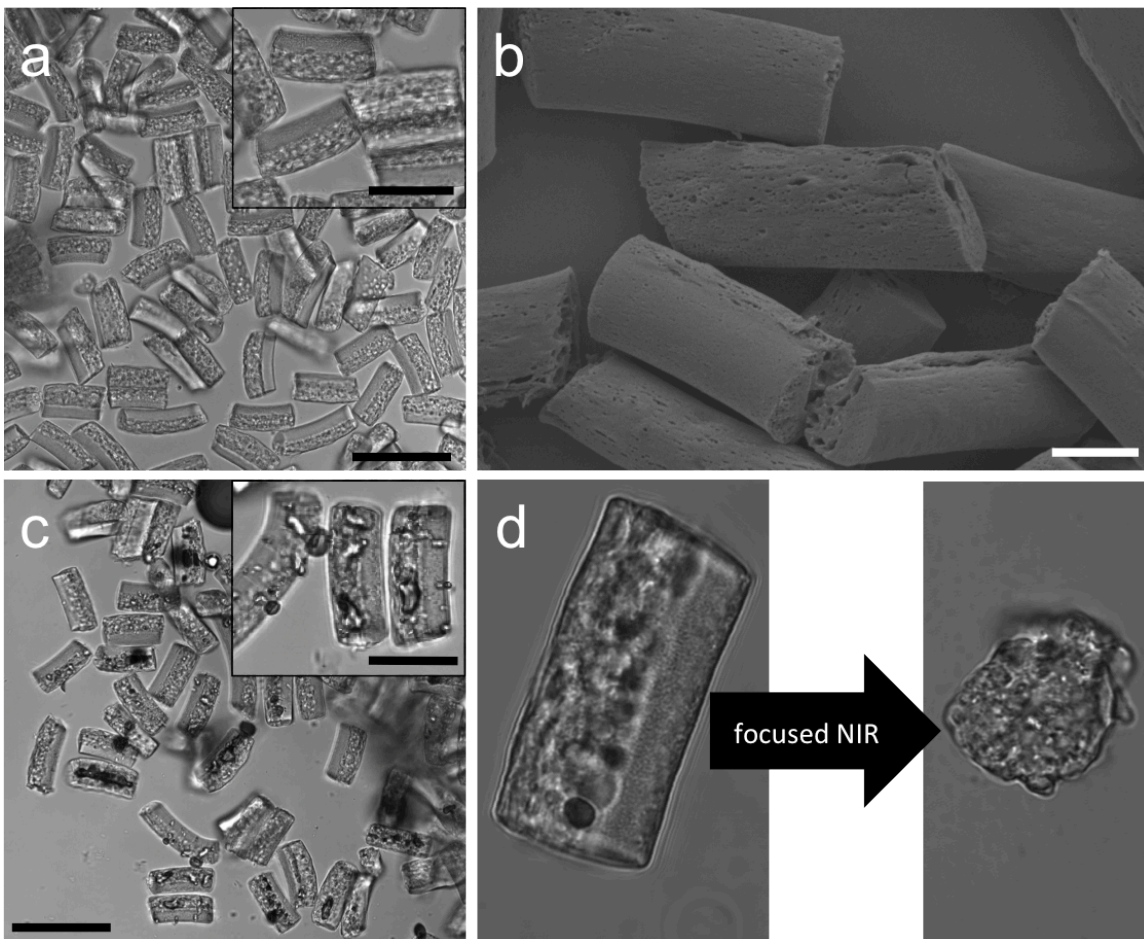


Figure 2-15. (a) DIC image of Au NR loaded PLGA carriers. (b) SEM of carriers showing porosity only on one side. (c) DIC image of carriers during NIR irradiation (no changing of focus). (d) DIC images of a carrier before (left) and after (right) NIR irradiation with focusing maintained manually throughout. Scale bars are (a, c) 50 μm (insets are 25 μm) and (b) 10 μm .

Given the robust response of the microcylinders to NIR light, we attempted to show another capability of these carriers that our group has previously described as shape-shifting,¹⁰⁰ in which polymeric particles may change their shape when local temperatures are increased above the glass transition temperature. We suspected that, despite high enough temperatures to boil solvent, the Au NR loaded carriers did not change shape as they move rapidly out of focus, and therefore the duration of the local temperature increase is not sufficiently long enough for shape shifting to occur; hence we manually controlled the focus

on a single microparticle for around 15 minutes, after which we observe a roughly spherically shaped particle (Figure 2-15d), consistent with the shape-shifting of PLGA microcylinders reported before.

Hence, the loading of Au NRs in PLGA based carriers may allow for temperature-dependent phenomenon, bubble formation and shape-shifting, using NIR-induced SPR effects. However, more studies are required before the hypothesized SPR-based mechanisms are validated. Firstly, it is important to note that we observe water boiling by NIR light, especially at high laser powers, which may also be shown by previous studies.¹⁰³⁻¹⁰⁵ This observation may imply another mechanism for the selective bubble formation – rather than the Au NRs, the porosity of the cylinders may cause maintenance of local temperature increases, due to relative lack of convective heat transfer to the bulk solution. Indeed, such a mechanism has been recently used for triggered drug release from PLGA nanoparticles.¹⁰⁶ These inconsistencies may be further compounded by the potential for some Au NRs to leech out as some PEI dissolves; we visually observed Au NRs separate the microcylinders after about a month-long incubation at ambient conditions. To further elucidate whether the observed phenomenon can be attributed to SPR of the Au NRs, the fabrication of Au NR loaded microcylinders without porosity may require further development.

In addition to Au NRs, gold nanospheres (Au NSs) and gold nanodumbbells (Au NDBs) were loaded into PLGA based carriers. As a control, we first experimented with the jetting of Au NSs. The colloidal stability of nanoparticles in a relatively complex jetting solution may be a concern, and so before jetting, the UV-Vis spectra of the solutions were measured. As seen in Figure 2-16a, the organic solvents and PLGA do not contribute much absorbance in the UV-Vis region, and the spectra of the PLGA Au NSs mixture is roughly the same as pure Au NSs, with a small amount of red shifting, indicating minor levels of aggregation. We then proceeded to jet and fabricate Au NS loaded PLGA microparticles. Upon examination via TEM (Figure 2-16b), we observe that while there are occasionally single Au NSs distributed, they are mostly aggregated and confined to one area within a particle. As seen in Figure 2-16c, the Au NS aggregates appear well ordered. We then turned to Au NDBs, which are able to generate especially strong fields by SPR in certain regions, sometimes denoted as hot spots.¹⁰⁷⁻¹¹⁰ We find that the Au NDBs remain colloidal stable in a solution with PLGA, with no observable red shifting in the UV-Vis spectra (Figure 2-16d). Similar to the Au NS

jetting, we observe occasionally single Au NDBs in PLGA microparticles (Figure 2-16e); for the most part, however, they are found confined to a few areas in aggregates as seen in Figure 2-16f. Unlike with Au NSs, however, the Au NDB aggregates do not appear ordered, and there are not as many particles per aggregate. Hence, jetting with Au NSs and NDBs result in them being compartmentalized in one or few areas within a PLGA carrier.

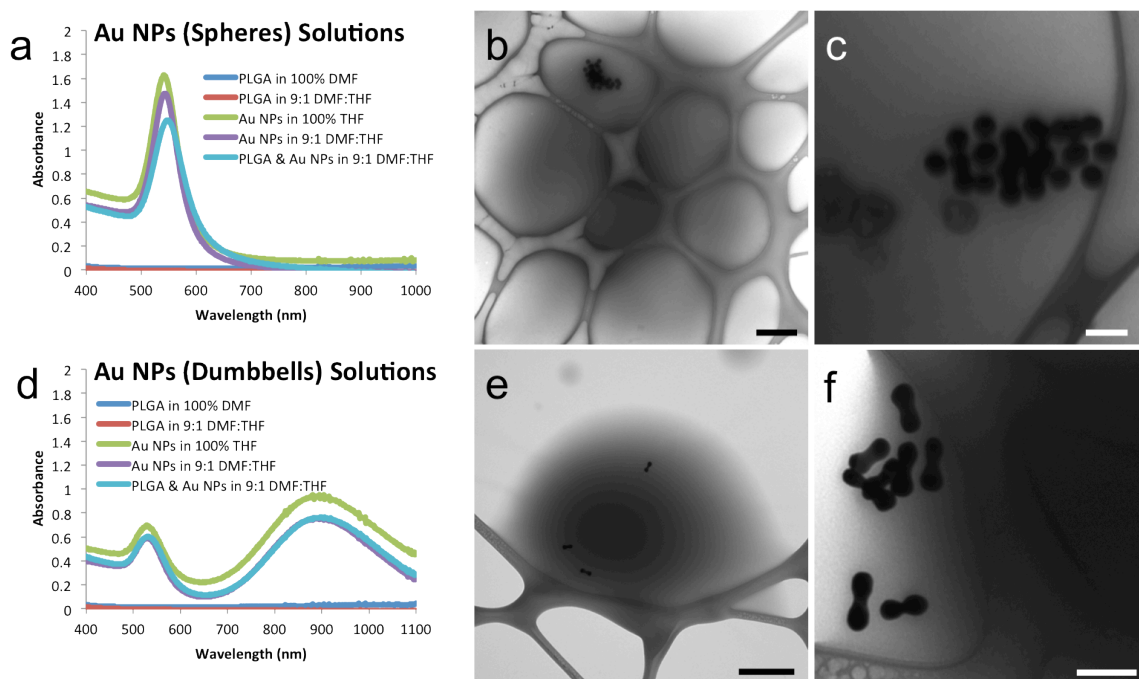


Figure 2-16. (a) UV-Vis spectra of PLGA, Au NS, and PLGA + Au NS solutions. (b), (c) TEM images of Au NS loaded carriers. (d) UV-Vis spectra of PLGA, Au NDB, and PLGA + Au NDB solutions. (e), (f) TEM images of Au NDB loaded carriers. Scale bars are (b, e) 500 nm and (c, f) 100 nm.

Even though there were few Au NDBs found in each PLGA microparticle, we hypothesized that we could detect and locate them by Raman confocal microscopy given their ability to generate potentially strong Raman signal via hot spots on each Au NDB. Upon examination by Raman confocal of several particles (Figure 2-17a), we noted two different Raman signatures (other than the substrate's signature), presumably representing PLGA and Au NDBs. After estimating the pure component spectra, basis analysis was performed, and color maps were generated representing the relative weights of the Au NDB and PLGA Raman signatures (Figures 2-17b and 2-17c, respectively) contributing to the spectra at each pixel. The overlay is displayed in Figure 2-17d. From these Raman confocal images, we can determine that the Au NDBs are compartmentalized in small areas of the PLGA

microparticles. It is uncertain whether aggregates or single Au NDBs can be distinguished, but nonetheless Au NDBs can be located within PLGA microparticles.

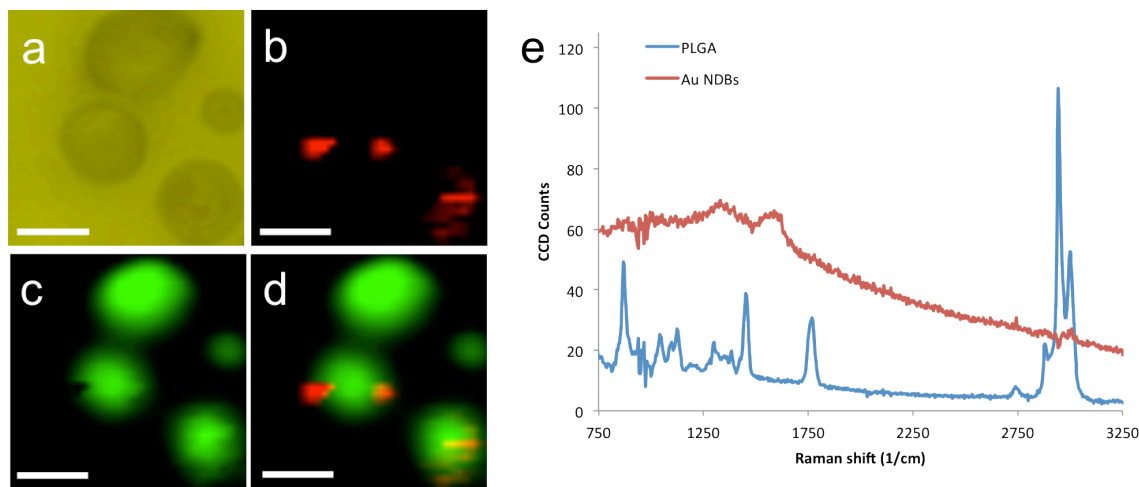


Figure 2-17. Raman confocal microscopy of Au NDB loaded PLGA carriers. (a) Bright field image. (b) Color map of Au NDB contribution to Raman spectra. (c) Color map of PLGA contribution. (d) Overlay of Au NDB and PLGA contributions. (e) Estimated pure Raman spectra of PLGA (blue) and Au NDBs (red) used in analysis. All scale bars are 2 μm .

The absolute signal of the Au NDB spectra is not significantly higher than the PLGA spectra (Figure 2-17e), which may have been expected given the hot spots on Au NDBs. However, this discrepancy may simply be accounted for by the relative amounts of Au NDBs and PLGA within a carrier – since the bulk is primarily PLGA we can expect a robust PLGA signal. Hence, if we are able to obtain a higher loading of plasmonic nanoparticles, the signal from them may increase. Unfortunately, given the intricate synthesis of these unique particles, Au NDBs are difficult to make in large quantities, and so we loaded PLGA carriers with silver nanocubes (Ag NCs). We again measured the Raman spectra over an area (Figure 2-18a), and determined pure spectra for PLGA and Ag NCs. Here, instead of confined areas, we observe rather broad distribution of Ag NCs within a microparticle, as seen in the Raman images (Figures 2-18b – 2-18d), which may be due to the extremely high loading of Ag NCs. We can also clearly see from the Raman spectra (Figure 2-18e) that the Ag NC signal is 1-2 orders of magnitude higher than the PLGA signal; so PLGA carriers with high loadings of Ag NCs may be for SERS applications.

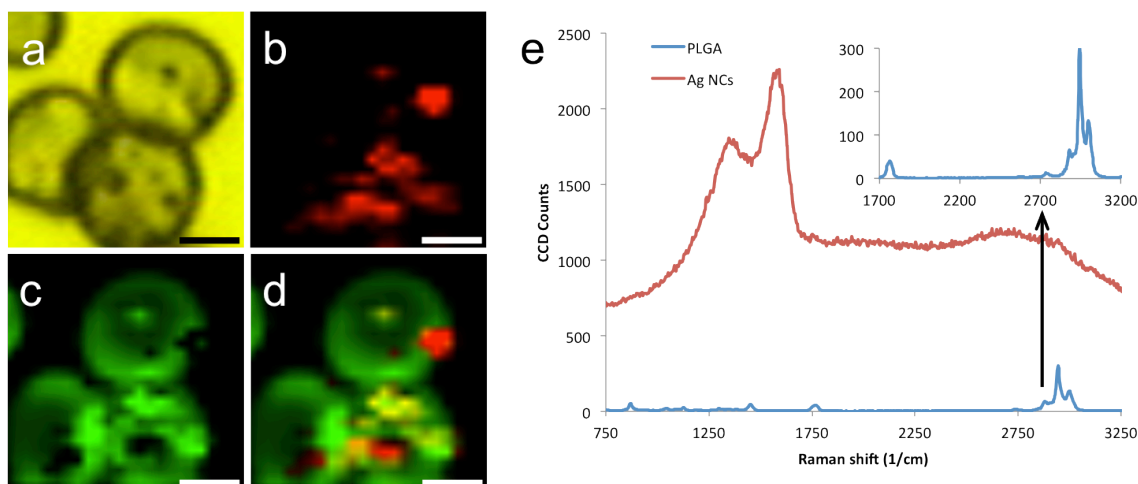


Figure 2-18. Raman confocal microscopy of Ag NC loaded PLGA carriers. (a) Bright field image. (b) Color map of Ag NC contribution to Raman spectra. (c) Color map of PLGA contribution. (d) Overlay of Ag NC and PLGA contributions. (e) Estimated pure Raman spectra of PLGA (blue) and Ag NCs (red) used in analysis (top right is zoom in of PLGA spectra). All scale bars are 5 μm .

2.3.4 Summary

Here we have demonstrated the ability of EHD co-jetting to fabricate PLGA based carriers loaded with a number of plasmonic nanoparticles, and shown that such carriers gain their SPR-associated properties. Au NR loaded carriers are able to exhibit thermal responsiveness to NIR light, with localized heat generation that can be controlled to either form bubbles or generate enough heat to shape-shift the carrier itself. Au NS and Au NDB loaded carriers exhibit ordered and disordered aggregates, respectively, confined to small areas within the carriers. Additionally, Au NDBs can be spatially located within a particle using Raman confocal microscopy. Finally, we were able to achieve high loadings of Ag NCs in PLGA carriers, as evidenced by the high Raman signal generated.

These particle systems may be further explored in great detail for a number of applications. The exact mechanism of the bubbling phenomenon must be elucidated, and may allow for more sophisticated hybrid inorganic-organic carriers with Au NRs. From a scientific perspective, the ordering of Au NSs as opposed to Au NDBs may warrant further investigation. Additionally, the potential applications of SERS is broad; given the relatively toxicity of silver nanoparticles, Ag NC loaded PLGA carriers may be a less toxic alternative for biomedical applications.

2.4 References

- 1 Mintzer, M. A. & Simanek, E. E. Nonviral Vectors for Gene Delivery. *Chem Rev* **109**, 259-302, doi:Doi 10.1021/Cr800409e (2009).
- 2 Pack, D. W., Hoffman, A. S., Pun, S. & Stayton, P. S. Design and development of polymers for gene delivery. *Nat Rev Drug Discov* **4**, 581-593, doi:Doi 10.1038/Nrd1775 (2005).
- 3 Whitehead, K. A., Langer, R. & Anderson, D. G. Knocking down barriers: advances in siRNA delivery. *Nat Rev Drug Discov* **8**, 129-138, doi:Doi 10.1038/Nrd2742 (2009).
- 4 Niidome, T. & Huang, L. Gene therapy progress and prospects: Nonviral vectors. *Gene Ther* **9**, 1647-1652, doi:Doi 10.1038/Sj.Gt.3301923 (2002).
- 5 Somiari, S. *et al.* Theory and in vivo application of electroporative gene delivery. *Mol Ther* **2**, 178-187, doi:Doi 10.1006/Mthe.2000.0124 (2000).
- 6 Fisher, K. J. *et al.* Recombinant adeno-associated virus for muscle directed gene therapy. *Nat Med* **3**, 306-312, doi:Doi 10.1038/Nm0397-306 (1997).
- 7 Kay, M. A., Glorioso, J. C. & Naldini, L. Viral vectors for gene therapy: the art of turning infectious agents into vehicles of therapeutics. *Nat Med* **7**, 33-40, doi:Doi 10.1038/83324 (2001).
- 8 Conner, S. D. & Schmid, S. L. Regulated portals of entry into the cell. *Nature* **422**, 37-44, doi:Doi 10.1038/Nature01451 (2003).
- 9 Hu, L., Mao, Z. W. & Gao, C. Y. Colloidal particles for cellular uptake and delivery. *J Mater Chem* **19**, 3108-3115, doi:Doi 10.1039/B815958k (2009).
- 10 Zhu, C. H. *et al.* Co-delivery of siRNA and paclitaxel into cancer cells by biodegradable cationic micelles based on PDMAEMA-PCL-PDMAEMA triblock copolymers. *Biomaterials* **31**, 2408-2416, doi:Doi 10.1016/J.Biomaterials.2009.11.077 (2010).
- 11 You, J. O. & Auguste, D. T. The effect of swelling and cationic character on gene transfection by pH-sensitive nanocarriers. *Biomaterials* **31**, 6859-6866, doi:Doi 10.1016/J.Biomaterials.2010.04.048 (2010).
- 12 Akinc, A., Thomas, M., Klibanov, A. M. & Langer, R. Exploring polyethylenimine-mediated DNA transfection and the proton sponge hypothesis. *J Gene Med* **7**, 657-663, doi:Doi 10.1002/Jgm.696 (2005).
- 13 Boussif, O. *et al.* A Versatile Vector for Gene and Oligonucleotide Transfer into Cells in Culture and in-Vivo - Polyethylenimine. *P Natl Acad Sci USA* **92**, 7297-7301, doi:Doi 10.1073/Pnas.92.16.7297 (1995).
- 14 Godbey, W. T., Wu, K. K. & Mikos, A. G. Poly(ethylenimine) and its role in gene delivery. *J Control Release* **60**, 149-160, doi:Doi 10.1016/S0168-3659(99)00090-5 (1999).
- 15 Vinogradov, S. V., Kohli, E. & Zeman, A. D. Comparison of nanogel drug carriers and their formulations with nucleoside 5'-triphosphates. *Pharm Res* **23**, 920-930, doi:Doi 10.1007/S11095-006-9788-5 (2006).
- 16 Bronich, T. K., Vinogradov, S. V. & Kabanov, A. V. Interaction of nanosized copolymer networks with oppositely charged amphiphilic molecules. *Nano Lett* **1**, 535-540, doi:Doi 10.1021/Nl0100365 (2001).
- 17 Santra, S., Kaittanis, C., Grimm, J. & Perez, J. M. Drug/Dye-Loaded, Multifunctional Iron Oxide Nanoparticles for Combined Targeted Cancer Therapy and Dual Optical/Magnetic Resonance Imaging. *Small* **5**, 1862-1868, doi:Doi 10.1002/Sml.200900389 (2009).

- 18 Bagalkot, V. *et al.* Quantum dot - Aptamer conjugates for synchronous cancer imaging, therapy, and sensing of drug delivery based on Bi-fluorescence resonance energy transfer. *Nano Lett* **7**, 3065-3070, doi:Doi 10.1021/NI071546n (2007).
- 19 Loo, C., Lowery, A., Halas, N. J., West, J. & Drezek, R. Immunotargeted nanoshells for integrated cancer imaging and therapy. *Nano Lett* **5**, 709-711, doi:Doi 10.1021/NI050127s (2005).
- 20 Moffatt, S., Wiehle, S. & Cristiano, R. J. A multifunctional PEI-based cationic polyplex for enhanced systemic p53-mediated gene therapy. *Gene Ther* **13**, 1512-1523, doi:Doi 10.1038/Sj.Gt.3302773 (2006).
- 21 Hubbell, J. A. Multifunctional polyplexes as locally triggerable nonviral vectors. *Gene Ther* **13**, 1371-1372, doi:Doi 10.1038/Sj.Gt.3302763 (2006).
- 22 Boeckle, S., Fahrmeir, J., Roedl, W., Ogris, M. & Wagner, E. Melittin analogs with high lytic activity at endosomal pH enhance transfection with purified targeted PEI polyplexes. *J Control Release* **112**, 240-248, doi:Doi 10.1016/J.jconrel.2006.02.002 (2006).
- 23 Wagner, E. Strategies to improve DNA polyplexes for in vivo gene transfer: Will "artificial viruses" be the answer? *Pharm Res* **21**, 8-14, doi:Doi 10.1023/B:Pham.0000012146.04068.56 (2004).
- 24 Desai, M. P., Labhasetwar, V., Walter, E., Levy, R. J. & Amidon, G. L. The mechanism of uptake of biodegradable microparticles in Caco-2 cells is size dependent. *Pharm Res* **14**, 1568-1573, doi:Doi 10.1023/A:1012126301290 (1997).
- 25 Cartiera, M. S., Johnson, K. M., Rajendran, V., Caplan, M. J. & Saltzman, W. M. The uptake and intracellular fate of PLGA nanoparticles in epithelial cells. *Biomaterials* **30**, 2790-2798, doi:Doi 10.1016/J.Biomaterials.2009.01.057 (2009).
- 26 Win, K. Y. & Feng, S. S. Effects of particle size and surface coating on cellular uptake of polymeric nanoparticles for oral delivery of anticancer drugs. *Biomaterials* **26**, 2713-2722, doi:Doi 10.1016/J.Biomaterials.2004.07.050 (2005).
- 27 Roh, K. H., Martin, D. C. & Lahann, J. Biphasic Janus particles with nanoscale anisotropy. *Nature materials* **4**, 759-763, doi:Doi 10.1038/Nmat1486 (2005).
- 28 Roh, K. H., Martin, D. C. & Lahann, J. Triphasic nanocolloids. *J Am Chem Soc* **128**, 6796-6797, doi:Doi 10.1021/Ja060836n (2006).
- 29 Lee, K. J., Yoon, J. & Lahann, J. Recent advances with anisotropic particles. *Curr Opin Colloid In* **16**, 195-202, doi:Doi 10.1016/J.Cocis.2010.11.004 (2011).
- 30 Bhaskar, S., Pollock, K. M., Yoshida, M. & Lahann, J. Towards Designer Microparticles: Simultaneous Control of Anisotropy, Shape, and Size. *Small* **6**, 404-411, doi:Doi 10.1002/Sml.200901306 (2010).
- 31 Lim, D. W., Hwang, S., Uzun, O., Stellacci, F. & Lahann, J. Compartmentalization of Gold Nanocrystals in Polymer Microparticles using Electrohydrodynamic Co-Jetting. *Macromolecular rapid communications* **31**, 176-182, doi:Doi 10.1002/Marc.200900597 (2010).
- 32 Hwang, S. *et al.* Anisotropic hybrid particles based on electrohydrodynamic co-jetting of nanoparticle suspensions. *Physical Chemistry Chemical Physics* **12**, 11894-11899, doi:Doi 10.1039/C0cp00264j (2010).
- 33 Govender, T., Stolnik, S., Garnett, M. C., Illum, L. & Davis, S. S. PLGA nanoparticles prepared by nanoprecipitation: drug loading and release studies of a water soluble drug. *J Control Release* **57**, 171-185, doi:Doi 10.1016/S0168-3659(98)00116-3 (1999).
- 34 Lin, R. Y., Ng, L. S. & Wang, C. H. In vitro study of anticancer drug doxorubicin in PLGA-based microparticles. *Biomaterials* **26**, 4476-4485, doi:Doi 10.1016/J.Biomaterials.2004.11.014 (2005).

- 35 Betancourt, T., Brown, B. & Brannon-Peppas, L. Doxorubicin-loaded PLGA nanoparticles by nanoprecipitation: preparation, characterization and in vitro evaluation. *Nanomedicine-Uk* **2**, 219-232, doi:Doi 10.2217/17435889.2.2.219 (2007).
- 36 Suh, J., Paik, H. J. & Hwang, B. K. Ionization of Poly(Ethylenimine) and Poly(Allylamine) at Various Phs. *Bioorg Chem* **22**, 318-327, doi:Doi 10.1006/Bioo.1994.1025 (1994).
- 37 Behr, J. P. The proton sponge: A trick to enter cells the viruses did not exploit. *Chimia* **51**, 34-36 (1997).
- 38 Panyam, J. & Labhasetwar, V. Dynamics of endocytosis and exocytosis of poly(D,L-lactide-co-glycolide) nanoparticles in vascular smooth muscle cells. *Pharm Res* **20**, 212-220, doi:Doi 10.1023/A:1022219003551 (2003).
- 39 Lv, H. T., Zhang, S. B., Wang, B., Cui, S. H. & Yan, J. Toxicity of cationic lipids and cationic polymers in gene delivery. *J Control Release* **114**, 100-109, doi:Doi 10.1016/J.jconrel.2006.04.014 (2006).
- 40 Zintchenko, A., Philipp, A., Dehshahri, A. & Wagner, E. Simple modifications of branched PEI lead to highly efficient siRNA carriers with low toxicity. *Bioconjugate Chem* **19**, 1448-1455, doi:Doi 10.1021/Bc800065f (2008).
- 41 Thomas, M., Ge, Q., Lu, J. J., Chen, J. Z. & Klivanov, A. M. Cross-linked small polyethylenimines: While still nontoxic, deliver DNA efficiently to mammalian cells in vitro and in vivo. *Pharm Res* **22**, 373-380, doi:Doi 10.1007/S11095-004-1874-Y (2005).
- 42 Goldin, A. & Mantel, N. The Employment of Combination of Drugs in the Chemotherapy of Neoplasia - a Review. *Cancer Res* **17**, 635-654 (1957).
- 43 Chou, T. C. Drug Combination Studies and Their Synergy Quantification Using the Chou-Talalay Method. *Cancer Res* **70**, 440-446, doi:Doi 10.1158/0008-5472.Can-09-1947 (2010).
- 44 Chou, L. Y. T., Ming, K. & Chan, W. C. W. Strategies for the intracellular delivery of nanoparticles. *Chem Soc Rev* **40**, 233-245, doi:Doi 10.1039/C0cs00003e (2011).
- 45 Sonawane, N. D., Szoka, F. C. & Verkman, A. S. Chloride accumulation and swelling in endosomes enhances DNA transfer by polyamine-DNA polyplexes. *J Biol Chem* **278**, 44826-44831, doi:Doi 10.1074/Jbc.M308643200 (2003).
- 46 Yang, C. *et al.* Mitigated Cytotoxicity and Tremendously Enhanced Gene Transfection Efficiency of PEI through Facile One-Step Carbamate Modification. *Adv Health Mater* **2**, 1304-1308, doi:Doi 10.1002/Adhm.201300046 (2013).
- 47 Misra, A. C., Bhaskar, S., Clay, N. & Lahann, J. Multicompartmental Particles for Combined Imaging and siRNA Delivery. *Advanced Materials* **24**, 3850-3856, doi:Doi 10.1002/Adma.201200372 (2012).
- 48 Erbacher, P. *et al.* Transfection and physical properties of various saccharide, poly(ethylene glycol), and antibody-derivatized polyethylenimines (PEI). *J Gene Med* **1**, 210-222 (1999).
- 49 Malek, A., Czubayko, F. & Aigner, A. PEG grafting of polyethylenimine (PEI) exerts different effects on DNA transfection and siRNA-induced gene targeting efficacy. *J Drug Target* **16**, 124-139, doi:10.1080/10611860701849058 (2008).
- 50 Kim, S. H., Mok, H., Jeong, J. H., Kim, S. W. & Park, T. G. Comparative evaluation of target-specific GFP gene silencing efficiencies for antisense ODN, synthetic siRNA, and siRNA plasmid complexed with PEI-PEG-FOL conjugate. *Bioconjugate Chem* **17**, 241-244, doi:Doi 10.1021/Bc050289f (2006).

- 51 Liang, B. *et al.* Synthesis and characterization of folate-PEG-grafted-hyperbranched-PEI for tumor-targeted gene delivery. *Biochem Bioph Res Co* **367**, 874-880, doi:Doi 10.1016/J.Bbrc.2008.01.024 (2008).
- 52 Augst, A. D., Kong, H. J. & Mooney, D. J. Alginate hydrogels as biomaterials. *Macromol Biosci* **6**, 623-633, doi:Doi 10.1002/Mabi.200600069 (2006).
- 53 Yang, J. S., Xie, Y. J. & He, W. Research progress on chemical modification of alginate: A review. *Carbohydr Polym* **84**, 33-39, doi:Doi 10.1016/J.Carbpol.2010.11.048 (2011).
- 54 Pawar, S. N. & Edgar, K. J. Alginate derivatization: A review of chemistry, properties and applications. *Biomaterials* **33**, 3279-3305, doi:Doi 10.1016/J.Biomaterials.2012.01.007 (2012).
- 55 Babak, V. G. *et al.* Hydrophobically associating alginate derivatives: Surface tension properties of their mixed aqueous solutions with oppositely charged surfactants. *J Colloid Interf Sci* **225**, 505-510, doi:Doi 10.1006/Jcis.2000.6788 (2000).
- 56 Leonard, M., De Boissesson, A. R., Hubert, P., Dalencon, F. & Dellacherie, E. Hydrophobically modified alginate hydrogels as protein carriers with specific controlled release properties. *J Control Release* **98**, 395-405, doi:Doi 10.1016/J.Jconrel.2004.05.009 (2004).
- 57 Pawar, S. N. & Edgar, K. J. Chemical Modification of Alginates in Organic Solvent Systems. *Biomacromolecules* **12**, 4095-4103, doi:Doi 10.1021/Bm201152a (2011).
- 58 Pawar, S. N. & Edgar, K. J. Alginate esters via chemoselective carboxyl group modification. *Carbohydr Polym* **98**, 1288-1296, doi:Doi 10.1016/J.Carbpol.2013.08.014 (2013).
- 59 Yoo, H. S., Lee, J. E., Chung, H., Kwon, I. C. & Jeong, S. Y. Self-assembled nanoparticles containing hydrophobically modified glycol chitosan for gene delivery. *J Control Release* **103**, 235-243, doi:Doi 10.1016/J.Jconrel.2004.11.033 (2005).
- 60 Vanoss, C. J., Arnold, K., Good, R. J., Gawrisch, K. & Ohki, S. Interfacial-Tension and the Osmotic-Pressure of Solutions of Polar Polymers. *J Macromol Sci Chem* **A27**, 563-580 (1990).
- 61 Cohen, J. A., Podgornik, R., Hansen, P. L. & Parsegian, V. A. A Phenomenological One-Parameter Equation of State for Osmotic Pressures of PEG and Other Neutral Flexible Polymers in Good Solvents. *J Phys Chem B* **113**, 3709-3714, doi:Doi 10.1021/Jp806893a (2009).
- 62 Stubbe, B. G. *et al.* Tailoring the swelling pressure of degrading dextran hydroxyethyl methacrylate hydrogels. *Biomacromolecules* **4**, 691-695, doi:Doi 10.1021/Bm020129w (2003).
- 63 Kany, H. P., Hasse, H. & Maurer, G. Thermodynamic properties of aqueous dextran solutions from laser-light-scattering, membrane osmometry, and isopiestic measurements. *J Chem Eng Data* **44**, 230-242, doi:Doi 10.1021/Je980193u (1999).
- 64 Temenoff, J. S., Athanasiou, K. A., LeBaron, R. G. & Mikos, A. G. Effect of poly(ethylene glycol) molecular weight on tensile and swelling properties of oligo(poly(ethylene glycol) fumarate) hydrogels for cartilage tissue engineering. *J Biomed Mater Res* **59**, 429-437, doi:Doi 10.1002/Jbm.1259 (2002).
- 65 Kim, S. W., Bae, Y. H. & Okano, T. Hydrogels - Swelling, Drug Loading, and Release. *Pharm Res* **9**, 283-290, doi:Doi 10.1023/A:1015887213431 (1992).
- 66 Brannonpeppas, L. & Peppas, N. A. Equilibrium Swelling Behavior of Ph-Sensitive Hydrogels. *Chem Eng Sci* **46**, 715-722, doi:Doi 10.1016/0009-2509(91)80177-Z (1991).

- 67 Guner, A. & Kibarar, G. The important role of thermodynamic interaction parameter in the determination of theta temperature, dextran/water system. *Eur Polym J* **37**, 619-622, doi:Doi 10.1016/S0014-3057(00)00152-X (2001).
- 68 van Oss, C. J. Development and applications of the interfacial tension between water and organic or biological surfaces. *Colloid Surface B* **54**, 2-9, doi:Doi 10.1016/J.Colsurfb.2006.05.024 (2007).
- 69 Bachelder, E. M., Beaudette, T. T., Broaders, K. E., Dashe, J. & Frechet, J. M. J. Acetal-derivatized dextran: An acid-responsive biodegradable material for therapeutic applications. *J Am Chem Soc* **130**, 10494-+, doi:Doi 10.1021/Ja803947s (2008).
- 70 Broaders, K. E., Cohen, J. A., Beaudette, T. T., Bachelder, E. M. & Frechet, J. M. J. Acetalated dextran is a chemically and biologically tunable material for particulate immunotherapy. *P Natl Acad Sci USA* **106**, 5497-5502, doi:Doi 10.1073/Pnas.0901592106 (2009).
- 71 Li, Y. L. *et al.* Reversibly Stabilized Multifunctional Dextran Nanoparticles Efficiently Deliver Doxorubicin into the Nuclei of Cancer Cells. *Angew Chem Int Edit* **48**, 9914-9918, doi:Doi 10.1002/Anie.200904260 (2009).
- 72 Levine, M. *et al.* Vitamin C pharmacokinetics in healthy volunteers: Evidence for a recommended dietary allowance. *P Natl Acad Sci USA* **93**, 3704-3709, doi:Doi 10.1073/Pnas.93.8.3704 (1996).
- 73 Mirvish, S. S. Blocking Formation of N-Nitroso Compounds with Ascorbic-Acid In Vitro and In Vivo. *Ann Ny Acad Sci* **258**, 175-180, doi:Doi 10.1111/J.1749-6632.1975.Tb29277.X (1975).
- 74 Hathcock, J. N. *et al.* Vitamins E and C are safe across a broad range of intakes. *Am J Clin Nutr* **81**, 736-745 (2005).
- 75 Wong, K. *et al.* PEI-g-chitosan, a novel gene delivery system with transfection efficiency comparable to polyethylenimine in vitro and after liver administration in vivo. *Bioconjugate Chem* **17**, 152-158, doi:Doi 10.1021/Bc0501597 (2006).
- 76 Gao, J. Q. *et al.* Gene-carried chitosan-linked-PEI induced high gene transfection efficiency with low toxicity and significant tumor-suppressive activity. *Int J Pharm* **387**, 286-294, doi:Doi 10.1016/J.Ijpharm.2009.12.033 (2010).
- 77 Eustis, S. & El-Sayed, M. A. Why gold nanoparticles are more precious than pretty gold: Noble metal surface plasmon resonance and its enhancement of the radiative and nonradiative properties of nanocrystals of different shapes. *Chem Soc Rev* **35**, 209-217, doi:Doi 10.1039/B514191e (2006).
- 78 Willets, K. A. & Van Duyne, R. P. Localized surface plasmon resonance spectroscopy and sensing. *Annu Rev Phys Chem* **58**, 267-297, doi:Doi 10.1146/Annurev.Physchem.58.032806.104607 (2007).
- 79 Jain, P. K., Huang, X., El-Sayed, I. H. & El-Sayed, M. A. Review of some interesting surface plasmon resonance-enhanced properties of noble metal nanoparticles and their applications to biosystems. *Plasmonics* **2**, 107-118, doi:Doi 10.1007/S11468-007-9031-1 (2007).
- 80 Khlebtsov, N. G. & Dykman, L. A. Optical properties and biomedical applications of plasmonic nanoparticles. *J Quant Spectrosc Ra* **111**, 1-35, doi:Doi 10.1016/J.Jqsrt.2009.07.012 (2010).
- 81 Huang, X. H., El-Sayed, I. H., Qian, W. & El-Sayed, M. A. Cancer cell imaging and photothermal therapy in the near-infrared region by using gold nanorods. *J Am Chem Soc* **128**, 2115-2120, doi:Doi 10.1021/Ja057254a (2006).
- 82 Kuo, W. S. *et al.* Gold Nanorods in Photodynamic Therapy, as Hyperthermia Agents, and in Near-Infrared Optical Imaging. *Angew Chem Int Edit* **49**, 2711-2715, doi:Doi 10.1002/Anie.200906927 (2010).

- 83 von Maltzahn, G. *et al.* Computationally Guided Photothermal Tumor Therapy Using Long-Circulating Gold Nanorod Antennas. *Cancer Res* **69**, 3892-3900, doi:Doi 10.1158/0008-5472.Can-08-4242 (2009).
- 84 von Maltzahn, G. *et al.* SERS-Coded Gold Nanorods as a Multifunctional Platform for Densely Multiplexed Near-infrared Imaging and Photothermal Heating. *Advanced Materials* **21**, 3175-+, doi:Doi 10.1002/Adma.200803464 (2009).
- 85 Agarwal, A. *et al.* Targeted gold nanorod contrast agent for prostate cancer detection by photoacoustic imaging. *J Appl Phys* **102**, doi:Artn 064701
Doi 10.1063/1.2777127 (2007).
- 86 Kim, K. *et al.* Photoacoustic imaging of early inflammatory response using gold nanorods. *Appl Phys Lett* **90**, doi:Artn 223901
Doi 10.1063/1.2743752 (2007).
- 87 Li, P. C. *et al.* Photoacoustic imaging of multiple targets using gold nanorods. *IEEE T Ultrason Ferr* **54**, 1642-1647, doi:Doi 10.1109/Tuffc.2007.435 (2007).
- 88 Anker, J. N. *et al.* Biosensing with plasmonic nanosensors. *Nature materials* **7**, 442-453, doi:Doi 10.1038/Nmat2162 (2008).
- 89 Becker, J., Trugler, A., Jakab, A., Hohenester, U. & Sonnichsen, C. The Optimal Aspect Ratio of Gold Nanorods for Plasmonic Bio-sensing. *Plasmonics* **5**, 161-167, doi:Doi 10.1007/S11468-010-9130-2 (2010).
- 90 Dondapati, S. K. *et al.* Label-free Biosensing Based on Single Gold Nanostars as Plasmonic Transducers. *ACS nano* **4**, 6318-6322, doi:Doi 10.1021/Nn100760f (2010).
- 91 Mulvihill, M. J., Ling, X. Y., Henzie, J. & Yang, P. D. Anisotropic Etching of Silver Nanoparticles for Plasmonic Structures Capable of Single-Particle SERS. *J Am Chem Soc* **132**, 268-274, doi:Doi 10.1021/Ja906954f (2010).
- 92 Potara, M., Gabudean, A. M. & Astilean, S. Solution-phase, dual LSPR-SERS plasmonic sensors of high sensitivity and stability based on chitosan-coated anisotropic silver nanoparticles. *J Mater Chem* **21**, 3625-3633, doi:Doi 10.1039/C0jm03329d (2011).
- 93 Qian, X. M. *et al.* In vivo tumor targeting and spectroscopic detection with surface-enhanced Raman nanoparticle tags. *Nat Biotechnol* **26**, 83-90, doi:Doi 10.1038/Nbt1377 (2008).
- 94 Qian, X. M. & Nie, S. M. Single-molecule and single-nanoparticle SERS: from fundamental mechanisms to biomedical applications. *Chem Soc Rev* **37**, 912-920, doi:Doi 10.1039/B708839f (2008).
- 95 Keren, S. *et al.* Noninvasive molecular imaging of small living subjects using Raman spectroscopy. *P Natl Acad Sci USA* **105**, 5844-5849, doi:Doi 10.1073/Pnas.0710575105 (2008).
- 96 Jackson, J. B. & Halas, N. J. Surface-enhanced Raman scattering on tunable plasmonic nanoparticle substrates. *P Natl Acad Sci USA* **101**, 17930-17935, doi:Doi 10.1073/Pnas.0408319102 (2004).
- 97 Lv, W. P. *et al.* Anisotropic Janus Catalysts for Spatially Controlled Chemical Reactions. *Small* **8**, 3116-3122, doi:Doi 10.1002/Sml.201200192 (2012).
- 98 Bhaskar, S., Hitt, J., Chang, S. W. L. & Lahann, J. Multicompartmental Microcylinders. *Angew Chem Int Edit* **48**, 4589-4593, doi:Doi 10.1002/Anie.200806241 (2009).
- 99 Saha, S. *et al.* Chemically Controlled Bending of Compositionally Anisotropic Microcylinders. *Angew Chem Int Edit* **51**, 660-665, doi:Doi 10.1002/Anie.201105387 (2012).
- 100 Lee, K. J. *et al.* Spontaneous shape reconfigurations in multicompartmental microcylinders. *P Natl Acad Sci USA* **109**, 16057-16062, doi:Doi 10.1073/Pnas.1213669109 (2012).

- 101 Sokolovskaya, E., Yoon, J., Misra, A. C., Brase, S. & Lahann, J. Controlled Microstructuring of Janus Particles Based on a Multifunctional Poly(ethylene glycol). *Macromolecular rapid communications* **34**, 1554-1559, doi:Doi 10.1002/Marc.201300427 (2013).
- 102 Rahmani, S. *et al.* Chemically Orthogonal Three-Patch Microparticles. *Angew Chem Int Edit* **53**, 2332-2338, doi:Doi 10.1002/Anie.201310727 (2014).
- 103 Langford, V. S., McKinley, A. J. & Quickenden, T. I. Temperature dependence of the visible-near-infrared absorption spectrum of liquid water. *J Phys Chem A* **105**, 8916-8921, doi:Doi 10.1021/Jp010093m (2001).
- 104 Gulsoy, M., Dereli, Z., Tabakoglu, H. O. & Bozkulak, O. Closure of skin incisions by 980-nm diode laser welding. *Laser Med Sci* **21**, 5-10, doi:Doi 10.1007/S10103-006-0375-0 (2006).
- 105 Tabakoglu, H. O., Topaloglu, N. & Gulsoy, M. The Effect of Irradiance Level in 980-nm Diode Laser Skin Welding. *Photomed Laser Surg* **28**, 453-458, doi:Doi 10.1089/Pho.2009.2569 (2010).
- 106 Viger, M. L. *et al.* Near-infrared-induced heating of confined water in polymeric particles for efficient payload release. *ACS nano* **8**, 4815-4826, doi:10.1021/nn500702g (2014).
- 107 Grzelczak, M. *et al.* Influence of Iodide Ions on the Growth of Gold Nanorods: Tuning Tip Curvature and Surface Plasmon Resonance. *Adv Funct Mater* **18**, 3780-3786, doi:Doi 10.1002/Adfm.200800706 (2008).
- 108 Rodriguez-Gonzalez, B. *et al.* Surface Plasmon Mapping of Dumbbell-Shaped Gold Nanorods: The Effect of Silver Coating. *Langmuir* **28**, 9063-9070, doi:Doi 10.1021/La300269n (2012).
- 109 Alvarez-Puebla, R. A. & Liz-Marzan, L. M. Traps and cages for universal SERS detection. *Chem Soc Rev* **41**, 43-51, doi:Doi 10.1039/C1cs15155j (2012).
- 110 Abalde-Cela, S. *et al.* Surface-enhanced Raman scattering biomedical applications of plasmonic colloidal particles. *J R Soc Interface* **7**, S435-S450, doi:Doi 10.1098/Rsif.2010.0125.Focus (2010).

Chapter 3

Carriers with Targeting Capabilities

Part of the material in this chapter has been adapted with modifications from the following article:

A. C. Misra, T.-H. Park, R. P. Carney, F. Stellacci, J. Lahann. "Virus-Mimicking Particles with Compositionally Anisotropic Surfaces." *In Preparation*.

3.1 Targeting Cell Membranes with Virus-mimicking Particles

3.1.1 Background and Motivation

Nature provides excellent examples of efficient delivery vehicles optimized through millions of years of evolution. For example, a virus, composed of elegantly few components, is able to transfect a host and hijack its physiology with exceptionally high efficiency. Viruses can display specific anisotropic envelopes and surface properties that allow them to selectively bind to and fuse with cellular membranes.¹⁻⁵ These astonishing targeting properties may be linked to hierarchical organization of proteins with both hydrophobic and hydrophilic domains.⁵⁻⁸ Synthetic materials have been able to mimic some of these specific properties.^{5,6,9-14} For example, polyethylene glycol (PEG) is a synthetic polymer that prevents protein adsorption and cell adhesion, much like some hydrophilic polysaccharides.⁹⁻¹³ On the other hand, gold nanoparticles (AuNPs) with a striped surface of alternating hydrophobic and hydrophilic stabilizing ligands can directly traverse the cell membrane and enter the cytosol without accumulation in endosomes, a hallmark of some cell-penetrating peptides.^{5,6,14}

While it has been shown that synthetic materials can imitate aspects of nature, it is still quite difficult to construct functional devices that can mimic entire viruses. One of the challenges in achieving this goal is ability to control three-dimensional architecture, and in particular, anisotropy, as virtuously as nature. For example, some particles have been

developed to mimic a virus' ability to interact intimately with cells, in some cases binding to the cell membrane.^{15,16} However, these particles often contain non-synthetic materials such as proteins, which come with their own challenges regarding material's integration and scale up. Additionally, for medical applications, proteins can cause immunogenic responses in in vivo settings.^{17,18} Hence, there is a potential to vastly improve the functionality of synthetic particles by more closely mirroring the anisotropic architecture of viruses.

Electrohydrodynamic (EHD) co-jetting is a process that allows for fabrication of particulate carriers with spatially and temporally controllable composition and function.¹⁹⁻³³ Since the spatial composition of the particles is controlled, topological control of the particle surface may be achieved by incorporation of chemically functional materials.^{19,26,34-37} Selective surface modification of particles fabricated by EHD co-jetting has been demonstrated using several different chemistries, including bio-orthogonal click reactions.^{26,37} A variety of molecules have been selectively conjugated to a particular area on a surface, including dyes and peptides.^{19,36} Macromolecules and polymers may also be selectively grafted from or on a selected portion of the surface.^{26,35}

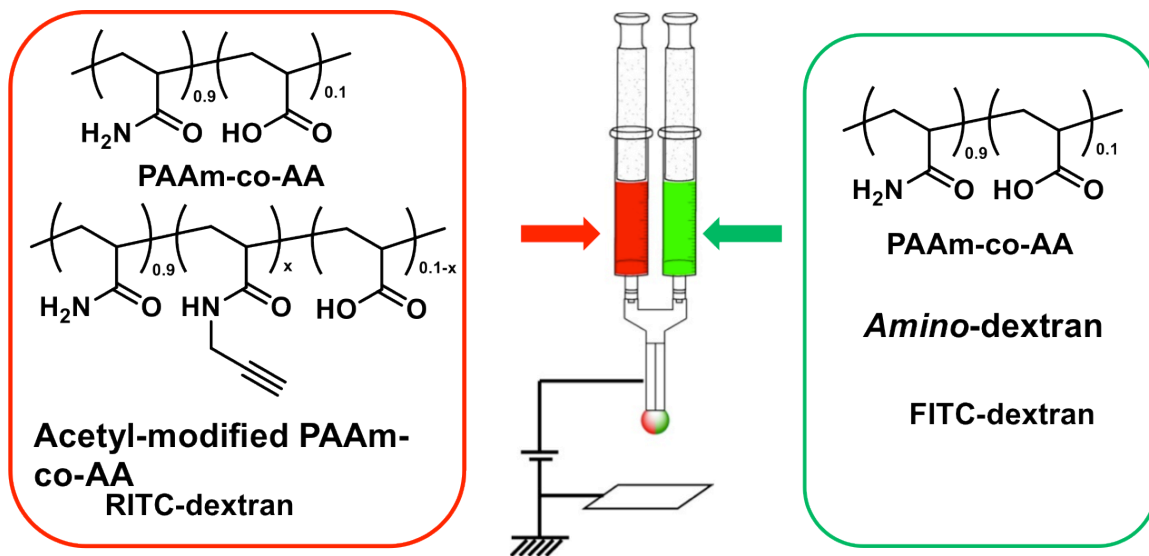


Figure 3-1. Schematic showing the EHD co-jetting process and fabrication of the particles.

We now exploit our ability to fabricate such chemically functionalized particles in order to manipulate particle surfaces in a spatially anisotropic manner, so as to resemble the natural architecture of viruses. In this case, we designed particles that mimic viruses' ability to selectively bind to cell membranes. For this purpose, we manufacture polymeric particles

containing two different chemically reactive polymers that may undergo reactions orthogonal to one another (Figure 3-1). Half of the surface is conjugated with striped AuNPs that are able to penetrate through cell membranes,³⁸ while the other half is coated with PEG, which is known to prevent protein and cell adhesion.¹⁰⁻¹² Our hypothesis is that this balance of cell binding affinities would result in the particles being confined to the cell membranes when incubated with cells. Here we prove this hypothesis in an in vitro setting using hierarchically functionalized bicompartamental particles and demonstrate that this anisotropic particle design is a necessary feature for cell membrane targeting.

3.1.2 Methods

Materials. Poly(acrylamide-co-acrylic acid, sodium salts) (PAAm-co-AA) (MW 200 kD, 10% acrylic acid residues) was purchased from Polysciences (PA, USA). Amino dextran (MW 70 kD) was purchased from Molecular Probes (Oregon, USA). Rhodamine B isothiocyanate conjugated dextran (RITC-dextran, MW 70 kD) and fluorescein isothiocyanate conjugated dextran (FITC-dextran, MW 70 kD) were purchased from Sigma Aldrich. Acetylene-modified PAAm-co-AA was synthesized as described previously.³⁵ Synthesis of azide-functionalized striped and control gold nanoparticles have been described previously by the Stellacci group.³⁸ MDA-MB-231/GFP cells were obtained from Cell Biolabs, Inc. All cell culture materials were purchased from Invitrogen.

Fabrication of Bicompartamental Particles. The preparation of bicompartamental PAAm-co-AA particles was slightly modified from the method previously described.^{19,20,39} One solution was prepared by dissolving 50 mg PAAm-co-AA, 10 mg acetylene-modified PAAm-co-AA, and 2 mg of RITC-dextran in 1 mL of H₂O. The other jetting solution was made by dissolving 50 mg PAAm-co-AA, 10 mg amino-dextran, and 2 mg of FITC-dextran. Both solutions were stirred overnight. The prepared jetting solutions were loaded to two 1-mL syringes and set up side-by-side. A dual channel needle with two 26 gauge tips and 3.25 inch in length (Fibrijets SA-0105, Micromedics, Inc., MN, USA) was connected to the syringes. The flow rates of the two solutions were simultaneously controlled by a single syringe pump (0.2–0.25 mL/h). A voltage around 15-18 kV was applied to the needles using a high potential generator (ES30P, Gamma High Voltage Research, Inc., USA) and the ground was connected to a piece of aluminium foil as a collecting substrate at a 25 cm distance from the end of

needle. After EHD co-jetting, the particles were thermally crosslinked at 175 °C for 3 hrs. The final product (particle 1) was collected as a powder.

Surface Modification of Bicompartamental Particles. 5 mg of bicompartamental particles and 20 mg of PEG-NHS were added to 0.5 mL H₂O and the mixture was stirred for 3 hrs. The suspension was centrifuged and the supernatant was removed. The particles were washed via two cycles of redispersion in fresh water and centrifugation. These particles were freeze-dried using a Labconco Freezone 4.5 to obtain particle 2. After the washing procedure, 1 mg of N₃-functionalized AuNPs (unstructured to obtain particle 3, striped to obtain VMPs), 0.2 mL of 0.03 M CuSO₄ (aq) and 0.2 mL H₂O was added to the PEGylated particles. Finally, 20 mg of sodium ascorbate was added and the suspension was agitated for 3 hrs. The mixture was centrifuged and the supernatant was removed. The residue was washed with water two times, 0.03 M Na₂EDTA·2H₂O (aq) three times, and water three times. The anisotropically functionalized bicompartamental particles were collected after freeze-drying.

Particle Characterization. An Olympus FluoView 500 Confocal Laser Scanning Microscopes (CLSM) was used to examine the compartmentalized fluorescence distributions of the anisotropic particles prepared in this study. Ar/ArKr laser ($\lambda = 488$ nm) and GreNe laser ($\lambda = 543$ nm) were used to excite FITC and rhodamine B, respectively. The emission wavelength ranges collected were 508–523 nm for FITC and 580–595 nm for rhodamine B. Transmission electron microscopy (TEM, JEOL 3011) was employed for the microscopic imaging of bicompartamental particles using a copper TEM grid coated with a carbon film (400 meshes, Ted Pella). Cells were imaged by scanning electron microscopy (SEM) using an AMRAY 1910 Field Emission Scanning Electron Microscope.

Cell culture. MDA-MB-231/GFP cells were grown in Dulbecco's Modified Eagle Medium (DMEM) supplemented with 10% fetal bovine serum (FBS), 1X non-essential amino acids (NEAA), and 1X penicillin-streptomycin. All in vitro experiments were done using cells that had been passaged no more than seven times.

In vitro particle incubation experiments. Cells were seeded at 50,000 cells/well on circular glass coverslips in 12-well plates and incubated at 37 °C overnight. Media was exchanged

with particles in media at a given concentration, and incubated at 37 °C for a designated amount of time. After incubation, cells were washed with PBS 2-3 times, and then fixed with either 4% paraformaldehyde (for confocal imaging) or 2.5% glutaraldehyde (for SEM) for 30 minutes. For confocal, coverslips were washed with PBS once more, mounted on glass slides with ProLong Gold, and subsequently imaged using the Olympus FluoView 500 CLSM. For SEM, cell samples were prepared after glutaraldehyde fixing by sequential ethanol washing to remove water – cells were incubated sequentially with 10%, 30%, 50%, 70%, 90% (2x), and 100% (2x) ethanol in water solutions for 5-10 minutes at each concentration. Cells were then washed and incubated with HMDS; HMDS was exchanged twice after 5-10 minute intervals and the final HMDS was allowed to evaporate overnight (critical point drying) in a laminar flow hood. Cell samples were then gold sputter-coated and imaged using the AMRAY SEM.

Clustering analysis. Using MATLAB, K-mean clustering was performed on the coordinates of particles determined by image processing of the red fluorescent confocal images. Optimal number of clusters K was determined for each image by choosing K with the highest mean silhouette number, exploring K between 2-25.

3.1.3 Results and Discussion

Fabrication and characterization. Bicompartamental particles were fabricated through EHD co-jetting of two different polymer solutions of polyacrylamide/poly(acrylic acid) copolymers (PAAm-co-AA) containing PAAm-co-AA modified with acetylene groups³⁵ in one side and dextran modified with amine groups in the other. These functional additives enable surface functionalization via chemical coupling reactions with functional materials. Fluorescein isothiocyanate (FITC)- and rhodamine-tagged dextrans were further added to the respective jetting solutions to enable characterization of the particle compartmentalization using confocal laser scanning microscopy (CLSM).³⁹

The hierarchical assembly of virus-mimicking particles (VMPs) was achieved by first conjugating PEG on one half of the surface. The amine groups of the particle hemisphere were reacted with N-hydroxylsuccinimide-functionalized polyethylene glycol (PEG-NHS). Then the acetylene groups on the other hemisphere surface were selectively conjugated with azide-functionalized striped gold nanoparticles via Huisgen 1,3-dipolar cycloaddition,

resulting in VMPs (particle 4) that are anisotropically decorated with cell-penetrating nanoparticles on the hemisphere surface and cell-repelling brushes on the other surface (Figure 3-2a). Note that the bicompartamental architecture of the particles is intact throughout the surface elaboration, as confirmed by CLSM (Figure 3-2b).

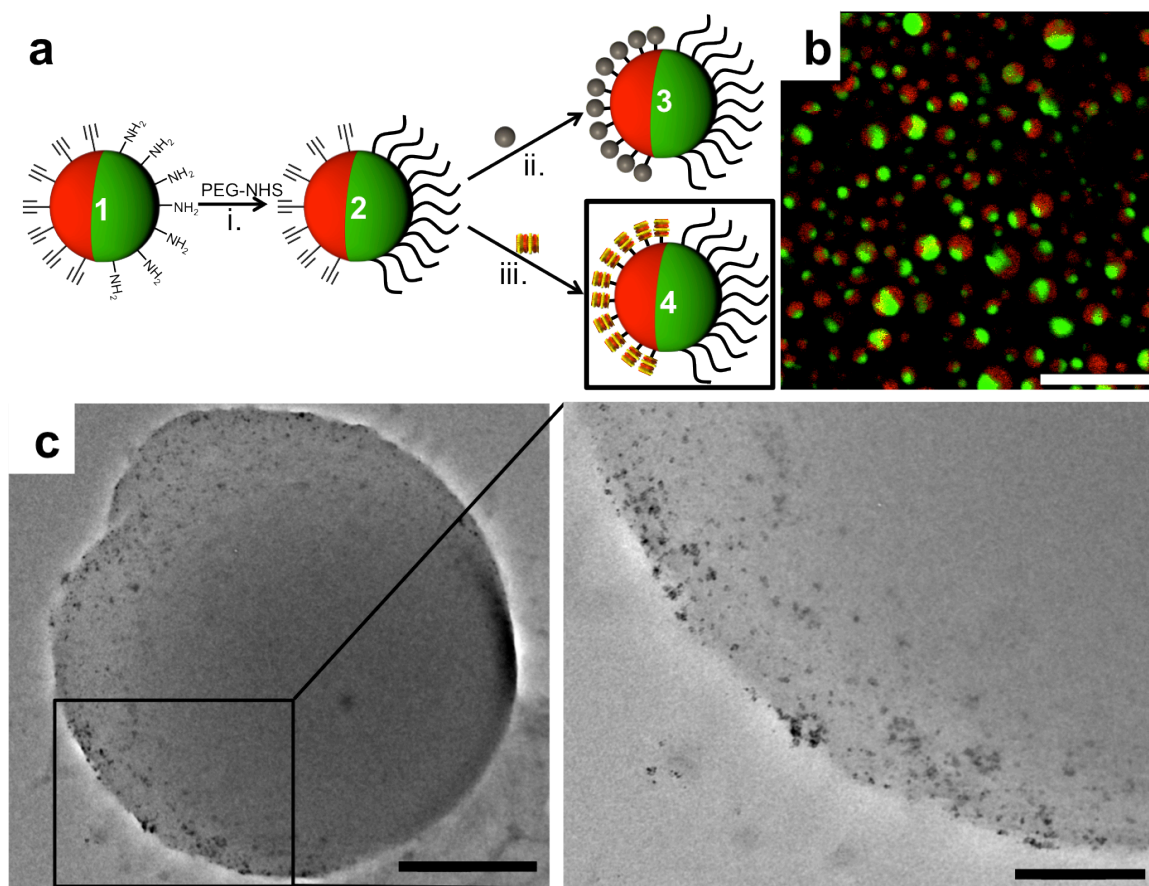


Figure 3-2. (a) Design and synthesis scheme of control particles (1-3) and virus-mimicking particles, VMPs (4). (b) Fluorescent CLSM overlay image of VMPs demonstrating their bicompartamental architecture. Scale bar is 20 μm . (c) TEM image of a VMP (with a magnified image of it on the right), showing selective surface modification with striped gold nanoparticles on one side of the particle surface. Scale bars are 500 nm for the left TEM image, and 200 nm for the right TEM image.

Since the acetyl-functionalized copolymer and amino-dextran are localized in their respective compartments, the surface-functionalization of these particles should be specific to their corresponding surfaces, which is evidenced by tunneling electron microscopy (TEM) showing AuNPs that are selectively on one side of the surface (Figure 3-2c). For comparison, we also synthesized differently functionalized bicompartamental particles (1-3). As illustrated in Figure 1a, particle 1 was prepared by jetting and subsequently thermally

crosslinking. Particle 2 was prepared by PEGylation on the amine side of particle 1 via conjugation using N-hydroxysuccinimide terminated PEG. Particle 3 was obtained by 1,3-dipolar cycloaddition between particle 2 and unstructured, azide-functionalized AuNPs coated with 11-mercapto-1-undecanesulphonate.

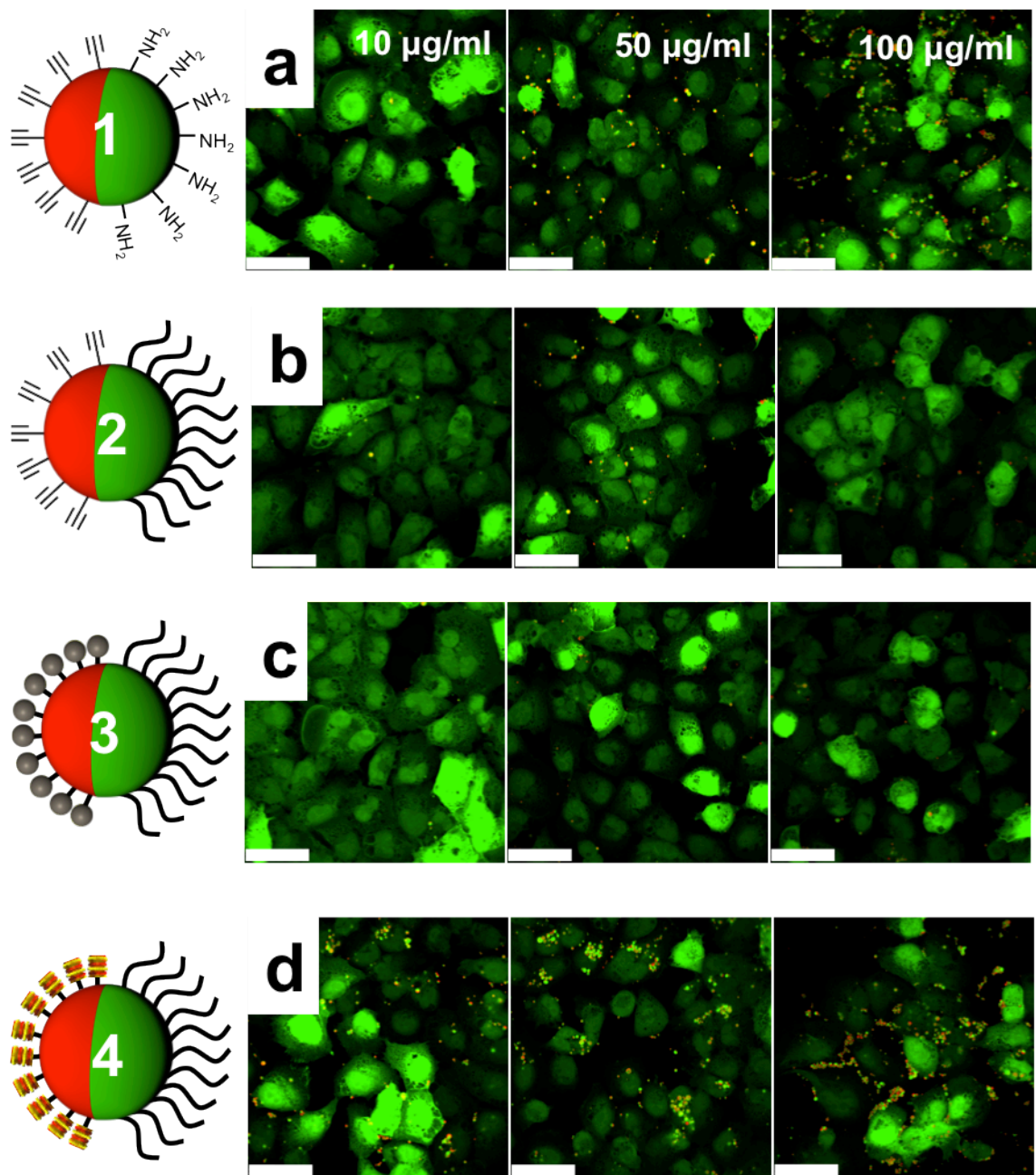


Figure 3-3. Fluorescent CLSM overlay images of MDA-MB-231/GFP cells incubated with particles 1 (a), 2 (b), 3 (c), and 4 (d) for 6 hours at concentrations of 10 (left), 50 (middle), and 100 (right) µg/ml. Scale bars are 50 µm.

Concentration-dependence study. To elucidate the impact of virus-mimicking particles on cells, we incubated each particle sample group (1-4) with a breast cancer cell line that expresses green fluorescent protein, MDA-MB-231/GFP, for 6 hours. CLSM analysis was used to assess binding of the bicompartmental particles to cells. Typical CLSM images are shown in Figure 3-3 and reveal that the level of binding significantly varies between groups and depends on the surface composition. Quantification of the number of particles associated per cell based the confocal micrographs (Figure 3-4) suggests that significantly more particles from sample groups 1 and 4 bound to the cancer cells than for particle groups 2 and 3, indicating both of particles 1 (not PEGylated) and 4 (virus-mimicking) have substantial affinity to the breast cancer cells, but particles 2 and 3, both with a PEGylated side, do not.

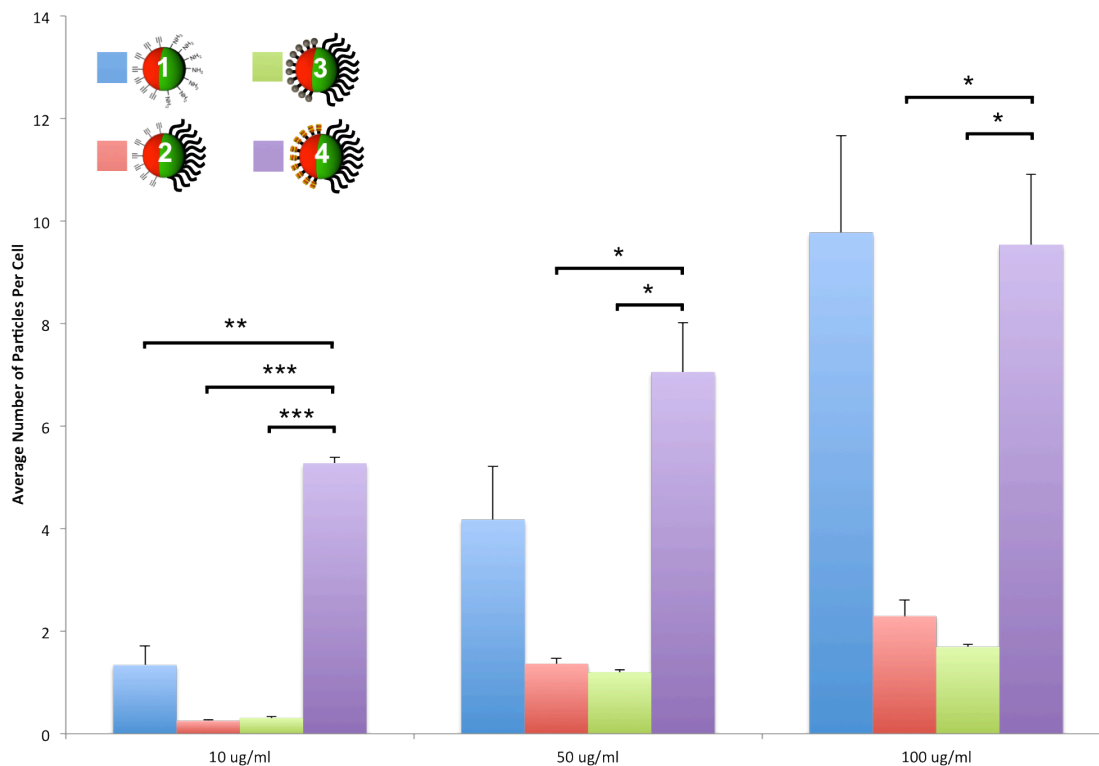


Figure 3-4. Quantification of average number of bound and/or internalized particles per cell for 6-hour incubation experiments (Figure 3-3). Significance levels are: * $p < 0.01$, ** $p < 0.001$. *** $p < 0.0001$.

Additionally, the cell-bound number of particle 1 significantly increased with concentration of particles, suggesting a non-specific binding interaction. Such high binding levels may be attributed to the positive charges on the surface derived from the amine groups of amino-

dextran in one compartment. We have also previously shown that there existed a considerable non-specific binding between PAAm-co-AA particles modified with streptavidin in one compartment and human endothelial cells.³⁵ There are very few particles from sample groups 2 and 3 associated with cells, regardless of concentration, implying that the PEG brushes on the hemisphere surface (as well as potentially lower electrostatic interactions) significantly mitigate non-specific binding. Notably, the unstructured AuNPs on the surface of particle 3 do not influence the affinity of anisotropic particles to the cell. On the other hand, the VMPs (particle 4), functionalized with striped AuNPs on the surface of one compartment, are seen to be substantially associated with the breast cancer cells, as shown in the last row of Figure 4-3, compared to particles 2 and 3. Although the PEGs on the one compartment significantly moderate non-specific binding to the cell like particles 2 and 3, the cell-penetrable striped AuNPs on the VMPs extensively augment the interfacial interaction between the cell membrane and the VMPs, leading to its better cell affinity than particle 1 even at low particle concentrations.

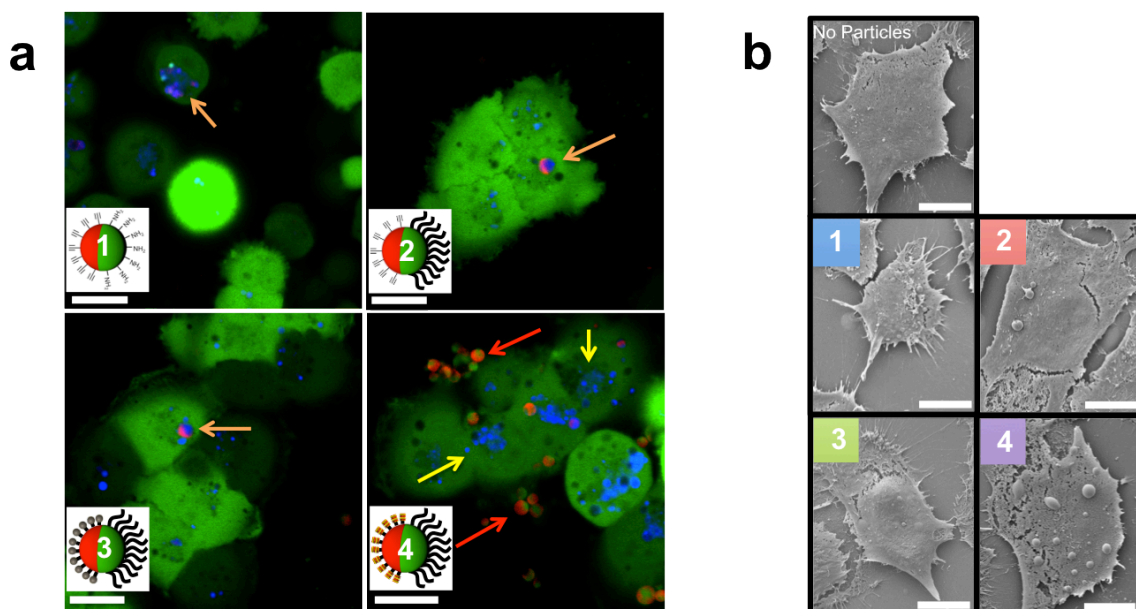


Figure 3-5. (a) Fluorescent CLSM images from endosomal staining studies with 10 $\mu\text{g}/\text{ml}$ of particles 1 – 4 (red & green) were incubated with MDA-MB-231/GFP cells (green) for 6 hours, followed by incubation with an endosomal stain (blue). Scale bars are 10 μm . (b) SEM images of MDA-MB-231/GFP cells after incubation with 10 $\mu\text{g}/\text{ml}$ of particles 1-4. Scale bars are 20 μm .

Endosomal staining and surface morphology. Since particles 1-3 appear to associate with cells in a non-specific manner, we hypothesized that their fate would be different from that

of the VMPs. Because a 6-hour incubation would be sufficient for an endocytic mechanism to take place to internalize polymeric particles,⁴⁰ additional studies were performed by staining the endosomes with a blue fluorescent dye (LysoTracker) that selectively stains lysosomal compartments of cells. After incubation with this dye, the location of the particles relative to the cells was evaluated. In Figure 3-5a, the CLSM images from the incubation of particles 1-3 display that the particle fluorescence is colocalized with the blue fluorescence, indicated by the orange arrows. On the other hand, the VMPs, indicated by red arrows, are not within the stained endosomes (yellow arrows). These different behaviors were also observed by SEM. Figure 3-5b shows that very few control particles (1-3) are found on the surface of cells due to endocytosis (and PEGs for particles 2 and 3) whereas a relatively large number of VMPs are found on the cell surfaces.

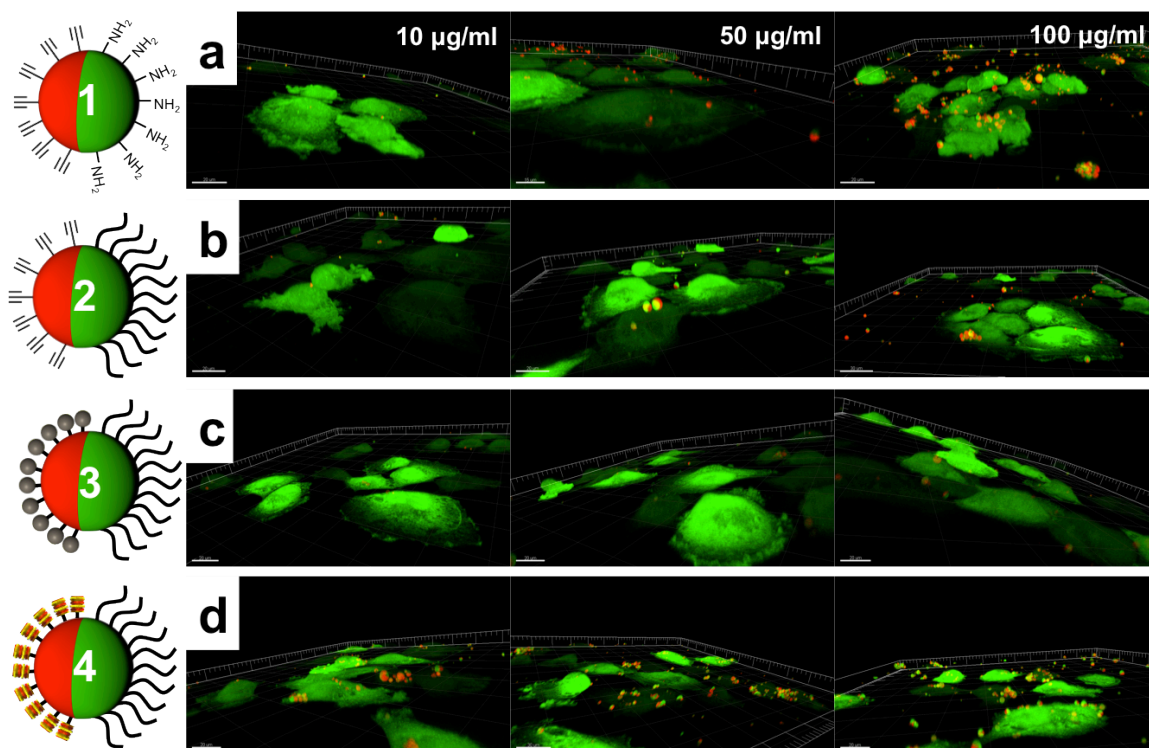


Figure 3-6. 3d reconstructions of zstacks corresponding to 6-hour incubation experiments shown in Figures 3-3 and 3-4.

Furthermore, the examination of 3D reconstructions of confocal z-stacks imply that the controls (particles 1-3) are within the cells, while the VMPs are actually bound to cell membranes (Figure 3-6). Therefore, within 6 hours, the VMPs bind to cell membranes with high specificity as compared to the corresponding control particles. Both the material

properties and the anisotropy of the surface of VMPs are necessary for such behavior; the striped AuNPs lead to directional binding of the VMPs whereas the oppositely functionalized PEG brushes mitigate non-specific binding as well as retard internalization. If one or both of the surface components are different or removed, the resulting control particles are endocytosed as opposed to remaining bound to cell membranes.

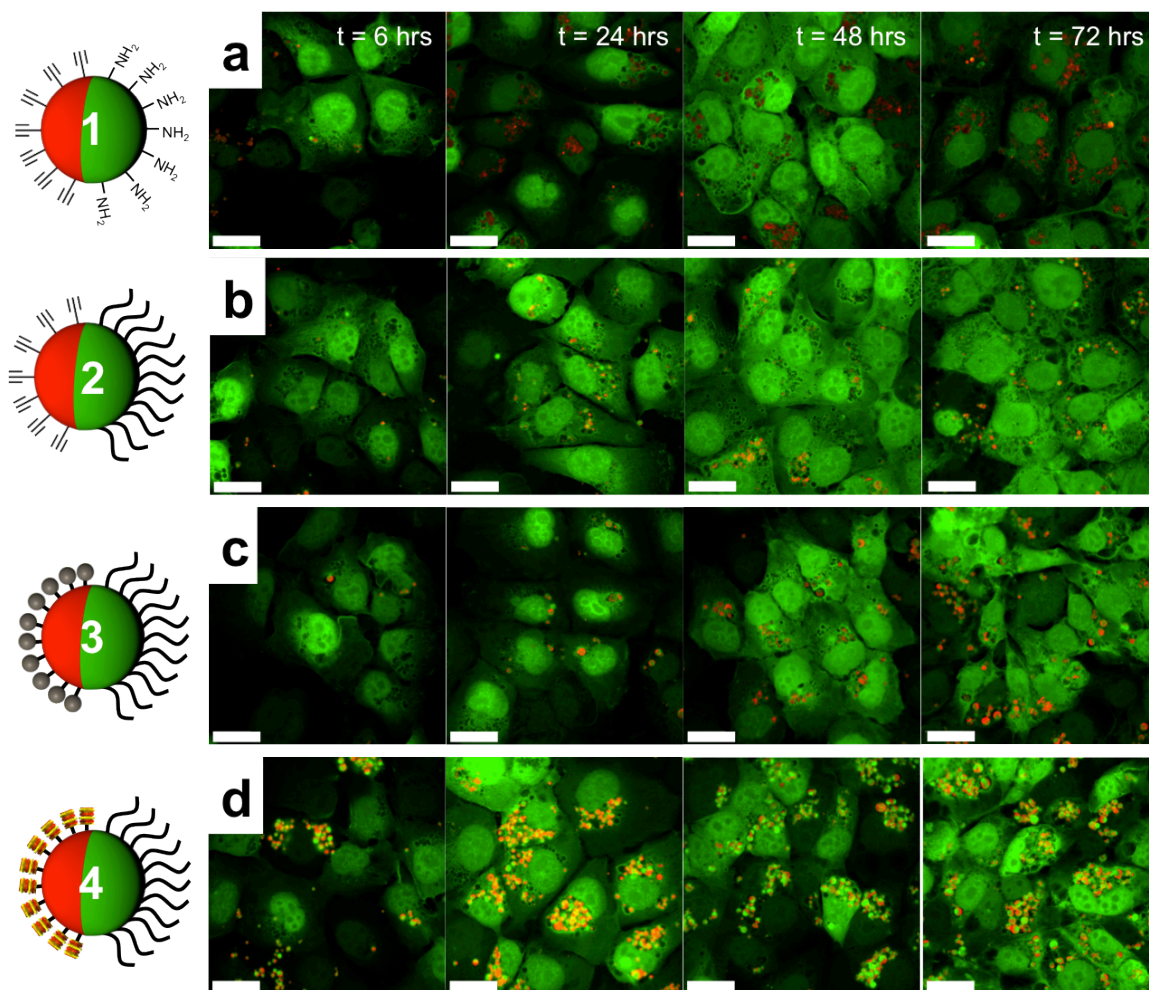


Figure 3-7. Representative fluorescent CLSM overlay images from long-term incubation studies with particles 1 (a), 2, (b), 3 (c), and 4 (d) at a fixed concentration of 100 $\mu\text{g}/\text{ml}$, with incubation times of 6 (leftmost), 24 (second left), 48 (third left), and 72 (rightmost) hours. Scale bars are 25 μm .

Long-term incubation. For biomedical applications, it would be useful to understand the long-term behavior of the VMPs. We therefore performed particle incubations with cells for 6, 24, 48, and 72 hours (Figure 3-7). At no time do we observe significant cell death, indicating that these particles are biocompatible. As time passes, we observe that the

control particles remain confined in endosomes. Over time, more of the control particles with PEG are endocytosed, and by 72 hours, amount of these control particles visually appear roughly the same as the number of endocytosed unmodified control particles. It also observed that there is some endocytosis of VMPs, but many appear to aggregate on certain portions of the cell membrane.

To compare the clustering of VMPs with the clustering, if any, of particles 1-3, K-means analysis was performed on particle locations determined by red fluorescent confocal images corresponding to the overlays shown in Figure 3-7. As seen in Figure 3-8a, there are considerably more VMP particles found in each cluster than the clusters of control particles determined by K-means. Additionally, the average radius of each VMP cluster is generally larger than the control particle counterparts (Figure 3-8b). The low number of particles per cluster and small cluster radius for the controls are indicative of poor clustering as the optimum clustering determined by K-means results in a relatively high number of clusters (and hence low number of particles per cluster). On the other hand, the clustering of the VMPs appears robust, especially given the higher number of particles per cluster. Hence, the VMPs appear to exhibit a different clustering behavior on cells, while particles 1-3 have rather different behavior, and may not cluster at all, as indicated by K-means analysis.

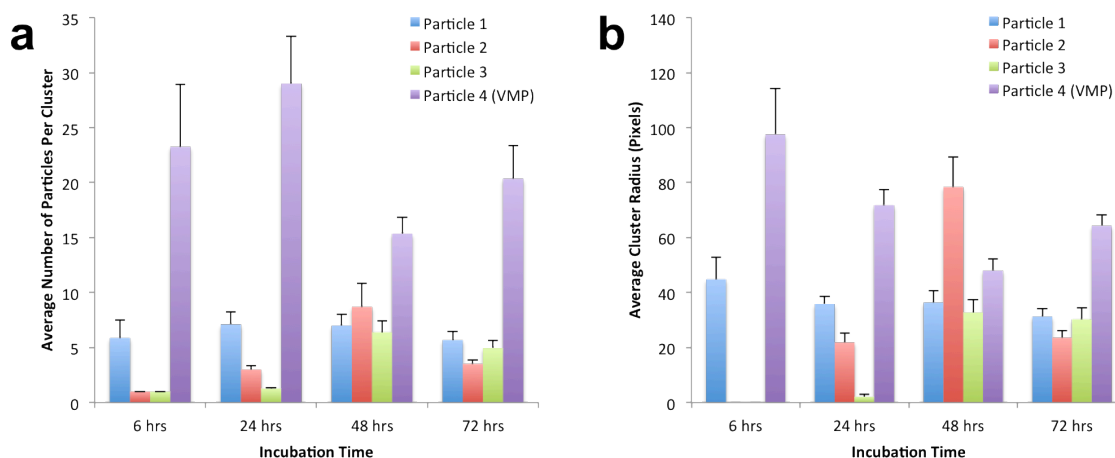


Figure 3-8. K-means clustering analysis of particles 1-4 at different incubation times, showing (a) average number of particles per cluster and (b) average cluster radius. Error bars are standard error.

The mechanism for this clustering phenomenon is unknown. It perhaps may be explained by a cooperative binding mechanism, in which VMPs associated with the cell membrane

allow for more facile binding (less energy intensive) of additional VMPs; hence VMPs dispersed in the media are more likely to bind to these lower energy areas of the membrane, and thus such clustering of VMPs may be observed. However, further studies must be done to further elucidate the mechanism of this clustering behavior.

3.1.4 Summary

The studies presented elucidate structure-behavior relationships between specific anisotropic properties of particles and their corresponding interactions with cells. The PEGylation of one side of a particle significantly reduces particle uptake by cells, but doesn't completely prevent uptake. The immobilization of striped gold nanoparticles on one half affords cell-penetrating capabilities, but the VMPs, which are PEGylated on one side, do not completely enter cells but rather stay bound to the cell membrane. On the other hand, immobilization of standard gold nanoparticles affords no such effect, and the resultant particles are endocytosed, but the uptake is relatively low due to PEGylation of one side. In the cases of particle 1-3, a concentration dependent cell binding is observed, indicative of a nonspecific interaction with the cell, which we have elucidated to be an endocytic mechanism, while the VMPs demonstrate high cell-binding even at low concentrations. Additionally, the mechanism and degree of penetration into the cell membrane by the VMPs is unknown, and warrants further investigation – elucidation of this mechanism may also provide insight into the clustering phenomenon observed after longer incubation times.

The ability to closely mimic viruses can be of interest for a number of applications. VMPs may be used in drug delivery, for example, to deliver a number of sensitive payloads such as proteins and genetic material. However, unlike conventional particulate methods, the payload can be delivered directly into the cytosol like a virus, as opposed to requiring passing through some endocytic process where the payload could be compromised. Additionally, they do not have the immunogenicity concerns that viruses have for in vivo applications. Hence, VMPs serve as a platform that has the potential to deliver payloads as efficient as natural organisms.

3.2 Targeting Triple Negative Breast Cancers via CXCR4

3.2.1 Background and Motivation

While ground-breaking treatments for receptor positive breast cancers have had a significant impact, triple negative breast cancers (TNBC) generally do not respond to these therapeutic interventions.⁴¹ TNBC has a worse short-term prognosis than other types of breast cancer, and can have a more aggressive progression.^{41,42} Currently, the standard of care includes various chemotherapeutics as adjuvants, with variable outcomes in terms of survival and recurrence of disease.^{41,43} Recently, however, much advancement has been made in understanding the biology and pathophysiology of TNBC. In particular, pathways involving CXCR4 have been implicated in both TNBC and metastatic breast cancer.^{43,44} CXCR4, a cell surface receptor overexpressed in TNBC, signaling promotes cell proliferation and chemotaxis.^{45,46} In TNBC, among several other cancers, the CXCR4 pathway has been shown to be involved in tumor growth and metastasis.⁴⁷ Additionally, the degree of CXCR4 overexpression in TNBC positively correlates with worse prognosis.⁴⁸

Given its overexpression and role in growth and metastatic potential, CXCR4 may be an effective target for therapy. Blocking CXCR4 signaling has been shown to prevent invasion and metastasis by breast cancer cells,^{49,50} and CXCR4-targeted nanocarriers have been used for imaging breast cancer in lymph nodes.⁵¹ Several targeting ligands and CXCR4 antagonists have been developed, including antibodies, small peptides, and CXCL12 (the chemokine ligand for CXCR4) analogs.^{52,53} Specifically, AMD3100 is a small molecule with exceptionally high affinity for CXCR4 that has been shown to block CXCR4 signaling in *in vivo* models and in clinical trials.^{44,54,55} However, to date few studies have employed AMD3100 as a targeting ligand on nanocarriers.^{56,57} Given its high binding affinity to CXCR4⁵⁴ and relative nontoxicity,⁵⁸ carriers immobilized with high densities of this small molecule may have great targeting potential.

Electrohydrodynamic (EHD) co-jetting is a technique with the capability to rapidly fabricate multicompartamental carriers.^{19-21,25} In particular, our group has developed a library of functionalized polylactides (PLAs) that may be incorporated into such carriers, allowing for facile, selective surface conjugation.³³ Specifically, an acrylate-functionalized PLA may be employed to react with the secondary amines of AMD3100 via Michael addition. This reaction has been used previously to fabricate an AMD3100-containing polymer that may

be used for CXCR4-targeted transfection.⁵⁷ Here we demonstrate the ability to selectively immobilize AMD3100 by using an acrylate-functionalized PLA incorporated into EHD co-jetted carriers. Furthermore, we show that such carriers can not only target CXCR4, but also inhibit CXCL12-induced signaling in an *in vitro* model.

3.2.2 Methods

Materials. Poly(DL-lactide-co-glycolic acid) (PLGA, 85:15 lactide:glycolide, 50-75 kg/mol), polyethyleneimine (PEI, Mn = 60 kg/mol, Mw = 760 kg/mol), blue fluorescent poly[(*m*-phenylenevinylene)-alt-(2,5-dihexyloxy-*p*-phenylenevinylene)] (PMPDHPV), Tween 20, diisopropylamine (DIA), and all solvents were purchased from Sigma. Dithiobis(succinimidyl propionate) [DSP] and paraformaldehyde were obtained from Thermo Scientific. Phosphate buffered saline (PBS), ProLong Gold, Dulbecco's Modified Eagle Medium (DMEM), fetal bovine serum (FBS), non-essential amino acids (NEAA), and penicillin-streptomycin (pen-strep) were obtained from Invitrogen. 20 base pair DNA conjugated with AlexaFluor 546 (20bpDNA-AF546) was obtained from Integrated DNA Technologies. CXCR4 expressing MDA-MB-231 cells were provided by the Luker group. Acrylate functionalized PLA (PLA-acryl) was synthesized as described previously,³³ courtesy of Dr. Hakan Durmaz.

Fabrication of microcylinders & AMD3100 immobilization. Fabrication of microcylinders with PLA-acryl in one compartment and a blue fluorescent dye in the other were made by a previously described procedure of the cryosectioning of EHD co-jetted fibers.^{28,30,59} The fibers were manufactured by the co-jetting of the following solutions at 0.05 ml/hr and around 12.75 kV: 1) 30 w/v% PLGA with <0.05 mg/ml PMPDHPV, and 2) 33 w/v% 10:1 w/w PLGA:PLA-acryl, both in 95:5 CHCl₃:DMF. The microcylinders were then incubated in 2-3 mg/ml of AMD3100 in a total of 2 ml PBS (with .01 v/v% Tween 20); 14 ul of DIA was added, and the mixture was rotated, allowing it to react for 16 hours at ambient conditions. After washing three times by centrifugation and resuspension with fresh 0.01 v/v% Tween 20 in PBS, the microcylinders were then incubated in 1 ml of PBS (with Tween 20) with 20 µl of 0.13 mg/ml 20bpDNA-AF546, rotated at ambient conditions for 3 hours. They were then washed again three times and fluorescent confocal imaging of them was performed on a FluoView 500 Laser Scanning Confocal Microscope (CLSM).

Fabrication of AMD3100-conjugated nanocarriers. Nanoparticles were synthesized, as described previously,²⁵ with the incorporation of PLA-acryl by the co-jetting of the following solutions at 30 cm, 0.1 ml/hr, and 9.75 – 10.05 kV: 1) 6.25 w/v% 4:1 w/w PLGA:PLA-acryl (for signaling study, 5.5 w/v% 10:1 w/w PLGA:PLA-acryl was used instead) with <0.05 mg/ml PMPDHV, and 2) 5.25 w/v% 1:1:0.1 w/w/w PLGA:PEI:DSP, both in 1:1 v/v CHCl₃:DMF; after jetting the particles were allowed to crosslink for at least 72 hours at room temperature. Due to the basic conditions required for the AMD3100 conjugation, the reaction time was shortened to around 3 hours for immobilization on nanoparticles to avoid their degradation; additionally, 0.1 v/v% tween 20 in PBS was used as the solvent for conjugation and washing. Control nanoparticles were made by placing in same conditions for conjugation, but with no AMD3100. Nanoparticles were characterized with an AMRAY 1910 field emission scanning electron microscope (SEM) and by dynamic light scattering (DLS) with a Malvern Zetasizer Nano ZSP.

In vitro studies. MDA-MB-231 cells overexpressing a CXCR4-GFP fusion protein were provided by the Luker group. Cells were cultured in DMEM supplemented with 10% FBS, 1X NEAA, and 1X pen-strep. For uptake studies, cells were seeded on circular glass coverslips in 12-well plates. The seeded cells were cultured for 24 hours, and then incubated with control and AMD3100-immobilized nanocarriers for 1 hour, both at a concentration of 10 µg/ml. They were then washed 3 times with PBS, incubated in 4% paraformaldehyde for 30 minutes, washed 4 more times, and the coverslips were then mounted on glass slides with ProLong Gold. Imaging was performed using a FluoView 500 CLSM. CXCR4 signaling studies were performed by the Luker group.

3.2.3 Results and Discussion

After fabricating microcylinders with PLA-acrylate, we performed Michael addition of AMD3100 with the acrylate groups on the surface (Figure 3-9a). We then incubated the reacted microcylinders with 20bpDNA-AF546, as we expected electrostatic interactions between the amines of AMD3100 and the phosphates of the DNA. As seen from the confocal images in Figures 3-9b – 3-9d, the red fluorescence from the 20bpDNA-AF546 is mostly compartmentalized and separate from the blue fluorescence, which labels the compartment without PLA-acrylate. Because the DNA binds selectively to the unlabeled compartment with PLA-acrylate, we may conclude that the AMD3100 was successfully immobilized

selectively on one side by reaction with surface acrylate groups, allowing for subsequent electrostatic binding of the DNA.

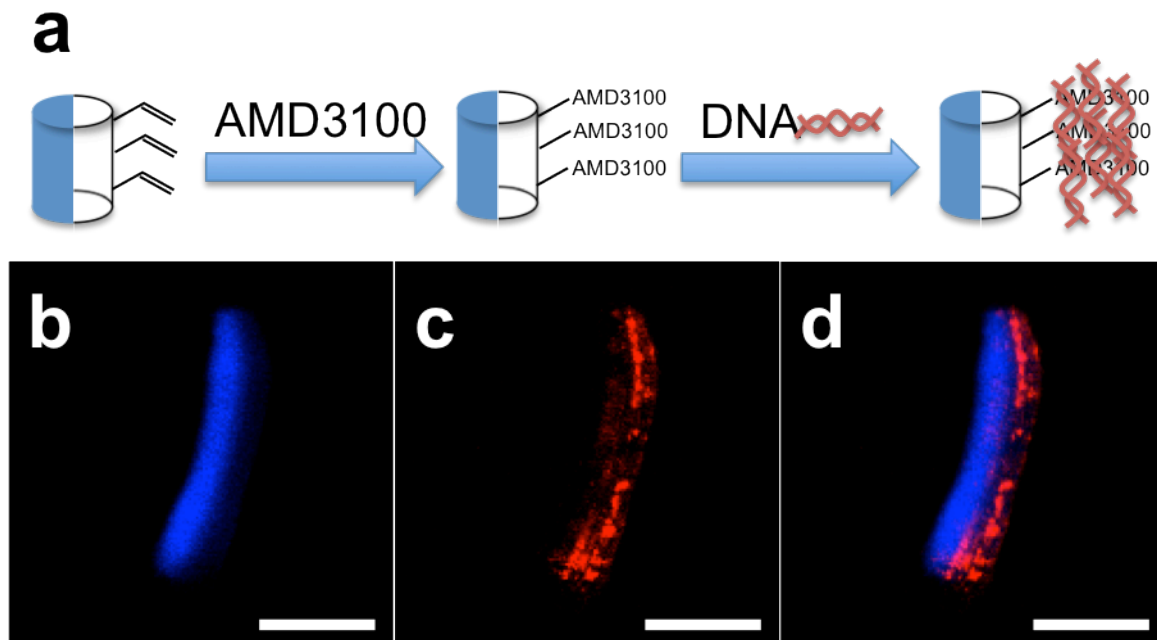


Figure 3-9. (a) Reaction scheme for selective immobilization of AMD3100 and fluorescently labeled DNA. (b), (c) Confocal images of a microcylinder (blue on one side) after AMD3100 immobilization and labeling with fluorescent DNA (red). (d) Overlay of (b) and (c). Scale bars are 20 μm .

After confirming that AMD3100 can be selectively immobilized using co-jetted carriers incorporating PLA-acrylate, we then manufactured endosome-sensing nanocarriers with PLA-acrylate, and conjugated AMD3100 to their surfaces. As shown in Figure 3-10, the co-jetted carriers have a bimodal distribution, with most falling in the range of 50-100 nm, but there are some that are 200-500 nm. After fabricating AMD3100-immobilized nanocarriers, we explored their *in vitro* behavior by incubating them with MDA-MB-231 cells expressing a CXCR4-GFP fusion protein. To visualize them, a blue fluorescent dye was incorporated into the carriers. As seen in Figure 3-11, we observe a higher density of blue fluorescence from AMD3100-immobilized carriers colocalized with the green fluorescence from the cells than from unmodified carriers. We may hence infer that AMD3100-immobilized carriers are uptaken by the CXCR4 expressing cells at a high rate than unmodified carriers.

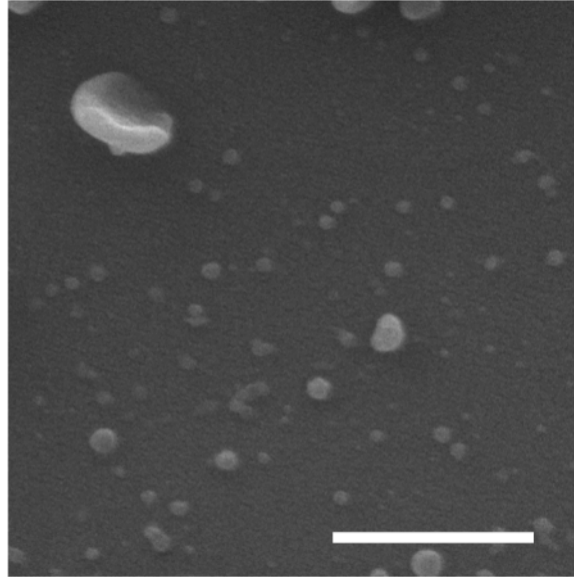


Figure 3-10. (a) SEM image of co-jetted carriers containing PLGA and PLA-acryl on one side, and PLGA, PEI, and DSP on the other side. Scale bar is 1 μm . (b) DLS of the carriers in 0.01 v/v% Tween20/PBS.

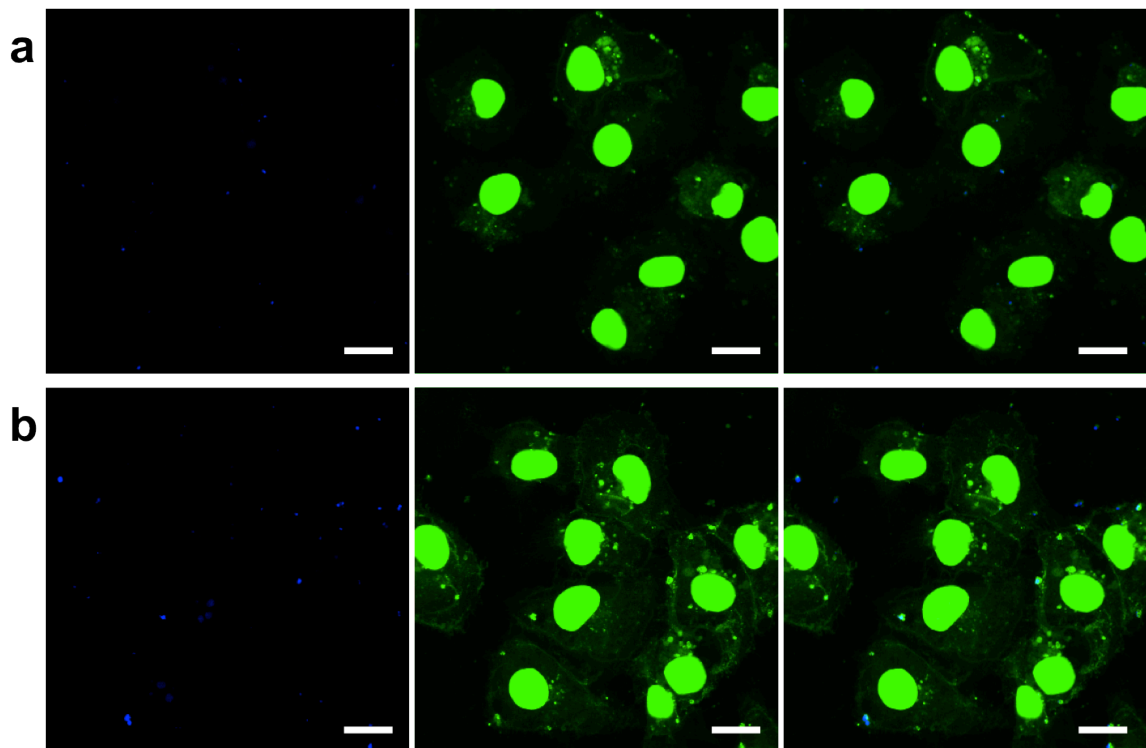


Figure 3-11. Confocal images of CXCR4-expressing cells (green) incubated with either AMD3100-immobilized (a) or unmodified control (b) carriers (blue) and their overlays. Scale bars are 20 μm .

In addition to the selective uptake of these carriers, we also explored their ability to arrest CXCR4 signaling, which may potentially prevent further tumor growth and metastasis. We used β -arrestin levels as a measure of downstream CXCR4 signaling; as shown in Figure 3-12, incubation of cells with 300 ng/ml CXCL12 results in a 100% increase in β -arrestin levels, while incubating additionally with AMD3100-immobilized carriers reduce β -arrestin levels to only about a 25% increase, whereas carriers not immobilized with AMD3100 have no such effect. In comparison, the decrease in β -arrestin levels is similar to competitive inhibition by free AMD3100. Hence, AMD3100-immobilized nanocarriers not only show selective uptake in CXCR4 expressing cells, but also are able to inhibit CXCR4 signaling.

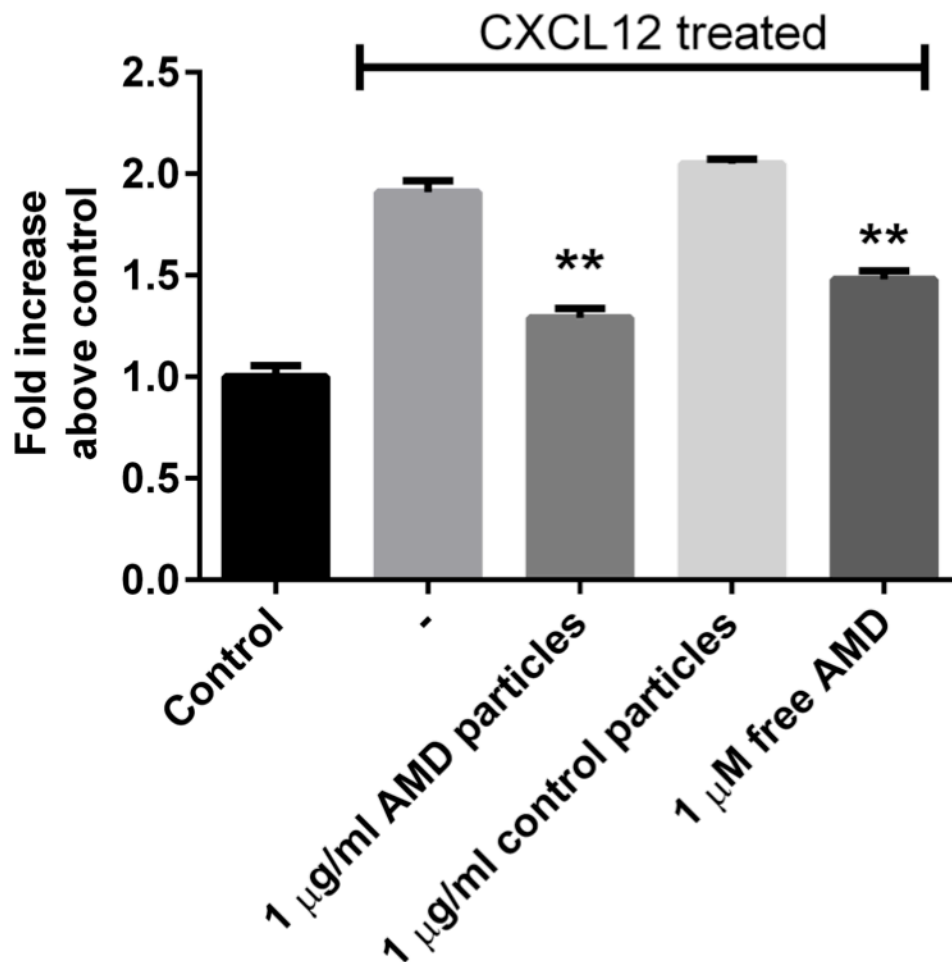


Figure 3-12. Measurement of β -arrestin levels after incubation with CXCL12 and various carriers. Control represents cells that were not incubated with CXCL12, AMD3100 or carriers. The '-' sample represents cells incubated only with CXCL12. AMD particles represents cells incubated with 1 μ g/ml AMD-immobilized carriers. Control particles represents cells incubated with 1 μ g/ml unmodified carriers. Free AMD represents cells incubated with 1 μ M free AMD3100. Study was done by the Luker group.

3.2.4 Summary

The results described before show the potential for AMD3100-immobilized carriers in the treatment of CXCR4 overexpressing cancers such as TNBC. Surface immobilization of AMD3100 is possible via Michael addition with the use of an acrylate functionalized PLA. Furthermore, PLGA based carriers surface immobilized with AMD3100 are uptaken by CXCR4-expressing breast cancer cells at a higher rate than bare PLGA carriers, allowing for the potential of targeted delivery of therapeutics, as will be discussed in Chapter 5. Additionally, AMD3100-immobilized carriers can block CXCR4 signaling; these carriers may hence be used to help prevent growth and metastasis of TNBCs.

3.3 Targeting Neuroblastomas via Norepinephrine Transporters

3.3.1 Background and Motivation

Neuroblastoma, a malignancy common in pediatric populations, has a variable clinical presentation.⁶⁰ In some cases, the disease is fully curable, but in high-risk neuroblastoma, five-year survival rates are less than 50%, often relapsing despite responding to initial chemotherapy.⁶⁰⁻⁶² Even with successful treatment, long-term survivors of neuroblastomas may suffer from significant long-term side effects such as cardiotoxicity and hearing deficits; these effects may be attributed to the toxicities associated with the therapeutics used, which can especially affect growth and development in children.^{63,64} Therefore, targeted therapies, selectively acting only upon neuroblastoma cells, are highly desirable.

The norepinephrine transporter (NET), expressed in very few select tissues, has been found to be overexpressed in a number of neuroblastoma models.⁶⁵ Drug delivery by targeting NET may therefore serve as a viable strategy for the treatment of neuroblastomas. In particular, meta-iodobenzylguanidine (MIBG) has been found to accumulate both in *in vitro* and *in vivo* models of neuroblastoma, as well as in patients.⁶⁵⁻⁶⁷ Moreover, radioactive MIBG has been used as a therapy, especially for recurrent high-risk neuroblastoma.⁶⁸⁻⁷⁰ Hence, MIBG may serve as a targeting ligand to neuroblastomas; for example, an MIBG tethered to polyethylene glycol (PEG) would allow for facile surface modification of nanocarriers for targeted therapy to neuroblastomas. However, chemical modification of MIBG has proven difficult, generally requiring multiple steps.⁷¹ Additionally, the specific structure of MIBG is important for successful targeting.⁷²

Here we present a one-step synthesis of an MIBG conjugate that is tethered to a fluorescein isothiocyanate (FITC) PEG, denoted MIBG-PEG-FITC. We show that MIBG-PEG-FITC is capable of selectively binding to NET-expressing neuroblastoma cell lines in an *in vitro* setting. Furthermore, we demonstrate that this binding is NET-mediated, indicating that MIBG-PEG-FITC binds specifically to NET.

3.3.2 Methods

Materials. Triethylamine (TEA), copper iodide (CuI), bis(triphenylphosphine)palladium(II) dichloride (Pd(PPh₃)₂Cl₂), ethylenediaminetetraacetic acid disodium salt (Na₂EDTA), and all solvents were purchased from Sigma-Aldrich. Alkyne functionalized poly(ethylene glycol) labeled with fluorescein isocyanate (alkyne-PEG-FITC, MW 3400 g/mol) was obtained from Nanocs. Meta-iodobenzylguanidine (MIBG) was provided by the Yanik group. SK-N-BE(2) and BE(2)-C cells were purchased from ATCC. ProLong Gold, Dulbecco's Modified Eagle Medium (DMEM), F12K medium, fetal bovine serum (FBS), penicillin-streptomycin (pen-strep), and trypsin, were obtained from Invitrogen.

Synthesis of MIBG-PEG-FITC. Synthesis of the MIBG conjugate, in which the iodine is substituted with PEG-FITC, was achieved by the Sonogashira coupling of MIBG and alkyne-PEG-FITC. Briefly, 0.186 g alkyne-PEG-FITC was dissolved in 4 ml DMF, to which 0.5 ml TEA was added. 0.053 g MIBG was then added to the mixture and allowed to stir for 10 min, followed by the addition of 5.20 mg CuI and 9.60 mg Pd(PPh₃)₂Cl₂. The mixture was stirred for 2 days under nitrogen at room temperature, then dialyzed against deionized water with a 1000 Da cutoff membrane overnight, and finally freeze-dried. This crude product was dissolved once more in water and 10 mg of Na₂EDTA was added; the mixture was stirred overnight, dialyzed once more against a 1000 Da cutoff membrane, and finally followed by freeze-drying. The resulting purified product, a pale yellow solid, was then characterized by ¹H NMR. Synthesis and characterization of MIBG-PEG-FITC were courtesy of Dr. Hakan Durmaz and Artak Shahnas.

In vitro studies. SK-N-BE(2) and BE(2)-C cells were cultured in a 1:1 v/v mixture of DMEM and F12K supplemented with 10% FBS and 1X pen-strep. Cells were seeded on either 12-well plates on circular glass coverslips, for fluorescence confocal imaging, or in 6-well plates, for flow cytometry. In 12-well plates, cells were incubated for 15 minutes with 100

μM of either alkyne-PEG-FITC or MIBG-PEG-FITC at 37 °C. The cells were then washed with PBS and fixed in 4% paraformaldehyde for 20 minutes; the coverslips (with fixed samples) were mounted on glass slides with ProLong Gold, and imaging was done with a FluoView 500 Laser Scanning Confocal Microscope (CLSM). For 6-well plates, cells were incubated either with 100 μM MIBG-PEG-FITC for 15 minutes or with 500 μM desipramine for 15 minutes followed by 100 μM MIBG-PEG-FITC (desipramine was not removed before adding MIBG-PEG-FITC). Cells were collected from the plates by vigorous pipetting, and, following washing with PBS by centrifugation (1000 rpm, 5 min) and resuspension, flow cytometry was performed using a Beckman Coulter MoFlo Astrios.

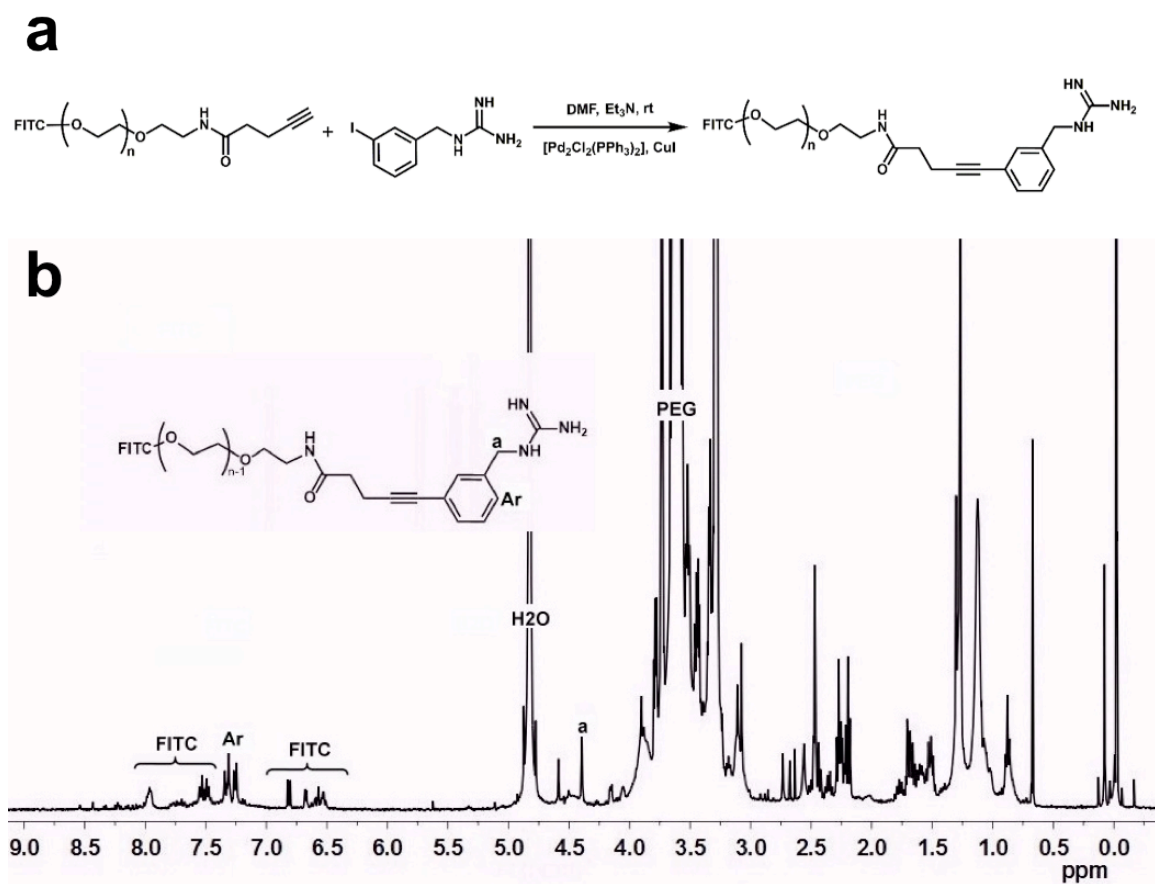


Figure 3-13. (a) Synthesis of MIBG-PEG-FITC conjugate by Sonogashira coupling, and (b) corresponding ^1H NMR of the product. Synthesis and characterization were performed by Dr. Hakan Durmaz and Artak Shahnas.

3.3.3 Results and Discussion

We first demonstrated the feasibility of synthesizing a conjugate of MIBG tethered to PEG; such a macromolecule could then be subsequently functionalized on the surface of nanocarriers for targeted therapy. MIBG-PEG-FITC was obtained by Sonagashira coupling, as shown in Figure 3-13a; unreacted MIBG and other small molecules were removed by dialysis, leaving a mixture of MIBG-PEG-FITC and unconjugated PEG-FITC (unreacted). From ^1H NMR of this purified product (Figure 3-13b), based on the ratio of integrations of the methylene proton peaks from MIBG and backbone proton peaks from PEG, we determined that 60% of the PEGs were successfully conjugated with MIBG. Given the challenges with chemical modification of MIBG, an efficiency of 60% is fairly high, and we determined it sufficient for performing *in vitro* studies.

We compared MIBG-PEG-FITC binding with alkyne-PEG-FITC binding to SK-N-BE(2) cells using fluorescence microscopy. We observe somewhat more localization of fluorescence of MIBG-PEG-FITC on cells than that of alkyne-PEG-FITC, as seen from Figures 3-14a and 3-14b. The difference is arguably difficult to discern visually, and so the fluorescence intensity from the images was quantified using ImageJ – as shown in Figure 3-14c, the average fluorescence intensity found on cells from MIBG-PEG-FITC is almost twice as much as the intensity from alkyne-PEG-FITC.

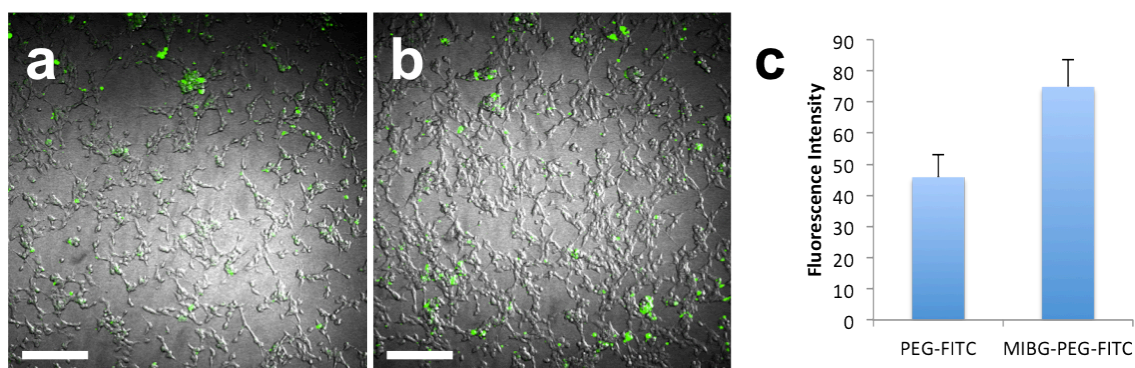


Figure 3-14. Confocal images of SK-N-BE(2) cells after incubation with 100 μM (a) alkyne-PEG-FITC and (b) MIBG-PEG-FITC. Scale bars are 200 μm . (c) Quantification of the fluorescence intensity from images using ImageJ.

To more quantitatively determine the specificity of binding of MIBG-PEG-FITC, flow cytometry was employed. Desipramine, a tricyclic anti-depressant, is known to bind to NETs, and has been shown to block binding or uptake of MIBG.^{65,66,73} As seen in Figure 3-15, we

observe that, after incubation with MIBG-PEG-FITC, roughly 16.2% of cells have high fluorescence intensity, compared to about 8.5% of cells when they are preincubated with desipramine. This relative decrease indicates a specific interaction between MIBG-PEG-FITC and SK-N-BE(2) cells, which can be blocked by desipramine, hence showing that MIBG retains at least some affinity to NETs even when conjugated to PEG.

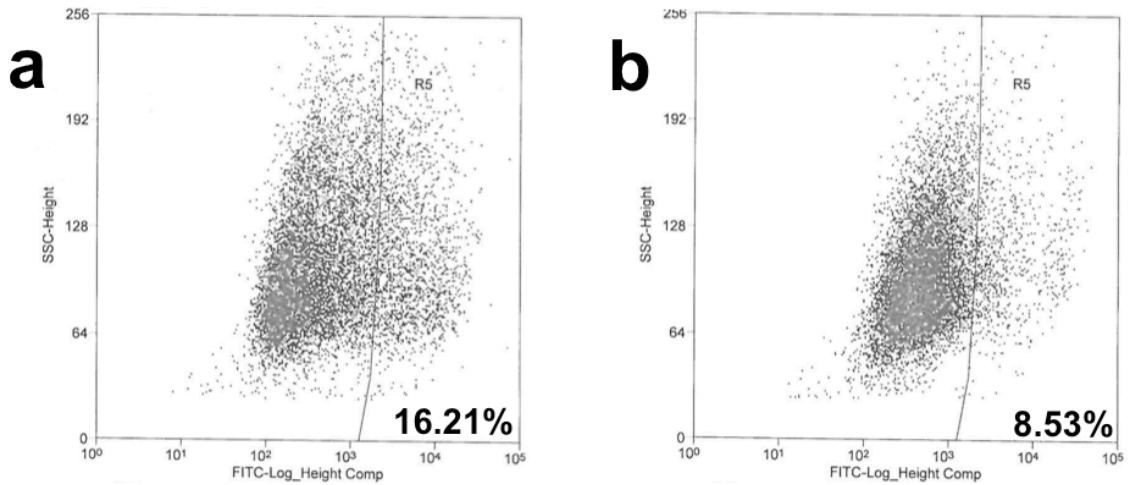


Figure 3-15. Flow cytometry results after incubation of SK-N-BE(2) cells with (a) 100 μ M MIBG-PEG-FITC and (c) 50 μ M desipramine followed by 100 μ M MIBG-PEG-FITC.

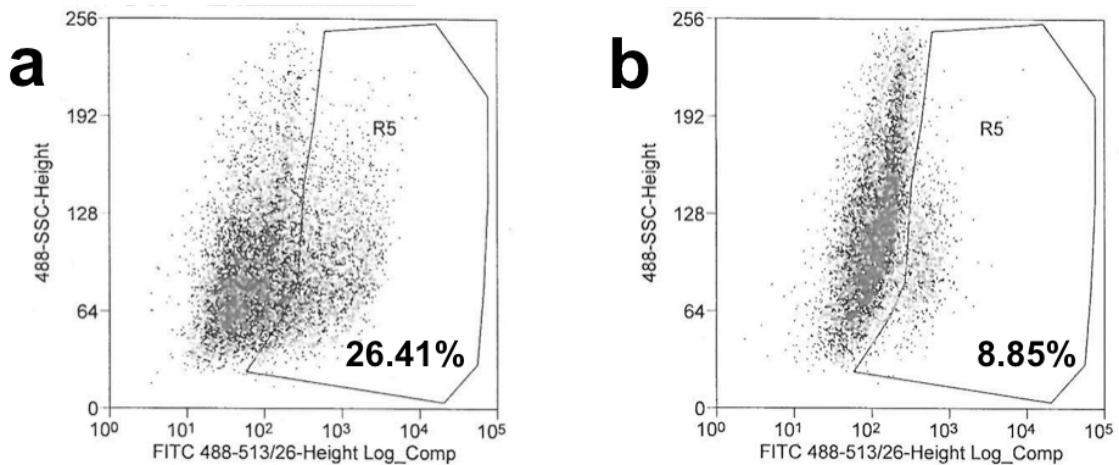


Figure 3-16. Flow cytometry results after incubation of BE(2)-C cells with (a) 100 μ M MIBG-PEG-FITC and (b) 500 μ M desipramine followed by 100 μ M MIBG-PEG-FITC.

BE(2)-C cells, an adherent neuroblastoma cell line derived from SK-N-BE(2), has been shown to potentially have higher NET expression than SK-N-BE(2).⁶⁵ We therefore repeated the binding experiment with untreated vs. desipramine-treated BE(2)-C cells. As seen from the flow cytometry data in Figure 3-16, we found specific MIBG-PEG-FITC binding with

26.4% of untreated cells, while 8.9% of desipramine-treated cells had MIBG-PEG-FITC bound. In this case we find a larger knockdown of binding to MIBG-PEG-FITC by desipramine (as compared to the study with SK-N-BE(2)), perhaps reflective of higher NET expression by BE(2)-C cells.

It is important to note the significance of gating in analyzing flow cytometry data. It can be seen from Figure 3-15 that nearly all cells were measured to have some degree of fluorescence in the FITC channel. Based on the fluorescence imaging (Figure 3-14), it may be that much of this fluorescence can be attributed to non-specific binding. Specific interactions, then, may be correlated to high levels of fluorescence, indicative of more binding by MIBG-PEG-FITC. Therefore, cells that measured about three orders of magnitude higher than baseline were counted as cells in which specific binding could be detected. Choosing to gate at this level, however, is fairly arbitrary. Interpretations regarding the degree of binding based on these percentages of cells calculated from flow cytometry data may hence be inaccurate. Nonetheless, we can conclude that MIBG-PEG-FITC binds less to desipramine-treated cells than untreated cells. More sophisticated experimentation, however, is required to further assess and quantify this binding.

3.3.4 Summary

Here, we have demonstrated the ability to synthesize an MIBG conjugate in which MIBG is tethered to the end of a PEG molecule labeled with FITC. We have also shown some preliminary experiments that indicate that this MIBG-PEG-FITC has some binding specificity for two NET-expressing neuroblastoma cell lines, SK-N-BE(2) and BE(2)-C. This binding can be blocked by treatment with desipramine, which also binds to NETs, suggesting that the mechanism of MIBG-PEG-FITC interaction with neuroblastoma cells is via specific binding with NETs. The degree of binding may correlate with NET expression, as incubation of BE(2) cells with desipramine resulted in a larger relative decrease in MIBG-PEG-FITC binding than for SK-N-BE(2) cells. The degree of binding of MIBG-PEG-FITC and how it compares to binding of free MIBG warrants further study, requiring more rigorous accounting of non-specific interactions. Additionally, studies immobilizing MIBG-PEG on particles and the relative uptake of such carriers by NET-expressing cells may allow for the potential of targeted therapy to neuroblastomas to be realized.

3.4 References

- 1 Lidmar, J., Mirny, L. & Nelson, D. R. Virus shapes and buckling transitions in spherical shells. *Phys Rev E* **68**, doi:Artn 051910
Doi 10.1103/Physreve.68.051910 (2003).
- 2 Glotzer, S. C. & Solomon, M. J. Anisotropy of building blocks and their assembly into complex structures. *Nature materials* **6**, 557-562, doi:Doi 10.1038/Nmat1949 (2007).
- 3 Douglas, T. & Young, M. Viruses: Making friends with old foes. *Science* **312**, 873-875, doi:Doi 10.1126/Science.1123223 (2006).
- 4 Glotzer, S. C. *et al.* Self-assembly of anisotropic tethered nanoparticle shape amphiphiles. *Curr Opin Colloid In* **10**, 287-295, doi:Doi 10.1016/J.Cocis.2005.09.011 (2005).
- 5 Hoekstra, D. & Kok, J. W. Entry Mechanisms of Enveloped Viruses - Implications for Fusion of Intracellular Membranes. *Bioscience Rep* **9**, 273-305, doi:Doi 10.1007/Bf01114682 (1989).
- 6 Harrison, S. C. Viral membrane fusion. *Nat Struct Mol Biol* **15**, 690-698, doi:Doi 10.1038/Nsmb.1456 (2008).
- 7 Petri, W. A., Pal, R., Barenholz, Y. & Wagner, R. R. Fluorescence Anisotropy of a Fatty-Acid Covalently Linked In vivo to the Glycoprotein of Vesicular Stomatitis-Virus. *J Biol Chem* **256**, 2625-2627 (1981).
- 8 Eckert, D. M. & Kim, P. S. Mechanisms of viral membrane fusion and its inhibition. *Annu Rev Biochem* **70**, 777-810, doi:Doi 10.1146/Annurev.Biochem.70.1.777 (2001).
- 9 Kodiyan, A., Silva, E. A., Kim, J., Aizenberg, M. & Mooney, D. J. Surface Modification with Alginate-Derived Polymers for Stable, Protein-Repellent, Long-Circulating Gold Nanoparticles. *ACS nano* **6**, 4796-4805, doi:Doi 10.1021/Nn205073n (2012).
- 10 Harris, J. M., Martin, N. E. & Modi, M. Pegylation - A novel process for modifying pharmacokinetics. *Clin Pharmacokinet* **40**, 539-551, doi:Doi 10.2165/00003088-200140070-00005 (2001).
- 11 Gref, R. *et al.* Biodegradable Long-Circulating Polymeric Nanospheres. *Science* **263**, 1600-1603, doi:Doi 10.1126/Science.8128245 (1994).
- 12 Veronese, F. M. & Pasut, G. PEGylation, successful approach to drug delivery. *Drug discovery today* **10**, 1451-1458, doi:Doi 10.1016/S1359-6446(05)03575-0 (2005).
- 13 Chen, S. F., Li, L. Y., Zhao, C. & Zheng, J. Surface hydration: Principles and applications toward low-fouling/nonfouling biomaterials. *Polymer* **51**, 5283-5293, doi:Doi 10.1016/J.Polymer.2010.08.022 (2010).
- 14 Gupta, B., Levchenko, T. S. & Torchilin, V. P. Intracellular delivery of large molecules and small particles by cell-penetrating proteins and peptides. *Advanced drug delivery reviews* **57**, 637-651, doi:Doi 10.1016/J.Addr.2004.10.007 (2005).
- 15 Gheysen, D. *et al.* Assembly and Release of Hiv-1 Precursor Pr55gag Virus-Like Particles from Recombinant Baculovirus Infected Insect Cells. *Cell* **59**, 103-112, doi:Doi 10.1016/0092-8674(89)90873-8 (1989).
- 16 Xu, L. *et al.* Self-assembly of a virus-mimicking nanostructure system for efficient tumor-targeted gene delivery. *Hum Gene Ther* **13**, 469-481, doi:Doi 10.1089/10430340252792594 (2002).
- 17 Kirnbauer, R., Booy, F., Cheng, N., Lowy, D. R. & Schiller, J. T. Papillomavirus L1 Major Capsid Protein Self-Assembles into Virus-Like Particles That Are Highly Immunogenic. *P Natl Acad Sci USA* **89**, 12180-12184, doi:Doi 10.1073/Pnas.89.24.12180 (1992).

- 18 Grgacic, E. V. L. & Anderson, D. A. Virus-like particles: Passport to immune recognition. *Methods* **40**, 60-65, doi:Doi 10.1016/J.Ymeth.2006.07.018 (2006).
- 19 Roh, K. H., Martin, D. C. & Lahann, J. Biphasic Janus particles with nanoscale anisotropy. *Nature materials* **4**, 759-763, doi:Doi 10.1038/Nmat1486 (2005).
- 20 Roh, K. H., Martin, D. C. & Lahann, J. Triphasic nanocolloids. *J Am Chem Soc* **128**, 6796-6797, doi:Doi 10.1021/Ja060836n (2006).
- 21 Bhaskar, S., Pollock, K. M., Yoshida, M. & Lahann, J. Towards Designer Microparticles: Simultaneous Control of Anisotropy, Shape, and Size. *Small* **6**, 404-411, doi:Doi 10.1002/Sml.200901306 (2010).
- 22 Hwang, S. *et al.* Anisotropic hybrid particles based on electrohydrodynamic co-jetting of nanoparticle suspensions. *Physical Chemistry Chemical Physics* **12**, 11894-11899, doi:Doi 10.1039/C0cp00264j (2010).
- 23 Lim, D. W., Hwang, S., Uzun, O., Stellacci, F. & Lahann, J. Compartmentalization of Gold Nanocrystals in Polymer Microparticles using Electrohydrodynamic Co-Jetting. *Macromolecular rapid communications* **31**, 176-182, doi:Doi 10.1002/Marc.200900597 (2010).
- 24 Lee, K. J. *et al.* Compartmentalized Photoreactions within Compositionally Anisotropic Janus Microstructures. *Macromolecular rapid communications* **32**, 431-437, doi:Doi 10.1002/Marc.201000558 (2011).
- 25 Misra, A. C., Bhaskar, S., Clay, N. & Lahann, J. Multicompartmental Particles for Combined Imaging and siRNA Delivery. *Advanced Materials* **24**, 3850-3856, doi:Doi 10.1002/Adma.201200372 (2012).
- 26 Saha, S. *et al.* Chemically Controlled Bending of Compositionally Anisotropic Microcylinders. *Angew Chem Int Edit* **51**, 660-665, doi:Doi 10.1002/Anie.201105387 (2012).
- 27 Lv, W. P. *et al.* Anisotropic Janus Catalysts for Spatially Controlled Chemical Reactions. *Small* **8**, 3116-3122, doi:Doi 10.1002/Sml.201200192 (2012).
- 28 Lee, K. J. *et al.* Spontaneous shape reconfigurations in multicompartmental microcylinders. *P Natl Acad Sci USA* **109**, 16057-16062, doi:Doi 10.1073/Pnas.1213669109 (2012).
- 29 Park, T. H. *et al.* Photoswitchable Particles for On-Demand Degradation and Triggered Release. *Small* **9**, 3051-3057, doi:Doi 10.1002/Sml.201201921 (2013).
- 30 Sokolovskaya, E., Yoon, J., Misra, A. C., Brase, S. & Lahann, J. Controlled Microstructuring of Janus Particles Based on a Multifunctional Poly(ethylene glycol). *Macromolecular rapid communications* **34**, 1554-1559, doi:Doi 10.1002/Marc.201300427 (2013).
- 31 Rahmani, S., Park, T. H., Dishman, A. F. & Lahann, J. Multimodal delivery of irinotecan from microparticles with two distinct compartments. *J Control Release* **172**, 239-245, doi:Doi 10.1016/J.Jconrel.2013.08.017 (2013).
- 32 Yoon, J., Kota, A., Bhaskar, S., Tuteja, A. & Lahann, J. Amphiphilic Colloidal Surfactants Based on Electrohydrodynamic Cojetting. *ACS Appl Mater Inter* **5**, 11281-11287, doi:Doi 10.1021/Am403516h (2013).
- 33 Rahmani, S. *et al.* Chemically Orthogonal Three-Patch Microparticles. *Angew Chem Int Edit* **53**, 2332-2338, doi:Doi 10.1002/Anie.201310727 (2014).
- 34 Bhaskar, S. *et al.* Engineering, Characterization and Directional Self-Assembly of Anisotropically Modified Nanocolloids. *Small* **7**, 812-819, doi:Doi 10.1002/Sml.201001695 (2011).
- 35 Yoshida, M. *et al.* Structurally Controlled Bio-hybrid Materials Based on Unidirectional Association of Anisotropic Microparticles with Human Endothelial Cells. *Advanced Materials* **21**, 4920-+, doi:Doi 10.1002/Adma.200901971 (2009).

- 36 Mandal, S., Bhaskar, S. & Lahann, J. Micropatterned Fiber Scaffolds for Spatially Controlled Cell Adhesion. *Macromolecular rapid communications* **30**, 1638-1644, doi:Doi 10.1002/Marc.200900340 (2009).
- 37 Bhaskar, S., Roh, K. H., Jiang, X. W., Baker, G. L. & Lahann, J. Spatioselective Modification of Bicompartmental Polymer Particles and Fibers via Huisgen 1,3-Dipolar Cycloaddition. *Macromolecular rapid communications* **29**, 1655-1660, doi:Doi 10.1002/Marc.200800459 (2008).
- 38 Verma, A. *et al.* Surface-structure-regulated cell-membrane penetration by monolayer-protected nanoparticles. *Nature materials* **7**, 588-595, doi:Doi 10.1038/Nmat2202 (2008).
- 39 Roh, K. H., Yoshida, M. & Lahann, J. Water-stable biphasic nanocolloids with potential use as anisotropic imaging probes. *Langmuir* **23**, 5683-5688, doi:Doi 10.1021/La062274r (2007).
- 40 Panyam, J., Sahoo, S. K., Prabha, S., Bargar, T. & Labhasetwar, V. Fluorescence and electron microscopy probes for cellular and tissue uptake of poly(D,L-lactide-co-glycolide) nanoparticles. *Int J Pharm* **262**, 1-11, doi:Doi 10.1016/S0378-5173(03)00295-3 (2003).
- 41 Foulkes, W. D., Smith, I. E. & Reis, J. S. Triple-Negative Breast Cancer. *New Engl J Med* **363**, 1938-1948, doi:Doi 10.1056/Nejmra1001389 (2010).
- 42 Dent, R. *et al.* Triple-negative breast cancer: Clinical features and patterns of recurrence. *Clin Cancer Res* **13**, 4429-4434, doi:Doi 10.1158/1078-0432.Ccr-06-3045 (2007).
- 43 Bosch, A., Eroles, P., Zaragoza, R., Vina, J. R. & Lluch, A. Triple-negative breast cancer: Molecular features, pathogenesis, treatment and current lines of research. *Cancer Treat Rev* **36**, 206-215, doi:Doi 10.1016/J.Ctrv.2009.12.002 (2010).
- 44 Smith, M. C. P. *et al.* CXCR4 regulates growth of both primary and metastatic breast cancer. *Cancer Res* **64**, 8604-8612, doi:Doi 10.1158/0008-5472.Can-04-1844 (2004).
- 45 Mizell, J., Smith, M., Li, B. D. L., Ampil, F. & Chu, Q. Y. D. Overexpression of CXCR4 in Primary Tumor of Patients with HER-2 Negative Breast Cancer was Predictive of a Poor Disease-Free Survival: A Validation Study. *Ann Surg Oncol* **16**, 2711-2716, doi:Doi 10.1245/S10434-009-0551-0 (2009).
- 46 Luker, K. E. & Luker, G. D. Functions of CXCL12 and CXCR4 in breast cancer. *Cancer Lett* **238**, 30-41, doi:Doi 10.1016/J.Canlet.2005.06.021 (2006).
- 47 Luker, K. E. *et al.* Scavenging of CXCL12 by CXCR7 promotes tumor growth and metastasis of CXCR4-positive breast cancer cells. *Oncogene* **31**, 4750-4758, doi:Doi 10.1038/Onc.2011.633 (2012).
- 48 Chu, Q. Y. D. *et al.* High Chemokine Receptor CXCR4 Level in Triple Negative Breast Cancer Specimens Predicts Poor Clinical Outcome. *Journal of Surgical Research* **159**, 689-695, doi:Doi 10.1016/J.Jss.2008.09.020 (2010).
- 49 Liang, Z. X. *et al.* Blockade of invasion and metastasis of breast cancer cells via targeting CXCR4 with an artificial microRNA. *Biochem Bioph Res Co* **363**, 542-546, doi:Doi 10.1016/J.Bbrc.2007.09.007 (2007).
- 50 Liang, Z. X. *et al.* Silencing of CXCR4 blocks breast cancer metastasis. *Cancer Res* **65**, 967-971 (2005).
- 51 Bunschoten, A. *et al.* Targeted non-covalent self-assembled nanoparticles based on human serum albumin. *Biomaterials* **33**, 867-875, doi:Doi 10.1016/J.Biomaterials.2011.10.005 (2012).

- 52 Burger, J. A. & Peled, A. CXCR4 antagonists: targeting the microenvironment in leukemia and other cancers. *Leukemia* **23**, 43-52, doi:Doi 10.1038/Leu.2008.299 (2009).
- 53 Tamamura, H. *et al.* T140 analogs as CXCR4 antagonists identified as anti-metastatic agents in the treatment of breast cancer. *FEBS letters* **550**, 79-83, doi:Doi 10.1016/S0014-5793(03)00824-X (2003).
- 54 De Clercq, E. The bicyclam AMD3 100 story. *Nat Rev Drug Discov* **2**, 581-587, doi:Doi 10.1038/Nrd1134 (2003).
- 55 Burger, J. A. & Kipps, T. J. CXCR4: a key receptor in the crosstalk between tumor cells and their microenvironment. *Blood* **107**, 1761-1767, doi:Doi 10.1182/Blood-2005-08-3182 (2006).
- 56 Le Bon, B. *et al.* AMD3100 conjugates as components of targeted nonviral gene delivery systems: Synthesis and in vitro transfection efficiency of CXCR4-expressing cells. *Bioconjugate Chem* **15**, 413-423, doi:Doi 10.1021/Bc034220o (2004).
- 57 Li, J., Zhu, Y., Hazeldine, S. T., Li, C. Y. & Oupicky, D. Dual-Function CXCR4 Antagonist Polyplexes To Deliver Gene Therapy and Inhibit Cancer Cell Invasion. *Angew Chem Int Edit* **51**, 8740-8743, doi:Doi 10.1002/Anie.201203463 (2012).
- 58 Cashen, A. F., Nervi, B. & DiPersio, J. AMD3100: CXCR4 antagonist and rapid stem cell-mobilizing agent. *Future Oncol* **3**, 19-27, doi:10.2217/14796694.3.1.19 (2007).
- 59 Bhaskar, S., Hitt, J., Chang, S. W. L. & Lahann, J. Multicompartmental Microcylinders. *Angew Chem Int Edit* **48**, 4589-4593, doi:Doi 10.1002/Anie.200806241 (2009).
- 60 Maris, J. M. Medical Progress: Recent Advances in Neuroblastoma. *New Engl J Med* **362**, 2202-2211, doi:Doi 10.1056/Nejmra0804577 (2010).
- 61 Brodeur, G. M. Neuroblastoma: Biological insights into a clinical enigma. *Nat Rev Cancer* **3**, 203-216, doi:Doi 10.1038/Nrc1014 (2003).
- 62 Cohn, S. L. *et al.* The International Neuroblastoma Risk Group (INRG) Classification System: An INRG Task Force Report. *J Clin Oncol* **27**, 289-297, doi:Doi 10.1200/Jco.2008.16.6785 (2009).
- 63 Bossi, G. *et al.* Echocardiographic evaluation of patients cured of childhood cancer: A single center study of 117 subjects who received anthracyclines. *Med Pediatr Oncol* **36**, 593-600, doi:Doi 10.1002/Mpo.1135 (2001).
- 64 Simon, T., Hero, B., Dupuis, W., Selle, B. & Berthold, F. The incidence of hearing impairment after successful treatment of neuroblastoma. *Klin Padiatr* **214**, 149-152, doi:Doi 10.1055/S-2002-33179 (2002).
- 65 Zhang, H. W. *et al.* Imaging the Norepinephrine Transporter in Neuroblastoma: A Comparison of [F-18]-MFBG and I-123-MIBG. *Clin Cancer Res* **20**, 2182-2191, doi:Doi 10.1158/1078-0432.Ccr-13-1153 (2014).
- 66 Lashford, L. S., Hancock, J. P. & Kemshead, J. T. Metaiodobenzylguanidine (Metaiodobenzylguanidine) Uptake and Storage in the Human Neuroblastoma Cell-Line Sk-N-Be(2c). *Int J Cancer* **47**, 105-109, doi:Doi 10.1002/Ijc.2910470119 (1991).
- 67 Howman-Giles, R., Shaw, P. J., Uren, R. F. & Chung, D. K. V. Neuroblastoma and other neuroendocrine tumors. *Semin Nucl Med* **37**, 286-302, doi:Doi 10.1053/J.Semnuclmed.2007.02.009 (2007).
- 68 Grunwald, F. & Ezziddin, S. I-131-Metaiodobenzylguanidine Therapy of Neuroblastoma and Other Neuroendocrine Tumors. *Semin Nucl Med* **40**, 153-163, doi:Doi 10.1053/J.Semnuclmed.2009.11.004 (2010).
- 69 Matthay, K. K. *et al.* Correlation of tumor and whole-body dosimetry with tumor response and toxicity in refractory neuroblastoma. treated with I-131-MIBG. *J Nucl Med* **42**, 1713-1721 (2001).

- 70 Garaventa, A. *et al.* I-131-metaiodobenzylguanidine (I-131-MIBG) therapy for residual neuroblastoma: a mono-institutional experience with 43 patients. *Brit J Cancer* **81**, 1378-1384, doi:Doi 10.1038/Sj.Bjc.6694223 (1999).
- 71 Vaidyanathan, G. Meta-iodobenzylguanidine and analogues: chemistry and biology. *Q J Nucl Med Mol Im* **52**, 351-368 (2008).
- 72 Vallabhajosula, S. & Nikolopoulou, A. Radioiodinated Metaiodobenzylguanidine (MIBG): Radiochemistry, Biology, and Pharmacology. *Semin Nucl Med* **41**, 324-333, doi:Doi 10.1053/J.Semnuclmed.2011.05.003 (2011).
- 73 Zhu, M. Y., Kim, C. H., Hwang, D. Y., Baldessarini, R. J. & Kim, K. S. Effects of desipramine treatment on norepinephrine transporter gene expression in the cultured SK-N-BE(2)M17 cells and rat brain tissue. *J Neurochem* **82**, 146-153, doi:Doi 10.1046/J.1471-4159.2002.00953.X (2002).

Chapter 4

Carriers with Long Circulation Half-Lives

4.1 Background and Motivation

Targeted therapies, in particular those employing drug-loaded micro- and nanoscale carriers, have great potential in the treatment of disease with high specificity and minimal side effects.¹⁻⁴ However, few carrier-based therapies have reached clinical use, in part because many physiological processes can interact with such carriers that hinder their efficacy.^{5,6} One main contributor to the obstruction of effective particulate-based targeted therapies is the immune system.^{1,7-9} Resident macrophages in the liver, spleen, and lungs, comprising part of the reticuloendothelial system (RES), are adept at phagocytosis of foreign materials at both the nano- and micro- scale, removing them from circulation.^{7,8} As a result, an overwhelming majority of carriers, untargeted and targeted, do not accumulate at the desired target, such as a tumor, but rather in the liver and spleen, as has been shown by many studies.^{3,7,8} Hence, much effort has been made to understand how particulate carriers interact with monocytes and macrophages, and how they may be designed and fabricated to avoid uptake by such cells of the RES.

Several surface modification techniques used to form nonfouling surfaces have been adapted for use in *in vivo* therapeutic applications. Specifically, surface modification of carriers with poly(ethylene glycol) (PEG) is a common technique employed to increase their circulation half-lives.^{3,7,10,11} This improvement in circulation is attributed to high hydrophilicity of PEG – a shell of water molecules is thought to surround PEG chains, reducing protein adhesion, as is the case in nonfouling surfaces, thereby helping prevent direct uptake by phagocytic cells and indirect uptake via opsonization.^{7,10} Additionally, studies have indicated that the density of PEG chains on the surface of a particle is critical for adequate nonfouling properties.¹⁰

PEG is not the only polymer that can be used for surface modification of carriers to evade clearance by the RES – other hydrophilic macromolecules, including zwitterionic polymers and polysaccharides like alginate and dextran, have also been shown to have nonfouling properties.^{1,7,12-14} Furthermore, properties besides hydrophilic surface characteristics affect clearance of carriers. Particular sizes, shapes, mechanical properties, and immobilization of cell surface markers have been implicated in helping evade the immune system.¹⁵⁻¹⁷

Despite these developments, advanced particulate carriers are still fairly inefficient at targeting, being effectively removed by the RES, albeit with somewhat marginally prolonged circulation half-lives.^{7,13} Furthermore, while a large body of evidence has accumulated, it is nonetheless difficult to generalize results in part due to the wide variability in carriers and their fabrication.⁵ Additionally, it is possible that successful evasion of the immune system may be achieved with a combination of specific physical properties, but most carrier systems are capable of achieving only a few of the desired properties.

Electrohydrodynamic (EHD) co-jetting is a technique, based on the more commonly known electrospraying and electrospinning, that allows for the fabrication of multicompartmental carriers, providing the spatial and temporal control over their composition.¹⁸⁻²⁷ EHD co-jetted carriers can hence exhibit multiple functionalities depending on the materials incorporated.^{22,24,26,27} In particular, a library of chemically functionalized polylactides (PLAs), synthesized previously, can be incorporated to allow for surface modification with a defined density of functional groups displayed on the surface depending on the relative amount of functional PLA incorporated in a jetting solution.²⁸

Incorporation of functionalized PLAs may provide few functional groups at the surface of a carrier, as most of the material is contained in its bulk. It then may be desirable to increase the number of functional groups presented at the surface as a way to increase the surface density of any ligand that may be immobilized. Sodium alginate (Na-alg) is an anionic polysaccharide that has been shown to may have some nonfouling properties,¹⁴ and has pendant acid groups allowing for further functionalization. Immobilization of Na-alg using a functionalized PLA may hence allow for multiple acid groups to be presented, providing a high surface density of functional groups.

Here, we show that EHD co-jetting maybe used to fabricate well-defined carriers that can be used to systematically explore various surface modifications and their ability to evade the immune system. Specifically, we demonstrate how high densities of PEG and CD47 can be selectively immobilized via Na-alg immobilization, and study their *in vitro* uptake by macrophages.

4.2 Methods

Materials. Poly(DL-lactide-co-glycolic acid) (PLGA, 85:15 lactide:glycolide, 50-75 kg/mol), blue fluorescent poly[(*m*-phenylenevinylene)-alt-(2,5-dihexyloxy-*p*-phenylenevinylene)] (PMPDHPV), green fluorescent poly[tris(2,5-bis(hexyloxy)-1,4-phenylenevinylene)-alt-(1,3-phenylenevinylene)] (PTBHPVPV), sodium alginate (120k – 190k g/mol, Na-alg), amine terminated methoxypolyethylene glycol (5000 g/mol, mPEG-NH₂), Tween 20, chloroform (CHCl₃) and N,N'-dimethylformamide (DMF) were purchased from Sigma-Aldrich. Paraformaldehyde, and 1-ethyl-3-(3-dimethylaminopropyl)carbodiimide hydrochloride (EDC) was obtained from Thermo Scientific. Rhodamine labeled, amine terminated polyethylene glycol (5000 g/mol, rhod-PEG-NH₂) was purchased from Nanocs. A recombinant mouse CD47 chimera was purchased from R & D Systems. Phosphate buffered saline (PBS), ProLong Gold, Alexa Fluor 488 phalloidin, ethidium homodimer-1, Dulbecco's Modified Eagle Medium (DMEM), fetal bovine serum (FBS), and penicillin-streptomycin (pen-strep) were obtained from Invitrogen. Raw264.7 cells were purchased from ATCC. Benzophenone functionalized PLA (PLA-BZ) was synthesized as described previously, courtesy of Dr. Hakan Durmaz.

Fabrication of microcylinders and microspheres. Bicompartmental fibers were made via EHD co-jetting the following solutions at 0.05 ml/hr and 12.9 – 13.5 kV: 1) 30 w/v% PLGA with <0.05 mg/ml PTBHPVPV, and 2) 37.5 w/v% 4:1 w/w PLGA:PLA-BZ with <0.05 mg/ml PMPDHPV, both in 95:5 v/v CHCl₃:DMF. Microcylinders were made by processing fibers using a previously described procedure.^{24,29,30} Microspheres were fabricated by the co-jetting of 6.25 w/v% 4:1 w/w PLGA:PLA-BZ in 1:1 v/v CHCl₃:DMF at 0.2 ml/hr and ~10.05 kV. Control carriers were obtained by collecting the jetted microspheres, dispersing in 0.1 v/v% tween20/PBS with tip sonication (pulsing, 1 s on, 5 s off, amplitude = 21%), and straining through a 40 µm filter.

Selective alginate immobilization. For alginate immobilization, microcylinders were suspended in a 1 w/v% Na-alg solution in .01 v/v% tween 20/PBS. The suspension was stirred in a 12-well plate and exposed to short wavelength UV light for 30 minutes using a UVP UVGL-25 Compact UV Lamp. After washing three times with .01 v/v% Tween 20/PBS by centrifuging and resuspending, the microcylinders were then incubated in 5 mg/ml EDC and 1 mg/ml rho-PEG-NH₂ for 1 hour. The cylinders were then washed three more times, and imaged using an Olympus FluoView 500 Confocal Laser Scanning Microscope (CLSM).

Preparation of surface modified carriers. PEGylated and CD47-immobilized carriers were obtained by immobilizing Na-alg (as describe above) on control carriers. PEG and CD47 immobilization were done by EDC coupling for 1 hour, using 5 mg/ml EDC with either 10 mg/ml mPEG-NH₂ or 5 µg/ml CD47. After reaction, PEG- and CD47- immobilized carriers were washed three times by centrifugation and resuspension.

In vitro studies. Raw264.7 cells were cultured in DMEM with 10% FBS and 1X pen-strep. For all studies, particles were incubated with cells for one hour at 100 µg/ml. Cells were seeded on circular glass coverslips in 12-well plates and on 6-well plates. After incubation, cells were washed with PBS three times. Cells on coverslips were fixed in 4% paraformaldehyde for 30 minutes, stained with phalloidin and ethidium homodimer, mounted on glass slides with ProLong Gold, and imaged with an Olympus FluoView 500 CLSM. Cells in 6-well plates were trypsinized and washed, and analyzed with a Beckman Coulter MoFlo Astrios.

4.3 Results and Discussion

To show that Na-alg can be selectively immobilized using a functionalized PLA, the photoreactive PLA-BZ, we first fabricated multicompartamental microcylinders with PLA-BZ incorporated in one side. Fluorescent dyes were also incorporated to label the compartments; a blue dye labels the PLA-BZ containing compartment, and a green dye labels the pure PLGA (control) compartment. These microcylinders were then immobilized with Na-alg, by UV irradiation, and, to show that the acid groups of immobilized Na-alg are still functional, EDC coupling with rhod-PEG-NH₂ was performed, as depicted in Figure 4-1a. As shown by the confocal images in Figures 4-1b – 4-1d, red fluorescence from the rhodamine labeled PEG is localized to the surface of the blue compartment. We can hence

conclude that alginate, with acid groups capable of subsequent functionalization, can be selectively immobilized using PLA-BZ.

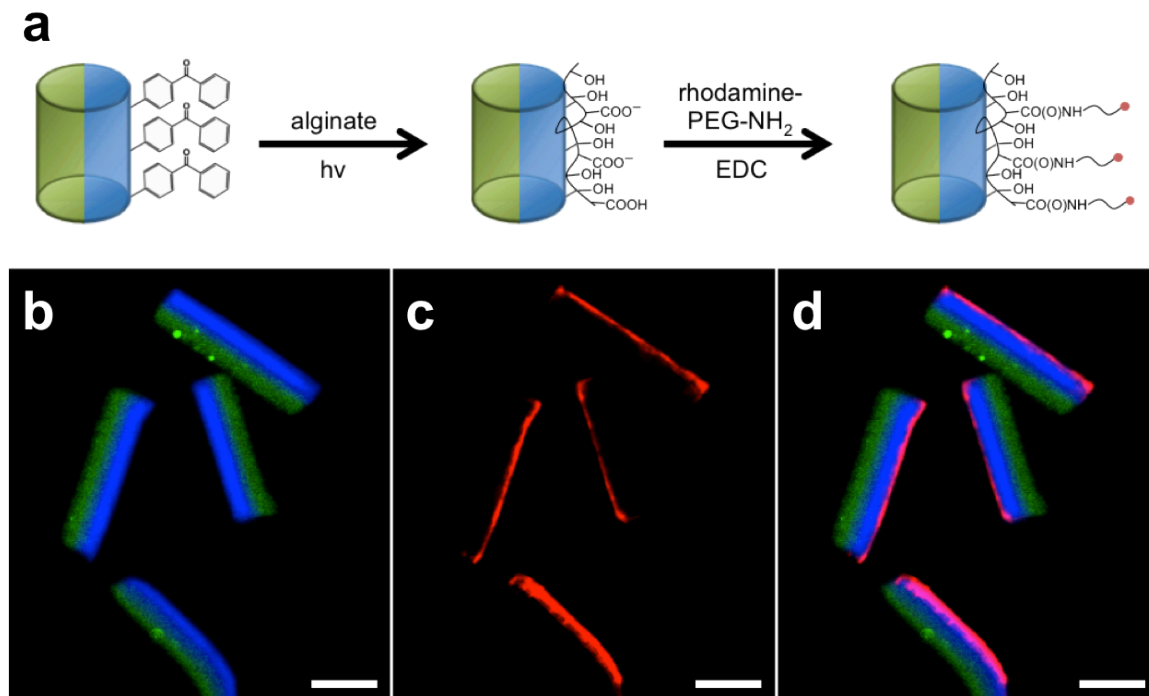


Figure 4-1. (a) Reaction scheme for selective immobilization of alginate. (b), (c) Confocal images of microcylinders (blue and green) after alginate immobilization and EDC coupling to rhodamine labeled PEG (red). (d) Overlay of (b) & (c). Scale bars are 20 μm .

We then fabricated three groups of carriers labeled with a blue fluorescent dye, a control group with no surface immobilization, and two groups of carriers immobilized with Na-alg, with further EDC coupling of either mPEG-NH₂ or CD47. To assess their ability to evade the immune system, these carriers were then incubated with Raw264.7, a murine-derived macrophage cell line. We observe a higher number of control carriers internalized by cells (Figure 4-2a) compared to the number of internalized PEG immobilized and CD47 immobilized carriers (Figures 4-2b and 4-2c, respectively). Of note, compared to the surface functionalized carriers, many more control carriers may be bound to cell surfaces, as we can observe several carriers outlining the contour of the cells delineated by the phalloidin-stained actin (green).

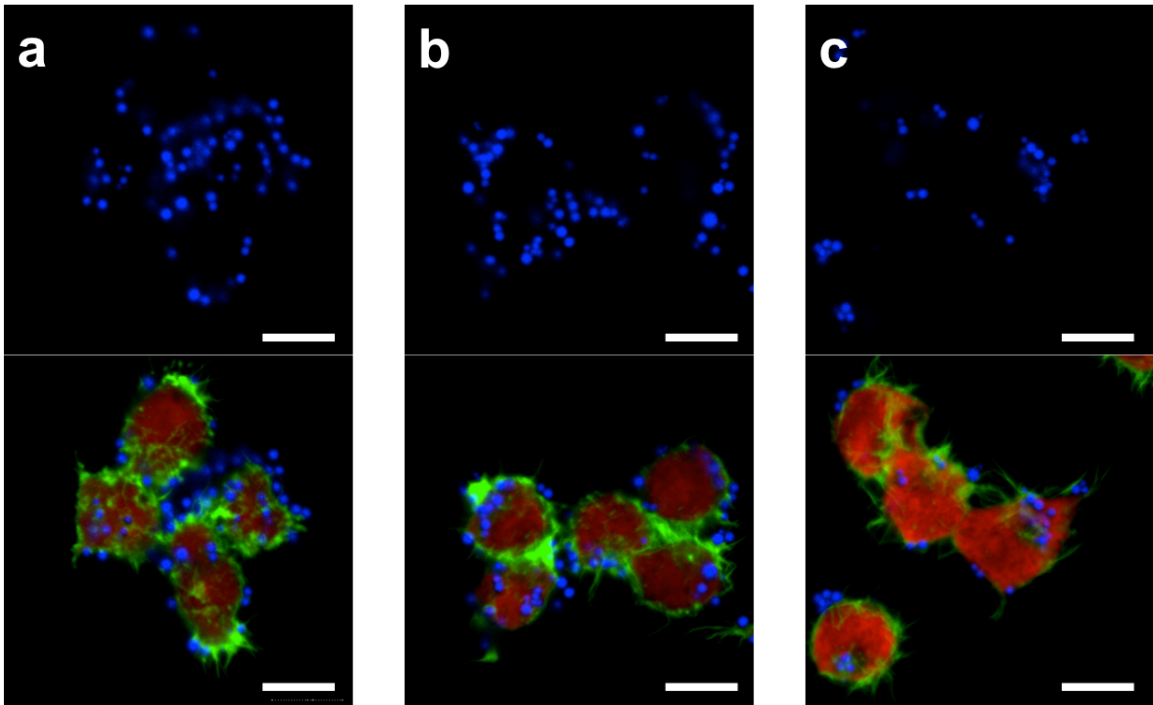


Figure 4-2. CLSM images of Raw264.7 cells (red & green) after 1 hour incubation with (a) control, (b) PEG immobilized, and (c) CD47 immobilized carriers (blue). Scale bars are 10 μm .

To obtain a more quantitative understanding of the difference in uptake between these different carriers, flow cytometry was performed. As shown in figure 4-3a, we observe that 95% of cells exhibit blue fluorescence from control carriers, indicating their high degree of association with cells, be it nonspecific binding or uptake (as flow cytometry cannot distinguish between particles bound to the surface of or internalized within a cell). In comparison, 87% of cells had associated with PEG immobilized carriers and 79% of cells associate with CD47 immobilized carriers (Figures 4-3b and 4-3c, respectively). Hence, based on this analysis, the immobilization of PEG or CD47 may only marginally decrease overall binding or uptake, in that most cells still associate with at least some carriers.

The choice of gating, however, can greatly affect the analysis of the data from flow cytometry. While virtually all cells were measured to have some degree of fluorescence, we may note a difference between the various carriers incubated in the percentage of cells with an exceptionally high degree of fluorescence. Gating at two orders of magnitude above the baseline, we see that 51% of cells incubated with control carriers have a high degree of fluorescence (Figure 4-3d). In contrast, only around 6.6% and 8.6% of cells incubated with

PEG immobilized and CD47 immobilized carriers, respectively, have such high fluorescence, as seen in Figures 4-3e and 4-3f, respectively. A higher degree of fluorescence may correlate with a higher number of carriers binding to or internalized by cells. Hence, we may infer that surface immobilization with PEG or CD47 may indeed help prevent binding or uptake by Raw264.7, even though most cells will still associate with some carriers. Considering, as seen from the confocal images in Figure 4-2, the high number of control carriers bound to the surface, the difference in the percentage of cells with high fluorescence in the flow cytometry data may be due to prevention of initial binding to cell surface. Nonetheless, there is still a basal level of uptake by cells seen in by confocal, and is reflected in flow cytometry as most cells exhibit at least some fluorescence.

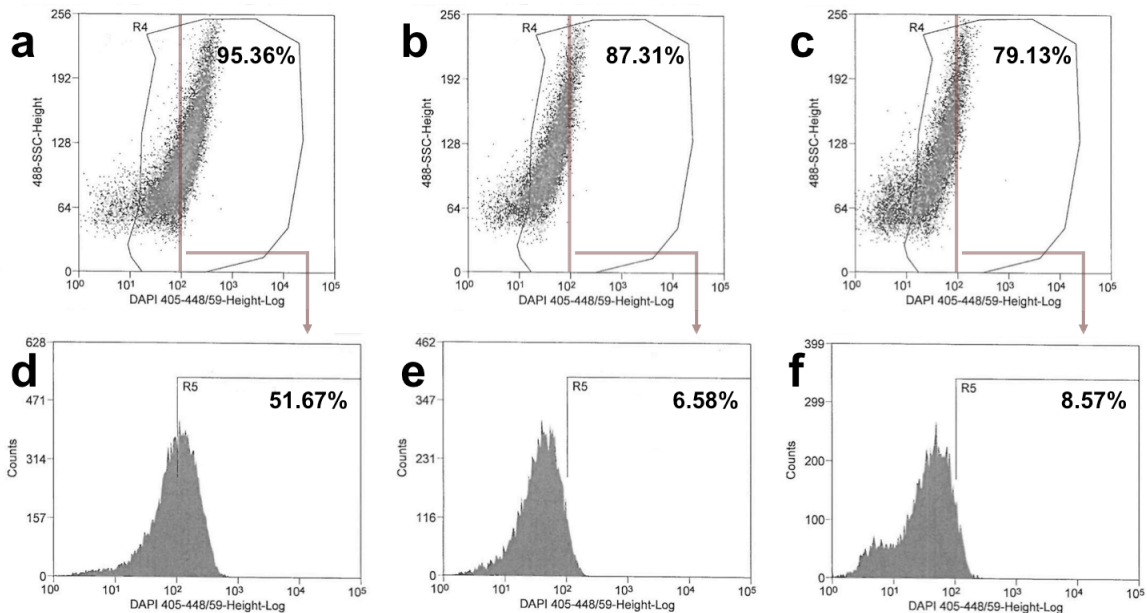


Figure 4-3. Flow cytometry data for Raw264.7 cells after incubation with (a) control, (b) PEG immobilized, and (c) CD47 immobilized carriers. (d) – (f) Corresponding histogram representations of flow data with gating at two orders of magnitude above baseline.

4.4 Summary

We have shown how alginate may be selectively immobilized on the surface of PLGA based carriers and can be used for subsequent functionalization with PEG and CD47. Additionally, we observe *in vitro* that PEG and CD47 immobilized carriers associate less with macrophages than carriers with an unmodified surface. Control carriers are both internalized and bound to the surface in higher numbers than PEG and CD47 immobilized carriers. While neither PEG nor CD47 completely blocks association to macrophages, they

may serve to reduce the degree of binding or uptake, as noted by the differences in high degrees of fluorescence seen by flow cytometry. We noted no difference between PEG and CD47; it is possible that any observable difference may have been masked by the non-fouling effect of alginate,¹⁴ but even assuming this possibility implies that the difference is be small.

Much further work is required to elucidate several other factors contributing to these carriers binding to cells. For example, determining the exact density of PEG and CD47 on the surface, and whether it can be controlled based on the amount of alginate immobilized would allow for systematic studies of how PEG may compare to CD47. Additionally, developing strategies to immobilize both PEG and CD47 will allow for the exploration of any potential synergistic prevention of binding, which may allow for significant improvement in circulation times *in vivo*.

4.5 References

- 1 Brannon-Peppas, L. & Blanchette, J. O. Nanoparticle and targeted systems for cancer therapy. *Advanced drug delivery reviews* **64**, 206-212, doi:Doi 10.1016/J.Addr.2012.09.033 (2012).
- 2 Cho, K. J., Wang, X., Nie, S. M., Chen, Z. & Shin, D. M. Therapeutic nanoparticles for drug delivery in cancer. *Clin Cancer Res* **14**, 1310-1316, doi:Doi 10.1158/1078-0432.Ccr-07-1441 (2008).
- 3 Peer, D. *et al.* Nanocarriers as an emerging platform for cancer therapy. *Nat Nanotechnol* **2**, 751-760, doi:Doi 10.1038/Nnano.2007.387 (2007).
- 4 Wickline, S. A. & Lanza, G. M. Nanotechnology for molecular imaging and targeted therapy. *Circulation* **107**, 1092-1095, doi:Doi 10.1161/01.Cir.0000059651.17045.77 (2003).
- 5 Petros, R. A. & DeSimone, J. M. Strategies in the design of nanoparticles for therapeutic applications. *Nat Rev Drug Discov* **9**, 615-627, doi:Doi 10.1038/Nrd2591 (2010).
- 6 Whitehead, K. A., Langer, R. & Anderson, D. G. Knocking down barriers: advances in siRNA delivery. *Nat Rev Drug Discov* **8**, 129-138, doi:Doi 10.1038/Nrd2742 (2009).
- 7 Alexis, F., Pridgen, E., Molnar, L. K. & Farokhzad, O. C. Factors affecting the clearance and biodistribution of polymeric nanoparticles. *Mol Pharmaceut* **5**, 505-515, doi:Doi 10.1021/Mp800051m (2008).
- 8 Longmire, M., Choyke, P. L. & Kobayashi, H. Clearance properties of nano-sized particles and molecules as imaging agents: considerations and caveats. *Nanomedicine-Uk* **3**, 703-717, doi:Doi 10.2217/17435889.3.5.703 (2008).
- 9 Zhang, L. *et al.* Nanoparticles in medicine: Therapeutic applications and developments. *Clin Pharmacol Ther* **83**, 761-769, doi:Doi 10.1038/Sj.Clpt.6100400 (2008).
- 10 Owens, D. E. & Peppas, N. A. Opsonization, biodistribution, and pharmacokinetics of polymeric nanoparticles. *Int J Pharm* **307**, 93-102, doi:Doi 10.1016/J.Ijpharm.2005.10.010 (2006).
- 11 Otsuka, H., Nagasaki, Y. & Kataoka, K. PEGylated nanoparticles for biological and pharmaceutical applications. *Advanced drug delivery reviews* **55**, 403-419, doi:Doi 10.1016/S0169-409x(02)00226-0 (2003).
- 12 Yuan, Y. Y. *et al.* Surface Charge Switchable Nanoparticles Based on Zwitterionic Polymer for Enhanced Drug Delivery to Tumor. *Advanced Materials* **24**, 5476-5480, doi:Doi 10.1002/Adma.201202296 (2012).
- 13 Moghimi, S. M., Hunter, A. C. & Murray, J. C. Long-circulating and target-specific nanoparticles: Theory to practice. *Pharmacol Rev* **53**, 283-318 (2001).
- 14 Kodiyan, A., Silva, E. A., Kim, J., Aizenberg, M. & Mooney, D. J. Surface Modification with Alginate-Derived Polymers for Stable, Protein-Repellent, Long-Circulating Gold Nanoparticles. *ACS nano* **6**, 4796-4805, doi:Doi 10.1021/Nn205073n (2012).
- 15 Geng, Y. *et al.* Shape effects of filaments versus spherical particles in flow and drug delivery. *Nat Nanotechnol* **2**, 249-255, doi:Doi 10.1038/Nnano.2007.70 (2007).
- 16 Merkel, T. J. *et al.* Using mechanobiological mimicry of red blood cells to extend circulation times of hydrogel microparticles. *P Natl Acad Sci USA* **108**, 586-591, doi:Doi 10.1073/Pnas.1010013108 (2011).
- 17 Rodriguez, P. L. *et al.* Minimal "Self" Peptides That Inhibit Phagocytic Clearance and Enhance Delivery of Nanoparticles. *Science* **339**, 971-975, doi:Doi 10.1126/Science.1229568 (2013).

- 18 Roh, K. H., Martin, D. C. & Lahann, J. Biphasic Janus particles with nanoscale anisotropy. *Nature materials* **4**, 759-763, doi:Doi 10.1038/Nmat1486 (2005).
- 19 Roh, K. H., Martin, D. C. & Lahann, J. Triphasic nanocolloids. *J Am Chem Soc* **128**, 6796-6797, doi:Doi 10.1021/Ja060836n (2006).
- 20 Lee, K. J. *et al.* Compartmentalized Photoreactions within Compositionally Anisotropic Janus Microstructures. *Macromolecular rapid communications* **32**, 431-437, doi:Doi 10.1002/Marc.201000558 (2011).
- 21 Saha, S. *et al.* Chemically Controlled Bending of Compositionally Anisotropic Microcylinders. *Angew Chem Int Edit* **51**, 660-665, doi:Doi 10.1002/Anie.201105387 (2012).
- 22 Misra, A. C., Bhaskar, S., Clay, N. & Lahann, J. Multicompartmental Particles for Combined Imaging and siRNA Delivery. *Advanced Materials* **24**, 3850-3856, doi:Doi 10.1002/Adma.201200372 (2012).
- 23 Hwang, S. & Lahann, J. Differentially Degradable Janus Particles for Controlled Release Applications. *Macromolecular rapid communications* **33**, 1178-1183, doi:Doi 10.1002/Marc.201200054 (2012).
- 24 Lee, K. J. *et al.* Spontaneous shape reconfigurations in multicompartmental microcylinders. *P Natl Acad Sci USA* **109**, 16057-16062, doi:Doi 10.1073/Pnas.1213669109 (2012).
- 25 Park, T. H. *et al.* Photoswitchable Particles for On-Demand Degradation and Triggered Release. *Small* **9**, 3051-3057, doi:Doi 10.1002/Sml.201201921 (2013).
- 26 Rahmani, S., Park, T. H., Dishman, A. F. & Lahann, J. Multimodal delivery of irinotecan from microparticles with two distinct compartments. *J Control Release* **172**, 239-245, doi:Doi 10.1016/J.Jconrel.2013.08.017 (2013).
- 27 Yoon, J., Kota, A., Bhaskar, S., Tuteja, A. & Lahann, J. Amphiphilic Colloidal Surfactants Based on Electrohydrodynamic Cojetting. *Acs Appl Mater Inter* **5**, 11281-11287, doi:Doi 10.1021/Am403516h (2013).
- 28 Rahmani, S. *et al.* Chemically Orthogonal Three-Patch Microparticles. *Angew Chem Int Edit* **53**, 2332-2338, doi:Doi 10.1002/Anie.201310727 (2014).
- 29 Bhaskar, S., Hitt, J., Chang, S. W. L. & Lahann, J. Multicompartmental Microcylinders. *Angew Chem Int Edit* **48**, 4589-4593, doi:Doi 10.1002/Anie.200806241 (2009).
- 30 Sokolovskaya, E., Yoon, J., Misra, A. C., Brase, S. & Lahann, J. Controlled Microstructuring of Janus Particles Based on a Multifunctional Poly(ethylene glycol). *Macromolecular rapid communications* **34**, 1554-1559, doi:Doi 10.1002/Marc.201300427 (2013).

Chapter 5

Towards Multifunctional Carriers

5.1 Background and Motivation

The potential of targeted carrier-based therapies for the treatment of many diseases, especially resistant and metastatic cancers, has yet to be realized, perhaps attributable to the complex interactions between carriers and physiological processes. These barriers can result in several challenges, including the effective delivery of therapeutic functionalities, evasion of the immune system, and efficient accumulation at the desired target.¹⁻⁴ Addressing these challenges has resulted in a multitude of carrier systems composed of various materials and having varying physicochemical properties.⁴⁻¹⁰ However, to date, there have not been many successful approaches to fabricate carriers that may address all barriers that targeted carriers encounter *in vivo*.

Carriers capable of efficacious targeted therapy may require complex compositions, incorporating properties of several different carrier systems that have been previously successful in addressing a specific barrier. Hence, the development of multicompartmental carriers that may incorporate different functional materials that are spatially segregated, and therefore decoupled, may have the potential to address multiple barriers at once. Electrohydrodynamic (EHD) co-jetting is a technique that allows for rapid production of such multicompartmental carriers.¹¹⁻²⁰

In the past few chapters, we have shown that EHD co-jetted carriers retain the functionalities of materials that are incorporated into them. Here, we demonstrate a few carrier systems that incorporate multiple functional materials from the previous chapters to generate multifunctional carriers, and show some preliminary results of how they may be used *in vitro* and *in vivo*. Specifically, we show multifunctional carriers capable of live

imaging, and multifunctional carriers capable of targeting and cytosolic delivery through endosome sensing.

5.2 Methods

Materials. Poly(DL-lactide-co-glycolic acid) (PLGA, 85:15 lactide:glycolide, 50-75 kg/mol), polyethyleneimine (PEI, Mn = 60 kg/mol, Mw = 760 kg/mol), blue fluorescent poly[(*m*-phenylenevinylene)-alt-(2,5-dihexyloxy-*p*-phenylenevinylene)] (PMPDHPV), glycol chitosan (GC, 80 kg/mol), polyethylene glycol diglycidyl ether (PEGDE, 526 g/mol), Pluronic F127, Tween 20, diisopropylamine (DIA), and all solvents were purchased from Sigma. Dithiobis(succinimidyl propionate) [DSP] and paraformaldehyde were obtained from Thermo Scientific. Small interfering RNA against GFP (siRNA-GFP) was purchased from Qiagen. Azide functionalized IRDye 800CW (IRDye800CW-N₃) was obtained from LI-COR Biosciences. Phosphate buffered saline (PBS), ProLong Gold, Dulbecco's Modified Eagle Medium (DMEM), fetal bovine serum (FBS), non-essential amino acids (NEAA), and penicillin-streptomycin (pen-strep) were obtained from Invitrogen. MDA-MB-231 cells expressing a CXCR4-GFP fusion protein were provided by the Luker group. Acrylate functionalized PLA (PLA-acryl) and cyclooctyne functionalized PLA (PLA-COT) were synthesized as described previously, courtesy of Dr. Hakan Durmaz.

Fabrication of multifunctional carriers. For *in vivo* imaging studies, GC based carriers were synthesized by EHD co-jetting the following solutions at 0.1 ml/hr, 30 cm, and 11.85 – 12.3 kV: 1) 1.25 w/v% 4:1 w/w PLGA:PLA-COT with .05 mg/ml IRDye800CW-N₃ in 100% DMF, and 2) 1.3 w/v% 10:1:2 w/w/w GC:Pluronic F127:PEGDE with 5 nmol/ml siRNA-GFP in 1:1 v/v DMF:H₂O. The solution with IRDye800CW-N₃ was allowed to stir for at least one hour to allow for click reaction to occur with PLA-COT, and PEGDE was added just prior to jetting to minimize crosslinking during solution preparation. After jetting, GC based carriers were crosslinked for 72 hours at 37 °C. For *in vitro* CXCR4 targeting and siRNA delivery, PLGA/PEI carriers were fabricated similar to a previously described procedure,¹⁹ by co-jetting the following solutions at 0.1 ml/hr, 30 cm, and ~11.25 kV: 1) 5.5 w/v% 10:1 w/w PLGA:PLA-acryl with < 0.05 mg/ml PMPDHPV, and 2) 5.25 w/v% 10:10:1 w/w/w PLGA:PEI:DSP with 5 nmol/ml siRNA-GFP, both in 1:1 v/v CHCl₃:DMF. The PEI based carriers were allowed to crosslink for 72 hours at room temperature before surface modification. AMD3100-immobilized carriers were synthesized by incubating 2 mg of PEI

based carriers with ~2-3 mg AMD3100 in 2 ml of 0.1 v/v% Tween 20/PBS, followed by adding 14 μ l DIA. The mixture was rotated for 3 hours and then washed three times by centrifugation and resuspension. Control carriers were synthesized under the same conditions as AMD3100-immobilized carriers, except no AMD3100 was added.

Imaging studies. Imaging studies were performed using severe combined immunodeficiency (SCID) mice implanted subcutaneously with bilateral GFP expressing MDA-MB-231 tumors. Carriers were injected intratumorally or intravenously. At an hour and 24 hours after injection, after anesthetizing the animals, they were imaged with a PerkinElmer IVIS scanner. All IVIS imaging and *in vivo* studies were performed by the Luker group.

Targeting studies. CXCR4-GFP expressing MDA-MB-231 cells were cultured in DMEM with 10% FBS, 1x NEAA, and 1x pen-strep. For targeting study, cells were seeded at 5000 cells/well in a 96 well plate. The following day cells were incubated with different concentrations of AMD3100 immobilized and unmodified control carriers, both loaded with siRNA-GFP, for 1 hour. 48 hours after incubation, GFP fluorescence intensities of the cells were measured using a Biotek Synergy2 plate reader.

5.3 Results and Discussion

We first explored the possibility of *in vivo* delivery of multifunctional carriers that contain both a NIR imaging agent loaded in a PLGA compartment and an endosome-sensing compartment with siRNA against GFP (Figure 5-1a). We coupled IRDye800CW-N₃ to PLGA-COT by copper-free click chemistry, while the jetting solution was prepared. The NIR dye would then be tethered to a hydrophobic polymer, preventing release of the dye in aqueous media. We chose glycol chitosan (GC) as the endosome-sensing material as opposed to PEI, which we have used *in vitro*, because of concerns about the toxicity of PEI. As seen by the SEM and TEM images in Figures 5-1b and 5-1c, respectively, the carriers are around 50-100 nm in diameter. The measure hydrodynamic diameter by dynamic light scattering (DLS), however, is around 260 nm, most likely due to the swelling of the GC compartment. We confirmed that we can see these NIR dye loaded carriers using the IVIS live animal scanner, as seen in Figure 5-1d.

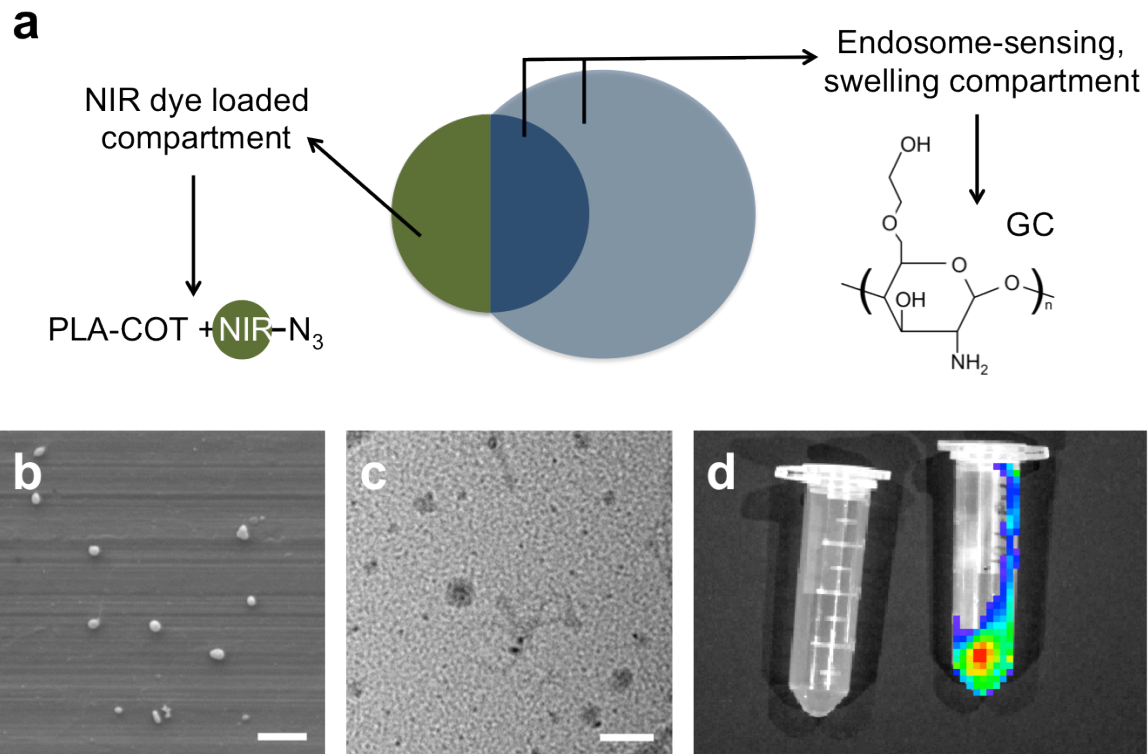


Figure 5-1. (a) Design of multifunctional GC based carrier, showing key functional materials used in each compartment. (b) SEM and (c) TEM image of the EHD co-jetted GC based carriers. (d) IVIS image, with NIR fluorescence overlaid, of a blank eppendorf (left) and an eppendorf containing the GC based carriers. Scale bars are (b) 1 μm and (c) 200 nm.

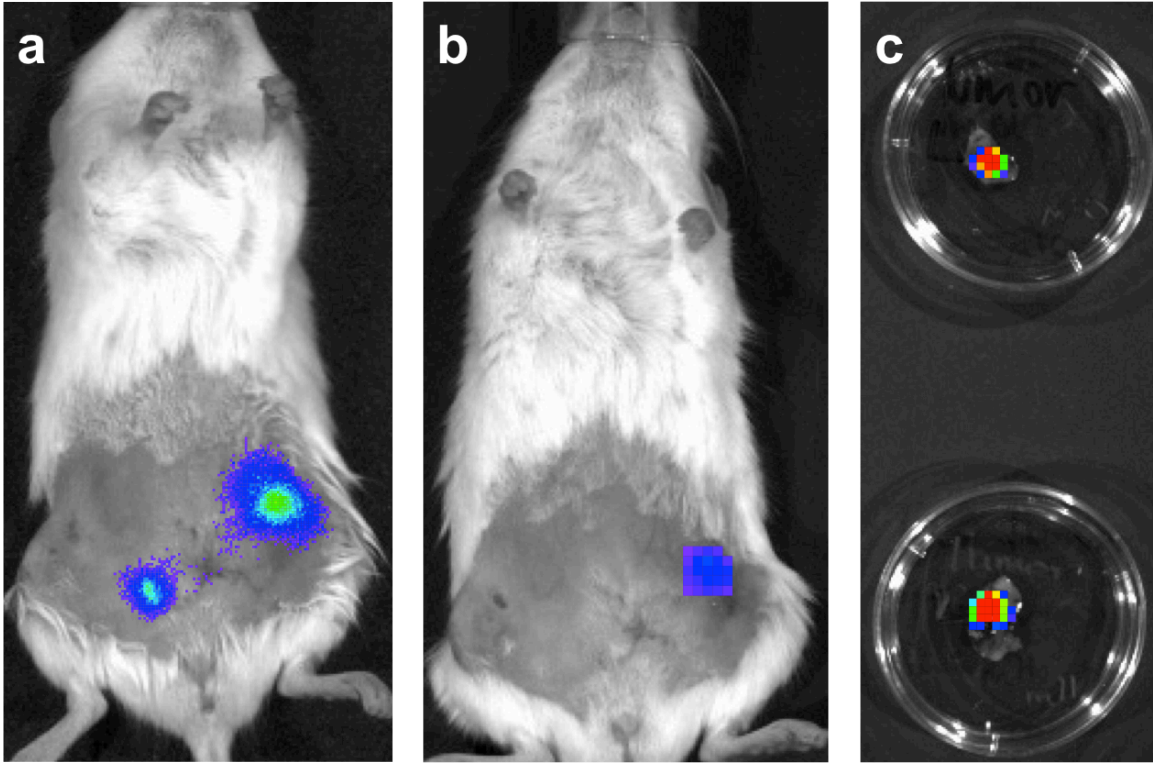


Figure 5-2. IVIS imaging, with NIR fluorescence overlaid, of mouse injected directly into the tumors with GC based carriers. (a) 1 hour and (b) 24 hours after injection. (c) Image of excised tumors, showing localization of carriers.

Next, we injected these carriers intratumorally with the goal of simultaneously silencing tumor GFP expression, via endosome-sensing, and monitoring their location. The imaging functionality of the carriers works considerably well, as they can be clearly seen in both tumors of a mouse one hour after injection (Figure 5-2a). However, 24 hours later, carriers in only one of the tumors could be visualized (Figure 5-2b), implying that the carriers may be degraded or cleared from the tumors. On the other hand, we may clearly see NIR fluorescence signal from the excised tumors (Figure 5-2c). Hence, there are enough carriers still concentrated in the tumor to generate a signal, but not necessarily during live imaging after 24 hours, which may be attributed to noise from tissues surrounding the tumors.

Of note, we did not observe any decrease in GFP fluorescence by the tumors, perhaps due to several reasons. Because of issues of diffusion, the carriers may not have spread throughout the tumor, and so even if the cells surrounding the injection site were successfully silenced, their lack of fluorescence may not be noted from the high overall GFP expression of the whole tumor. Additionally, significant necrosis was observed at the center of the tumors,

and the dead cancer cells here would not express GFP, as is shown in Figure 5-3. Hence the silencing effect of carriers injected in the center of the tumors would be unobservable, especially given the difficulty of carriers to diffuse to the edges of the tumor where viable cells remain.

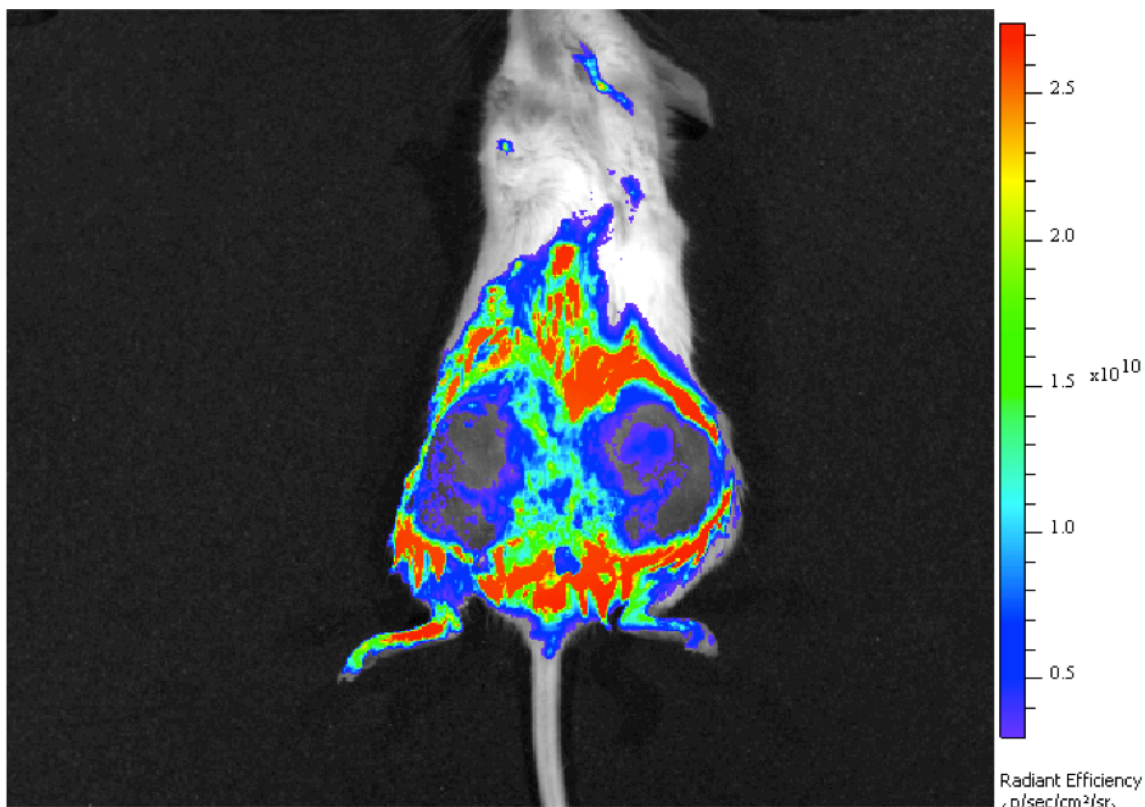


Figure 5-3. IVIS imaging, with GFP fluorescence overlay, of mouse (Figure 5-2) implanted with bilateral GFP expressing MDA-MB-231 tumors. The centers of the tumors are necrotic.

We then injected the GC based carriers through the tail vein to see if any of them may localize at the tumors due to the enhanced permeation and retention (EPR) effect.^{1,21-23} As seen in Figure 5-4a, 1 hour after injection, the highest signal from the carriers was observed in the liver and lungs, where significant parts of the reticuloendothelial system (RES) reside.^{2,24} 24 hours after injection, no live signal is detectable (Figure 5-4b), and after excision of the organs, the carriers were confirmed to be primarily in the liver and lungs, as seen in Figures 5-4c and 5-4d, respectively. It may be concluded that the carriers were rapidly cleared by the RES. Even though we may expect some passive targeting to the tumors due to the EPR effect, undetectable accumulation of carriers were observed in the tumors, which may be due to the positively charged character of the carriers (due to GC)

and their lack of passivated surfaces by poly(ethylene glycol) (PEG).¹ One may expect some nonfouling properties by the hydrophilic polysaccharide GC, but the positive charge from the amines may be too toxic, rendering the polymer ineffective for evasion of the RES. As these carriers cannot be injected and accumulate in tumors by EPR effect, multifunctional carriers with active targeting are necessary.

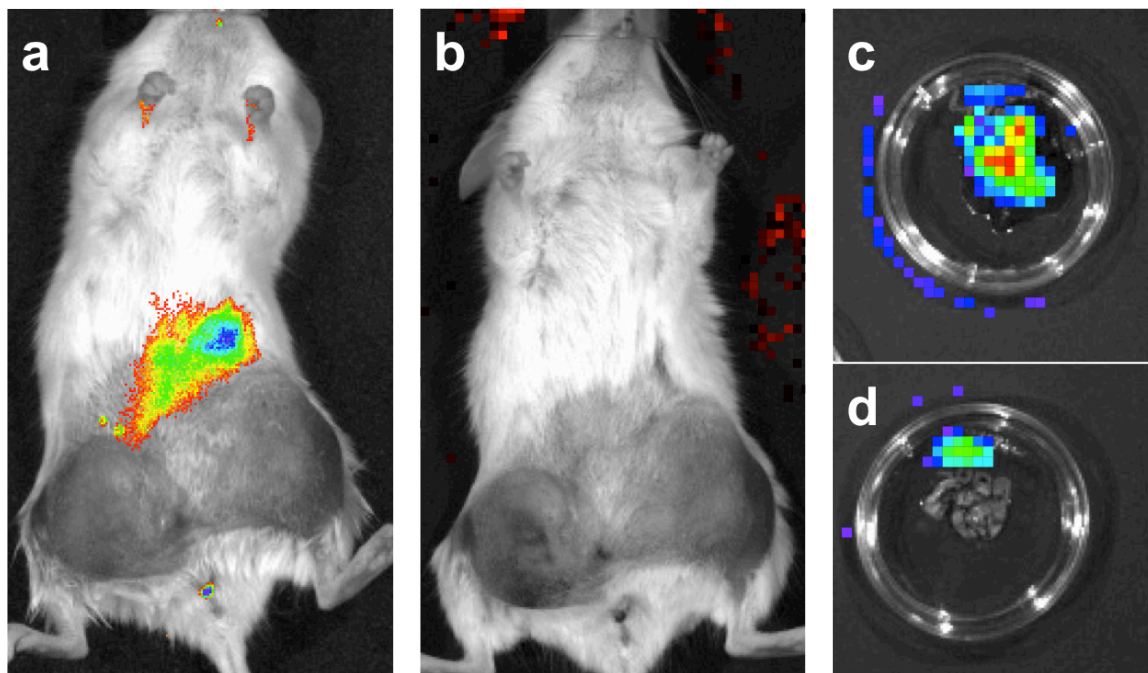


Figure 5-4. IVIS imaging, with NIR fluorescence overlaid, of mouse injected with GC based carriers through tail vein. (a) 1 hour and (b) 24 hours after injection. Image of excised (c) liver and (d) lungs, showing localization of carriers.

Finally, we fabricated a multifunctional carrier, based on PEI, that incorporates targeting functionalities, and assessed its functionalities *in vitro*. Even though PEI can be toxic, we have shown PEI based carriers to be effective at endosome-sensing. In this case, we incorporate PLA-acryl in one compartment to allow for selective surface immobilization of AMD3100, as described in Chapter 3. We prepared AMD3100-immobilized (targeted) and control (untargeted) carriers, both loaded with siRNA against GFP, and incubated them at various concentrations with CXCR4-GFP expressing breast cancer cells for one hour. As seen in Figure 5-5, after 48 hours we observe that both carriers cause GFP knockdown at a concentration of 100 $\mu\text{g}/\text{ml}$. Moreover, cells incubated with AMD3100-immobilized carriers expressed less GFP than those incubated with untargeted carriers, indicating that the targeted carriers may be uptaken at a higher rate, resulting in higher delivery of siRNA. It is

also may be noted that at 50 $\mu\text{g/ml}$, cells incubated with targeted carriers have significant GFP knockdown while cells incubated with untargeted carriers do not. Therefore, targeting may allow for lower doses than used previously to achieve GFP silencing, hence increasing the therapeutic index relative to untargeted carriers.

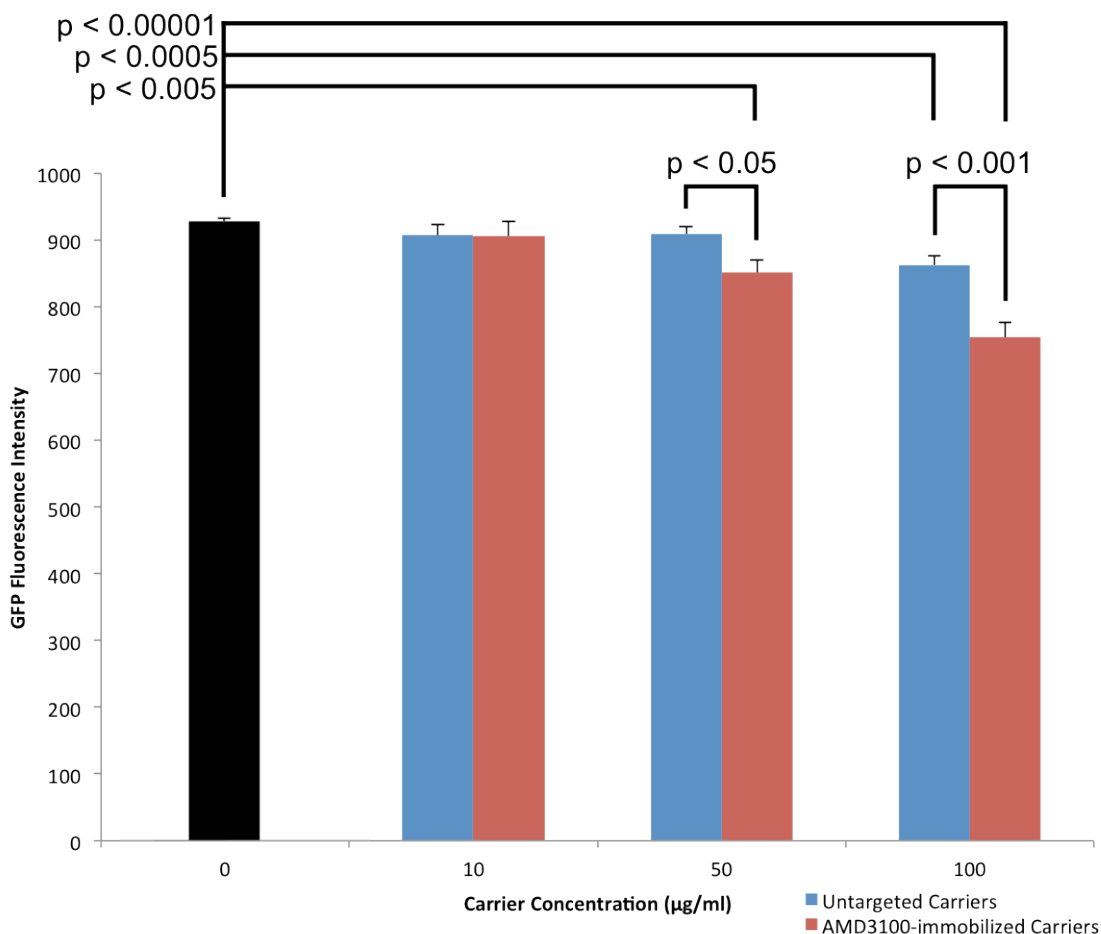


Figure 5-5. GFP fluorescence intensities of cells measured by plate reader 48 hours after one hour incubation with AMD3100-immobilized and untargeted (no AMD3100) carriers.

5.4 Summary

Here we have shown how EHD co-jetting may be used to incorporate multiple functionalities, developed in the previous chapters, into a single carrier, allowing for the potential to address multiple barriers in carrier-based therapy. We first combine endosome-sensing functionality with imaging to develop carriers that are capable of live imaging and cytosolic delivery using a commercially available NIR fluorescent dye and GC as an endosome-sensing material. The carriers can be imaged clearly 1 hour after injection,

and may be observed in some cases after 24 hours. However, further work is necessary to improve the imaging functionality to be able to visualize the carriers for extended durations. Additionally, GFP knockdown was not observed *in vivo* by either intratumoral or IV injection, indicating that additional functionalities are required for effective silencing, including targeting.

We hence fabricated targeted carriers that could effectively knockdown GFP *in vitro* more than untargeted carriers, and may be used effectively at lower doses. Therefore, these carriers demonstrated both targeting and cytosolic delivery functionalities. Given these results, we may further explore the efficacy of these carriers *in vivo*.

5.6 References

- 1 Petros, R. A. & DeSimone, J. M. Strategies in the design of nanoparticles for therapeutic applications. *Nat Rev Drug Discov* **9**, 615-627, doi:Doi 10.1038/Nrd2591 (2010).
- 2 Alexis, F., Pridgen, E., Molnar, L. K. & Farokhzad, O. C. Factors affecting the clearance and biodistribution of polymeric nanoparticles. *Mol Pharmaceut* **5**, 505-515, doi:Doi 10.1021/Mp800051m (2008).
- 3 Brannon-Peppas, L. & Blanchette, J. O. Nanoparticle and targeted systems for cancer therapy. *Advanced drug delivery reviews* **64**, 206-212, doi:Doi 10.1016/J.Addr.2012.09.033 (2012).
- 4 Whitehead, K. A., Langer, R. & Anderson, D. G. Knocking down barriers: advances in siRNA delivery. *Nat Rev Drug Discov* **8**, 129-138, doi:Doi 10.1038/Nrd2742 (2009).
- 5 Allen, T. M. Liposomal drug delivery. *Curr Opin Colloid In* **1**, 645-651 (1996).
- 6 Liong, M. *et al.* Multifunctional inorganic nanoparticles for imaging, targeting, and drug delivery. *ACS nano* **2**, 889-896, doi:Doi 10.1021/Nn800072t (2008).
- 7 Slowing, I. I., Vivero-Escoto, J. L., Wu, C. W. & Lin, V. S. Y. Mesoporous silica nanoparticles as controlled release drug delivery and gene transfection carriers. *Advanced drug delivery reviews* **60**, 1278-1288, doi:Doi 10.1016/J.Addr.2008.03.012 (2008).
- 8 Kumari, A., Yadav, S. K. & Yadav, S. C. Biodegradable polymeric nanoparticles based drug delivery systems. *Colloid Surface B* **75**, 1-18, doi:Doi 10.1016/J.Colsurfb.2009.09.001 (2010).
- 9 Zhang, L. *et al.* Nanoparticles in medicine: Therapeutic applications and developments. *Clin Pharmacol Ther* **83**, 761-769, doi:Doi 10.1038/Sj.Clpt.6100400 (2008).
- 10 Ganta, S., Devalapally, H., Shahiwala, A. & Amiji, M. A review of stimuli-responsive nanocarriers for drug and gene delivery. *J Control Release* **126**, 187-204, doi:Doi 10.1016/J.Jconrel.2007.12.017 (2008).
- 11 Roh, K. H., Martin, D. C. & Lahann, J. Biphasic Janus particles with nanoscale anisotropy. *Nature materials* **4**, 759-763, doi:Doi 10.1038/Nmat1486 (2005).
- 12 Roh, K. H., Martin, D. C. & Lahann, J. Triphasic nanocolloids. *J Am Chem Soc* **128**, 6796-6797, doi:Doi 10.1021/Ja060836n (2006).
- 13 Roh, K. H., Yoshida, M. & Lahann, J. Water-stable biphasic nanocolloids with potential use as anisotropic imaging probes. *Langmuir* **23**, 5683-5688, doi:Doi 10.1021/La062274r (2007).
- 14 Bhaskar, S., Roh, K. H., Jiang, X. W., Baker, G. L. & Lahann, J. Spatioselective Modification of Bicompartamental Polymer Particles and Fibers via Huisgen 1,3-Dipolar Cycloaddition. *Macromolecular rapid communications* **29**, 1655-1660, doi:Doi 10.1002/Marc.200800459 (2008).
- 15 Yoshida, M. *et al.* Structurally Controlled Bio-hybrid Materials Based on Unidirectional Association of Anisotropic Microparticles with Human Endothelial Cells. *Advanced Materials* **21**, 4920-+, doi:Doi 10.1002/Adma.200901971 (2009).
- 16 Lim, D. W., Hwang, S., Uzun, O., Stellacci, F. & Lahann, J. Compartmentalization of Gold Nanocrystals in Polymer Microparticles using Electrohydrodynamic Co-Jetting. *Macromolecular rapid communications* **31**, 176-182, doi:Doi 10.1002/Marc.200900597 (2010).
- 17 Lee, K. J. *et al.* Compartmentalized Photoreactions within Compositionally Anisotropic Janus Microstructures. *Macromolecular rapid communications* **32**, 431-437, doi:Doi 10.1002/Marc.201000558 (2011).

- 18 Lee, K. J. *et al.* Spontaneous shape reconfigurations in multicompartmental microcylinders. *P Natl Acad Sci USA* **109**, 16057-16062, doi:Doi 10.1073/Pnas.1213669109 (2012).
- 19 Misra, A. C., Bhaskar, S., Clay, N. & Lahann, J. Multicompartmental Particles for Combined Imaging and siRNA Delivery. *Advanced Materials* **24**, 3850-3856, doi:Doi 10.1002/Adma.201200372 (2012).
- 20 Saha, S. *et al.* Chemically Controlled Bending of Compositionally Anisotropic Microcylinders. *Angew Chem Int Edit* **51**, 660-665, doi:Doi 10.1002/Anie.201105387 (2012).
- 21 Maeda, H., Wu, J., Sawa, T., Matsumura, Y. & Hori, K. Tumor vascular permeability and the EPR effect in macromolecular therapeutics: a review. *J Control Release* **65**, 271-284, doi:Doi 10.1016/S0168-3659(99)00248-5 (2000).
- 22 Fang, J., Nakamura, H. & Maeda, H. The EPR effect: Unique features of tumor blood vessels for drug delivery, factors involved, and limitations and augmentation of the effect. *Advanced drug delivery reviews* **63**, 136-151, doi:Doi 10.1016/J.Addr.2010.04.009 (2011).
- 23 Acharya, S. & Sahoo, S. K. PLGA nanoparticles containing various anticancer agents and tumour delivery by EPR effect. *Advanced drug delivery reviews* **63**, 170-183, doi:Doi 10.1016/J.Addr.2010.10.008 (2011).
- 24 Longmire, M., Choyke, P. L. & Kobayashi, H. Clearance properties of nano-sized particles and molecules as imaging agents: considerations and caveats. *Nanomedicine-Uk* **3**, 703-717, doi:Doi 10.2217/17435889.3.5.703 (2008).

Chapter 6

Conclusions and Future Directions

6.1 Impact of Multicompartmental Carriers in Targeted Therapy

In these studies we have shown how electrohydrodynamic (EHD) co-jetting may be used to fabricate several different multicompartmental carriers that can retain the functionalities of the materials incorporated, and shown how they may be used for some therapeutic applications. In addition, we present carrier systems that may uniquely be fabricated by EHD co-jetting and provide unique functionalities, such as the targeting of cell membranes. Furthermore, we begin to show how these carriers may be used to simultaneously address multiple barriers affecting targeted therapy.

Significant further development, however, is required before EHD co-jetted carriers may be comparable to other well-developed carriers, and be able to effectively address several barriers. Development of more reproducible fabrication methods capable of high yields is necessary. Additionally, optimization of the carriers developed in this work and additional *in vitro* and *in vivo* studies are needed.

6.2 Towards Mass Production of Multicompartmental Carriers

6.2.1 Uniformity and Reproducibility

One of the primary issues with EHD co-jetting is its ability to consistently produce uniform particles. The co-jetting process is sensitive not only to various solution (concentration, solvent, etc.) and process parameters (voltage, flow rate, etc.), but also to environmental factors such as humidity. Despite the wide parameter space and its effect on the morphology and size of the resulting carriers, we have observed some common elements regarding the non-uniformity and irreproducibility of co-jetted carriers. In particular, we generally observe a bimodal distribution, regardless of solvent, flow rate, or concentration, as shown in Figures 6-1a – 6-1c. The bimodal distribution is often with respect to the size of

the carriers, although the morphology can be different as well (Figure 6-1d). Additionally, it appears that regardless of the size regime, microscale or nanoscale, two distinct populations are observed (Figures 6-1e and 6-1f).

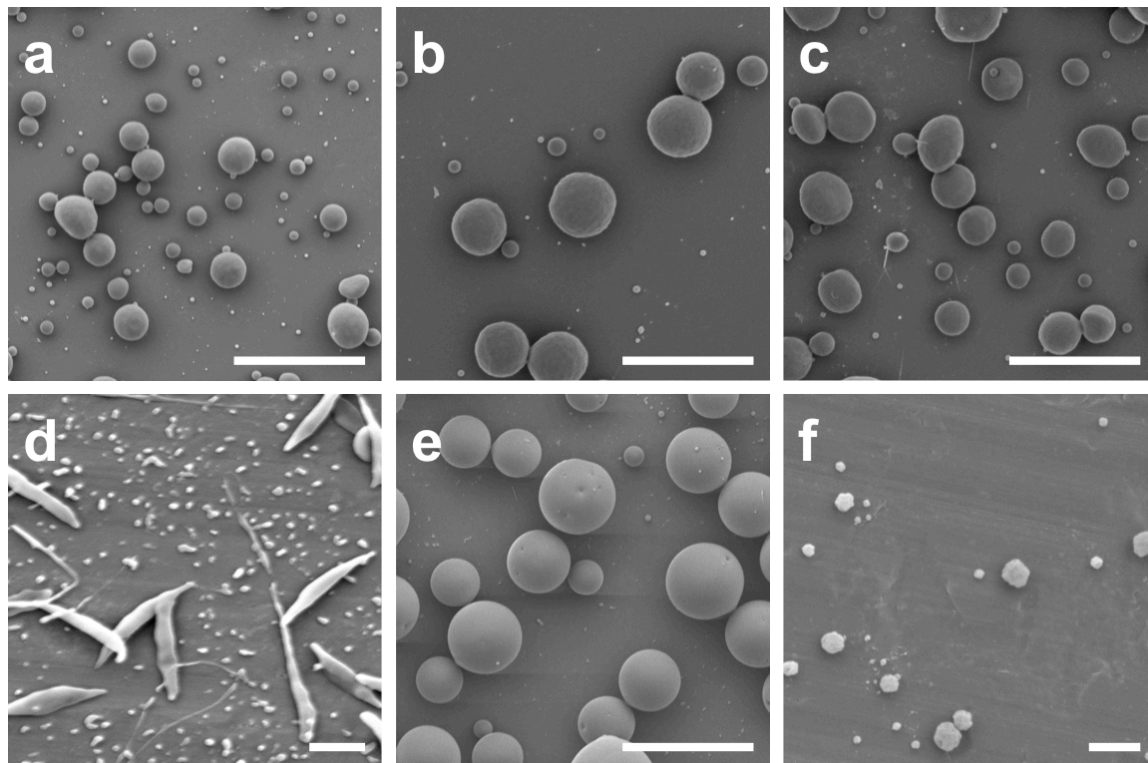


Figure 6-1. SEM images showing the bimodal distribution of various carriers fabricated EHD co-jetting with different parameters. (a) PLGA particles from a pure DMF solution. (b) PLGA particles from a 1:1 v/v THF:DMF. (c) Particles made from the same solution as (b), but at a five times higher flow rate. (d) PLGA particles from a low concentration solution. (e) Low molecular weight polystyrene particles. (f) High molecular weight polystyrene particles. Scale bars are (a, b, c, e) 10 μm and (d, f) 2 μm .

One clear way to improve the monodispersity of co-jetted carriers is by purification. By centrifuging, one may enrich the supernatant with smaller particles, and a pellet of larger particles will form. As shown by DLS, co-jetted PLGA and PEI based carriers have a clear bimodal size distribution (Figure 3-2a). We may isolate the smaller size carriers by centrifugation and removal of the pellet. However, this process is highly dependent on how carefully the pellet and supernatant are separated, as some particles may remain in both fractions, as evidenced by the tail in the DLS of the supernatant shown in Figure 3-2b. Additionally, this purification results in significant losses of particles. Hence, it would be ideal to fabricate uniform carriers directly from EHD co-jetting.

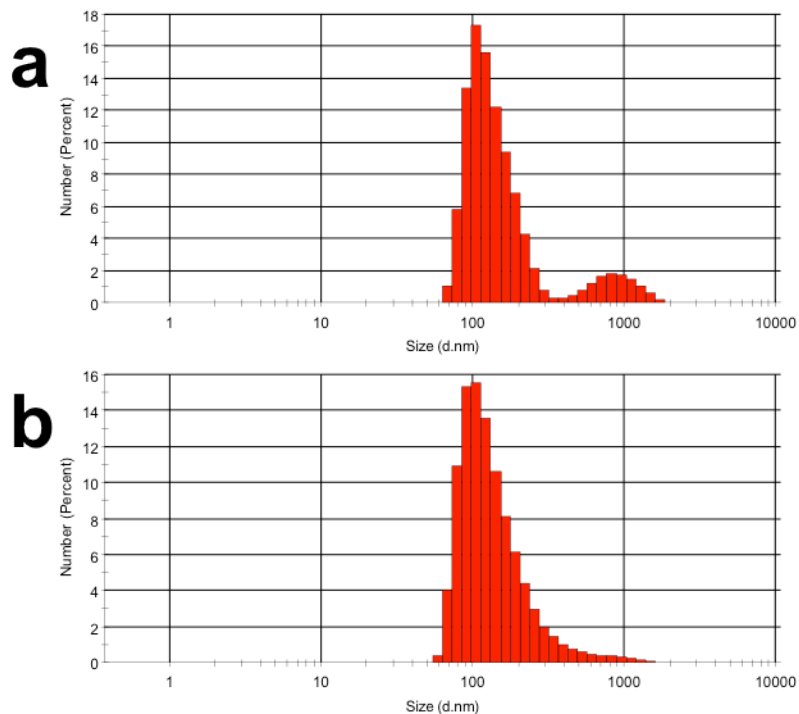


Figure 6-2. DLS of PEI based nanocarriers described in Chapter 2, (a) before centrifugation, and (b) the supernatant after centrifugation.

One possible way to generate reproducible, uniform carriers is to use particular solvents. Specifically, in the case of co-jetting PLGA, we explored incorporating a poor solvent, ethanol (EtOH). We suspected that EtOH would help reduce chain entanglement between individual PLGA chains, and thus allow for more uniform droplet production, and therefore more uniform particles. Compared to jetting in pure *N,N'*-dimethylformamide (DMF), shown in Figure 3-3a, jetting in a mixture of EtOH and DMF results in large particles that are more spherical than teardrop-shaped (Figure 3-3b). We find that EtOH can be incorporated into two solvent systems to help improve morphology as well; the heterogeneous rough shape large particles jetted in a mixture of acetone and DMF (Figure 3-3c) can be improved by using a mixture of acetone, DMF, and EtOH (Figure 3-3d). However, in both two and three solvent systems, we can still observe a bimodal distribution with respect to size.

The general observation of bimodal distributions suggests an underlying mechanism, or several, that account for the resulting two different populations, and is a fundamental aspect of the co-jetting process. One explanation may be the formation of satellite droplets, small droplets that break from the primary droplets from the jet, a phenomenon typically observed in electrospaying, but not necessarily predicted by Rayleigh instability theory.¹⁻⁴

Another explanation might be that transient jet behavior contributes significantly to particles fabrication. While a steady state jet may have fairly uniform droplet sizes, the size of the droplets resulting from initialization of the jet till it reaches a steady state may not be so predictable.⁵ Additionally, while generally a jet may remain stable for extended durations, there are occasionally instabilities that may occur periodically. The instabilities and other transient behaviors may account for the bimodal distribution. However, assuming this explanation to be valid, it is not necessarily clear which of the two populations are resulting from these phenomenon. More fundamental studies, theoretical and experimental, may provide more insight and perhaps allow for better control of the co-jetting process to formulate more uniformly sized carriers.

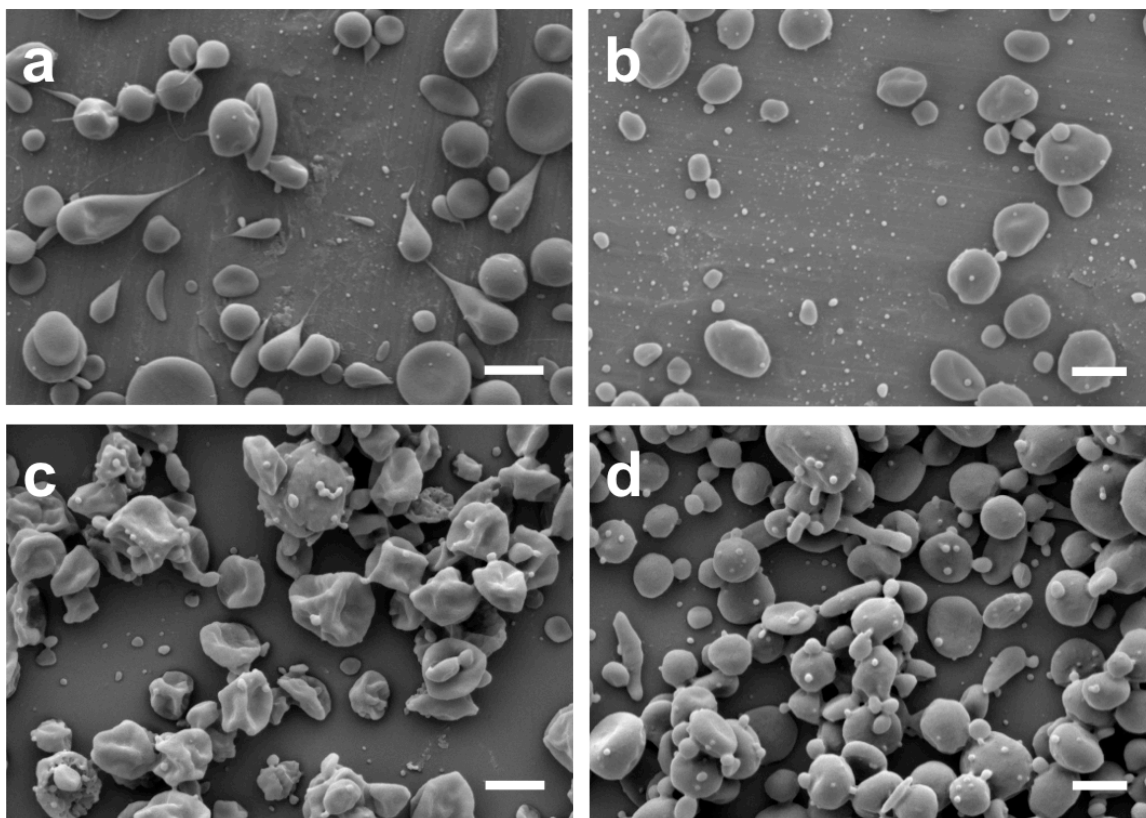


Figure 6-3. PLGA particles jetted from (a) pure DMF, (b) 1:1 v/v EtOH:DMF, (c) 1:1 v/v acetone:DMF, and (d) 1:1:2 v/v/v acetone:EtOH:DMF. Scale bars are 2 μm .

6.2.2 High Yield Production

Another challenge in using EHD co-jetting is its ability to generate high yields of nanoscale carriers. Generally, a flat, grounded collector is used to collect co-jetted particles, which are then subsequently harvested mechanically by scraping them off with a blade. However, this

method can cause aggregation of particles that are difficult to disperse in solution, hence resulting in large losses. Co-jetting into a liquid bath can avoid the necessity of harvesting steps, and may result in less aggregation as each individual particle may be separately embedded in a stabilizing medium. In principle this could work well, but after attempting a few different approaches, we determined that some more development is required before making jetting into a liquid bath a viable method.

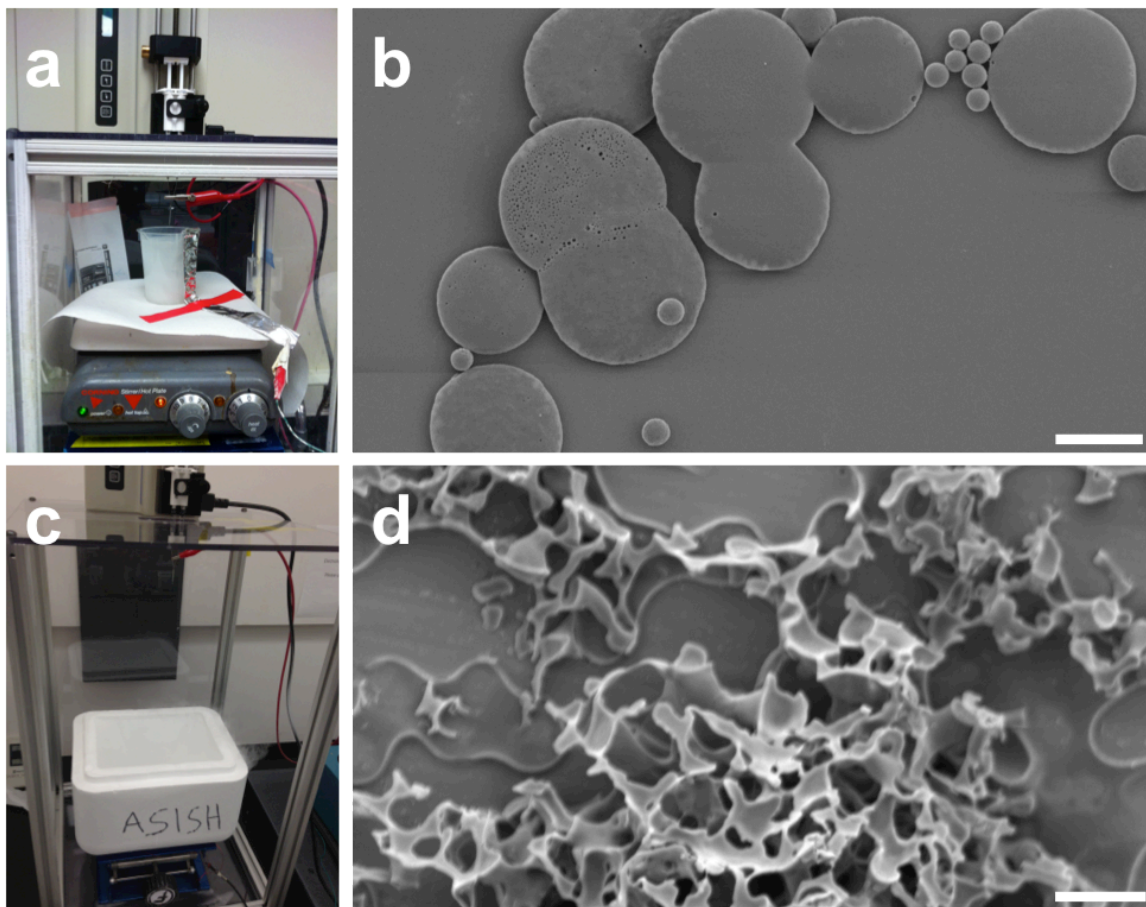


Figure 6-4. (a) Photo of EHD co-jetting into a water bath. (b) SEM image of PLGA particles made using the setup in (a). (c) Photo of EHD co-jetting into a liquid nitrogen bath. (d) SEM of PLGA structures made using the setup in (d). All scale bars are 10 μm .

In one attempt, PLGA solutions were co-jetted into an agitated water bath with surfactant (Figure 6-4a). We observed that jetted droplets remain on the water-air interface, as in the case of using chloroform as a solvent, resulting in flat or hemispherical particles (Figure 6-4b). When using miscible solvent such as acetone, much of the jetted solution contributed to a PLGA film forming at the interface. These observations may be attributable to the

potential inability of the jetted droplets to break through the surface and enter into the bulk water medium. One possible modification to this system could be to agitate the water bath in a way so as to prevent a contiguous water-air interface from being maintained.

Another approach we explored is co-jetting into a liquid nitrogen (liq. N₂) bath, as shown in Figure 6-4c. We expected that the jet droplets might more easily penetrate liq. N₂ than water because of its significantly lower surface tension. After co-jetting, we allowed the liq. N₂ to evaporate. However, we observed aggregates of wavy, porous PLGA films, shown in Figure 6-4d. The jetted droplets may have not completely evaporated, and therefore retain frozen solvent in the liq. N₂ bath. After evaporation of the liq. N₂, the droplets may melt and coalesce, resulting in the formation of such films. Hence, all the solvent in the droplets must be completely gone before reaching the bath to potentially manufacture particulate nanocarriers instead of films.

With further development, co-jetting into a liquid bath may serve as a viable method for high yield production of nanoparticles, but it may not be suitable for all biomedical applications. In particular, the co-jetting of drug-loaded nanoparticles into a water bath may be problematic, as drug would be released into the bath. Hence, other methods must still be developed and explored for generating high yields of multicompartmental nanocarriers.

6.3 Further Development of Current Systems

6.3.1 Tailored Environment-sensing Materials

Besides improving upon the EHD co-jetting process, significant further development can be made on many of the materials presented in these studies, many of which are not suitable particularly for *in vivo* studies. Much effort was focused on the development of endosome-sensing through pH-responsive materials. While endosomes are one of the few physiological environments where an acidic pH is encountered, low pH environments can also be found in, for instance, areas of inflammation and even cancer microenvironments.⁶⁻⁸ Hence it may be advantageous to further develop pH-sensitive materials (Chapter 2), such as poly(protected vitamin c) (PPVC) and acetalated high molecular weight dextran (AHM_wD), with responsiveness to, for example, the redox state of the environment, as intracellular spaces can contain high concentrations of glutathione.⁹ Developing a material tailored to swell or generate high osmotic pressures only within an endosome will allow for

the fabrication of carriers with a high specificity for escaping endosomes, and may result in exceptionally high efficiencies for cytosolic delivery.

6.3.2 Applications of Virus-mimicking Particles

EHD co-jetting is critical in the ability to fabricate the virus-mimicking particles (VMPs) developed in Chapter 3. The unique *in vitro* interactions of VMPs with plasma membranes warrant further investigation and exploration of potential applications. One aspect that has not been explored is whether the orientation of the VMPs can be controlled. As seen in Figure 6-5, despite having selective affinity for the cell membranes, the VMPs do not appear to be ordered in any manner on cells. It is possible that a small patch of the particles displaying striped gold nanoparticles (sAuNPs) is needed for selective binding to the membrane to occur. If so, it may be desirable to determine the minimum required amount of area covered with sAuNPs necessary for such affinity. Minimizing this area may result in ordered assemblies of VMPs on cells, and may be achieved by controlling the Janus balance via modulation of relative flow rates for each jetting solution during EHD co-jetting.

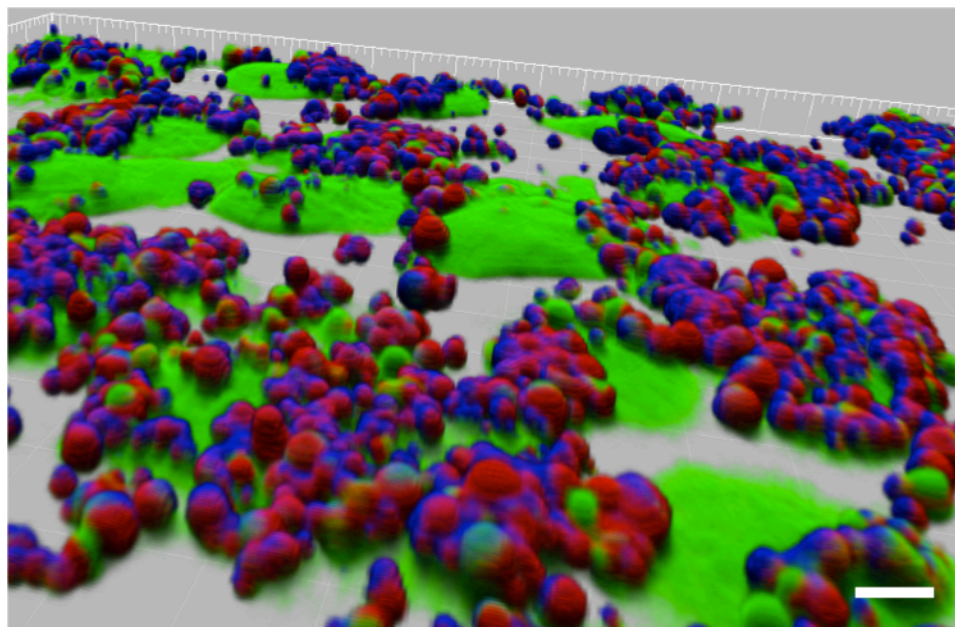


Figure 6-5. 3D reconstruction of a confocal zstack showing virus-mimicking particles (blue and red) bound to the membranes of breast cancer cells (green). Scale bar is 10 μm .

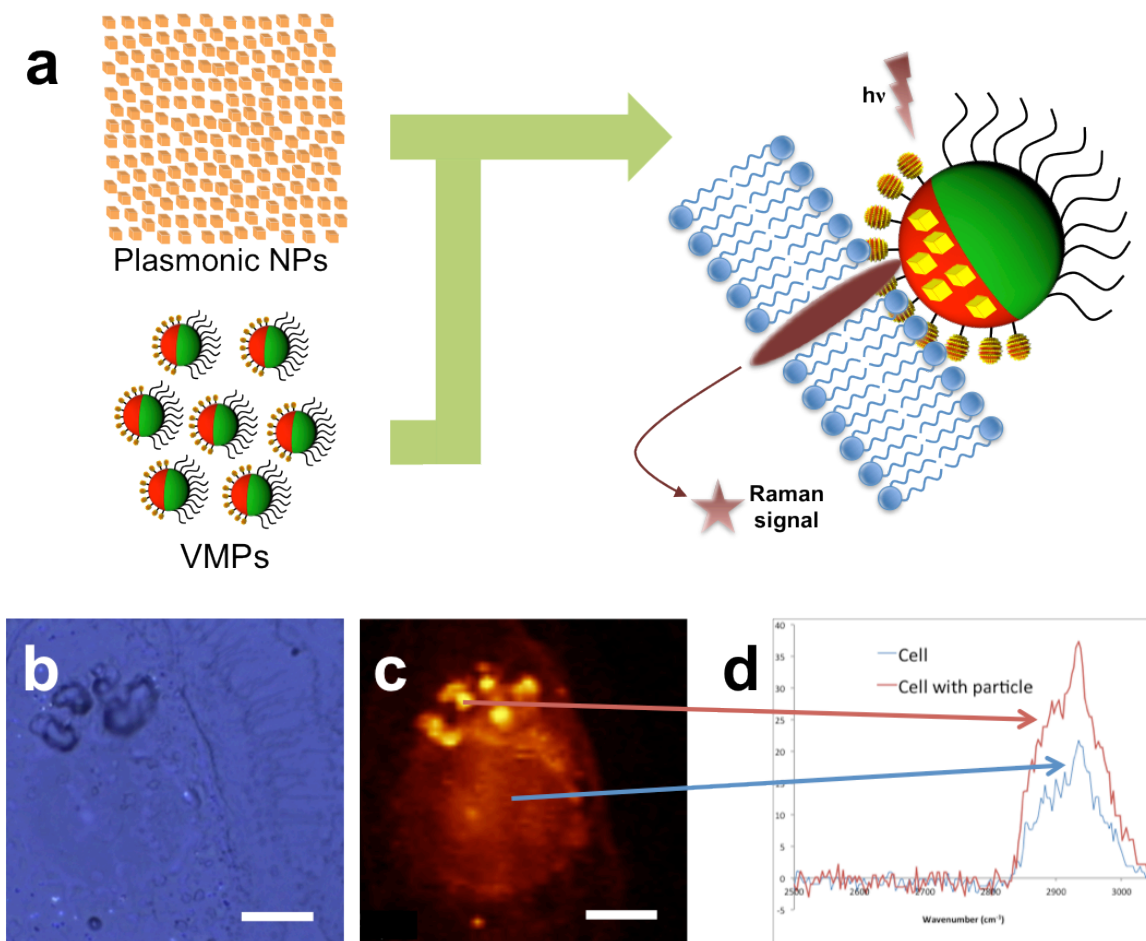


Figure 6-6. (a) Diagram showing how plasmonic nanoparticles may be incorporated into VMPs to investigate cell membranes using SERS. (b) Confocal brightfield image of VMPs bound to the surface of a cell. (c) Color map generated from the integration of C-H Raman peak. (d) Representative Raman spectra from a point on the cell, and from a point with both cellular material and a VMP. Scale bars are 10 μm .

Ordered assemblies of VMPs may have a number of potential applications. For instance, if controllable, precise domains can bind to cell membranes, then selective interrogation of features on the surface and in the membrane of a cell may be feasible. One such tool to study cell membranes may be surface enhanced Raman spectroscopy (SERS). Selective incorporation of plasmonic nanoparticles in a compartment of the VMPs, as depicted in Figure 6-6a, may allow for enhanced Raman signaling of membrane components. To investigate this possibility, we fixed VMPs on cells and scanned them with a Raman confocal microscope. On brightfield (Figure 6-6b), the VMPs are clearly identifiable from cells, allowing for validation of any color maps generated by Raman data. Figure 6-6c shows a color map representing the integration of a C-H peak, where we can identify cell components, as well as VMPs as brighter spots. Looking at the Raman spectra (Figure 6-6d),

the C-H Raman signal from a point where the cell and a particle are colocalized is roughly twice as large as the signal from a point with only cellular material. Given that SERS signals are several orders of magnitude higher than traditional Raman signals, we can expect that this two-fold difference will not mask any SERS signaling. As we have incorporated plasmonic nanoparticles in Chapter 2, integration of SERS-active particles with the fabrication of VMPs is a feasible next step.

6.3.3 Multicompartmental Capsular Carriers for Longer Circulation

In Chapter 4, we showed how EHD co-jetting may be used to fabricate carriers that could be subsequently surface modified with potentially high densities of nonfouling molecules such as polyethylene glycol (PEG). However, surface modifications alone are not capable of providing carriers with sufficiently long circulation times. It would hence be desirable if EHD co-jetting may be used to fabricate carriers with a number of other properties that can promote evasion of the immune system, such as soft mechanical properties.¹⁰ One possible way to achieve such properties is through selective deposition of polyelectrolytes by layer-by-layer (LbL) onto EHD co-jetted PLGA microcylinders; dissolution of the PLGA would leave capsular, nonrigid carriers that may have potentially longer circulation half-lives than their rigid counterparts.

As a proof of concept, we selectively attached PEI via EDC coupling to cylinders with acid groups on one side, and then deposited alternating layers of alginate and PEI, as shown in Figure 6-7a. The microcylinders appear porous (Figure 6-7b), but after LbL it can be seen in some cases that one side of the microcylinder appears smooth (Figure 6-7c), indicating selective LbL deposition. Dissolution of PLGA microcylinders with acetone yields shrunken objects (Figure 6-7d), potentially representing collapsed capsular structures. Further investigation into the selectivity of the LbL process is necessary, and performing two orthogonal LbL processes on the same microcylinder may allow for the synthesis of multicompartmental capsules. Additionally, it must be validated that the capsules remain uncollapsed and flexible in aqueous media, as the SEM images only show as shrunken or collapsed structures.

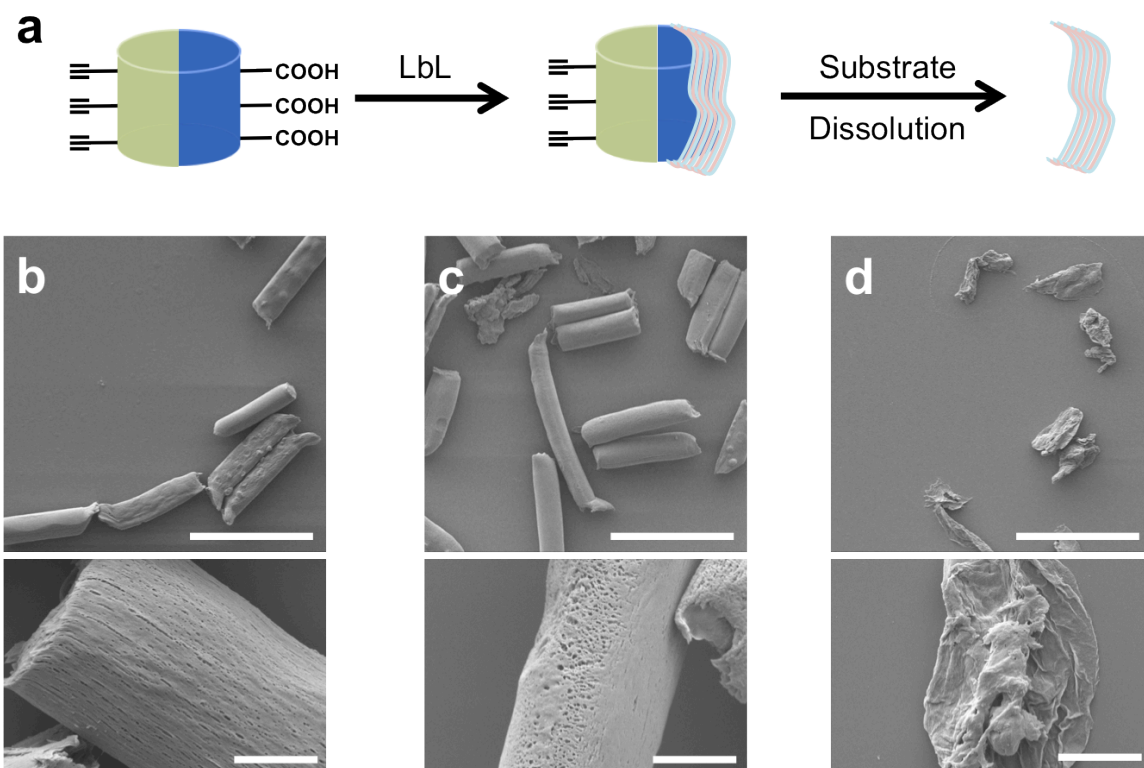


Figure 6-7. (a) Schematic showing how LbL based capsules were fabricated from EHD co-jetted microcylinders. SEM images of (b) microcylinders, (c) microcylinders after LbL, and (d) remaining microstructures after PLGA dissolution. Scale bars are 100 μm (top images) and 10 μm (bottom images).

6.4 Future Outlook

The work presented here may provide some foundation for how to fabricate multifunctional carriers via EHD co-jetting. In addition, some of the carrier systems developed here have been validated by *in vitro* studies, with the potential to move forward to sophisticated *in vivo* studies. To perform more extensive studies, larger yields of uniform carriers will be required. Therefore, improvements to the current fabrication process and novel methods are necessary, which may include a more detailed understanding of the dynamics and mechanics involved in EHD co-jetting. Experimentally validated theoretical models may provide robust predictive power and allow for guided searches of the parameter space, allowing for more efficient discovery of conditions necessary for uniformity and reproducibility.

Additionally, the materials underlying these carrier systems can be further developed. More sophisticated materials capable of sensing very specific environments like the endosome will

allow for exquisite control over the specificity in which a carrier may respond to its environment. To validate such materials, novel methods to test their abilities may be necessary. For example, the ability to measure the mechanical properties of and osmotic pressure within an endosome would allow for direct comparison and validation of different endosome-sensing materials. The combination of the development of more sophisticated materials and reproducible EHD co-jetting processes may allow for the development of efficient, multifunctional carriers with high therapeutic potential.

6.5 References

- 1 Tang, K. Q. & Smith, R. D. Physical/chemical separations in the break-up of highly charged droplets from electrosprays. *J Am Soc Mass Spectr* **12**, 343-347, doi:Doi 10.1016/S1044-0305(01)00222-7 (2001).
- 2 Taflin, D. C., Ward, T. L. & Davis, E. J. Electrified Droplet Fission and the Rayleigh Limit. *Langmuir* **5**, 376-384, doi:Doi 10.1021/La00086a016 (1989).
- 3 Chen, D. R., Pui, D. Y. H. & Kaufman, S. L. Electrospraying of Conducting Liquids for Monodisperse Aerosol Generation in the 4 Nm to 1.8 Mu-M Diameter Range. *J Aerosol Sci* **26**, 963-977, doi:Doi 10.1016/0021-8502(95)00027-A (1995).
- 4 Wilhelm, O., Madler, L. & Pratsinis, S. E. Electrospray evaporation and deposition. *J Aerosol Sci* **34**, 815-836, doi:Doi 10.1016/S0021-8502(03)00034-X (2003).
- 5 Paine, M. D. Transient electrospray behaviour following high voltage switching. *Microfluid Nanofluid* **6**, 775-783, doi:Doi 10.1007/S10404-008-0350-0 (2009).
- 6 Potts, D. E., Taryle, D. A. & Sahn, S. A. Glucose-Ph Relationship in Parapneumonic Effusions. *Arch Intern Med* **138**, 1378-1380, doi:Doi 10.1001/Archinte.138.9.1378 (1978).
- 7 Willerson, J. T. & Ridker, P. M. Inflammation as a cardiovascular risk factor. *Circulation* **109**, 2-10, doi:Doi 10.1161/01.Cir.0000129535.04194.38 (2004).
- 8 Yamagata, M., Hasuda, K., Stamato, T. & Tannock, I. F. The contribution of lactic acid to acidification of tumours: studies of variant cells lacking lactate dehydrogenase. *Brit J Cancer* **77**, 1726-1731, doi:Doi 10.1038/Bjc.1998.289 (1998).
- 9 Schafer, F. Q. & Buettner, G. R. Redox environment of the cell as viewed through the redox state of the glutathione disulfide/glutathione couple. *Free Radical Bio Med* **30**, 1191-1212, doi:Doi 10.1016/S0891-5849(01)00480-4 (2001).
- 10 Merkel, T. J. *et al.* Using mechanobiological mimicry of red blood cells to extend circulation times of hydrogel microparticles. *P Natl Acad Sci USA* **108**, 586-591, doi:Doi 10.1073/Pnas.1010013108 (2011).

Appendix A

Dispersion of Gold Nanorods in Organic Solvents

The material in this chapter has been adapted with modifications from the following article: A. C. Misra, H. Zhang, N. A. Kotov, J. Lahann. "Facile dispersion of gold nanorods in organic solvents by polymer complexation." *In Preparation*.

A.1 Background and Motivation

Gold nanorods (Au NRs) are a versatile class of gold nanoparticles with unique properties such as longitudinal surface plasmon resonance.¹ They are employed in diverse applications including optical memory,¹ tissue engineering,² cellular imaging,³ and in vivo drug delivery.⁴ Typically gold nanorods are manufactured by a nucleation process in which gold in salt form is reduced by ascorbic acid in the presence of cetyltrimethylammonium bromide (CTAB).⁵ By varying the ratio of concentration of gold salt, ascorbic acid, and CTAB, Au NRs of different sizes and aspect ratios can be synthesized.⁵ The gold nanorods are colloidally stable in water, stabilized by the surfactant CTAB. However, the rods cannot be dried and redispersed in organic solvents, which may be desirable for various processes such as electrospinning, layer-by-layer techniques, or drop casting of films. Additionally, for biologically applications, CTAB is not suitable as it is toxic.⁶

To achieve dispersion of gold nanorods in organic solvents, ligand exchange may be employed, in which another ligand is dissolved in an organic phase, and this phase is mixed with an aqueous dispersion of Au NRs, and the mixture is stirred for some time, allowing for the rods to transfer from the aqueous phase to the organic phase.⁶ These "phase transfer" steps may need to be repeated several times until the desired capping ligands are achieved.⁶ However, these methods do not necessarily have high yields and can often require a significant amount of time, solvent, and reagents.

Here we demonstrate a simple method employing polyethyleneimine (PEI) as a complexing or stabilizing agent for Au NRs that may displace CTAB while in aqueous dispersion. After lyophilization, these rods can be dispersed in a variety of solvents, including water, chloroform, tetrahydrofuran, dimethylformamide, and alcohols.

A.2 Methods

Materials. CTAB-capped gold nanorods (Au NRs) with a surface plasmon resonance (SPR) peak around 808 nm were purchased from Nanopartz and used without further purification. Polyethyleneimine (PEI, 60000 g/mol), polylactide-block-poly(ethylene glycol)-block-poly(lactide) (PLA-PEG-PLA), and poly(diallyldimethylammonium chloride) (PDDA) were purchased from Sigma-Aldrich. PEI and PDDA were freeze-dried and resuspended in double-deionized water (ddH₂O) to form concentrated solutions, and the PLA-PEG-PLA was dissolved in ddH₂O to form a concentrated solution as well.

Preparation of Au NR PEI complexes. Varying amounts of the aqueous PEI solution were added to constant amounts (20 µg) Au NRs in solution. The subsequent suspensions were vortexed for about 30 seconds and then kept at room temperature for at least 5 minutes. The suspensions were then frozen using liquid nitrogen and lyophilized overnight. The resulting Au NR PEI complexes were then resuspended in water and a variety of organic solvents. Other polymers were tested using this procedure, except instead of using PEI, polymers such as PLA-PEG-PLA and PDDA were tested.

Characterization. The complexes were characterized by visualization in organic solvents, and transmission electron microscopy (TEM) was performed as well, using a JOEL-2010F. UV-Vis spectroscopy was used to characterize the Au NR polymer complexes.

A.3 Results and Discussion

Upon visualization, when adding PEI to an aqueous Au NR solution, no color change was observable, as seen in Figure A-1a. When lyophilized and dispersed in chloroform (CHCl₃), the resulting dispersion appeared very close in color to the corresponding aqueous dispersion (Figure A-1b). In contrast, a clear color change, indicating aggregation, is visible from dispersing Au NRs complexed with PLA-PEG-PLA, as seen in Figure A-1c. To more clearly note any aggregation, we observed the CHCl₃ dispersions under TEM by drying them

on grids; Au NRs complexed with PEI appeared relatively well dispersed, while large aggregates of Au NRs complexed with PLA-PEG-PLA were observed (Figures A-1d and A1e). In addition, we attempted to complex Au NRs with PDDA, however, they did not disperse in CHCl_3 ; unlike PLA-PEG-PLA, large visible aggregates were observed with PDDA in chloroform. PLA-PEG-PLA, while soluble in both aqueous and organic solvents, is not cationic, while PDDA is cationic but not soluble in organic solvents. Hence, it is possible that PEI successfully stabilizes Au NRs in CHCl_3 due to both its cationic character and solubility.

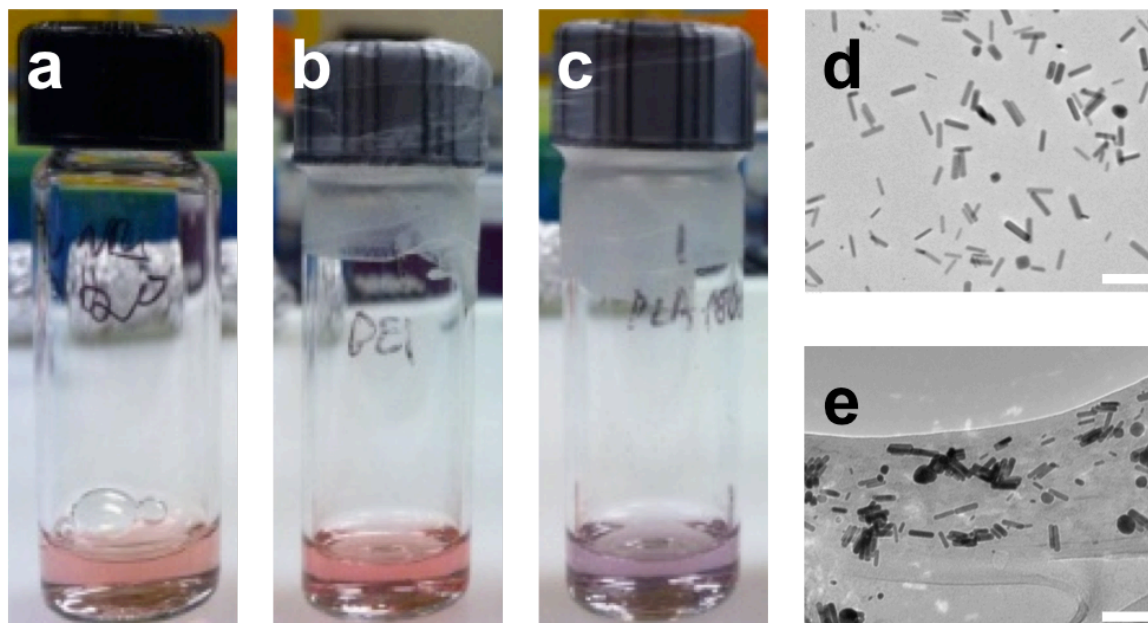


Figure A-1. (a) PEI added to Au NRs in water. (b) Au NR PEI complexes dispersed in CHCl_3 . (c) Au NR PLA-PEG-PLA complexes dispersed in CHCl_3 . TEM images of CHCl_3 dispersions of (d) Au NR PEI complexes and (e) Au NR PLA-PEG-PLA Complexes dried on TEM grids.

We then characterized dispersions of Au NR PEI complexes by UV-Vis spectrometry, as shown in Figure A-2. In CHCl_3 , some right shifting of the SPR peak by ~ 35 nm was observed as compared to pure Au NRs and Au NR PEI complexes in water, as shown in Figure A-2. The red shifting may suggest aggregation; however, no color change was appreciated and no aggregates were observed by TEM. We hence suspected that the shift might be accounted for by the difference in refractive index between water and CHCl_3 .

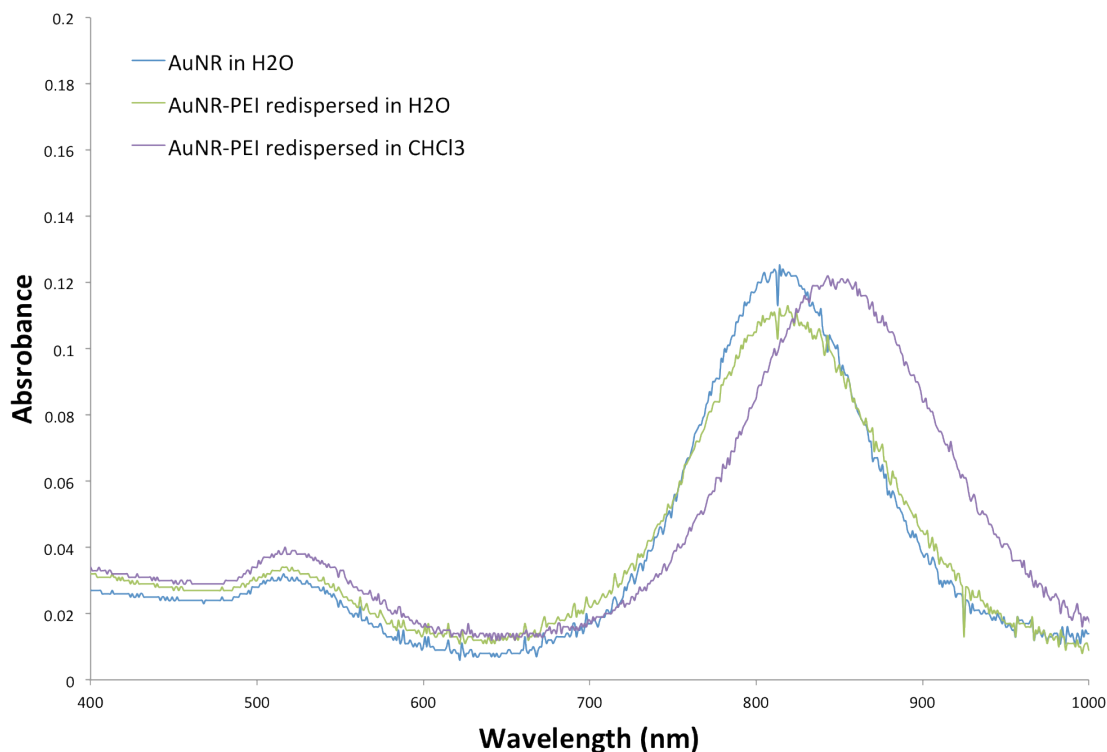


Figure A-2. UV-Vis spectra of Au NRs in H₂O and Au NR PEI complexes in H₂O and CHCl₃.

To determine whether the red shifting was a result of aggregation, we complexed Au NRs and PEI at different weight-by-weight ratios. If aggregation occurs after dispersion in CHCl₃, we would expect the degree of red shift to change depending on the relative ratio of PEI and Au NRs. As seen in Figure A-3, at high ratios of Au NRs to PEI, we observe an absence of the SPR peak, and found visible aggregates. However, once the ratio of Au NRs to PEI is 1:10 or lower, we observed the same SPR peak around 845 nm for all Au NR PEI complexes with sufficient amounts of PEI. Of note, the shift in SPR peak is constant and does not vary with the amount of PEI complexed with Au NRs. Hence, we may conclude that this shift is not a result of aggregation, but may be accounted for solely by the difference in refractive indices between water and CHCl₃.

Additionally, we found, from at least visual inspection, that the Au NR PEI complexes may disperse well in several other organic solvents, including ethanol, isopropanol, and N,N'-dimethylformamide (DMF). However, the complexes could not be dispersed in all organic solvents, notably tetrahydrofuran (THF), where large aggregate were observed. The

inability to disperse these complexes may be attributed to PEI's relatively low solubility in THF, resulting in the complexes crashing out of solution.

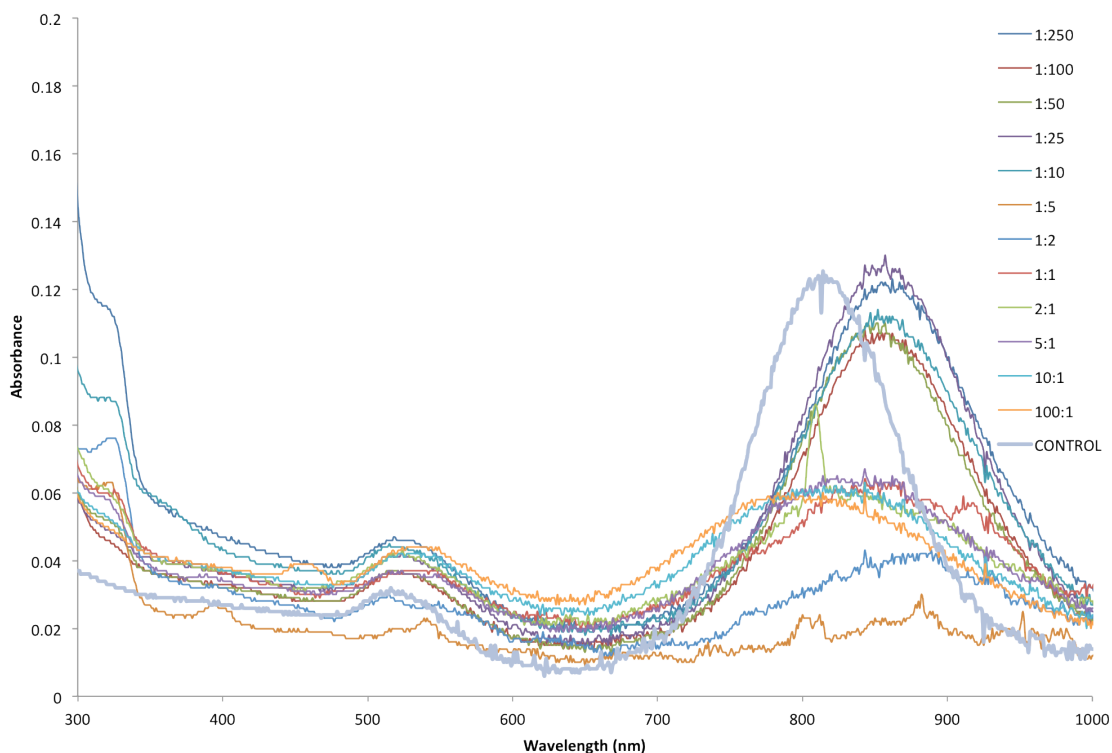


Figure A-3. UV-Vis spectra of CHCl_3 dispersions of Au NR PEI complexes prepared by varying weight-by-weight ratios of Au NRs to PEI. Control represents UV-Vis spectra of pure Au NRs in H_2O .

A.4 Summary

We have developed a 100% yield method (unlike methods such as ligand exchange) for transferring gold nanorods from an aqueous dispersion to a variety of organic solvents. PEI, which is both cationic and soluble in aqueous and organic solvents, allows for dispersion of gold nanorods without aggregation, as confirmed by visual inspection, TEM, and UV-Vis spectroscopy. The process requires a small amount of PEI, and therefore it is expected that processing of these PEI-Au NR complexes for other applications can be performed with minimal effect from the polymer. While this complexation with PEI can allow for dispersion in many organic solvents, it does not work for all, in particular, THF.

Not all cationic polymers or polymers with versatile solubility can be used as PEI has to disperse Au NRs in organic solvents, as is demonstrated by PDDA and PLA-PEG-PLA,

respectively. These observations imply that PEI's relative uniqueness, as a polymer that is both cationic and soluble in both organic and aqueous solvents, is a necessary property for this dispersion method.

A.5 References

- 1 Zijlstra, P., Chon, J. W. M. & Gu, M. Five-dimensional optical recording mediated by surface plasmons in gold nanorods. *Nature* **459**, 410-413, doi:Doi 10.1038/Nature08053 (2009).
- 2 Sisco, P. N. *et al.* The Effect of Gold Nanorods on Cell-Mediated Collagen Remodeling. *Nano Lett* **8**, 3409-3412, doi:Doi 10.1021/Nl802142h (2008).
- 3 Huang, X. H., El-Sayed, I. H., Qian, W. & El-Sayed, M. A. Cancer cell imaging and photothermal therapy in the near-infrared region by using gold nanorods. *J Am Chem Soc* **128**, 2115-2120, doi:Doi 10.1021/Ja057254a (2006).
- 4 von Maltzahn, G. *et al.* Nanoparticles that communicate in vivo to amplify tumour targeting. *Nature materials* **10**, 545-552, doi:Doi 10.1038/Nmat3049 (2011).
- 5 Jana, N. R., Gearheart, L. & Murphy, C. J. Wet chemical synthesis of high aspect ratio cylindrical gold nanorods. *J Phys Chem B* **105**, 4065-4067, doi:Doi 10.1021/Jp0107964 (2001).
- 6 Wijaya, A. & Hamad-Schifferli, K. Ligand customization and DNA functionalization of gold nanorods via round-trip phase transfer ligand exchange. *Langmuir* **24**, 9966-9969, doi:Doi 10.1021/La8019205 (2008).

Appendix B

Data Analysis for Raman Confocal Microscopy

B.1 Background and Motivation

Confocal Raman maps are derived from plotting of some quantity calculated from the Raman spectra at each point of a 2D scan obtained by a Raman confocal microscope. Here, we use a WITec alpha300R system, the software for which contains a robust set of analysis tools that were used to generate these maps.¹ For the work presented in this dissertation, two primary techniques were used for data analysis, peak integration and basis analysis.

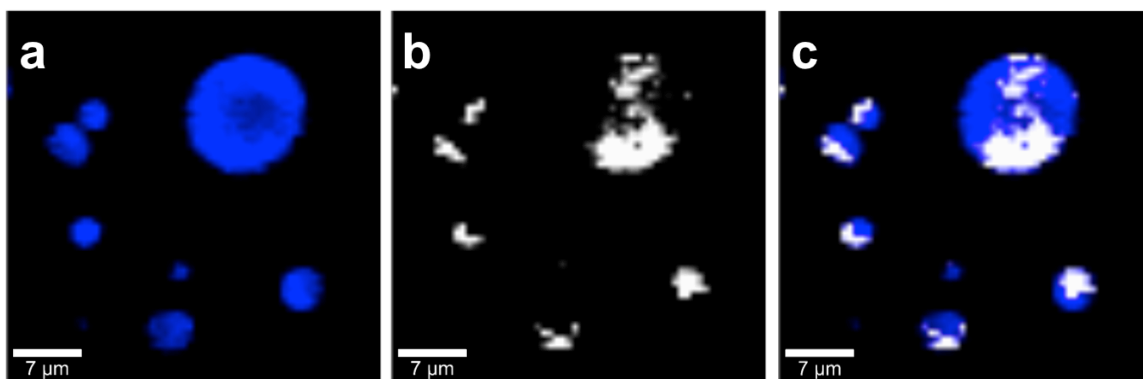


Figure B-1. Raman confocal color maps generated by peak integration from a scan of EHD co-jetted PLGA/PLGA-PS bicompartamental carriers on a silicon substrate. Color map of integration of (a) carboxyl peak ($1720\text{-}1815\text{ cm}^{-1}$) for PLGA, (b) $1575\text{-}1615\text{ cm}^{-1}$ for PS, and (c) overlay.

B.2 Methods

Raman maps are often used to show the localization of various different materials, each of which has a unique Raman signature. Often times, if there are Raman peaks unique to each material, those peaks may be integrated and the intensities may be plotted with color maps, as we have shown previously,² and shown in Figure B-1, where bicompartamental particles consisting of a pure PLGA compartment, and a PLGA/PS blend compartment. However,

when materials have no unique peaks, determining the relative location of different species in a confocal image may require the use of basis analysis.

Basis analysis relies on the assumption that the Raman spectrum \vec{S} at any point is a superposition of the unique pure Raman spectrum \vec{e}_i of each individual i material at that point: $\vec{S} = \sum_{i=1}^n a_i \vec{e}_i$, where a_i is a scalar quantity representing the relative contribution of material i to the overall Raman spectra \vec{S} . Hence, the set of pure spectra \vec{e}_i forms a basis set from which all possible spectra in the confocal scan could be generated by a linear combination of them. Given \vec{e}_i for all materials, one may perform a best fit to the spectrum \vec{S} at each point. These best-fitted weights can then be used to generate color maps spatially showing the relative amounts of each material. In particular, the WITec software allows for facile computation of a least squares regression, where the square of the residual at each wavelength j are summed:

$$\min_{a_1, \dots, a_n} \sum_j \left[\vec{S}(j) - \sum_{i=1}^n a_i \vec{e}_i \right]^2$$

One particular caveat of using this method is the requirement of having the pure spectra \vec{e}_i , which are not necessarily known. In this case, one must estimate the pure spectra \vec{e}_i . One method of estimation may be to determine areas of the scan where only a few species (less than the total number of species) are known to be colocalized. We may use peak integration as a rough estimate to determine such areas, average the spectra over those areas. After linearly transforming this set of averaged spectra we may then obtain estimates of the pure Raman signature for each species, and then perform the basis analysis (least squares regression). This process is illustrated in Figure B-2 for the PLGA/PLGA-PS bicompartmental particles – based on peak integration we could identify three areas – an area with only substrate (black), areas with PLGA and substrate (blue), and areas with PLGA, PS and substrate (white and blue overlaid). The linear transformation in this case would involve subtracting the substrate spectra from the blue averaged spectra, resulting in an estimate of the pure PLGA spectrum, and then the pure PS spectrum may be estimated from the white and blue overlaid areas by subtracting the a weighted sum of the substrate and PLGA spectra.

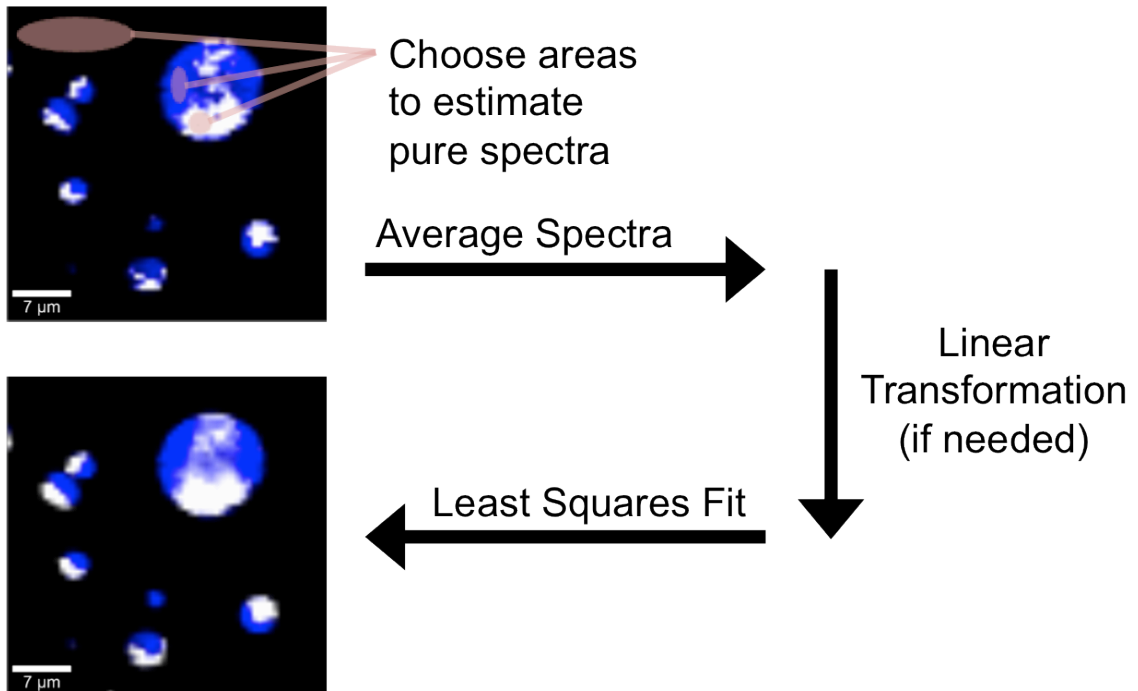


Figure B-2. Flow diagram showing how to estimate pure spectra from a color map obtained by peak integration (top), and the resulting color map (bottom) from basis analysis.

B.3 References

- 1 Gierlinger, N., Keplinger, T. & Harrington, M. Imaging of plant cell walls by confocal Raman microscopy. *Nat Protoc* **7**, 1694-1708, doi:Doi 10.1038/Nprot.2012.092 (2012).
- 2 Rahmani, S. *et al.* Chemically Orthogonal Three-Patch Microparticles. *Angew Chem Int Edit* **53**, 2332-2338, doi:Doi 10.1002/Anie.201310727 (2014).